Structural and biochemical characterization of USP28 inhibition by small molecule inhibitors

Strukturelle und biochemische Charakterisierung der Hemmung von USP28 durch niedermolekulare Inhibitoren

Doctoral Thesis

for a doctoral degree at the Graduate School of Life Sciences
Julius-Maximilians-Universität-Würzburg
Section Biomedicine

Submitted by

Radhika Karal Nair

From Bangalore, India

Würzburg 2022

Submitted on: ……

Office Stamp

Members of *Promotionskomittee*:

Chairperson: Prof. Dr. Jürgen Seibel

Primary Supervisor: Prof. Dr. Caroline Kisker

Supervisor (Second): Prof. Dr. Nikita Popov

Supervisor (Third): Prof. Dr. Alexander Buchberger

Supervisor (Fourth): Prof. Dr. Christoph Sotriffer

Date of Public Defence: ……

Date of Receipt of Certificates: ……

The truth is, most of us discover where we are headed when we arrive.

– Bill Watterson, creator, *Calvin and Hobbes*

AFFIDAVIT

I hereby confirm that my thesis entitled **Structural and biochemical characterization of USP28 inhibition by small molecule inhibitors** is a result of my own work. I did not receive any help from commercial consultants. All sources and/or materials applied are listed and specified in this thesis.

Furthermore, I confirm that this thesis has not yet been submitted as part of another examination process neither in identical nor similar form.

Würzburg, ...

Date Signature

EIDESSTATTLICHE ERKLÄRUNG

Hiermit erkläre ich an Eides statt, dass die Dissertation **Strukturelle und biochemische Charakterisierung der Hemmung von USP28 durch niedermolekulare Inhibitoren** eigenständig, d.h. insbesondere selbstständig und ohne Hilfe eines kommerziellen Promotionsberaters, angefertigt und keine anderen als die von mir angegebenen Quellen und Hilfsmittel verwendet zu haben.

Ich erkläre außerdem, dass die Dissertation weder in gleicher noch in ähnlicher Form bereits in einem anderen Prüfungsverfahren vorgelegen hat.

Würzburg, ...

Datum Unterschrift

ABSTRACT

Ubiquitination is an important post-translational modification that maintains cellular homeostasis by regulating various biological processes. Deubiquitinases (DUBs) are enzymes that reverse the ubiquitination process by catalyzing the removal of ubiquitin from a substrate. Abnormal expression or function of DUBs is often associated with the onset and progression of various diseases, including cancer. Ubiquitin specific proteases (USPs), which constitute the largest family of DUBs in humans, have become the center of interest as potential targets in cancer therapy as many of them display increased activity or are overexpressed in a range of malignant tumors or the tumor microenvironment.

Two related members of the USP family, USP28 and USP25, share high sequence identities but play diverse biological roles. USP28 regulates cell proliferation, oncogenesis, DNA damage repair and apoptosis, whereas USP25 is involved in the anti-viral response, innate immunity and ER-associated degradation in addition to carcinogenesis. USP28 and USP25 also exhibit different oligomeric states – while USP28 is a constitutively active dimer, USP25 assumes an auto-inhibited tetrameric structure. The catalytic domains of both USP28 and USP25 comprise the canonical, globular USP-domain but contain an additional, extended insertion site called **U**SP25/28 **c**atalytic domain **i**nserted **d**omain (UCID) that mediates oligomerization of the proteins. Disruption of the USP25 tetramer leads to the formation of an activated dimeric protein. However, it is still not clear what triggers its activation.

Due to their role in maintaining and stabilizing numerous oncoproteins, USP28 and USP25 have emerged as interesting candidates for anti-cancer therapy. Recent advances in small-molecular inhibitor development have led to the discovery of relatively potent inhibitors of USP28 and USP25. This thesis focuses on the structural elucidation of USP28 and the biochemical characterization of USP28/USP25, both in complex with representatives of three out of the eight compound classes reported as USP28/USP25-specific inhibitors. The crystal structures of USP28 in complex with the AZ compounds, Vismodegib and FT206 reveal that all three inhibitor classes bind into the same allosteric pocket distant from the catalytic center, located between the palm and the thumb subdomains (the S1-site). Intriguingly, this binding pocket is identical to the UCID-tip binding interface in the USP25 tetramer, rendering the protein in a locked, inactive conformation. Formation of the binding pocket in USP28 requires a shift in the helix α5, which induces conformational changes and local distortion of the binding channel that typically accommodates the C-terminal tail of

Ubiquitin, thus preventing catalysis and abrogating USP28 activity. The key residues of the USP28-inhibitor binding pocket are highly conserved in USP25. Mutagenesis studies of these residues accompanied by biochemical and biophysical assays confirm the proposed mechanism of inhibition and similar binding to USP25.

This work provides valuable insights into the inhibition mechanism of the small molecule compounds specifically for the DUBs USP28 and USP25. The USP28-inhibitor complex structures offer a framework to develop more specific and potent inhibitors.

ZUSAMMENFASSUNG

Ubiquitinierung ist eine wichtige posttranslationale Modifikation, die die zelluläre Homöostase aufrechterhält, indem sie verschiedene biologische Prozesse reguliert. Deubiquitinasen (DUBs) sind Enzyme, die den Ubiquitinierungsprozess umkehren, indem sie die Entfernung von Ubiquitin von einem Substrat katalysieren. Eine abnorme Expression oder Funktion von DUBs wird häufig mit dem Auftreten und Fortschreiten verschiedener Krankheiten, einschließlich Krebs, in Verbindung gebracht. Ubiquitin-spezifische Proteasen (USPs), die im Menschen die größte Familie der DUBs bilden, sind als potenzielle Ziele in der Krebstherapie von besonderem Interesse, da viele von ihnen in bösartigen Tumoren oder deren Mikroumgebung abnormal aktiv oder überexprimiert sind.

Die zwei eng verwandten Mitglieder der USP-Familie, USP28 und USP25, weisen eine hohe Sequenzidentität auf, sind aber an unterschiedlichen biologischen Prozessen beteiligt. USP28 reguliert die Zellproliferation, die Onkogenese, die Reparatur von DNA-Schäden und die Apoptose, während USP25 eine Rolle bei der antiviralen Reaktion, der angeborenen Immunität, dem ER-assoziierten Abbau und der Carcinogenese spielt. USP28 und USP25 weisen auch unterschiedliche oligomere Zustände auf. Während USP28 ein konstitutiv aktives Dimer bildet, tritt USP25 als auto-inhibiertes Tetramer auf. Strukturell bestehen die katalytischen Domänen sowohl von USP28 als auch von USP25 aus der kanonischen globulären USP-Domäne enthalten jedoch eine zusätzliche Insertion, die als „**U**SP25/28 **c**atalytic domain **i**nserted **d**omain (UCID)“ bezeichnet wird und die Oligomerisierung der Proteine vermittelt. Die Dissoziation des USP25 Tetramers in Dimere führt zu einem aktivierten USP25-Protein. Es ist jedoch immer noch nicht klar, was seine Aktivierung auslöst.

Aufgrund ihrer Rolle bei der Aufrechterhaltung und Stabilisierung zahlreicher Onkoproteine haben sich USP28 und USP25 als interessante Kandidaten für die Entwicklung von Medikamenten in der Krebstherapie erwiesen. Jüngste Fortschritte in der Entwicklung von niedermolekularen Inhibitoren haben zur Entdeckung von relativ potenten Inhibitoren von USP28 und USP25 geführt. Diese Arbeit konzentriert sich auf die Strukturaufklärung von USP28 und die biochemische Charakterisierung von USP28/USP25, beide im Komplex mit Vertretern von drei der acht Verbindungsklassen, die als USP28/USP25-spezifische Inhibitoren bekannt sind. Die Kristallstrukturen von USP28 im Komplex mit den AZ-Verbindungen, Vismodegib und FT206 zeigen, dass alle Inhibitoren in einer ähnlichen

Region an USP28 binden - einer allosterischen Tasche, die in der Nähe des katalytischen Zentrums liegt und sich zwischen der Handflächen- und der Daumen-Subdomäne befindet. Diese Bindungstasche ist identisch mit der Position, an der der „UCID-tip“ im USP25-Tetramer bindet und das Protein in eine verschränkte, inaktive Konformation versetzt. Die Bildung der Bindungstasche in USP28 erfordert eine Verschiebung der α5-Helix, die zu Konformationsänderungen und einer lokalen Verzerrung des Bindungskanalsführt, der normalerweise den C-terminus des Ubiquitin-Moleküls bindet und so die Katalyse verhindert und die Aktivität von USP28 hemmt. Die Schlüsselreste der USP28-Inhibitor-Bindungstasche sind in USP25 hoch konserviert. Mutagenese-Studien dieser Aminosäuren, begleitet von biochemischen und biophysikalischen Analysen, bestätigen den vorgeschlagenen Mechanismus der Hemmung und eine ähnliche Bindung der Inhibitoren an USP25.

Diese Arbeit liefert wertvolle Einblicke in den Hemmungsmechanismus der Kleinmolekülverbindungen, die spezifisch für die DUBs USP28 und USP25 entwickelt worden sind. Die Strukturen der USP28-Inhibitor-Komplexe bieten eine Grundlage für die zukünftige Entwicklung spezifischerer und wirksamerer Inhibitoren.

TABLE OF CONTENTS

1. INTRODUCTION

1.1 The Ubiquitin System

1.1.1 Ubiquitin

Ubiquitin (Ub), a 76-amino acid, highly conserved protein, was first discovered over forty years ago as a post-translational modification that labels proteins for degradation (Ciechanover, 2015). Since then, Ub has emerged as a crucial player that regulates virtually all aspects of eukaryotic biology. From yeast to humans, all eukaryotes possess the enzymatic machinery to modify target proteins with Ub through a process called ubiquitination or ubiquitylation. This process involves the covalent attachment of Ub *via* an isopeptide bond, formed between its terminal glycine residue and the ε-amino group of a lysine residue on the target protein.

Ubiquitination regulates multiple aspects of cellular proliferation and survival, including DNA repair, macromolecular trafficking, signaling and immunological recognition though it is arguably best known for its role in mediating controlled protein degradation (Hershko & Ciechanover, 1998; Goldberg, 2007). Malfunction or dysregulation of ubiquitination can lead to detrimental consequences – it may cause abnormal activation or deactivation of signaling pathways, accumulation of misfolded or damaged proteins, mislocalization or mistrafficking of proteins from their associated compartments, all of which can severely hinder regular cell functioning. Thus, defects in ubiquitin signaling have been associated with numerous human diseases and pathologies such as cancers, developmental, immune and neurodegenerative disorders (Ciechanover, 2003; Ciechanover & Schwartz, 2004).

The transfer of a single Ub (monoubiquitination) to a substrate lysine residue marks the first step in ubiquitination. This process often occurs in cells and serves a variety of functions. However, Ub can be polymerized by ubiquitinating any of the seven internal lysine residues (K6, K11, K27, K29, K33, K48 and K63) or the α-amino group of the N-terminal methionine (M1) within Ub. This contributes to a diverse Ub topology, often called the 'ubiquitin code', comprising eight types of homotypic polyubiquitin chains and a wide range of heterotypic, mixed, and branched polyubiquitin chains, each accompanied by a variety of cellular effects (Komander & Rape, 2012). For example, polyubiquitination *via* K48 targets substrate proteins for degradation by the proteasome (Hochstrasser, 1996; Hicke, 2001), while

K63-linked chains are involved in signaling functions independent of proteolysis (Chen, 2005; Terzic et al., 2007; Iwai & Tokunaga, 2009) (Figure 1.1).

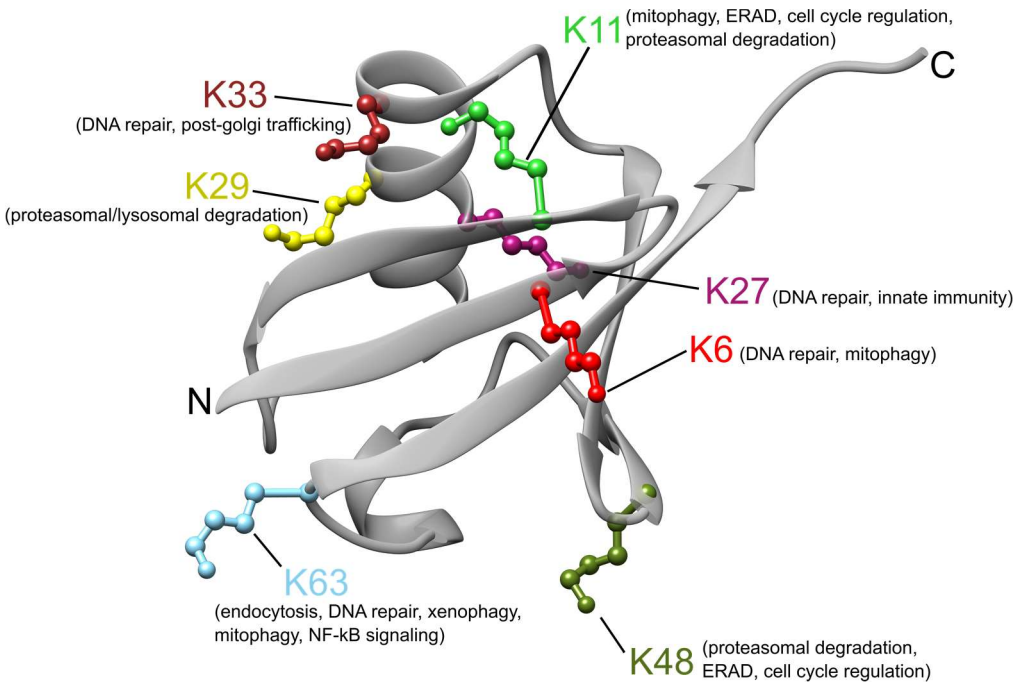

Figure 1.1: Structure of Ubiquitin (from 1UBQ) illustrating the N-terminus, the seven lysine side chains and the C-terminus that can be covalently linked to the target lysine *via* an isopeptide bond. The downstream biochemical processes regulated by each chain type are mentioned in parentheses.

1.1.2 Ubiquitination cascade

The covalent attachment of Ub molecules to target proteins requires the concerted action of three enzymes: the Ub-activating enzyme (E1), the Ub-conjugating enzyme (E2), and the Ub-ligase (E3) (Figure 1.2) (Amerik & Hochstrasser, 2004; S. Fang & Weissman, 2004).

The E1 enzyme catalyzes the ATP-dependent activation of Ub by forming a thioester bond between the C-terminus of Ub and a cysteine residue in the E1 active site. The activated Ub is then transferred to the E2 enzyme. The final transfer of activated Ub to the target proteins is carried out by the E3 ligases, either directly by forming a covalent bond intermediate with the Ub (HECT-type E3 ligases) or by acting as a scaffold between the Ub-loaded E2 enzyme and the target protein (RING-type E3 ligase) (Sarikas et al., 2011). The third type of E3 ligase is the RING-between-RING (RBR) E3s containing a RING domain and an active site Cys, combining properties of the HECT-type and the RING-type E3s (Dove & Klevit, 2017).

While the human genome encodes only 2 E1 enzymes, the identification of ~40 E2 and ~1000 E3 enzymes add to the substrate specificity and versatility of the ubiquitination process.

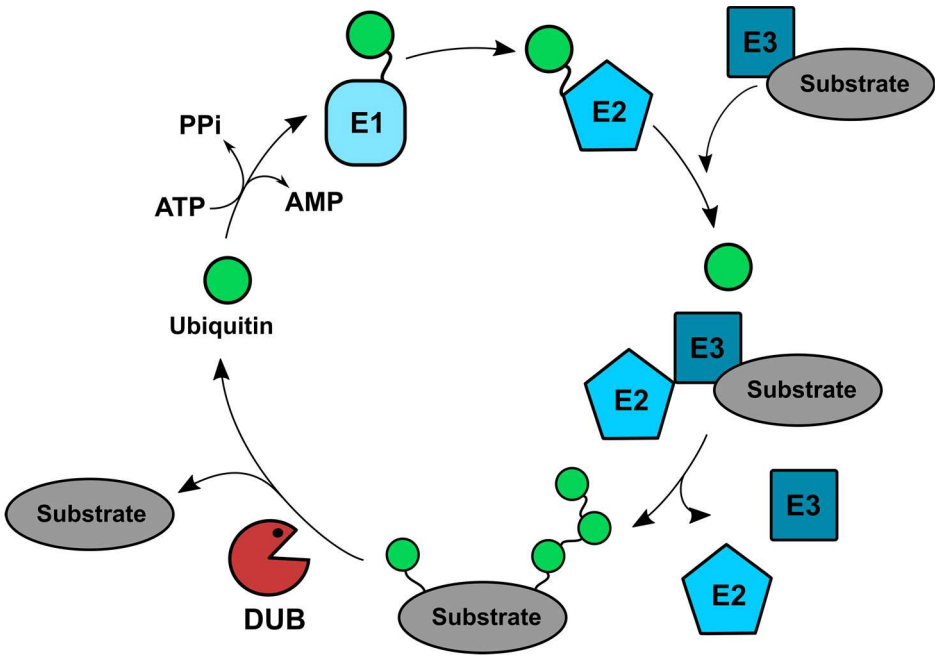

Figure 1.2: The ubiquitination pathway is a multi-enzymatic cascade resulting in the transfer of an activated Ub-molecule to a target protein. This cycle can also occur repeatedly, resulting in a polyubiquitinated substrate.

1.1.3 Deubiquitinases

Deubiquitinases (DUBs) are enzymes that catalyze the removal of Ub moieties from target proteins or polyubiquitin chains by hydrolyzing the isopeptide bond between them. DUBs are also involved in the *de novo* synthesis of Ub – they generate free, active Ub molecules by the cleavage of multiple precursors that are encoded by four genes (UBC, UBB, UBA52 & UBA80) (Callis, 2014; Park & Ryu, 2014). They can reverse Ub signaling and rescue proteins fated for proteasomal or lysosomal degradation by removing Ub chains, thus stabilizing the protein. DUBs also contribute to Ub homeostasis by recycling Ub from degraded proteins into the free Ub pool (Park & Ryu, 2014).

DUBs identify their substrates either directly or by the specific Ub chain that they carry. As mentioned in Section 1.1.1, Ub chains comprise linkages *via* seven internal lysines or an N-terminal methionine. The Ub chains that form due to these different attachment points have different topologies that DUBs can identify. Most DUBs are promiscuous and can cleave several Ub chain types to some extent, in which case the ubiquitinated substrate, rather than

the Ub chain, is most likely used to infer specificity (Komander et al., 2009; Faesen et al., 2011). However, in some cases, DUBs can only process ubiquitin chains that they recognize directly. Whether polyubiquitin is cleaved from the distal or proximal end (exo-cleavage) or within a chain (endo-cleavage) is determined by the arrangement and kind of Ub-binding sites in DUBs (Clague et al., 2019).

1.1.3.1 Classification of DUBs

About 100 DUBs have been identified in humans, which are broadly classified into seven families based on sequence and domain conservation: Ubiquitin-specific proteases (USPs), Ubiquitin carboxy-terminal hydrolases (UCHs), Machado-Josephin domain-containing proteases (MJDs), ovarian tumor proteases (OTUs) (Komander et al., 2009; Mevissen & Komander, 2017), motifs interacting with ubiquitin-containing novel DUB family (MINDYs) (Abdul Rehman et al., 2016), zinc-finger with UFM1-specific peptidase domain proteins (ZUFSPs) (Kwasna et al., 2018) and the JAB1, MPN, MOV34 family (JAMMs) (Komander et al., 2009). While the first six DUB families are cysteine (iso)peptidases, the JAMMs are zinc metallopeptidases.

1.1.3.2 Ubiquitin Specific Proteases (USPs)

With close to 60 proteins encoded by the human genome, the USPs constitute the largest family of DUBs (Quesada et al., 2004). All members comprise a structurally conserved catalytic domain that assumes a papain-like fold resembling the palm, thumb and finger of a right hand. Embedded within the thumb and palm motifs are the residues of the catalytic triad (Cys, His, Asp/Asn) (Ye et al., 2009; Amerik & Hochstrasser, 2004). The junction between the thumb and palm regions form a cleft that accommodates the C-terminal tail of Ub and the active site residues responsible for catalysis.

The catalytic activity of USPs is often regulated either by substrate- or scaffold-induced conformational changes, as demonstrated in the case of USP7. In the *apo*- form, the catalytic triad residues of USP7 are found to be misaligned and in an inactive state. However, upon Ub-binding, a significant conformational change realigns these residues in close proximity to each other, thereby rendering the enzyme active (Hu et al., 2002).

All USPs comprise blocking loops 1 and 2 (BL1 and BL2) within their catalytic domain, although these may not be similar in length and sequence. In USP8 (Hu et al., 2005) and

USP14 (H. T. Kim & Goldberg, 2017), these blocking loops prevent catalysis by occluding the active site region in the *apo* state. Also adding to the regulation of USPs are the switching loops (SL), which are essential for catalytic activity.

Most USPs also contain additional domains that flank the central catalytic domain and are often responsible for substrate recognition, protein-protein interactions, and regulation of catalytic activity. These domains include ubiquitin-associated domains (UBAs), Ubiquitin-interacting motifs (UIMs), Ubiquitin-like domains (UBLs) and zinc-finger motifs (Komander et al., 2009; X. Zhu et al., 2007). UBLs adopt highly diverse roles from associating with the proteasome, regulating USP catalytic activity and serving as a binding scaffold for protein-protein interactions (H. T. Kim & Goldberg, 2018).

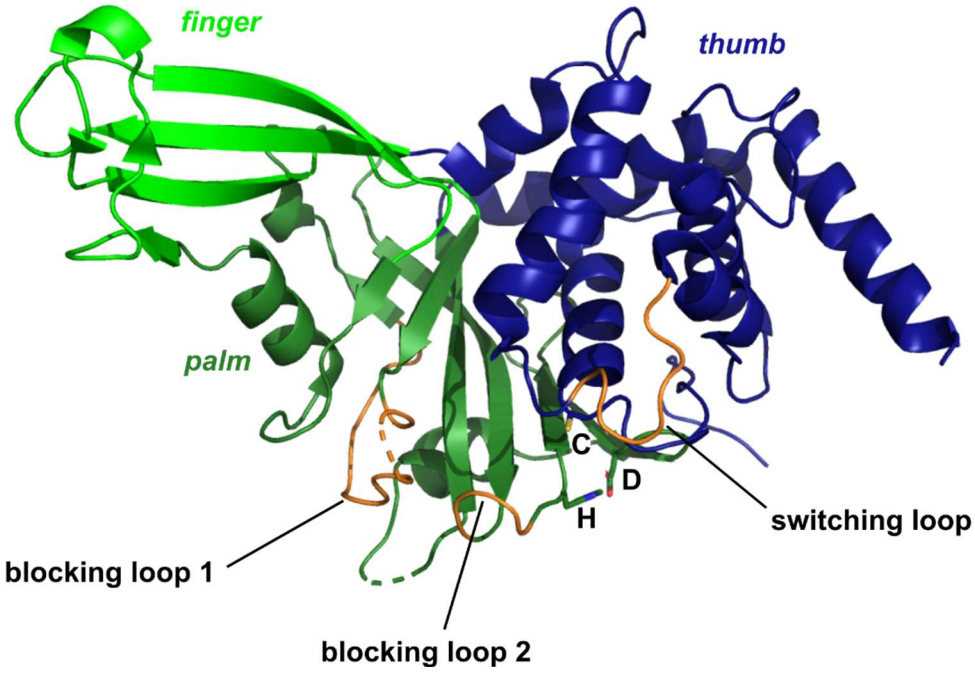

Figure 1.3: The catalytic domain of USPs exhibits a papain-like fold consisting of the thumb, palm and finger regions (as highlighted). The structure of USP7 (PDB: 1NB8) depicts the blocking loops and the switching loop (orange) that play important roles in USP regulation and catalysis. The catalytic triad residues are represented in sticks.

1.1.3.3 Catalytic mechanism of USPs

As described earlier, the catalytic triad of USPs comprises a cysteine residue that acts as a nucleophile, a histidine residue that serves as an acid-base to deprotonate the cysteine and an aspartate (or in some cases, asparagine) that stabilizes the histidine (Figure 1.4, step 1).

The deprotonated cysteine nucleophilically attacks the isopeptide bond linking the Ub molecule and the substrate (Figure 1.4, step 2). This results in a negatively charged tetrahedral intermediate, stabilized by an oxyanion hole (Figure 1.4, step 3). However, this 'oxyanion' state is volatile and collapses upon protonation assisted by the histidine, releasing the substrate (Figure 1.4, step 4). An active site water molecule nucleophilically attacks the carbonyl carbon of the thiol-ester intermediate, forming a second tetrahedral intermediate (Figure 1.4, step 5), driving the release of the Ub substrate. Subsequently, the DUB returns to its basal state (Figure 1.4, step 6).

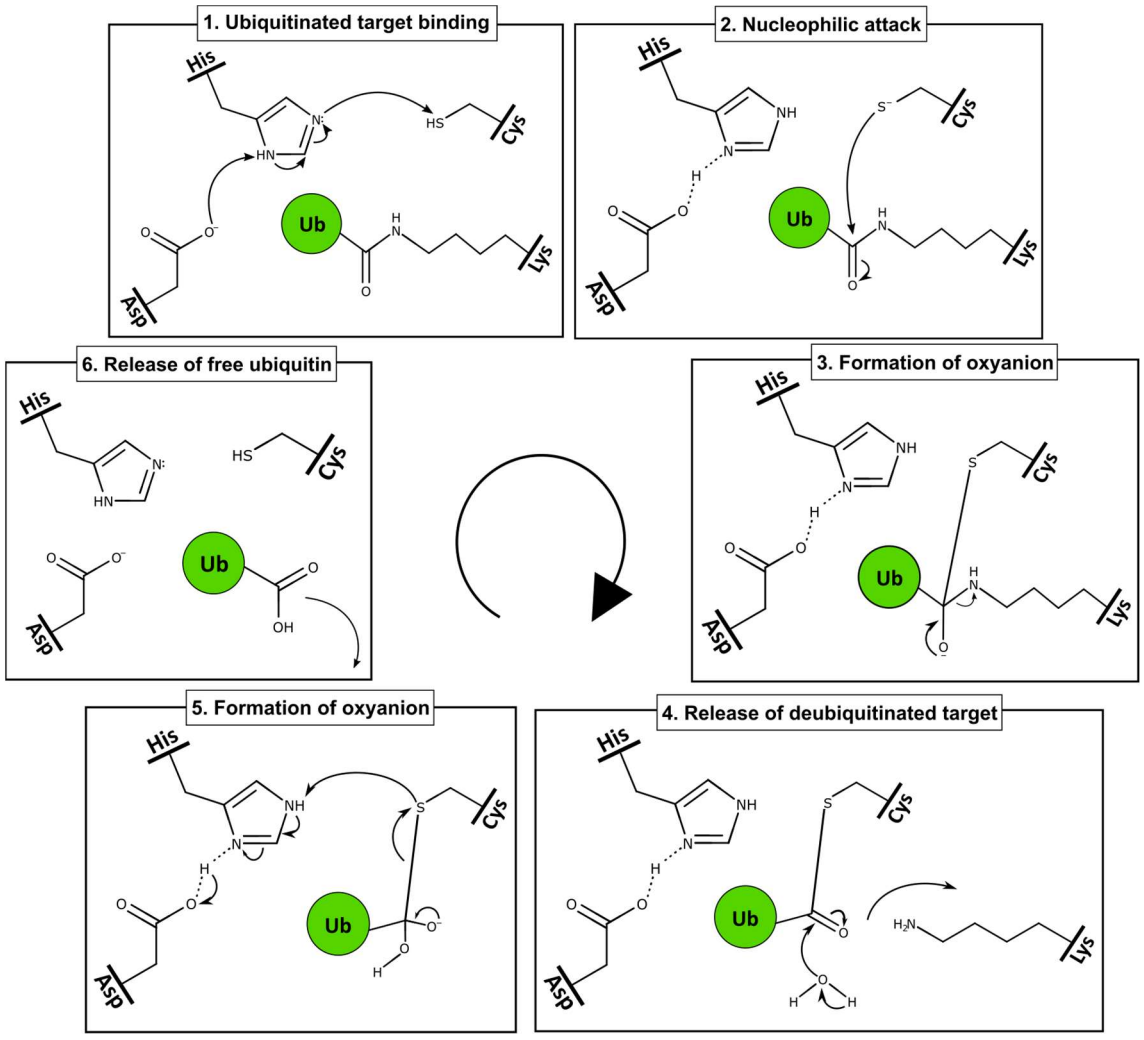

Figure 1.4: Mechanism of isopeptide-cleavage by the USPs. The active site histidine, stabilized by the aspartate of the catalytic triad, deprotonates the cysteine (1) and nucleophilically attacks the ubiquitinated substrate to form a tetrahedral intermediate (2). This precarious oxyanion state (3) collapses, releasing the free substrate. A water molecule acts as a nucleophile to attack the thiol-ester bond (4) to form another tetrahedral intermediate, driving Ub release and regenerating the free enzyme. Figure adapted from (R. Kim, 2019).

1.2 Ubiquitin specific proteases - USP28 and USP25

As this thesis focuses majorly on the two USP family members, USP28 and USP25, they will be described in detail below.

1.2.1 Biological functions of USP28 and USP25

Both USP28 and USP25 play a crucial role in a plethora of biological processes, summarized in Figure 1.5.

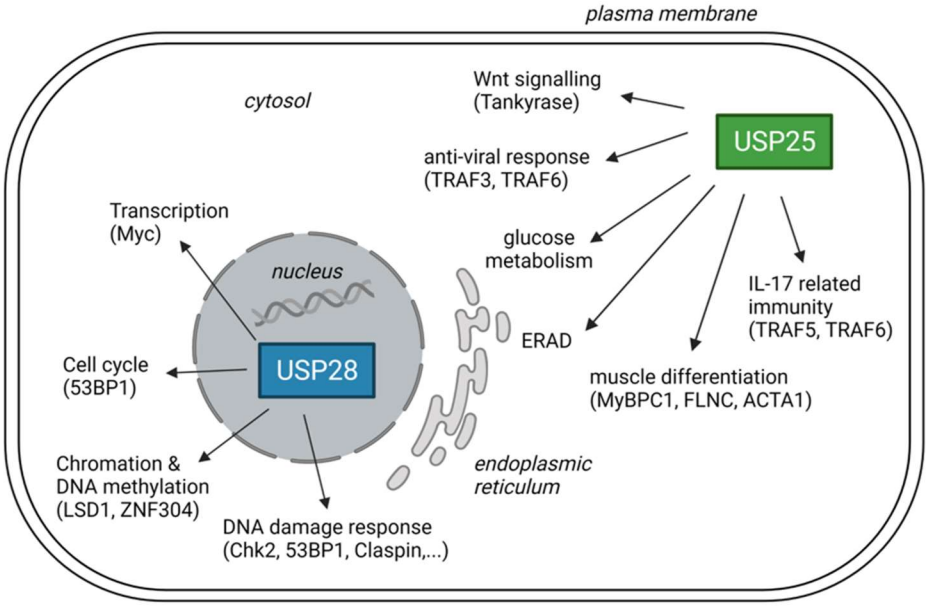

Figure 1.5: Biological roles of USP28 and USP25. A schematic representation of the currently known cellular functions linked to USP28 and USP25. Subcellular compartments and structures are labelled in italics. Figure adapted from Gersch et al., 2019 and created with Biorender.com.

1.2.1.1 USP28

USP28 regulates several processes, including cell proliferation, oncogenesis, DNA damage repair and apoptosis. It specifically cleaves K48-, K63- and K11- linked Ub chains (Zhen et al., 2014). While the shorter isoform missing 32 amino acids (Isoform 2) expresses ubiquitously, the expression of the longer isoform (Isoform 1) is seen in the heart, brain and muscle (Valero et al., 2001).

USP28 in cancer –

Localized in the nucleus, USP28 displays both tumor-promoting and tumor-suppressing properties due to its tissue-specific effects. It counteracts the activity of Fbxw7 and promotes c-MYC stability in cancer cells (Popov et al., 2007). Fbxw7 is an F-box protein that determines substrate specificity of the Skp1-cullin1-F-box (SCF) type E3 ligase. It, therefore, controls cell differentiation, cell proliferation and apoptosis by targeting key transcriptional factors of the UPS (Cremona et al., 2016). Previous studies using genetically engineered mouse models have demonstrated that loss of Fbxw7 function due to USP28 overexpression significantly accelerated the progression of murine colorectal tumors by accumulating oncoproteins such as c-MYC, c-Jun, Notch-1, ΔNp63 etc. Alternatively, USP28 deletion counteracted the loss of Fbxw7, decreasing oncoprotein stability (Diefenbacher et al., 2014, 2015).

Fbxw7 undergoes autocatalytic ubiquitination, and interestingly, USP28 deubiquitinates Fbxw7 and, therefore, directly stabilizes the protein (Schülein-Völk et al., 2014). This dual function of USP28 can be explained due to its varying levels in different cell types, thereby influencing the stability and regulation of Fbxw7 in these cells and aiding in maintaining the physiological levels of proto-oncogenic substrates of Fbxw7 (W. Xu et al., 2016).

USP28 is also involved in the maintenance of other carcinogenic substrates. It upregulates angiogenesis by antagonizing the glycogen synthase kinase 3β (GSK-3β) and Fbxw7-dependent degradation of the hypoxia-inducible factor-1α (HIF-1 α). HIF-1 α is a major regulator of various processes associated with hypoxic conditions. Upon phosphorylation by GSK-3β, Fbxw7 degrades HIF-1 α. However, this process is reversed on USP28 overexpression (Flügel et al., 2012; X. Wang et al., 2018).

USP28 is implicated in the epigenetic regulation of breast cancer as well. Based on a siRNA screen, USP28 was identified as the bona fide DUB of the lysine-specific demethylase (LSD1). LSD1 is an epigenetic regulator that regulates pluripotency and differentiation by demethylating the histone H3K4me1/2. Knockdown of USP28 leads to LSD1 destabilization, thereby suppressing cancer stem-cell-like characteristics *in vitro* and inhibiting tumorigenicity *in vivo* (Wu et al., 2013). In another study, histone deacetylase 5 (HDAC5) was found to promote USP28 stability and overexpression of USP28 reversed HDAC5-knockdown induced LSD1 degradation, implying that HDAC5 positively regulates LSD1 through stabilizing USP28 (Cao et al., 2017).

The function of USP28 in squamous cell carcinoma (SCC) was recently elucidated. USP28 is highly expressed in SCC and helps stabilize the squamous transcription factor ΔNp63, as well as other key oncoproteins such Notch1, c-MYC, and c-Jun. In SCC patients, USP28 gene expression was linked to a poor prognosis and shortened lifespan. SCC tumors in lung cancer mice models require high levels of the USP28-ΔNp63 axis to maintain the malignant phenotype, and the pharmacological inhibition of USP28 drastically decreases the number of SCC tumors in lung cancer mouse models (Prieto-Garcia et al., 2021; Prieto-Garcia et al., 2020). USP28 was also suggested as a promising target for treating squamous cell lung carcinoma (LSCC). In established LSCC, USP28 inactivation causes dramatic tumor regression. The treatment of USP28 with a small molecule inhibitor recapitulates LSCC regression in both mouse models and human LSCC xenografts. The protein levels of c-MYC, c-JUN, and Δp63 were significantly lowered when USP28 was absent or inhibited, suggesting a possible mode of action for the inhibitor compound (Ruiz et al., 2020).

USP28 enhances cell viability and aerobic glycolysis of colorectal cancer by stabilizing the protein Forkhead Box C1 (FOXC1). This protein binds to integrin α-7 or fibroblast growth factor 4 to promote and enhance colorectal cancer metastasis. In colorectal cancer cells treated with a protein synthesis inhibitor (cycloheximide), overexpression of USP28 enhanced FOXC1 expression, whereas its knockdown had an opposite effect, suggesting that deubiquitination of FOXC1 *via* USP28 could increase aerobic glycolysis in colorectal cancer cells (Z. Liu et al., 2021).

<u>USP28 in DNA damage repair</u> –

USP28 was initially identified as a binding partner of the double-strand break repair protein, 53BP1. USP28 interacts with and stabilizes 53BP1, which results in the phosphorylation of the serine residues S67 and S714 in USP28 in an ATM-dependent manner (Knobel et al., 2014; Zhang et al., 2006).

USP28 also regulates the stability of other proteins involved in DNA damage repair (DDR), such as checkpoint kinase 2 (Chk2) and mediator of DNA damage checkpoint protein 1 (MDC1) (Bohgaki et al., 2013; Zhang et al., 2006).

USP28 has also been implicated in the proliferation of triple-negative breast cancer (TNBC), a highly aggressive and malignant form of cancer that is not currently treated with any targeted therapies. USP28 regulates the expression of RECQL5, a member of the RecQ family of

helicases that is essential for the proliferation and survival of TNBC cells. shRNA-mediated knockdown or pharmacological inhibition of USP28 caused TNBC cells to arrest in the S/G2 phase, concurrent with DNA damage checkpoint activation (J. Wang et al., 2021).

USP28 in cell cycle regulation –

USP28 prevents the anaphase-promoting complex/cyclosome (APC/C) E3-ligase mediated degradation of CLASPIN, thus maintaining the G2/M phase DNA damage checkpoint during cell cycle (Ito et al., 2018).

Protein target	**Effect of USP28**	**Function of USP28**
53bp1	Increases stability	Tumor suppressor
CCNE	Increases stability	Oncoprotein
CDC44	Increases stability	Oncoprotein
Chk2	Increases stability	Tumor suppressor
c-Jun	Increases stability	Oncoprotein
CLASPIN	Increases stability	Tumor suppressor or oncoprotein (dependent on cellular context)
c-MYC	Increases stability	Oncoprotein
Fbxw7	Increases stability	Tumor suppressor
FOXC1	Increases stability	Oncoprotein
H2A	Enhances transcriptional activation	Tumor suppressor
HIF-1α	Increases stability	Tumor suppressor or oncoprotein (dependent on cellular context)
LIN28A	Increases stability	Oncoprotein
LSD1	Increases stability	Oncoprotein
MCL1	Increases stability	Oncoprotein
MDC1	Increases stability	Tumor suppressor
MTOR	Increases stability	Oncoprotein
Notch-1	Increases stability	Oncoprotein
p53	Increases stability	Tumor suppressor
STAT3	Increases stability	Oncoprotein
UCK1	Increases stability	Tumor suppressor
ZNF304	Increases stability	Oncoprotein
ΔNp63	Increases stability	Oncoprotein

Table 1.1: Comprehensive list of USP28 cellular targets and its impact on their stability (adapted from Prieto-Garcia et al., 2021)

1.2.1.2 USP25

As a result of alternative splicing, at least three isoforms of USP25 have been identified, of which two are expressed ubiquitously (Valero et al., 2001; Bosch-Comas et al., 2006; Blount et al., 2012). Isoform USP25a is found in most adult and fetal tissues, while isoform USP25b is found in all tissues except the heart and skeletal muscle. Isoform USP25m consists of an additional muscle-specific domain and is localized specifically in the heart and skeletal muscle, where it interacts with several sarcomeric proteins and is upregulated during myogenesis. It is also found in adipocytes. (Blount et al., 2012; Bosch-Comas et al., 2006).

USP25 preferentially cleaves K48-linked Ub substrates to K63-linked Ub substrates. The tandem UIMs in the protein display a binding preference to K48-linked chains by selectively holding the ubiquitin substrates in proximity to the catalytic core. (Kawaguchi et al., 2017).

USP25 in cancer –

USP25 is not only located in the nucleus and cytoplasm (Bosch-Comas et al., 2006; Denuc & Bosch-Comas, 2009) but is also found in the endoplasmic reticulum (ER), where it negatively regulates ER-associated degradation (ERAD) (Blount et al., 2012). Various human malignancies have been linked to disruptions of the UPS caused by changes in USP25 activity. Overexpression of USP25 was observed to be more than threefold in breast cancer tissues compared to adjacent normal tissues, indicating a significantly enhanced role of the protein in breast cancer (Deng et al., 2007). Similarly, USP25 mutations were found in the whole genome analysis of 27 Hepatocellular carcinoma (HCC) samples. (Fujimoto et al., 2012).

USP25 positively regulates the Wnt/β-catenin signaling by directly interacting with and stabilizing Tankyrases (TNKS). A scaffolding protein named axin negatively regulates Wnt-signaling by controlling the rate-limiting step in the destruction of β-catenin, the central activator of the Wnt pathway. TNKS-mediated poly(ADP-ribosyl)ation of axin promotes its proteolysis, thereby stabilizing β-catenin. USP25 deletion promotes degradation of TNKS, leading to stability of axin to antagonize Wnt signaling (D. Xu et al., 2017). Another associated study describes the identification of a small molecule, C44, that disrupts the USP25-TNKS interaction, thus increasing the half-life of axin. Selective inhibition of the USP25-TNKS interaction by C44 significantly reduces the proliferation of prostate cancer cells, as evidenced by both *in vivo* and *in vitro* experiments (Cheng et al., 2019).

The deletion or downregulation of USP25 has also been implicated in human lung cancer progression (Yamada et al., 2008), while its overexpression indicates a poor outcome in stomach adenocarcinoma (D. Fang & Lu, 2020). A recent elegant study by Shibata et al. demonstrates the role of USP25 inhibition to overcome tyrosine kinase inhibitor resistance. One of the significant drawbacks in treating chronic myeloid leukemia (CML) is the resistance to tyrosine kinase inhibitors. The breakpoint cluster region (BCR)-c-abl oncogene 1 (ABL) protein is a fusion gene commonly found in CML. shRNA mediated depletion of USP25 led to increased ubiquitination and thus degradation of BCR-ABL in Philadelphia (Ph)-positive leukemia patients. Furthermore, pharmacological inhibition of USP25 accelerated BCR-ABL degradation in cells carrying the Ph-chromosome, regardless of the patient's sensitivity to tyrosine kinase inhibitors (Shibata et al., 2020).

The evasion of receptor downregulation is an essential mechanism by which cancer cells show unregulated activation of the epidermal growth factor receptor (EGFR). Because it modulates receptor internalization, translocation, and degradation, EGFR ubiquitination is critical in this process. USP25 acts as a negative regulator of the EGFR downregulation by disrupting oncogenic growth signaling in EGFR-dependent malignancies. USP25 could prevent EGFR degradation in the early stages of internalization by promoting the E3 ubiquitin ligase c-Cbl interaction with EGFR (Niño et al., 2020).

USP25 in immune response –

While there is overwhelming evidence of its function in numerous cancers, USP25 also plays a vital role in inflammatory processes and immune responses. Overexpression of USP25 suppressed interleukin 17 (IL-17)–mediated signaling and inflammation by interacting with tumor necrosis factor receptor-associated factors 5 and 6 (TRAF5 and TRAF6). USP25 is essential for TRAF5 and TRAF6 deubiquitination but not for other TRAF proteins. The E3 ligase Act1 catalyzes K63-mediated ubiquitination of TRAF5 and TRAF6. However, IL-17 stimulation of USP25 induces its association with TRAF5 and TRAF6, thus opposing Act1 activity (Zhong et al., 2012).

USP25 is also an essential regulatory component of the lipopolysaccharide (LPS)-mediated macrophage activation and virus-triggered type I interferon (IFN) signaling pathway. When the toll-like receptor 4 (TLR4) is stimulated by the LPS, USP25 was found to reverse the K48-linked ubiquitination of TRAF3 preferentially. This action enhances the activation of transcription factor interferon regulatory factor 3 (IRF3) but attenuates TLR4-induced

activation of nuclear factor kappa-B (NF-κB). The subsequent phosphorylation and dimerization of IRF3 promotes its translocation from the cytoplasm to the nucleus and results in the activation of IFN-inducible genes and inflammatory mediator expression (Zhong et al., 2013). In addition, increased ubiquitination of TRAF3 due to USP25-knockdown induces endotoxin tolerance in macrophages (Wen et al., 2019).

Upon viral infection, USP25 associates with and protects TRAF3 and TRAF6 from virus-induced proteasome-dependent or independent degradation and thus, USP25-deficient mice were more susceptible to herpes simplex virus 1 or H5N1 virus infection (Lin et al., 2015).

USP25 in neurodegeneration –

USP25 also has important implications for Alzheimer's disease (AD). Overexpression of the amyloid precursor protein (APP) gene on chromosome 21 in Down syndrome (DS) has been linked to increased brain amyloid levels and early-onset of AD (Doran et al., 2017). In response to ER stress, UPS rapidly degrades APP, resulting in the production of β-amyloid (Aβ), the major pathological hallmark of AD. USP25 interacts with and enhances the stability of full-length APP, resulting in the accumulation of misfolded APP (Jung et al., 2015). In a study conducted by Zheng et al. with a combined DS-AD mouse model, triplication of homologous chromosome 21 genes displayed aggravated neuroinflammation. Overexpression of USP25, which is encoded by chromosome 21, induces microglial activation and causes synaptic and cognitive deficits in 5xFAD mice. However, USP25 genetic deletion lowers neuroinflammation and restores synaptic and cognitive function. Microglia-mediated overproduction of pro-inflammatory cytokines was diminished upon USP25 deletion. But, pharmacological inhibition of USP25 restored synaptic and cognitive function in mice *via* restoring homeostatic microglial signaling (Zheng et al., 2021).

Protein target	Effect of USP25	Function of USP25
APP	Increases its stability	Promotes development of AD
BCR-ABL	Increases its stability	Induces proliferation of myeloid leukemia
EGFR	Increases its stability	Modulates internalization of EGFR
HBO1	Increases its stability	Promotes inflammatory gene transcription
HDAC11	Increases its stability	Reduced USP25/HDAC11 may induce increased bacterial infection in smokers
MyBPC1	Increases its stability (only with USP25m)	Possible role in myopathies
PTEN	Increases its stability	Suppresses NSCLC progression
RIG-I	Increases its stability	Inhibits type-I IFN induction
TNKS	Increases its stability	Positively regulates Wnt/β-catenin pathway
TRAF2	Increases its stability	Inhibits type-I IFN induction
TRAF3	Increases its stability	Regulates TLR4-mediated immune response; promotes endotoxin tolerance
TRAF5	Increases its stability	Inhibits IL-17 mediated signaling
TRAF6	Increases its stability	Inhibits IL-17 mediated signaling
TUG	Promotes its proteolytic cleavage stimulated by insulin (only with USP25m)	Essential for translocation of glucose transporter (GLUT4)

Table 1.2: Comprehensive list of USP25 cellular targets and its involvement in associated pathways

1.2.2 Domain architecture and structural insights

Originating from a common ancestor (Valero et al., 2001), USP28 and USP25 are highly homologous, sharing the same overall domain architecture with the conserved USP fold and remarkable sequence conservation (Figure 1.6). The N-terminus harbors the Ub-binding region (UBR), comprising a Ub-associated domain (UBA) and two Ub-interacting motifs (UIMs). Additionally, a SUMO (small Ub-like modifier)-interacting motif (SIM) integrated into the UBR regulates both proteins (Meulmeester et al., 2008; Denuc & Bosch-Comas, 2009; Zhen et al., 2014). While a canonical catalytic USP domain is approx. 350 amino acids long, it spans in USP28/USP25 about 550 amino acids due to a long insertion of, until recently, unknown function (Ye et al., 2009). The remaining ~340 residues that form the C-terminal region is primarily α-helical (unpublished data, Klemm, 2020) and have been

suggested to play a role in substrate binding, which is established for several substrates in USP25 (Cholay et al., 2010; Lin et al., 2015; D. Xu et al., 2017).

As mentioned earlier, at least two isoforms of USP28 and three isoforms of USP25 resulting from alternate splicing have been identified. The longer isoforms exhibit muscle/tissue specificity, while the shorter isoforms are expressed ubiquitously (Valero et al., 2001; Bosch-Comas et al., 2006; Blount et al., 2012).

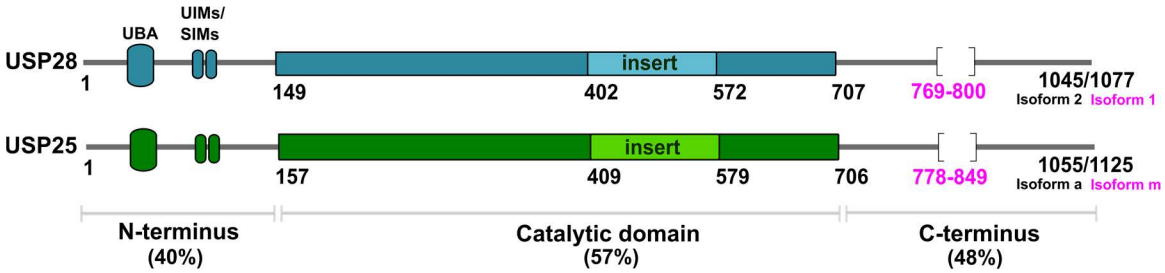

Figure 1.6: Domain architecture of USP28 (blue) and USP25 (green). The central catalytic USP domain extends by a 170 amino acid long insertion of a previously unknown function (indicated in light blue for USP28 and in light green for USP25). The N-terminus comprises the UBA, UIM and SIM. Isoform-specific sequences are indicated in pink. The sequence conservation between Isoform 2 of USP28 and Isoform a of USP25 is shown in parentheses. Figure adapted from (Klemm, 2020).

Despite the high conservation and sequence identity, recent structural and functional studies of the USP28 and USP25 catalytic domains (referred to as USP28cat and USP25cat, respectively) have provided interesting insights into how subtle differences in the sequences can alter the oligomeric state and impact the enzymatic activity (Gersch et al., 2019; B. Liu et al., 2018; Sauer et al., 2019).

Based on data from size exclusion chromatography coupled with multi-angle light scattering (SEC-MALS), sedimentation velocity analytical ultracentrifugation (SV-AUC) and small-angle X-ray scattering (SAXS) experiments, a dimeric state was shown for USP28cat, suggesting that the catalytic domain directly mediated self-association. Interestingly, USP25cat containing the insertion assumed a tetrameric state compared to the monomeric behavior of the insert-lacking form and the dimeric form of the UCID-tip lacking form.

1.2.2.1 Structure of USP28 catalytic domain

The structure of USP28cat revealed how the protein dimerizes. The domain adopts the canonical, globular USP fold with the thumb, palm and finger subdomains connected by a fourth subdomain, an insertion site formed by the 170 aa segment, referred to as the **U**SP25/28 **c**atalytic domain **i**nserted **d**omain (UCID) (Figure 1.7a.).

The UCID comprises two structurally distinct regions: the lower UCID-rod, formed by an anti-parallel, bipartite coiled-coil and the upper UCID-tip, forming an 80 aa long disordered loop. The UCID-rod extends from the palm region perpendicular to the finger domain, to which it is linked by several side-chain interactions. These interactions are responsible for the restricted positioning of the finger subdomain in USP28, while other USPs lacking such an insertion are less restricted with respect to the position of the finger subdomain, as can be readily observed, for example, in the structures of USP8 and USP18 (Avvakumov et al., 2006; Basters et al., 2017). Symmetric association of the upper regions of the two UCID-rods through the helix α9, the N-terminal part of helix α10 and the connecting loop between helices α8 and α9 leads to the dimerization of the protein. The dimerization is mediated by a large hydrophobic surface surrounded by several H-bonds and polar contacts. In addition, the thumb subdomain of both molecules is extended N-terminally by a short segment of five residues comprising 3_{10} helix α1 and points in the same direction as the C-terminus, thus suggesting proximity between them.

The binding of USP28cat to Ub is similar to that seen in USP7 (Ernst et al., 2013) and USP21 (Hu et al., 2002), wherein the globular Ub domain binds to a concave surface provided by the thumb, palm and finger subdomains (the S1 site) (Figure 1.7b). The C-terminal Ub-tail binds into a cleft formed between the thumb and the palm region, inducing conformational changes in blocking loops 1 and 2 (BL1 and BL2) and the switching loop (SL) (Figure 1.7b, inset). While BL1 becomes more ordered, forming H-bonds with the Ub-molecule, BL2 moves outwards and paves the way for the Ub-tail. The SL also becomes more ordered and acts as a lid to shield the cleft from above and, at the same time, stabilizes the Ub-tail through putative H-bonds. Since both USP28cat monomers bind to Ub, this suggests that they may simultaneously catalyze the reaction.

Multiple constructs of USP28cat were subjected to SEC-MALS to validate the observed dimeric interface. Data analysis shows that the variant lacking the UCID-tip region or modified *via* site-specific mutations did not alter the oligomeric state. However, introducing

a negative charge in the center of the hydrophobic interface of the two UCID rods prevented dimerization. This result established that the central hydrophobic core is sufficient to promote USP28 association while the adjacent UCID-tip region and the surrounding hydrophilic interactions are not essential.

Further investigations of differences in the enzymatic activities revealed that while the wild-type and monomeric variants displayed identical kinetic parameters, the insertion-lacking variant showed a 3-fold reduction in K_m but not K_{cat}. This variant also showed a drastic decrease in protein stability, whereas deletion of the UCID-tip region had no effect, as seen from thermal shift analysis (Gersch et al., 2019).

Data from these studies showed that although the insertion does not affect the enzymatic activity *per se*, it does seem to substantially impact the stability of the catalytic domain and the Ub-binding site, possibly due to the UCID's role in positioning the finger subdomain. Further structural data supported this hypothesis since a structure lacking the insert revealed that parts of the finger subdomain were disordered in the *apo*-structure but not in the Ub-bound forms (Gersch et al., 2019).

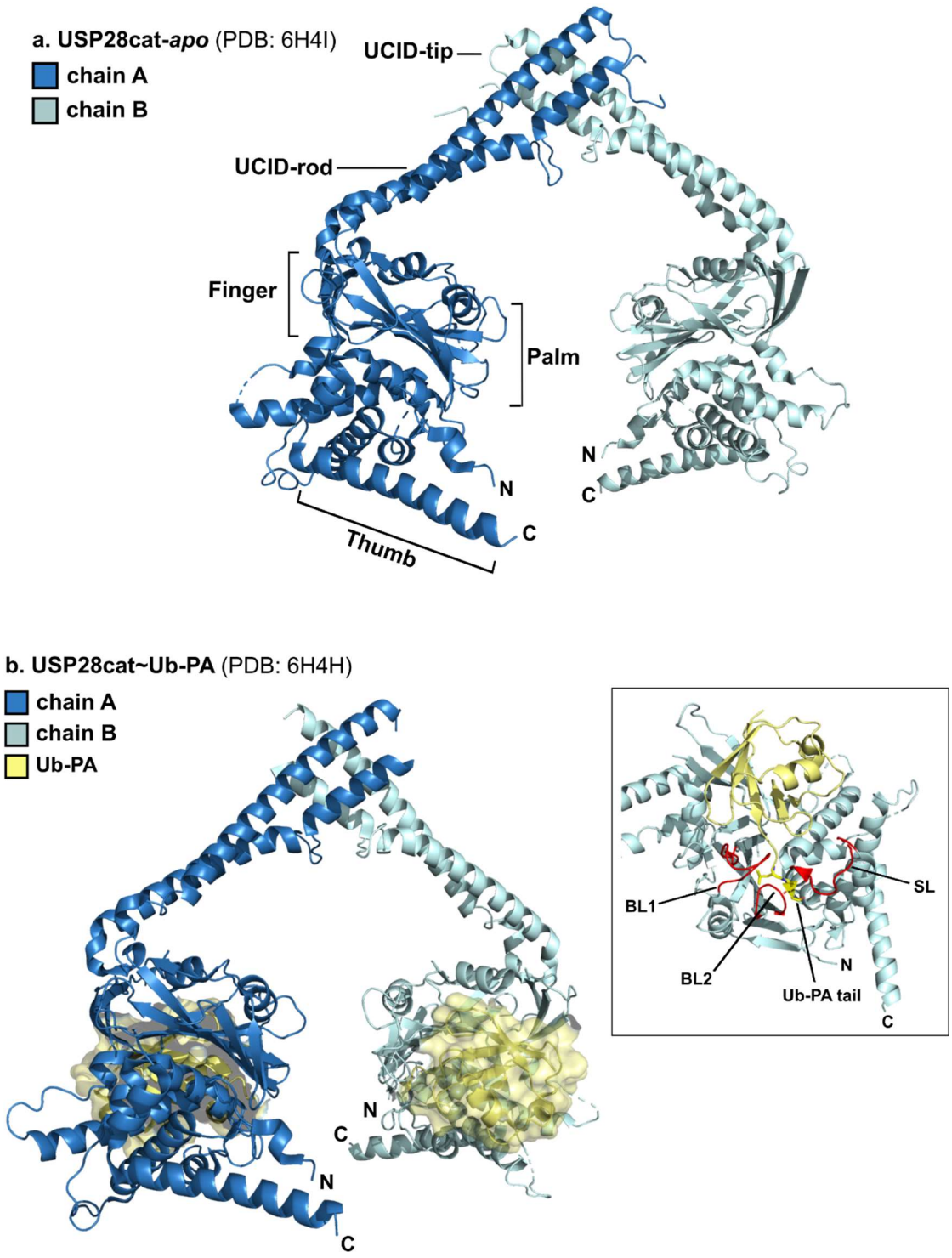

Figure 1.7: Structure of the USP28 catalytic domain. (a) The *apo* structure with the two monomers of the catalytic domains is indicated in blue and pale cyan. The globular USP core domain comprises the canonical thumb, palm and finger subdomains. An additional, inserted oligomerization domain consisting of a disordered UCID-tip region and UCID-rod region is indicated. The N- and C- termini of both monomers point in the same direction. **(b)** Structure of USP28cat bound to Ub-PA marked in yellow. (inset) The Ub-tail binds into a cleft formed by the thumb and palm in chain B. The BL1, BL2 and SL are indicated in red.

1.2.2.2 Structure of the USP25 catalytic domain

Due to the high sequence similarity, USP25cat shares the same four subdomain architecture as observed in USP28cat. However, a major difference in USP25 is that it assumes a symmetrical, tetrameric structure formed by two USP28-like dimers interlocking with one another to form a dimer of dimers (Figure 1.8a) (B. Liu et al., 2018; Gersch et al., 2019; Sauer et al., 2019). Tetramerization results from the interaction of the UCIDs of one dimer with the core USP domain of the other dimer and vice-versa. This interaction is mainly enabled by the C-terminal region of the now ordered UCID-tip (previously disordered in USP28cat) that extends into the Ub-binding site of the interacting USP domain (Figure 1.8b). This disables all four catalytic sites to bind ubiquitin, resulting in an autoinhibited tetramer.

Subsequent biochemical studies with the USP25cat variant lacking the UCID-tip region resulted in a dimeric protein, suggesting that the tip region is essential for higher-order oligomerization. This dimeric variant also exhibited a 6-fold higher activity than the tetrameric wild-type form. Monomer-inducing mutations of this region or complete deletion of the insertion site (equivalent to those in USP28cat) also resulted in significantly lower activity compared to the dimeric form reaffirming that the insertion in both USP25 and USP28 is crucial for stabilizing the catalytic domains and their Ub-binding sites.

A structure based-sequence alignment revealed that the most dissimilar portion between USP28 and USP25 lies in the UCID-tip (Figure 1.9a). But the binding surface for Ub in USP28 and the tip binding region in USP25 are virtually identical in sequence, the only structural difference being the tip-binding cleft – this assumes an open conformation in USP25 but not in USP28.

This difference most likely stems from the insertion of the UCID-tip into the catalytic domain, occupying a pocket below helix α5. The side chain of F259 (USP28)/F266 (USP25) in α5 rotates and moves >7 Å within the palm subdomain (Figure 1.9b) and is further stabilized by π-stacking interactions with F253 (USP25) on α4 thereby leading to an 'open' conformation of the cleft to accommodate the UCID-tip. In USP28, however, this movement anchors the helix α5 in an active position and links it to the active state of the catalytic cysteine, C171. In USP28, helix α4 is shorter, thus preventing the corresponding interaction of F246 and F259, leaving α5 anchored in an active position and resulting in a more flexible SL (Figure 1.9c).

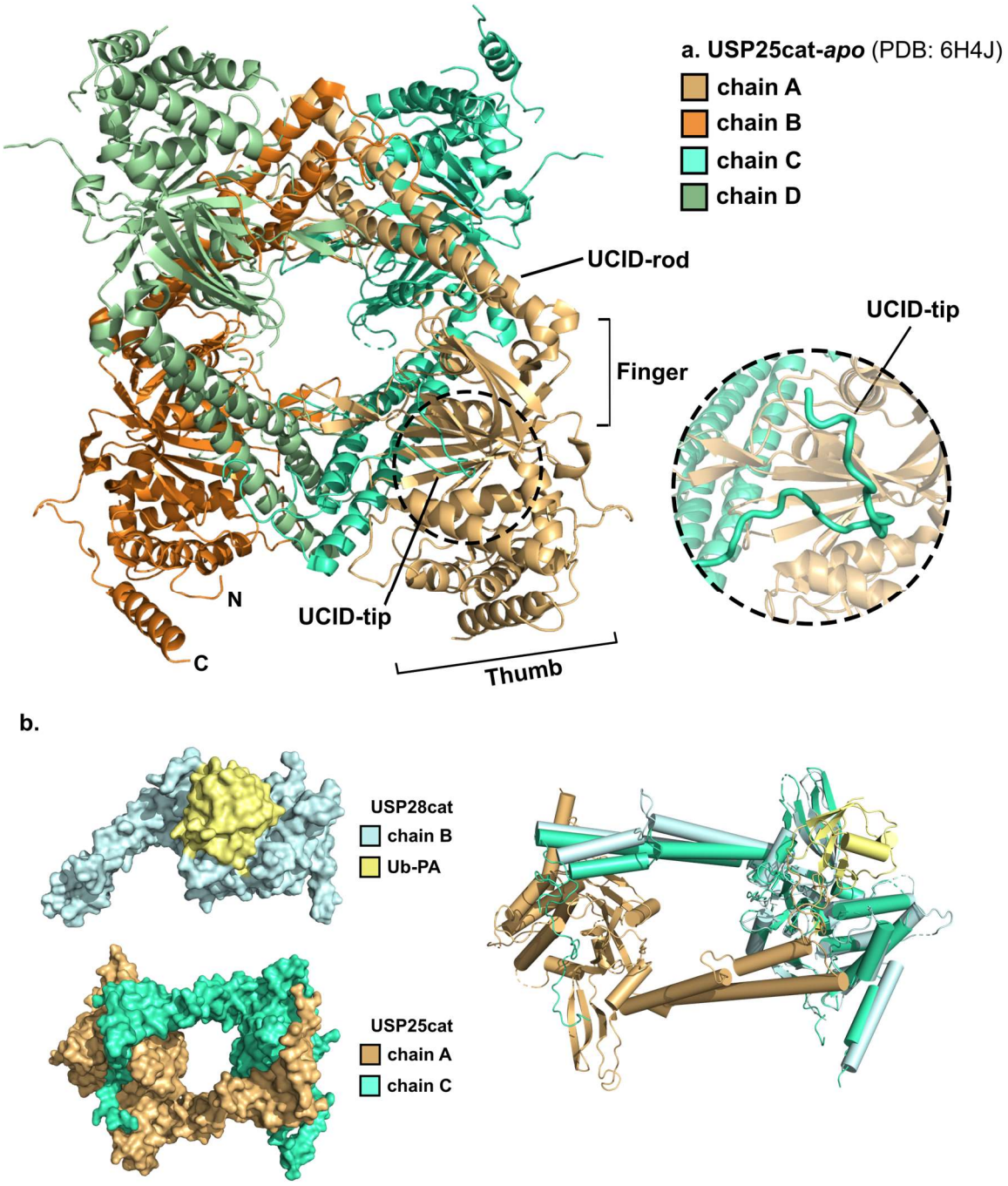

Figure 1.8: Structure of the USP25 catalytic domain. (a) The autoinhibited, tetrameric structure is formed by the intersection of two USP28-like dimers (chains A-B & C-D). The UCID-tip inserts into the core USP domain of the interacting dimer, as highlighted in the dotted circle. **(b)** Superposition of the USP28cat-UbPA bound structure with a USP25cat dimer shows that the UCID-tip blocks Ub binding in USP25.

Another critical difference between the two proteins is the BL1, which is disordered in the USP28cat *apo* structure but adopts a β-hairpin conformation in USP28cat-Ub bound and the USP25cat structures (Figure 1.9c). However, it is important to note that, while there are differences between the two proteins, they cannot be directly compared as USP25cat *apo* is

in an auto-inhibited, inactive form. As a result, it is unclear whether the active form would have the same features as seen in the USP28cat *apo* structure, such as the helix α5 position. It will be necessary to elucidate the structure of USP25cat in an active conformation to investigate this difference.

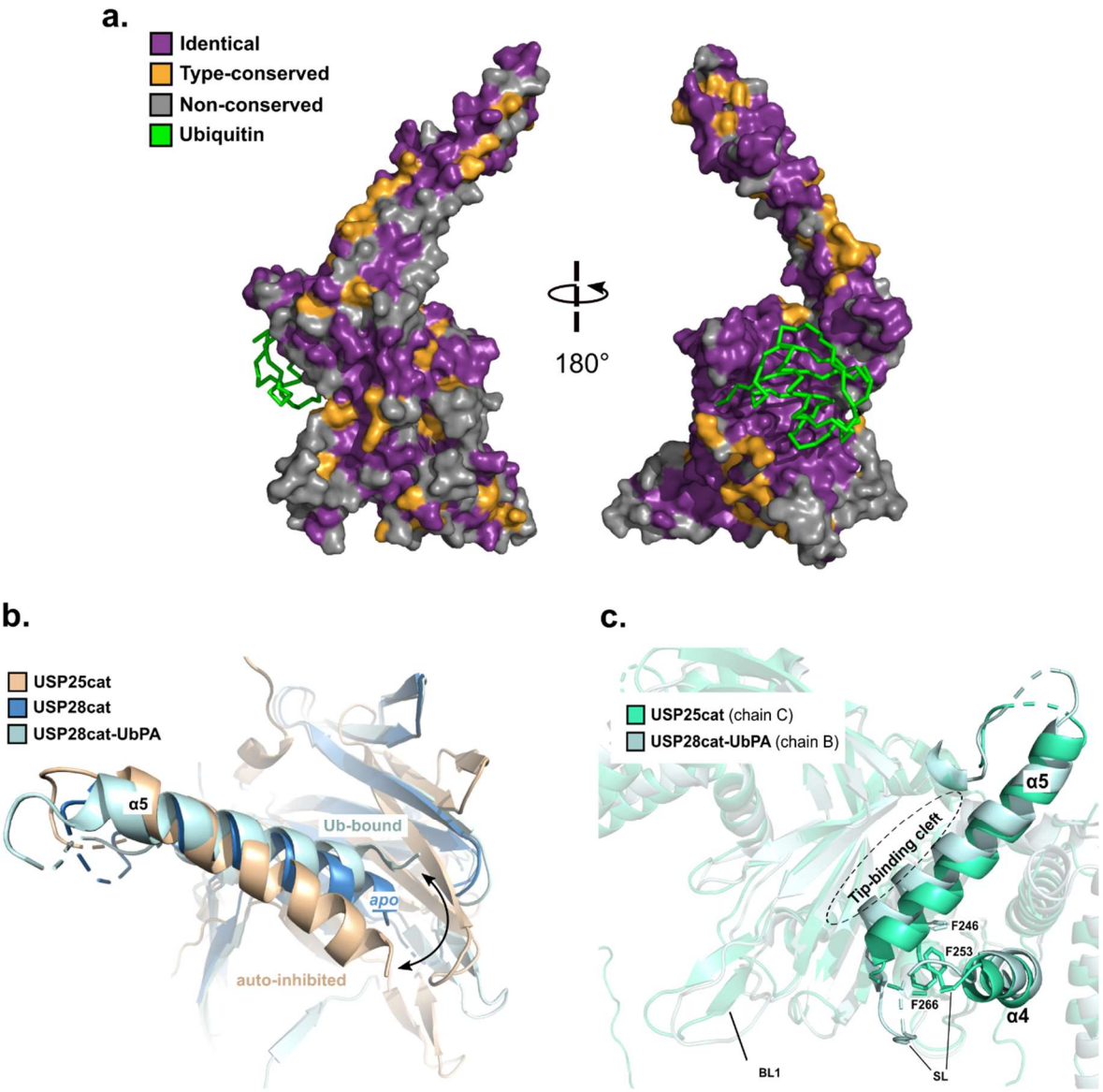

Figure 1.9. Differences in USP28cat and USP25cat structures. (a) Sequence conservation of the catalytic domains of USP28 and USP25 mapped on USP28cat. Identical residues are shown in deep purple, type-conserved residues in mustard yellow and non-conserved residues in gray. The Ub molecule is represented as a ribbon (green). **(b)** The superposition of the indicated structures shows a shift in α5 helix positioning in the catalytic USP domain, depending on auto-inhibition (USP25) and Ub-binding (USP28). **(c)** Superposition of the USP25cat and the USP28cat-UbPA structure shows an open tip-binding cleft resulting from the helix α5 repositioning, stabilized by the interaction between Phe266 and Phe 253 in USP25. This interaction is absent in USP28cat. Also seen is the β-hairpin conformation of the Blocking loop 1 and an elongated, more flexible switching loop in USP28.

1.2.3 Regulation of USP28 and USP25

A major insight into the regulatory mechanism of the two homologous proteins could be achieved from the elegant structural studies described in the previous sections. The differences in their oligomeric composition, mediated by a novel insertion site (UCID), lead to a constitutively active dimer in the case of USP28 and an autoinhibited tetramer in USP25. The quaternary structure in USP25 results from the occupation of an autoinhibitory motif that is primarily embedded into the Ub-binding site, rendering the enzyme inactive. The C-terminal domain of the full-length enzymes has little effect on oligomerization, whereas the N-terminal region influences the dimer–tetramer equilibrium of USP25 *in vitro* (Gersch et al., 2019).

The hyperactivation of USP25 due to cancer-associated mutations *in vitro* and *in vivo* implies a functional correlation between auto-inhibitory and pro-oncogenic effects (Sauer et al., 2019).

Listed below are other reported mechanisms that regulate the activity or expression of USP28 and USP25:

USP28 regulation –
Several cellular mechanisms affect the expression and enzymatic activity of USP28 in a context-specific manner (Table 1.2). Posttranslational modifications (PTM), in particular, impose strict control on USP28 activity. As described earlier, the kinase ATM phosphorylates USP28 on serine 67 and serine 714 in response to DNA damage, enhancing its enzymatic activity (Zhang et al., 2006). In addition, sumoylation can control USP28 by inhibiting its enzymatic activity (Lamoliatte et al., 2017).

Several DUBs undergo mono/polyubiquitination modifications that may be subjected to proteasomal degradation, resulting in a decrease in the DUB protein levels (Das et al., 2020; Haq & Ramakrishna, 2017). It could also be envisioned that USP28 deubiquitinates itself, avoiding proteasomal degradation and, as a result, controlling its own stability, as has been observed for other DUBs (Mistry et al., 2013; F. Wang et al., 2017). In support of this hypothesis, recent studies have found pharmacological inhibition leads to a decrease in USP28 in protein levels (Prieto-Garcia et al., 2020; Zheng et al., 2021).

Regulator	Type of regulation	Effect on USP28
ATM	Positive	Phosphorylates USP28 increasing its activity
CASPASE 8	Negative	Phosphorylates USP28 increasing its activity
c-Jun	Positive	Increases USP28 transcription
c-MYC	Positive	Increases USP28 transcription
Fbxw7 circular RNA	Negative	Reduces substrate recognition decreasing its activity
HDAC5	Positive	Increases USP28 stability; blocks its poly-ubiquitination
miR-216b	Negative	Reduces USP28 translation
mi-R3940-5p	Negative	Reduces USP28 translation
miR-500a-5p	Negative	Reduces USP28 translation
miR-92b-3p	Negative	Reduces USP28 translation
SENP1	Positive	Desumoylates USP28 increasing its activity

Table 1.3: Regulators of USP28 (adapted from Prieto-Garcia et al., 2021)

USP25 regulation –

Although the information on the post-transcriptional regulation of the USP25 protein is scarce, several studies threw light on the PTM of USP25 (Table 1.3). DUB modification by sumoylation affects Ub-chain binding and hydrolysis (Meulmeester et al., 2008). USP25 was previously shown to interact with SUMO1 and SUMO2/3 proteins (Mohideen & Lima, 2008). While SUMO1-USP25 interaction is weak, SUMO2/3 interaction depends on a SIM within USP25 (Figure 1.6). The SUMO2/3-specific binding and conjugation occur at seven residues within this region. Non-covalent attachment of SUMO2 to USP25-SIM inhibits the catalytic activity as it competes with the ubiquitinated substrate for interaction with USP25 (Yang et al., 2017).

USP25 is also regulated by phosphorylation. A study by Cholay et al. demonstrated that the spleen tyrosine kinase (SYK) interacts with and regulates USP25. They showed that the second Src homology-2 domain (SH2) of SYK physically interacted with a tyrosine-rich C-terminal region of USP25 in a non-phosphorylated state. Although SYK-mediated phosphorylation does not affect the catalytic activity, it does alter (downregulate) the cellular levels of USP25 (Cholay et al., 2010). Vaccinia-associated kinase 2 (VRK2)-mediated phosphorylation of USP25 (at T680, T727 and S745) inhibits its DUB activity, leading to the

ubiquitination and destabilization of the molecular chaperone protein called tailless complex polypeptide 1 ring complex (TRiC) (S. Kim et al., 2015).

Interestingly, USP25 can also be modified through ubiquitination. For example, the USP25m isoform can be monoubiquitinated and is capable of auto-deubiquitination. UBDs of USP25m facilitate monoubiquitination at K99, which can also be sumoylated, thereby inhibiting USP25's enzymatic activity. The K99R mutation significantly attenuates USP25m-mediated deubiquitination of myosin binding protein C1 (MyBPC1) (Denuc & Bosch-Comas, 2009). The SMAD specific E3 ubiquitin-protein ligase 1 (SMURF1) affects the stability of USP25 by modifying its K48-linked ubiquitination. This mechanism promotes the ubiquitination and degradation of USP25, thereby affecting the spread of infectious diseases (Qian et al., 2018).

Regulator	**Type of regulation**	**Effect on USP25**
miR-27a-3p	Negative	Downregulates USP25 transcription
SMURF1	Negative	Decreases USP25 stability modifying its K48-mediated ubiquitination
SUMO1	Negative	Sumoylates USP25 weakly; inhibits activity
SUMO2/3	Negative	Sumoylates USP25 efficiently; inhibits activity
SYK	Negative	Phosphorylates USP25; reduces cellular levels
Ubiquitin	Positive	Conjugates to K99; promotes catalytic activity
VRK2	Negative	Phosphorylates USP25; impairs catalytic activity

Table 1.4: Regulators of USP25 (adapted from W. Zhu et al., 2021)

1.3 Screening and identification of DUB inhibitors

DUBs have emerged as promising candidates for targeted therapy as they play a crucial role in protein turnover. DUB inhibition would lead to steady-state ubiquitination of specific substrates while having little effect on global protein or Ub levels. Over the past 15 years, small molecule modulators of DUBs have been sought as probes to address fundamental questions about the ubiquitin system and DUB activity and pharmacologically validate DUBs for the treatment of diseases.

Various assays are available to screen for and verify selective small molecule inhibitors of DUBs (Figure 1.10). These strategies are frequently used in tandem to boost confidence in

the inhibitor's quality and filter out sub-par compounds with broad, non-specific effects, which has been a concern with previously reported DUB inhibitors (Harrigan et al., 2018; Moon et al., 2021; Schauer et al., 2020).

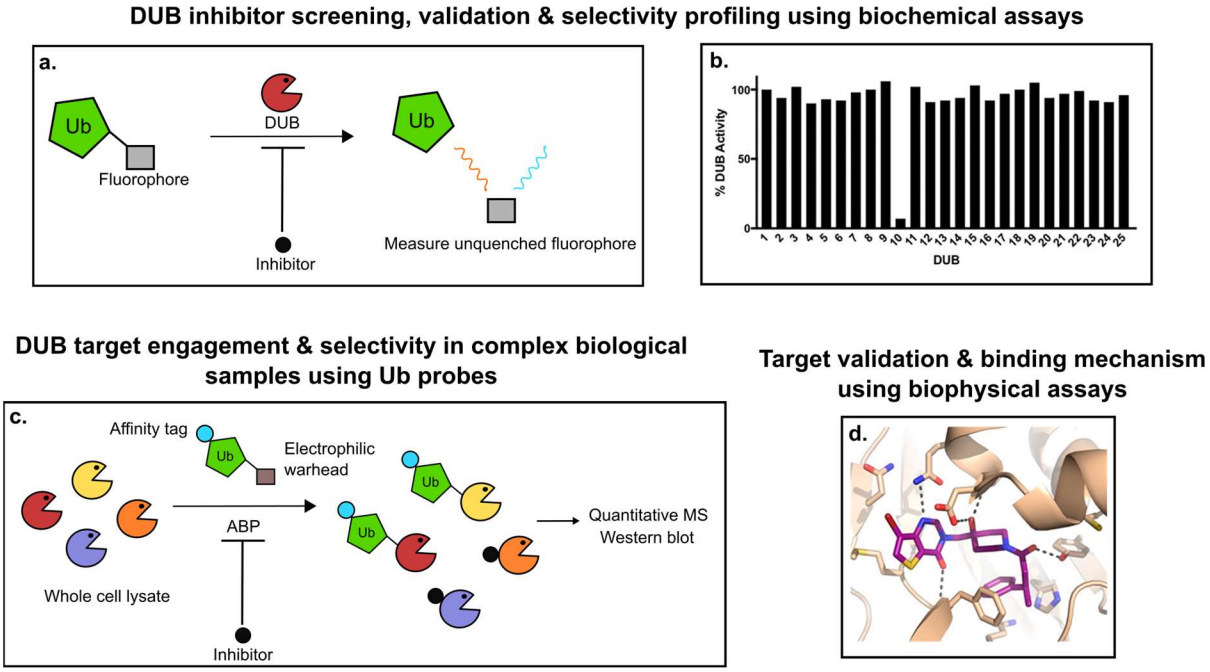

Figure 1.10: Target validation and selectivity profiling of a high-quality hit compound across orthogonal assays. Figure adapted and modified with permission from Schauer et al., 2020. Copyright © 2020, American Chemical Society.

Many of these techniques utilize chemically modified Ub-based probes such as Ub-Rhodamine (Ub-Rho) and Ub-7-amino-4-methylcoumarin (Ub-AMC) (Figure 1.10a; also see Section 2.2.3.8) as substrates for high-throughput DUB activity profiling.

Activity-based probe profiling (ABPP) (Figure 1.10c) is utilized to complement *in vitro* profiling and assess selectivity profiling *in situ*. In this method, small-molecule probes are used to determine the functional state of enzymes in native systems (Cravatt et al., 2008; Heal et al., 2011). An ABPP probe comprises two key features: 1) a *reactive group (warhead)* that binds and covalently modifies the active sites of a large number of enzymes that share conserved mechanistic and/or structural features, and 2) a *reporter tag* (fluorophore/biotin, HA-tag, FLAG-tag; marked as Affinity tag in Figure 1.10c) to enable detection, enrichment, and identification of probe-labelled enzymes by gel electrophoresis and in-gel fluorescence scanning or liquid chromatography-mass spectrometry (LC-MS) (Bachovchin et al., 2009; Galmozzi et al., 2014).

Activity-based probes (ABPs) that contain an electrophilic warhead instead of the C-terminal glycine of the Ub substrate help in assessing compound activity against a target DUB in a more physiologically relevant setting. For example, the nucleophilic cysteine of the DUB is labelled covalently and irreversibly by probes such as Ub- vinylmethylester (Ub-VME), Ub-vinylmethyl sulfone (Ub-VS) or Ub-propargylic acid (Ub-PA). This results in a shift in the molecular weight on an SDS-PAGE. To assess compound activity against a target DUB in complex biological samples, cells can either be pre-treated with the compounds prior to lysis or added directly to the lysates and subsequently used in downstream assays like Western blotting (WB) or quantitative mass-spectrometry (MS). Fluorescence polarization-based ABPs (Figure 1.11) such as Ubiquitin-Lys-5-Tetramethylrhodamine-Gly (Ub-Lys-TAMRA-Gly) mimic natural substrates as they consist of a native isopeptide bond between the TAMRA fluorophore and Ub. A K63-linked di-ubiquitin TAMRA probe was recently used in a fluorescence polarization assay to assess small molecule inhibitors of the zinc metalloprotease DUBs Rpn11 (Li et al., 2017).

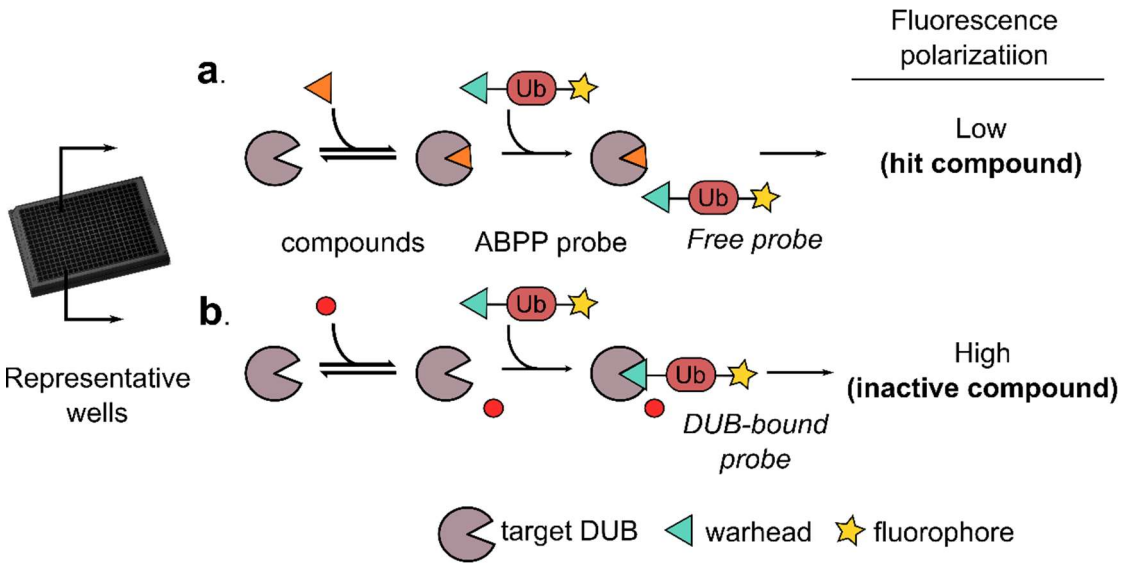

Figure 1.11: Schematic representation of fluorescence-based ABPP assay. A target DUB protein is dispensed into a 384-well plate, and a test compound is added to each well. The test compound can be a DUB inhibitor **(a)** or an inactive molecule **(b)**. A fluorescent ABPP probe is then added to the wells and incubated for a fixed time interval. The reaction of the fluorescent probe with the uninhibited **(b)** but not the inhibited **(a)** enzyme results in an apparent increase in the mass of the probe, resulting in a strong fluorescent polarization signal. Figure adapted and modified from Bachovchin et al., 2009.

Earlier reports of DUB inhibitors included selectivity screens against a minimal set of purified DUBs or other cysteine proteases (Figure 1.10b). Since then, DUB panels for *in vitro* profiling have increased in size and availability. These in-house DUB panels were complemented with Ubiquigent's DUB*profiler*™, a commercial DUB selectivity assay that assesses Ub-Rho cleavage against a panel of purified DUBs. DUB*profiler*™ originally comprised 23 DUBs but currently contains 44, allowing for routine and systematic profiling of potential DUB inhibitors. Additionally, a matrix-assisted laser desorption ionization time-of-flight (MALDI)-based platform is also used for assessing DUB activity in diubiquitin (di-Ub) cleavage assays (Ritorto et al., 2014).

Biochemical and biophysical characterization of the compounds viz., isothermal titration calorimetry (ITC), surface plasmon resonance (SPR), hydrogen-deuterium exchange mass spectroscopy (HDX-MS), differential scanning fluorimetry (DSF) etc., encompass a critical aspect of inhibitor development and confirm on-target binding.

Structure-activity relationships (SARs) are theoretical models that could be utilized to predict the physicochemical, biological and environmental properties of substances. A SAR is an association between a chemical substructure and the potential of a chemical containing the substructure to exhibit a certain biological quality or effect (Mohapatra, 2020). The emergence of multiple DUB−inhibitor complex structures has enabled the broader incorporation of structure-guided SAR (Figure 1.10d). A potential application of targeted SAR libraries could be ultimately useful for a target class approach, wherein newly synthesized compounds are tested against multiple DUBs to determine whether minor modifications to the core scaffold affect DUB selectivity.

1.4 Classification of DUB inhibitors

Based on the current structural and biochemical data, Lange and colleagues (Lange et al., 2021) conceptualize a classification for DUB inhibitors that can be divided into five distinct types -

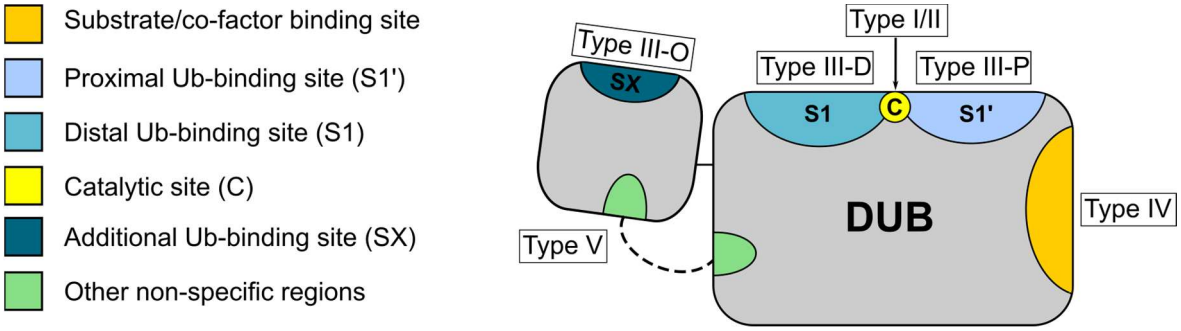

Figure 1.12: Schematic of a DUB with the type of inhibitor binding sites, as indicated. Figure adapted and modified with permission from Lange et al., 2021.

Type I inhibitors:

Inhibitors in this category bind directly to the active site in the catalytic domain of the DUB and stabilize it in an active conformation. Examples of non-covalent type I inhibitors are the series of molecules developed against the metalloprotease DUB, constitutive photomorphogenic-9 signalosome subunit 5 (CSN5) (Novartis). CSN5 is part of the COP9 signalosome and plays a central role in remodeling cullin-RING E3 ligases (CRLs) by removing the UBL NEDD8. The inhibitor CSN5i-3 targets the deneddylation activity of the DUB by binding the active site zinc and extending into the substrate-binding site. This category also includes covalent modifiers (Type I* inhibitors) that bind to the catalytic Cys and form a disulfide bond but do not interact with the other catalytic triad residues.

Type II inhibitors:

Unlike Type I inhibitors, these compounds interact directly with the active site residues but stabilize the target DUB in an inactive conformation due to misaligned residues. Mitoxantrone (MIX) is an FDA approved drug used in chemotherapy, primarily against acute leukemia, prostate cancer, breast cancer and lymphoma. Previous studies have demonstrated that USP15 and USP11, among others, are the cellular targets of MIX (Ward et al., 2018; Burkhart et al., 2013). USP15-MIX complex structures show that the compound binds non-covalently to the catalytic His while pushing away the catalytic Cys. Another well-

characterized example of the Type II* inhibitor is the USP7 inhibitor, FT827 (Figure 1.13) (Turnbull et al., 2017). FT827 competes with Ub and extends into its binding pocket, stabilizing the DUB in an inactive conformation.

Type III inhibitors:

These inhibitors compete with Ub and bind to the Ub-binding sites of the DUB and therefore allosterically block substrate recognition. However, they do not interact with the active site residues. Based on the Ub-binding pocket they prefer, Type III inhibitors are further divided into three subtypes-proximal Ub-binding/S1' site (Type III-P), distal Ub-binding/S1 site (Type III-D) and other Ub-binding (Type III-O) inhibitors.

Type III-D class harbors the largest number of the most potent and specific DUB inhibitors reported to date. Most of these DUB targets comprise the canonical USP-like fold where the S1 site is located between the thumb, palm and finger subdomains. An example of a Type III-D inhibitor that targets the thumb-palm cleft is the small molecule GRL0671 that interacts with the PLPro domain of SARS-CoV and sterically blocks access of the Ub-molecule to the active site. Some inhibitors bind to the thumb-finger region to block the binding of the distal Ub (Figure 1.13).

Type III-O inhibitors bind to a pocket other than the S1 and S1' sites. Recently, the structure of the USP5-zinc finger (ZnF) UBD with a small molecule showed that the inhibitor occupies the cleft that recognizes the C-terminal Gly-Gly motif of the Ub-molecule and thereby inhibits DUB activity (Mann et al., 2019).

So far, there are no reported candidates for the Type III-P inhibitors. However, DUBs like OTULIN, Cezanne and USP30 that rely on proximal Ub-binding for their activity may be considered promising targets.

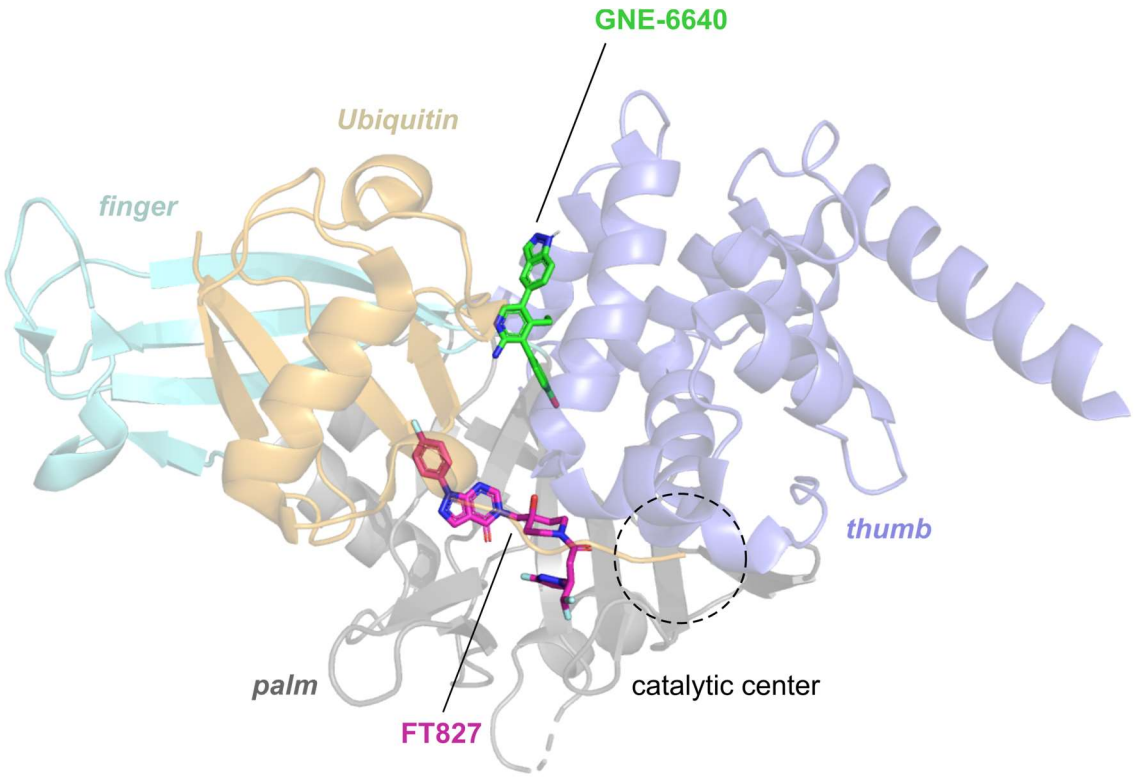

Figure 1.13: Structure of USP7 bound to its inhibitors. FT827 (magenta; PDB: 5NGE), a Type II* inhibitor, interacts with the catalytic Cys and stabilizes USP7 in an inactive conformation. Compound GNE-6640 (green; PDB: 5UVQ), a Type III-D inhibitor, non-covalently targets USP7 and attenuates Ub-binding by occupying a pocket embedded in the thumb-finger region. The thumb, palm and fingers subdomains are indicated. Ubiquitin bound to USP7 is shown in light orange.

Type-IV and Type-V inhibitors:

Type IV inhibitors constitute compounds that bind allosterically to a region external to the Ub-binding site. DUB activation triggered by structural changes upon substrate binding or co-factor interaction is an up-and-coming topic of great interest. Developing such allosteric inhibitors would be advantageous as they can be highly target-specific and thereby capable of regulating the mechanism of a specific DUB. However, identifying such a suitable regulatory site remains a considerable challenge. There are no Type IV inhibitors discovered to date.

Lange et al. predict Type V inhibitors to be bivalent inhibitors capable of binding two regions of a DUB, such as by tethering the catalytic domain to an adjacent inhibitory domain and arresting the DUB in an inactive conformation. This strategy could also be extended to achieve higher specificity directed towards the non-catalytic regions of the DUB. Although

no such inhibitors exist as of now, they have been developed against multiple protein kinases and phosphatases, e.g., c-Jun kinase 1 (JNK1) and protein tyrosine phosphatase 1B (PTP1B).

This approach could also be an exciting premise to consider for achieving specific inhibition of the DUBs USP28 or USP25, which will be discussed in detail in the following sections.

1.4.1 USP28-USP25 Inhibitors

Because of their involvement in maintaining and stabilizing numerous 'undruggable' proteins, USP28 and USP25 display immense potential as therapeutic targets. A recent upsurge in the development of small-molecule inhibitors against DUBs has led to the discovery of relatively potent inhibitors of USP28 and USP25, summarized in the following sections –

1.4.1.1 AZ inhibitors

A group of researchers from AstraZeneca (Wrigley et al., 2017) employed a high throughput screening approach with purified recombinant USP28 and the fluorogenic substrate Ub-Rho110 against a directed library of ~40,000 compounds. Subsequent profiling was performed with a subset of 42 compounds selected based on the combined data from a ratio-test assay and chemoinformatic analysis. This led to the identification of four structurally similar benzylaminoethanol derivatives (AZ1, AZ2, AZ3 and AZ4). Compounds AZ1, AZ2 and AZ4, exhibited an IC_{50} value (half-maximal inhibitory concentration) of 0.7, 1.1 and 2.0 μM, respectively, when tested against the cleavage of mono-, di- and tetra-Ub substrates while the non-substituted form, AZ3 was significantly less active with an IC_{50} of 59.6 μM.

Further biophysical characterization using ITC showed that the compounds AZ1, AZ2 and AZ4 bind to USP28 with high affinities (K_d = 0.2, 0.9 and 2.7 μM, respectively). Kinetic experiments revealed a non-competitive mode of inhibition. However, selectivity profiling of these three compounds also demonstrated a strong inhibition (>90%) for USP25 but not for other DUBs or other non-related proteases (14 USPs, CYLD, 4 UCHs, 3 OTUs and 1 JAMM). To further test their activity against USP25, the authors performed parallel dose-response testing of the compounds and found them to inhibit USP25 equipotently to USP28. In addition to the *in vitro* profiling, the compounds were also tested for their activity in a cellular environment. ABPP assays performed in HCT116 cells with Ub-VS as a probe were in agreement with the biochemical data and further confirmed a direct interaction with USP28 and USP25.

The compounds were also probed for their activity against the regulation of the USP28 substrate c-MYC, and it was shown that upon exposure to AZ1, AZ2 and AZ4, endogenous c-MYC levels were considerably reduced, which was mediated by proteasomal degradation. The compounds also induced apoptosis and reduced cell viability across a range of tumor cell lines from different tissues of origin and tissue-matched normal cells. However, no significant differentiation was observed in response between the tumor and normal cell types. The authors suggest that the lack of selective killing is because of the intricacy of the targeted pathways and the possibility for redundancy among family members such that the carcinogenic effects of specific gene amplifications are limited. The authors did not evaluate the functional impact of USP25 inhibition.

AZ1 has since then successfully been used as an *in vivo* probe. Prieto-Garcia et al. demonstrated that AZ1 blocks USP28-dependent stabilization of ΔNp63 and induces proteasomal degradation (Section 1.3.2.1) (Prieto-Garcia et al., 2020). AZ1 has also been used to assess the functional role of USP25 inhibition in 5xFAD mice. It ameliorates the neuropathological hallmarks of Alzheimer's disease (AD) by attenuating microglial activation, of which USP25 is a critical regulator (Section 1.3.2.2) (Zheng et al., 2021). Also, in a mouse model, AZ1 could impair USP25-induced bacterial infection in the intestine and enhance immune response while inhibiting the role of USP25 in promoting intestinal cancer (X.-M. Wang et al., 2020).

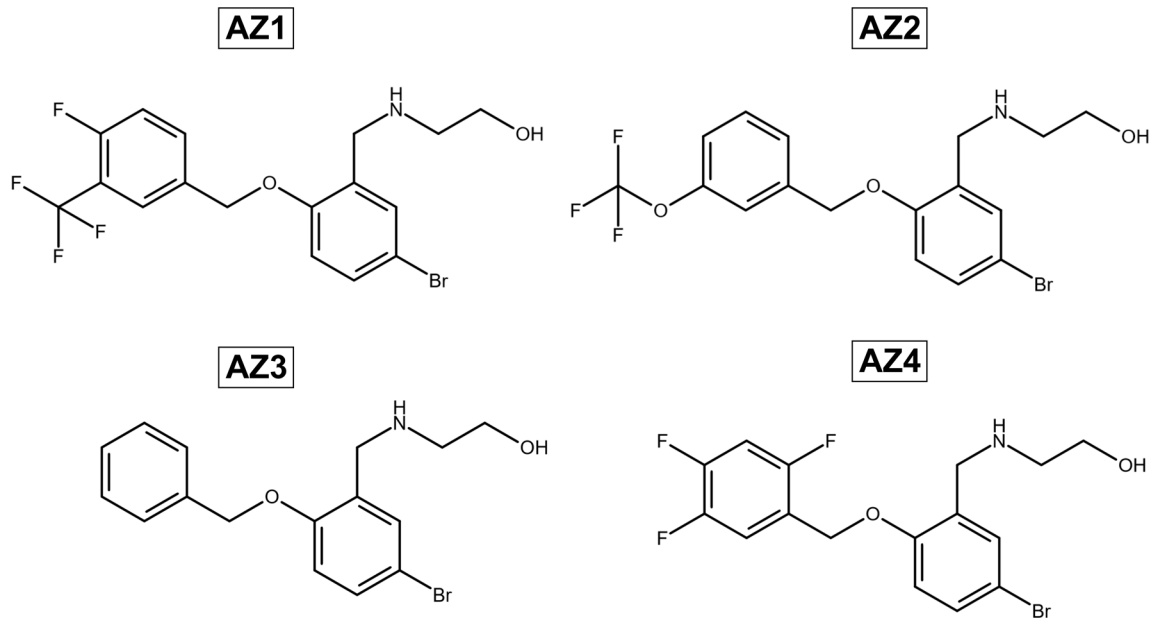

Figure 1.14: Chemical structures of the AZ inhibitors

1.4.1.2 Vismodegib

Vismodegib (Erivedge®) is an FDA approved drug used to treat unresectable or metastatic basal cell carcinoma (BCC). It was the first approved small molecule inhibitor to target the Hedgehog (Hh)-signaling pathway, which regulates cell growth and differentiation during embryogenesis and drives certain cancers. BCC is associated with the overactivation of the Hh-signaling pathway where loss-of-function mutations affect the protein Patched homologue 1 (PTCH1), which generally inhibits signaling by another protein receptor, Smoothened homologue (SMO). Vismodegib binds to and inhibits SMO, leading to the inactivation of transcription factors and associated target genes (Dlugosz et al., 2012).

Recently, Wang et al. (H. Wang et al., 2020) showed that Vismodegib inhibits USP28 and USP25 with an IC_{50} of 4.4 μM and 1.4 μM, respectively (against mono-Ub-AMC hydrolysis). Selectivity and direct binding of Vismodegib to USP28 were derived from a panel of five DUBs within the USP family, substantiated by ITC, STD-NMR and thermal shift assays. *In vivo* studies using colorectal cancer cell lines showed that the drug blocked the binding of mono-Ub-propargylamide (Ub-PA) to USP28 and USP25 in a concentration-dependent manner. The Hh-signaling pathway did not mediate the cellular effects as no changes were observed in the protein levels of Cyclin D1 and Bcl2, which are downstream targets of the pathway. Direct inhibition of USP28 and USP25 as a treatment option against human colorectal cancer cells with Vismodegib resulted in a significant decrease in the USP28 and USP25 substrates (c-Myc, c-Jun and TNKS1/2, respectively).

Time-resolved HDX-MS was used to locate the binding site of Vismodegib, and it was shown that the thumb helices 5 and 6 of USP28 were the major contributors to the interactions with the inhibitor. Further docking experiments led to the identification of a small pocket composed of Phe292, Tyr293 and Gln315 between these helices. This pocket is located close to the region in USP25, required to accommodate the auto-inhibitory tip. To confirm these observations, the above-mentioned residues were mutated and tested for their binding affinities and inhibitory activities. Interestingly, Vismodegib showed higher binding and increased inhibition in the presence of the Gln315 variant (Q315A) – even more potent compared to the WT protein. The authors speculated that Gln315 is required to move outwards by 3.2 Å to accommodate binding of Vismodegib in USP28.

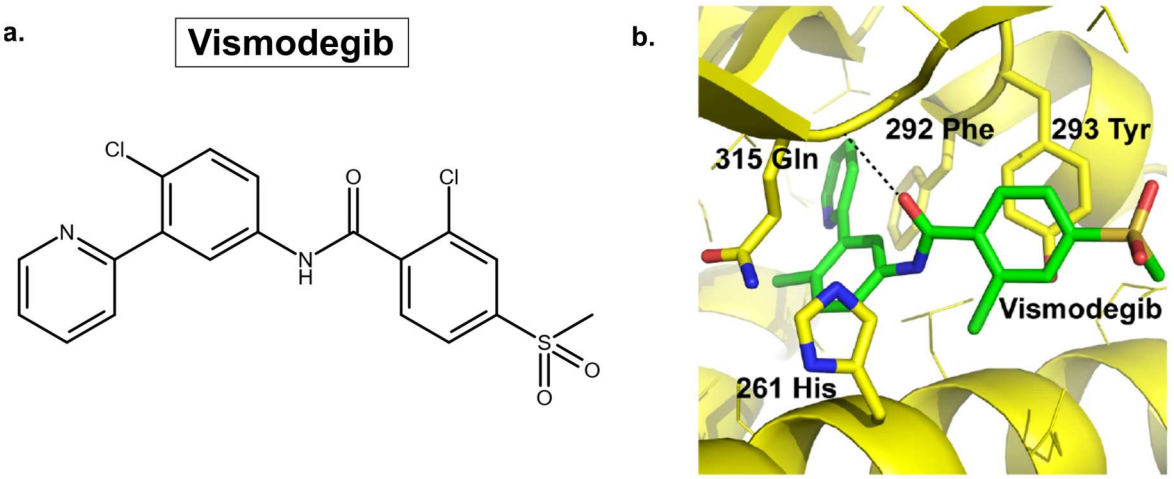

Figure 1.15: Chemical structure of Vismodegib (a) The possible binding site of Vismodegib in USP28 and the corresponding residues involved, based on docking studies **(b)**. Figure reproduced from H. Wang et al., 2020, with permission from John Wiley and Sons.

1.4.1.3 FT206

Based on a small molecule discovery campaign using the Ub-Rho110 assay, Forma Therapeutics (FT) developed and patented a series of substituted thienopyridine carboxamides as USP28/USP25 specific inhibitors (Guerin et al., 2017, Guerin et al., 2020, Zablocki et al., 2019). IC_{50} values for these compounds were similar for both USP28 and USP25 (<0.2 μM to 2.5 μM).

Quantitative SAR was used to develop a compound derivative of this series: FT206. This compound is by far the most superior in terms of drug metabolism and pharmacokinetic properties in this series while preserving potency and selectivity towards USP28/25 (Zablocki et al., 2019). Recently, FT206 treatment of USP28 was found to recapitulate LSCC regression in mouse models and human xenografts (Ruiz et al., 2021). Based on a cellular target engagement assay using Ub-PA, FT206 was found to interfere with the USP28/25 probe labelling in LSCC cell extracts with a higher potency (EC_{50}= ~0.3-1.0 μM) as compared to that of AZ1 (>30 μM).

Additionally, FT206 treatment of LSCC tumor cells resulted in a significant decrease in protein levels of c-Myc and c-Jun, suggesting that FT206 blocks USP28-mediated deubiquitination of its substrates while also increasing USP28 ubiquitination. Although the authors claim a preferential inhibition of USP28 compared to USP25 by FT206, no further

structural or biophysical characterization was explored. In another recent study (Nelson et al., 2022), FT206 mediated inhibition of USP25 led to reduced HIF1α activity in pancreatic ductal adenocarcinoma (PDAC) tumor cells affecting their survival in hypoxic tumor environment and subsequently leading to reduction in PDAC tumor growth *in vivo.* Interestingly, the sensitivity to FT206 was dependent on USP25 expression and significantly reduced organoid viability independently of USP28.

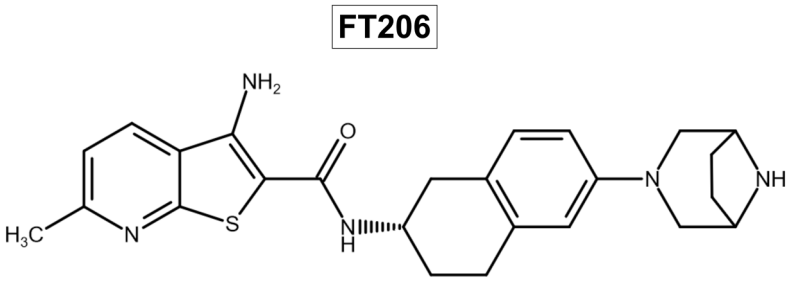

Figure 1.16: Chemical structure of FT206

1.4.1.4 Compound 19

Liu et al. (Z. Liu et al., 2020) examined a compound library of around six hundred molecules for their inhibition of USP28, which led to the identification of a hit compound to be used as a starting point for SAR studies. Out of the twenty-two molecules that were subsequently synthesized, which are all derivatives of [1,2,3]triazolo[4,5-d]pyrimidine, eight were inactive against the enzyme, and five inhibited the catalytic activity of USP28 with an $IC_{50} \leq 10$ μM (against mono Ub-AMC). 'Compound 19' was the most potent molecule within this analysis, also compared to AZ1, with an IC_{50} of 1.10 μM (vs 11.88 μM for AZ1).

Compound 19 bound reversibly to USP28 with a K_d of 40 nM, while it did not exhibit any inhibitory activity against USP7 and LSD1. However, this study was not extended to other DUBs; hence the selectivity is unknown. Cellular studies with compound 19 against a panel of gastric cancer cell lines showed a selective anti-proliferative effect compared to a non-cancerous, gastric epithelial immortalized cell line. The authors suggest that the inhibitory activity of compound 19 partially depended on USP28 inhibition. The molecule also induced proteasome-dependent degradation of USP28 substrates viz., c-Myc and LSD1, and USP28 itself. It was also shown to induce apoptosis and reduce cell migration and epithelial-mesenchymal-transition (EMT) progression, controlled by LSD1.

The authors performed docking studies using the Ub-bound crystal structure of USP28, which led to the identification of potential binding sites of compound 19. They suggest that the interaction involves residues on BL1 and BL2 and the palm region, which spans the Ub-tail binding region of the USP S1-site. They further propose π-π interactions between Phe370 and the triazolopyrimidine moiety of compound 19. However, no experiments were performed to validate the docking results.

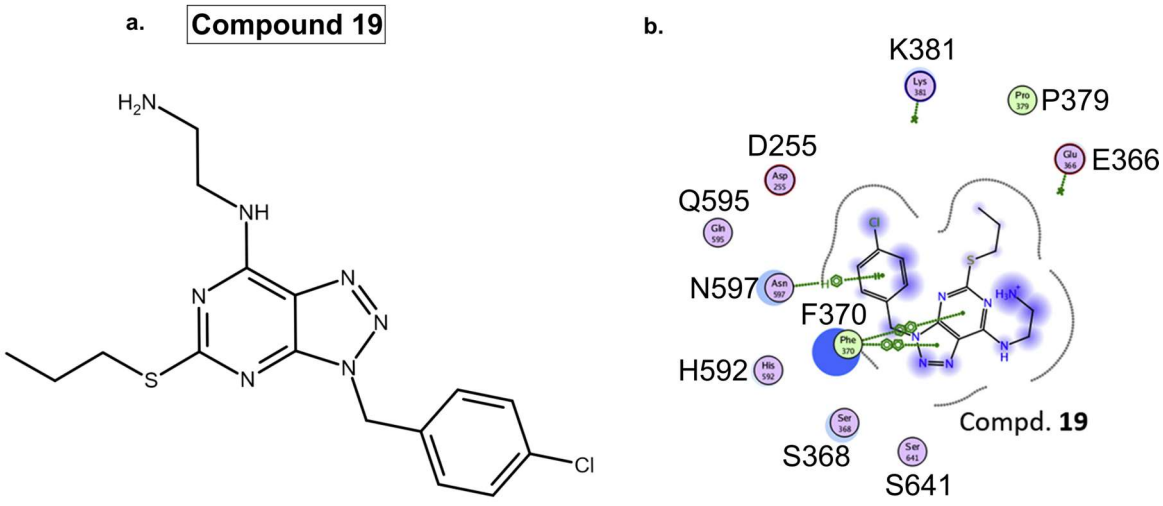

Figure 1.17: Chemical structure of Compound 19 (a) The 2D binding model of the compound with USP28 and the interacting residues, as predicted by docking studies **(b)**. Figure reproduced and adapted from Z. Liu et al., 2020; Copyright © 2020, Elsevier Inc.

1.4.1.5 Other inhibitors

In a recent study, Varca and colleagues (Varca et al., 2021) performed a high-throughput screening assay using the fluorogenic Ub-Rho substrate with eight DUBs spanning three DUB families against a 50,000 compound library to identify selective inhibitors for each DUB. Primary screening was followed by hit validation based on profiling dose-response against target DUBs, which could be assessed for further optimization. USP28 exhibited the highest number of hits satisfying the most stringent criteria. Inspection of these structures revealed multiple compounds to have the same core scaffold. Not surprisingly, all of the compounds showed activity against USP25 as well. After multiple screening steps, four inhibitors were selected that inhibited USP28 from the low nanomolar to the low micromolar range: AV-9606-99 (4.33 μM), AV-9606-129 (402 nM), AV-11324-75 (176 nM) and bin-01-07-07 (46 nM).

To assess target binding to the native enzyme and selectivity in cellular lysates, the authors performed competitive ABPP coupled with quantitative mass spectrometry. Although the authors observed strong binding to native USP25 with all four compounds, only the two most potent compounds, bin-01-07-7 and AV-9606-180 (a close derivative of screening hit AV-11324-75 with similar potency in the Ub-Rho dose-response assay) exhibited strong inhibition of USP28. Both compounds inhibit the DUB with IC_{50} values ≤100 nm, which is approx. 10-fold more potent than AZ1. These compounds also exhibit substantially stronger cellular target engagement in their studies.

The authors conclude that combining the two structurally different scaffolds can be utilized as probe compounds to study USP28/25 biology or as a starting point to tune selectivity towards one enzyme.

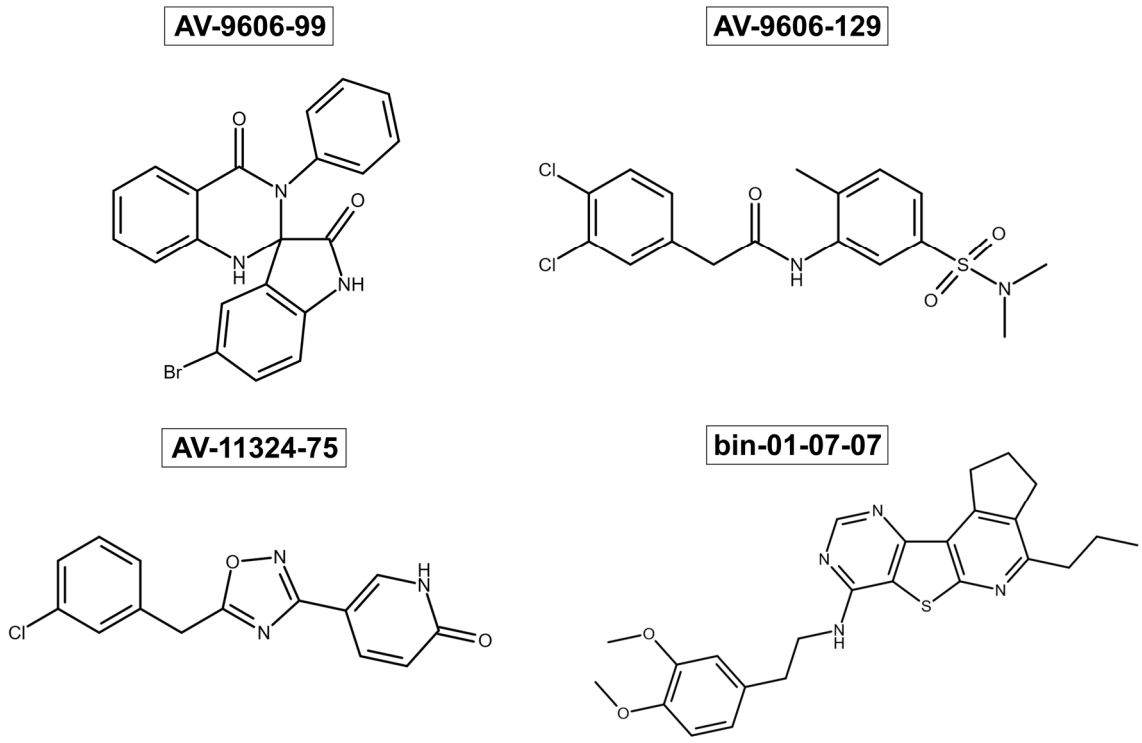

Figure 1.18: Chemical structure of the hit compounds specific for USP28 that were utilized for validation studies.

1.5 Aim of this study

Deubiquitinases have emerged as novel pharmacological targets for therapeutic intervention in cancer, immune disorders and neurodegenerative diseases. In the past several years, extensive research has unraveled numerous small molecule compounds that can target DUBs with great potential. However, these discoveries were not without challenges. Poor specificity, selectivity, and limited structural knowledge have impeded the identification of suitable inhibitors. However, recent advances in DUB studies have identified many features that could be targeted toward achieving selective inhibition. Structural characterization of target inhibition using techniques like X-ray crystallography, nuclear magnetic resonance and cryo-electron microscopy has also emerged as a crucial step to validate the expected binding mode and support the design of a more potent, successive generation of inhibitors.

The principle goal of this thesis is to elucidate the molecular basis of USP28 inhibition by the recently reported inhibitors. Understanding inhibitor binding to USP28 using X-ray crystallography may help identify unique characteristics that could be utilized to achieve selectivity as most of the reported inhibitors exhibit a dual-specificity for its homologue, USP25. Moreover, limited inhibitory parameters (especially IC_{50} values) have been reported for USP25, wherein the auto-inhibited protein was presumably utilized. Therefore, it was important to establish a common system, using fully activated forms of both proteins, to understand the effect of their inhibition. Validation of compound binding to these active forms using biophysical and biochemical methods would also provide valuable mechanistic insights into the inhibition mechanism, which could be applied to design more potent inhibitors.

Another important goal of this work was to identify new crystal forms that would help to improve the structural details of protein inhibition. High-resolution data could then be used to facilitate *de novo* inhibitor discovery in the future.

2. MATERIALS AND METHODS

2.1 Materials

2.1.1 Consumables

2.1.1.1 Chemicals and labware

All chemicals were purchased at analytical grade or higher. Buffers and other solutions were prepared using ultrapure water generated utilizing the TKA GenPure System.

Table 2.1 - Chemicals

Name	Supplier
2'-deoxyadenosine 5'-triphosphate (dATP) sodium salt	Sigma-Aldrich
2'-deoxyguanosine 5'-triphosphate (dGTP) sodium salt	Sigma-Aldrich
2'-deoxycytidine 5'-triphosphate (dCTP) sodium salt	Sigma-Aldrich
2'-deoxythymidine 5'-triphosphate (dTTP) sodium salt	Sigma-Aldrich
2-Propanol	Carl Roth
4-(2-hydroxyethyl)-1-piperazineethanesulfonic acid (HEPES)	Carl Roth
Acetic acid	Carl Roth
Acrylamide/Bis-acrylamide (37.5:1)	Carl Roth
Agar	Carl Roth
Agarose NEEO ultra quality	Carl Roth
Ammonium persulfate (APS)	Carl Roth
Ammonium sulfate	Sigma-Aldrich
Ampicillin sodium salt (Amp)	Carl Roth
Bis-Tris	Sigma-Aldrich
Bovine serum albumin (BSA)	Sigma-Aldrich
Bromophenol blue sodium salt	Carl Roth
Calcium chloride dihydrate	Carl Roth
Chloramphenicol (Cam)	Carl Roth
Citric acid	Sigma-Aldrich
cOmplete™, EDTA-free Protease Inhibitor Cocktail	Sigma-Aldrich (Roche)
Coomassie Brilliant Blue G-250	Carl Roth
D-Glucose	Carl Roth
Dimethyl sulfoxide (DMSO)	Carl Roth
Dipotassium hydrogen phosphate	Sigma-Aldrich
Disodium hydrogen phosphate	Carl Roth

Dithiothreitol (DTT)	Carl Roth
Ethanol	Carl Roth
Ethylenediaminetetraacetic acid (EDTA)	Carl Roth
Ethylene glycol	Sigma-Aldrich
Glycerol	Carl Roth
Glycine	Carl Roth
Hydrochloric acid	Carl Roth
Imidazole	Carl Roth
Isopropyl-β-D-thiogalactopyranoside (IPTG)	Carl Roth
Kanamycin sulfate (Kan)	Carl Roth
Lysogeny broth (LB) medium	Carl Roth
Magnesium chloride hexahydrate	Carl Roth
Magnesium sulfate	Sigma-Aldrich
Orange G DNA loading dye	Sigma-Aldrich
Perchloric acid	Sigma-Aldrich
Polyethylene glycol 3350 (PEG3350)	Sigma-Aldrich
Polyethylene glycol 400 (PEG400)	Sigma-Aldrich
Polyethylene glycol 4000 (PEG4000)	Sigma-Aldrich
Potassium dihydrogen phosphate	Carl Roth
Sodium acetate	Carl Roth
Sodium citrate tribasic dihydrate	Sigma-Aldrich
Sodium chloride	Carl Roth
Sodium dihydrogen phosphate	Carl Roth
Sodium dodecyl sulfate (SDS)	Carl Roth
Sodium hydroxide	Carl Roth
Sodium malonate dibasic monohydrate	Sigma-Aldrich
Streptomycin sulfate (Strep)	Carl Roth
Sypro® Orange	Sigma-Aldrich
Terrific Broth (TB) medium	Carl Roth
Tetramethylethylenediamine (TEMED)	Carl Roth
Tris-(2-carboxyethyl)-phosphine (TCEP)	Carl Roth
Tris-(hydroxymethyl)-aminomethane (Tris)	Carl Roth
Ubiquitin-Rhodamine110Gly (UbRh110)	UbiQ Bio
β-Mercaptoethanol	AppliChem

Table 2.2 - Labware

Type	Model	Supplier
24-well crystallization plates	Crystalgen SuperClear™ Plate	Jena Bioscience
384-well Microplate	Black bottom, non-binding	Greiner Bio-One
96-well crystallization plates	Crystalquick™ 1 square well, flat bottom, low profile	Greiner Bio-One
Centrifugal concentrator	Amicon® Ultra-0.5, 4 and 15 mL	Merck Millipore
Centrifuge tube	Cellstar® centrifuge tube – 15 and 50ml	Greiner Bio-One
Cover slides	Circular, Siliconized, 22mm	Jena Bioscience
Cuvettes	Rotilabo® -single-use	Carl Roth
Dialysis membranes	Spectra/Por®	Spectrum Laboratories
Dialysis tubes	D-Tube™ Dialyzer Midi (MWCO: 3.5 kDa)	Millipore
Filter paper		Sartorius
Gloves	Nitrile gloves	Star Lab
Optical quality sealing foil	VIEWseal™	Greiner Bio-One
Polymerase chain reaction (PCR) tubes	Multiply®-Pro cup 0.2ml, Multiply®-µStrip 0.2ml chain, 8-Lid chain, flat	Sarstedt
Pipette tips	Pipette tips – 10, 200, 1000 ml	Mettler-Toledo
Precast SDS-Gels	Mini-PROTEAN TGX 4-20% Gels	Bio-Rad Laboratories
Polyolefin Sealing foil	900 360 (Bio-inert sealing foil for microtiter-plates, deep well plates etc.)	HJ-BIOANALYTIC
Reaction tubes	SafeSeal tube – 0.5, 1.5 clear and brown, 2 ml	Sarstedt
Silicon grease	Bayer silicon grease medium viscosity	Jena Biosciences
Sterile filters	Acrodisc® sterile filter for syringe – 0.22 and 0.45 µm	Pall
Syringes	Omnifix® syringes – 1,5,10 and 20 ml	B. Braun

2.1.1.2 Kits

Table 2.3 - Kits

Type	Supplier
NucleoSpin ® Gel and PCR Clean-up kit	MACHEREY-NAGEL
NucleoSpin ® Plasmid	MACHEREY-NAGEL
Pierce™ Silver Stain Kit	Thermo Scientific™

2.1.1.3 Enzymes and reagents

Table 2.4 - Enzymes

Name	Supplier
DNaseI	AppliChem
DpnI	New England Biolabs
HRV-14, 3C protease	In-house production
Lysozyme	Carl Roth
PageRuler™ Prestained Protein Ladder	Thermo Fisher Scientific
Phusion® high fidelity DNA Polymerase	Thermo Fisher Scientific
T4 DNA Polymerase	New England Biolabs
Taq DNA Polymerase	New England Biolabs

Table 2.5 - Reagents

Name	Supplier
BSA	New England Biolabs
GeneRuler™ 1 kb DNA Ladder	Thermo Fisher Scientific
HF buffer (PCR)	New England Biolabs
Midori green Advance DNA stain	Biozym Scientific
NEBuffer™ 2 (Cloning)	New England Biolabs
Standard Taq Reaction Buffer	New England Biolabs

2.1.1.4 Small molecule inhibitors

All inhibitor compounds used in this thesis were dissolved in 100% DMSO (Stock conc: 10 mM), aliquoted into 20 µl volumes and stored at -20 °C.

Table 2.6 – Small molecule inhibitors

Compound name	Reference no.	Sample ID	Source
AZ1	AZ12618073	SN1036379374	Dr. Jonathan Wrigley (AstraZeneca, UK)
AZ2	AZ12334201	SN1034222656	
AZ4	AZ12618050	SN1026531160	
Vismodegib	HY10440	-	Hycultec
FT206	FT3951206	VH696	Dr. Victor Hernandez Olmos (Frauenhofer ITMP)

2.1.1.5 Primers

All primers for molecular cloning, site-directed mutagenesis and sequencing were purchased from Sigma-Aldrich®.

Table 2.7 - Primers

Construct name	5'-3' Sequence
U28Catdtip_458-SGSG_Fwd	AAAACCTGCCTCAAGCGGAAGCGGAGCTCCACG AACA
U28Catdtip_529_Rev	GCTCCACGAACAGTCACAGAT
H280P_U28Catdtip_Fwd	GTTAATGTTAACAGTCCCAGGAACAAATCTG
H280P_U28Catdtip_Rev	CAGATTTGTTCCTGGGACTGTTAACATTAAC
U28Catdtip_Y293H_Fwd	GTGCAGCTGTTCTATGGTACTTTCCTG
U28Catdtip_Y293H_Rev	CAGGAAAGTACCATAGAACAGCTGCAC
U28Catdtip_Y293R_Fwd	GTGCAGCTGTTCCGTGGTACTTTCCTG
U28Catdtip_Y293R_Rev	CAGGAAAGTACCACGGAACAGCTGCAC
U28Catdtip_Y293A_Fwd	GTGCAGCTGTTCGCAGGTACTTTCCTG
U28Catdtip_Y293A_Rev	CAGGAAAGTACCTGCGAACAGCTGCAC
U28Catdtip_F292A_Fwd	GTGCAGCTGTTCTATGGTACTTTCCTG
U28Catdtip_F292A_Rev	CAGGAAAGTACCATAGAACAGCTGCAC
U28Catdtip_M288H_Fwd	GAAAATCCAATGGTGCAGCTGTTCTATGGTACT
U28Catdtip_M288H_Rev	AGTACCATAGAACAGCTGCACCATTGGATTTTC
U28Catdtip_H261A_Fwd	GTGAGTGAATTCACACACAAGCTCCTG

U28Catdtip_H261A_Rev	CAGGAGCTTGTGTGTGAATTCACTCAC
U28Catdtip_D265S_Fwd	CACAAGCTCCTGGATTGGCTAGAGGAC
U28Catdtip_D265S_Rev	GTCCTCTAGCCAATCCAGGAGCTTGTG
U25Catdtip_L271F_Fwd	CACAAATTATTTGATTGGTTAGAAGATGCC
U25Catdtip_L271F_Rev	GGCATCTTCTAACCAATCAAATAATTTGTG
U25Catdtip_F299A_Fwd	CCCATGGTAGAGTTGGCCTATGGC
U25Catdtip_F299A_Rev	GCCATAGGCCAACTCTACCATGGG
U25Catdtip_Y300R_Fwd	CCCATGGTAGAGTTGTTCCGAGGCAGATTC
U25Catdtip_Y300R_Rev	GAATCTGCCTCGGAACAACTCTACCATGGG
U25Catdtip_Y300H_Fwd	CCCATGGTAGAGTTGTTCCACGGCAGATTC
U25Catdtip_Y300H_Rev	GAATCTGCCGTGGAACAACTCTACCATGGG
U25Catdtip_Y300A_Fwd	CCCATGGTAGAGTTGTTCGCCGGCAGATTC
U25Catdtip_Y300A_Rev	GAATCTGCCGGCGAACAACTCTACCATGGG
U28Catdtip_E366A_Fwd	GTGTTGACCTTTGCACTCTCAAGATTT
U28Catdtip_E366A_Rev	AAATCTTGAGAGTGCAAAGGTCAACAC
U28Catdtip_Y643A_Fwd	AGAAATGTTAGTGCTGCATGTCTGATG
U28Catdtip_Y643A_Rev	CATCAGACATGCAGCACTAACATTTCT
U25Catdtip_E373A_Fwd	CCTGTGTTAACATTTGCATTGTCAAGATTT
U25Catdtip_ E373A _Rev	AAATCTTGACAATGCAAATGTTAACACAGG

Fwd: Forward primer; Rev: Reverse primer

2.1.1.6 Plasmids

Table 2.8 – Plasmids

Vector	Host	Design	Resistance	Supplier
pCDF-14	Bacterial	6x His-[3C]-POI	Strep	Dr. Florian Sauer, RVZ Würzburg
pCDF-22	Bacterial	Thioredoxin (trx)-6x His-[3C]-POI	Strep	Dr. Florian Sauer, RVZ Würzburg
pColA-22	Bacterial	Trx-6x His-[3C]-POI	Kan	Dr. Florian Sauer, RVZ Würzburg
pET-30a	Bacterial	NdeI-POI-HindIII	Kan	Dr. Mohit Misra, RVZ Würzburg
pETM-14	Bacterial	6xHis-POI	Kan	EMBL, Hamburg

POI: protein of interest, trx: Thioredoxin, EMBL: European Molecular Biology Laboratory

2.1.1.7 Bacterial strains

Table 2.9 – Bacterial strains

Organism	Strain	Usage	Supplier
E. coli	DH5α	Cloning, plasmid amplification	Invitrogen
E. coli	BL21star (DE3) pRARE2	Protein expression	Invitrogen (BL21star) Novagen (pRARE2 plasmid from Rosetta2)
E. coli	Rosetta2 (DE3)	Protein expression	Novagen

2.1.1.8 Crystallization Screens

All crystallization screens listed below were prepared in-house by Ms. Nicole Bader (RVZ, University of Würzburg) with the automated liquid handling platform, LISSY®. The composition may vary from the original screens supplied by the respective companies.

Table 2.10 – Crystallization screens

Name	Supplier of original screen
$AmSO_4$ Suite	Qiagen
Crystal Screen™ 1+2	Hampton Research
Index	Hampton Research
JCSG+	Molecular Dimensions
MbClass II Suite	Qiagen
Nextal pH Clear	Qiagen
Nextal pH Clear II	Qiagen
Nextal-PEG Suite	Qiagen
Nextal-PEG Suite II	Qiagen
Nucleix Suite	Qiagen
Opti-Salts Suite	Qiagen
Protein Complex Suite	Qiagen
TOPAZ™ OptiMix™ 3	Fluidigm
TOPAZ™ OptiMix™ PEG	Fluidigm
Wizard 1+2	Emerald BioSystems
Wizard 3+4	Emerald BioSystems

2.1.2 Equipment

2.1.2.1 Instruments

Table 2.11- Instruments

Type	Model	Supplier
Agarose gel electrophoresis system	Mini-Sub® Cell GT System	Bio-Rad Laboratories
Autoclave	Systec V-150	Systec
Balance	XS 6002S Dual Range	Mettler Toledo
Balance, analytical	XS 105 Dual Range	Mettler Toledo
Block thermostat	Rotilabo® block thermostat H 250	Carl Roth
Cell disruption system	M-110P	Microfluidics
Centrifuges	5417 R 5424 5804 R 5430 R	Eppendorf
	Avanti J-26 XP Avanti J-HC	Beckmann Coulter
Centrifuge rotors	JLA 16.250 JA-25.50 JS-5.0 JLA-8.100	Beckman Coulter
Crystallographic handling tool	CrystalWand™ Magnetic	Hampton Research
Crystallization imager	ROCK IMAGER® (RI 1000)	FORMULATRIX®
Crystallographic loops	CryoLoop™	Hampton Research
	LithoLoops	MiTeGen/ Molecular Dimensions
Crystallographic sample holder	CrystalCap™ Magnetic	Hampton Research
Crystallographic sample vial	CryoVial	Hampton Research
Crystallographic storage pucks	SPINE Puck	Jena Bioscience
	Unipuck	MiTeGen
Electrophoresis	Mini-PROTEAN Tetra Cell	Bio-Rad Laboratories
Electrophoresis power supply	PowerPac™ Basic	Bio-Rad Laboratories
FPLC systems (Protein purification)	ÄKTA™ pure 25 ÄKTA™ avant 25 ÄKTA™ purifier 10	GE Healthcare

Gel-drying device	GelAir Gel Dryer	Bio-Rad Laboratories
Imaging Systems	Odyssey	LI-COR Biosciences
	ChemiDoc™ MP Imaging System	Bio-Rad Laboratories
Incubator	B15 Compact Incubator	Heraeus
Isothermal titration calorimeter	MicroCal iTC$_{200}$	MicroCal
Liquid handling robots	Honeybee 963	Digilab
	LISSY 2002	Zinsser Analytic
	NT-8®	Formulatrix
Magnetic stirrer	MR 3002	Heidolph Instruments
MALS detector	DAWN® 8 + HELEOS® II	Wyatt Technology
Microplate reader	CLARIOstar®	BMG LABTECH
Microscale thermophoresis	Monolith NT.LabelFree	NanoTemper Technologies
Microscope camera	AxioCam MRc	ZEISS
Microscope light source	KL 2500 LCD CL 1500 Eco	ZEISS
Microscopes	SteREO Discovery.V12, STEMI 2000-c	ZEISS
PCR-cycler	Mastercycler® EPgradient S Mastercycler® pro S	Eppendorf
pH meter	BlueLine 14pH	SCHOTT
Pipette (Multichannel)	Pipet-Lite Multi Pipette L8-20XLS+	Mettler-Toledo
Pipettes	XLS+ LTS PIPET 0.1-2UL XLS+ LTS PIPET 0.5-10UL XLS+ LTS PIPET 2-20UL XLS+ LTS PIPET 20-200UL XLS+ LTS PIPET 100-1000UL	Mettler-Toledo
Sealing robot	RoboSeal	HJ-BIOANALYTIC
Shaking incubators	ISF-1-W ISF-1-X LT-X	Kühner
Spectrophotometer	NanoDrop ND 1000	Peqlab
Thermomixer	Thermomix comfort	Eppendorf
Ultra-pure water system	TKA GenPure	Thermo Fisher Scientific

UV imaging system	Gel Doc™ XR System	Bio-Rad Laboratories
Vortex mixer	Vortex-Genie 2	Scientific Industries

2.1.2.2 Chromatography columns and resins

Table 2.12 – Chromatography columns and resins

Type	Model	Supplier
Analytical SEC FPLC columns	Superdex™ 200 10/300 GL Superdex™ 75 10/300 GL	GE Healthcare
Column body	Econo-Column®	Bio-Rad Laboratories
Immobilized metal-ion affinity chromatography resin	Protino® Ni-IDA	MACHEREY-NAGEL
Ion exchange columns	MonoQ® 5/50 GL Resource Q, 1ml Resource S, 1ml HiTrap® SP HP 5ml (SPHP)	GE Healthcare
Preparative SEC FPLC columns	HiLoad™ 16/600 Superdex™ 200 pg HiLoad™ 16/600 Superdex™ 75 pg	GE Healthcare

2.1.3 Software

2.1.3.1 Computer Applications

Table 2.13 - Computer applications

Name	Usage/Description	Source/Reference
AIMLESS	Scaling and merging of diffraction data	(Evans & Murshudov, 2013)
ASTRA® VI	MALS control and data analysis	Wyatt Technology
AxioVision	Microscopy imaging software	ZEISS
BUSTER	Structure refinement software	(Blanc et al., 2004)
CCP4	Software suite for macromolecular structure determination	(Winn et al., 2011)
COOT	X-ray crystallography; model building software	(Emsley et al., 2010)

ESPript 3.0	postscript output for aligned sequences with graphical enhancements	http://espript.ibcp.fr (Robert & Gouet, 2014)
ExPASy ProtParam	Estimation of physical and chemical properties of proteins	(Gasteiger et al., 2005)
GENtle 1.9.4 free software	Analysis and *in silico* editing of DNA & protein sequences; primer design	gentle.magnusmanske.de (Magnus Manske, University of Cologne)
GraphPad Prism 9.3.1	Data analysis and graphing software	GraphPad
ImageJ 1.52a	Image processing program	http://imagej.nih.gov/ij
Inkscape 0.92	Vector graphics software editor	www.inkscape.org, (open source software)
MARS	Data analysis software for CLARIOstar	BMG Labtech
MarvinSketch 21.14	Advanced chemical editor for drawing chemical structures, queries and reactions	ChemAxon
Microsoft Office 365 ProPlus Excel, Word	Spreadsheet and Word processing software	Microsoft Corporation
MXCuBE3	Beamline control and data acquisition software	
MxPro	RT-PCR cycler control; basic data processing	Agilent Technologies
ODYSSEY	Infrared Imaging software	LI-COR
OriginPro2020 (9.7.0) (Academic)	Data analysis and graphing software	Originlab Corporation
PHASER	X-ray crystallography; phasing software	(McCoy et al., 2007)
PHENIX refine	Software suite for macromolecular structure determination	(Adams et al., 2010)
PyMOL	3D visualization and graphical illustration software	(Schrödinger, LLC, 2015)
REFMAC	X-ray crystallography; macromolecular structure refinement	(Murshudov et al., 2011)
STARANISO server	Anisotropy correction	(Tickle I. J, et al., 2019)

T-Coffee server	Multiple sequence alignment	(Notredame et al., 2000)
ThermoFluor Script	Excel script for ThermoFluor data analysis	SGC, Oxford
UCSF Chimera	3D visualization and graphical illustration software	(Pettersen et al., 2004)
UNICORN	FPLC instrument management control; chromatogram analysis	GE Healthcare
XDS	X-ray data indexing, integration, data reduction and image processing	(Kabsch, 2010)

2.1.3.2 Databases

Table 2.14- Databases

Name	**Usage**	**Source**
Protein Data Bank (PDB)	Protein structures	rcsb.org
PubMed (NCBI)	Literature research	ncbi.nlm.nih.gov/pubmed/
UniProt	Information about proteins	uniprot.org

2.2 Methods

2.2.1 Molecular Biology Methods

2.2.1.1 Molecular cloning

All constructs of USP28 and USP25 used in this study were cloned either into the vectors pETM-14, pCDF-14/22 or pColA-22 using the *SLIC* method (as described below). Vectors pCDF-14/22 and pColA-22 have been modified to include the MCS of either pETM-14 with a 6x-His-3C tag at the N-terminus (pETM-14, pCDF-14) or pET-22 with a trx-His-3C tag at the N-terminus (pCDF-22, pColA-22). Both vectors comprise the plasmid backbone and antibiotic resistance cassette of pCDF (Strep) and pColA (Kan).

Sequence and Ligation Independent Cloning (SLIC)

The gene of interest was amplified *via* PCR with primers carrying the desired overhangs (homologous regions including the 3C cleavage site at the N-terminus and the multiple cloning site or MCS, downstream of the *BamHI* site at the C-terminus). Primers corresponding to the 3C/*BamHI* site in the opposite directions were used to linearize the vector. PCR was performed using the high-fidelity (HF) Phusion® DNA polymerase with suitable annealing temperatures and elongation times, as outlined below:

Table 2.15 - PCR setup

Components
Template DNA (up to 5-10 ng)
Forward primer (0.5 µM)
Reverse primer (0.5 µM)
dNTPs (10 mM each)
DMSO (3% final conc.)
5x Phusion® HF buffer (10 µl)
Phusion® DNA polymerase (1 U)
Nuclease-free water (up to 50 µl)

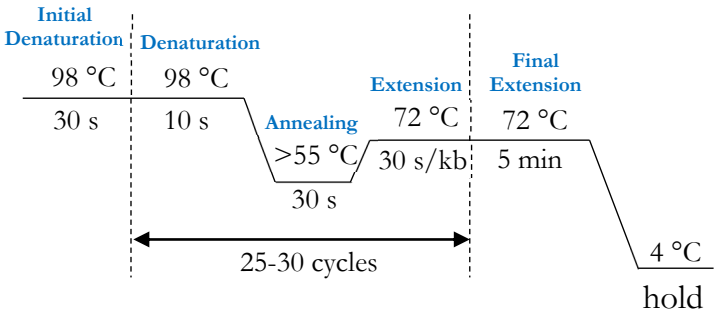

To eliminate the plasmid template, the PCR product was treated with 1 µl of *DpnI* at 37 °C for 1 hour, followed by a clean-up using the Nucleospin® Gel and PCR-cleanup kit according to the manufacturer's instructions. To generate single-stranded overhangs, the purified PCR product was incubated with T4 DNA polymerase as shown below:

Components
Vector/ Insert DNA (up to 1 µg)
10x NEB buffer 2 (5 µl)
T4 DNA polymerase (4.5 U)
Nuclease-free water (up to 50 µl)

Incubate at R T for 30 min and stop the reaction with dATP (final conc. of 1 mM)

For annealing, the vector and insert were mixed in a 1:4 ratio and incubated in a block thermostat at 75 °C for 5 min, subsequently cooled to 20 °C and transferred to ice. 10 µl of this mixture was transformed into *E. coli* DH5α (as described in Section 2.2.1.3). Positive clones were tested using colony PCR.

Colony PCR

To identify clones containing the desired insert, colony PCR was performed as shown below.

Table 2.16 – Colony PCR setup

Components
Forward primer (0.5 µM)
Reverse primer (0.5 µM)
dNTPs (10 mM each)
DMSO (3% final conc.)
10x Thermopol® buffer
Taq DNA polymerase (1 U)
Nuclease-free water (up to 20 µl/tube)

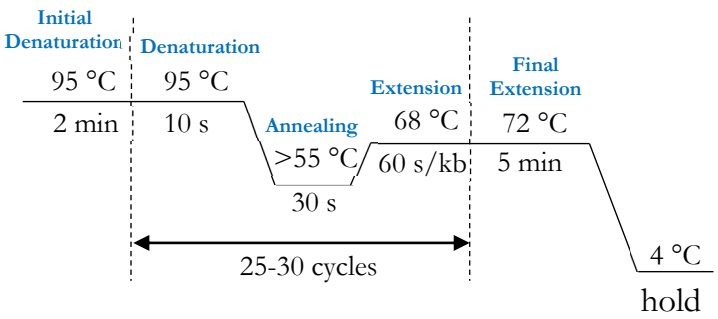

Single colonies were picked for the reaction, and the PCR was set up with vector- and insert-specific primers to identify the correct inserts. Positive clones were analyzed using agarose gel electrophoresis (as described in Section 2.2.1.2). The respective colonies were grown in 5 ml LB medium, supplemented with the appropriate antibiotic for plasmid isolation (with NucleoSpin® Plasmid kit). All recombinant plasmids were further verified by Sanger sequencing (performed by Microsynth Seqlab, Göttingen, Germany).

Site-directed mutagenesis (SDM)

Mutations were introduced using SDM with two primers carrying the desired mutation. PCR was performed using the SLIC method, as explained above, for 20 cycles. 3-5 µl of the purified PCR product (following *DpnI* digestion) was transformed into *E. coli* DH5α cells and the inserted mutation was verified by sequencing.

2.2.1.2 Agarose gel electrophoresis

TAE buffer:	40 mM Tris (pH 8.0), 20 mM acetic acid, 1 mM EDTA
DNA loading dye:	10 mM Tris-HCl (pH 7.6), 0.03% bromophenol blue, 0.03% xylene cyanol FF, 60% glycerol, 60 mM EDTA

Analysis of the PCR products was performed using Agarose gel electrophoresis. 0.8-1.5% agarose was dissolved by heating in 1x TAE buffer. Midori green dye was added (per the manufacturer's instructions), and then the gel was cast using the Minisub® Cell GT system. The gel was submerged in an electrophoresis chamber containing 1x TAE buffer. 5 µl of the DNA sample diluted 6:1 with the DNA loading dye was loaded, along with 2-3 µl of the DNA molecular weight ladder. The gel was run at 100-120 V at room temperature for 30-40 minutes and analyzed on a UV imaging system.

2.2.1.3 Chemical transformation of competent *E.coli* cells

50-100 ng of plasmid DNA was added to one aliquot (50-100 µl) of a thawed, chemically competent strain of *E.coli* cells and incubated on ice for 30 minutes. After incubation, the cells were subjected to a heat shock at 42 °C for 60 seconds and placed on ice for 5 minutes for recovery. 750 µl-1000 µl of warm LB medium was added to the vials and incubated on a Thermomixer with constant shaking for about 1 hour at 37 °C. Subsequently, the cells were applied to an LB agar plate with appropriate antibiotics and incubated overnight at 37 °C.

2.2.1.4 Protein Expression

Proteins were recombinantly expressed in *E.coli* strains BL21(DE3)-star-pRARE2 or Rosetta™2 (DE3). These strains contain the pRARE plasmid with Chloramphenicol (Cam) resistance that harbors genes for tRNAs expressing up to seven rare codons, thereby enhancing protein expression. For large scale expressions, pre-cultures were grown in 100 ml TB medium supplemented with 1% glucose (filtered & autoclaved) and the appropriate

antibiotic markers (working concentrations: Kanamycin-100 μg/ml, Streptomycin-50 μg/ml, Chloramphenicol-34 μg/ml) and incubated overnight at 37 °C in a shaker incubator.

On the next day, 2 L sterile TB medium (in 5 L Erlenmeyer flasks) was supplemented with 1% glucose and the same antibiotics and inoculated with 1% (v/v) of the pre-cultures and allowed to grow at 37 °C with continuous shaking (200 rpm). Protein expression was induced at an OD_{600} of 3.0 with 0.3 mM IPTG at 20 °C for 16-20 h. Cells were harvested by centrifugation at an rpm of 4,000 x g at 4 °C for 20 min, and cell pellets were stored at -80 °C until further use.

2.2.2 Protein Purification

All proteins used in this study, unless specified otherwise, were subjected to a two-step purification protocol that includes affinity chromatography, followed by size-exclusion chromatography.

2.2.2.1 Purification by Affinity Chromatography

Immobilized metal affinity chromatography (IMAC) was employed as the first step for protein purification. The ability of histidine to coordinate divalent metal cations makes this method a suitable strategy to purify proteins cloned with a histidine tag. Using this method, a crude cell lysate which also contains the overexpressed His-tagged protein, is passed through a stationary phase composed of Nickel ions (Ni^{2+}) immobilized *via* chelators such as Tris(carboxymethyl)ethylenediamine (TED) or iminodiacetic acid (IDA). The unbound proteins are eliminated with a high salt wash, while the Ni^{2+}-bound protein is eluted with imidazole, which competes with histidine for the metal-binding sites.

Lysis buffer (Buffer L):	50 mM HEPES (pH 8.0), 300 mM NaCl, 1 mM TCEP
Wash buffer (Buffer W):	50 mM HEPES (pH 8.0), 1 M NaCl, 10 mM Imidazole
Elution buffer (Buffer E):	50 mM HEPES (pH 8.0), 300 mM NaCl, 400 mM Imidazole
Dialysis buffer (Buffer D):	50 mM HEPES (pH 8.0), 300 mM NaCl, 0.05% β - ME

Frozen cell pellets were thawed and then resuspended in Buffer L (10 ml/g of cell pellet) supplemented with DNase (1 U/ml), lysozyme (0.5 mg/ml), one EDTA-free protease inhibitor tablet and 1 mM TCEP, added immediately before lysis.

Lysis was performed with two passages through a cell disruption system (pressure setting: 1.5 kbar). The insoluble fractions from the cell lysate were cleared with centrifugation at 30,000 x g and 4 °C for 45-60 min. The clarified lysate was then filtered through a 0.45 µ filter and loaded onto a column containing Protino® Ni-IDA beads pre-equilibrated with Buffer L. The column was washed with 10 CV of Buffer W and eluted in two fractions (15 ml and 10 ml) of Buffer E.

The concentration of the eluate fractions was determined spectrophotometrically, as described in Section 2.2.3.1. Samples from the purification steps were checked for purity by SDS-polyacrylamide gel electrophoresis (SDS-PAGE) (as described in Section 2.2.3.2), and fractions containing the purest form of the protein were pooled for further analyses.

The N-terminal 6x-His/trx-6x His-tag was proteolytically cleaved by adding *HRV14-3C* protease (recognition sequence: LEVLFQ↓GP, the arrow depicts the cleavage site) to the pooled eluate fractions in a 1:100 (w/w) ratio. The solution was then transferred into a pre-treated, standard RC dialysis tubing (3 kDa molecular weight cut-off) and dialyzed overnight in Buffer D (2 L) at 4 °C.

2.2.2.2 Purification by Ion-exchange Chromatography

The USP28 catalytic domain (WT) protein was initially also subjected to an ion-exchange purification step following IMAC. This method relies on the interaction (or exchange) of ions in the protein sample with fixed ionic groups of the opposite charge bound to the stationary phase or column. For USP28, a positively charged anion exchange column was selected. The protein is eluted by gradually increasing the ionic strength, thereby reducing the interactions between the resin and the protein.

ResQ Buffer A (low salt buffer):	50 mM HEPES (pH 8.0), 50 mM NaCl, 1 mM TCEP
ResQ Buffer B (high salt buffer):	50 mM HEPES (pH 8.0), 1 M NaCl, 1 mM TCEP

The dialyzed eluate (from Section 2.2.2.1) was diluted with ResQ Buffer A (until the apparent salt concentration was approximately 50-70 mM) and passed through a 0.45 µ filter. This solution was loaded onto an Anion-exchange column, RESOURCE™Q 1 ml, pre-equilibrated with ResQ Buffer A using the sample pump of an ÄKTA pure system. Bound proteins were eluted with a 20 CV linear gradient of 60-100% of ResQ Buffer B, followed by a wash step with 100% ResQ Buffer B. The elution fractions (0.5-1 ml each) were collected in a 96-deepwell-block. The samples were analyzed by SDS-PAGE, and pure fractions were pooled for concentration.

2.2.2.3 Purification by Size Exclusion Chromatography

Size Exclusion Chromatography (SEC) was used as a final step for purification. SEC is a technique that allows the separation of molecules based on their weight and/or hydrodynamic radius. A heterogeneous analyte is passed through a packed stationary phase with a defined pore size. The larger molecules in the sample are not retained within the pores and hence pass quickly through the column. Smaller molecules get occupied deep within the pores and have to traverse a larger volume, resulting in a longer retention time.

Gel Filtration buffer (GF buffer):	20 mM HEPES (pH 8.0), 150 mM NaCl, 1 mM TCEP

Proteins obtained from the above-described purification steps were concentrated using the Amicon® ultrafiltration device, with a suitable molecular weight cut-off, to a volume less than 5% of the column volume that was to be used. Concentrated samples were then centrifuged for 20-30 min at 25,000 x g and 4 °C before injecting them into a column, pre-equilibrated with the GF buffer. Catalytic domain constructs of USP28 (full length WT, ΔUCID-tip WT & variants) and USP25 (ΔUCID-tip WT & variants) were purified with the HiLoad™ 16/60 Superdex™200 pg column. The USP28cat (ΔUCID) protein was purified with the HiLoad™ 16/60 Superdex™75 pg column.

An ÄKTA pure system controlled the chromatographic procedure, and the purified protein was eluted over 1.2 CV at a constant flow rate of 1 ml/min. The elution fractions were collected in 2 ml volumes in a 96-deepwell block and analyzed by SDS-PAGE (as described in Section 2.2.3.2). The purest fractions were concentrated as before and either used immediately for further studies or flash frozen and stored in small aliquots at -80 °C until further use.

2.2.2.4 Purification of Ubiquitin

Ub lysis buffer:	50 mM Tris-HCl (pH 7.6), 100 mM NaCl
Ub buffer A:	50 mM Ammonium acetate (pH 4.5)
Ub buffer B:	50 mM Ammonium acetate, 600 mM NaCl
Ub storage buffer:	40 mM Tris-HCl (pH 7.5), 100 mM NaCl

The pellet from a 1 L culture was resuspended in 50 ml of Ub lysis buffer. Lysis was performed in two passages through a cell disruption system (pressure setting: 1.5 kbar). The insoluble fractions from the cell lysate were cleared with centrifugation at 30,000 x g and 4 °C for 45-60 min. The cleared lysate was then placed in an ice bath on a magnetic stirrer to ensure constant stirring. 0.4 ml of 60% perchloric acid was added to this solution dropwise and incubated for 10 minutes. The lysate was centrifuged at 35,000 x g for 30 minutes to remove the precipitate, and the cleared lysate was dialyzed against Ub buffer A at 4 °C overnight.

On the following day, the lysate was passed through a 0.45 µ filter and applied to a pre-packed cation exchange column (3 x 5 ml SP-HP columns), equilibrated with Ub buffer A. Ubiquitin was eluted with a linear gradient using Ub buffer B (approx. 60 CV). The fractions containing the protein were pooled, and the buffer was exchanged with Ub storage buffer during concentration using an ultrafiltration device.

2.2.3 Biochemical and Biophysical Analyses

2.2.3.1 UV/Vis Spectrophotometry

The concentrations of purified proteins and DNA were determined by measuring the UV absorbance using the NanoDrop™ 1000 spectrophotometer. Absorbance spectra in the wavelength range for DNA or protein were recorded with the reference buffer solution for blank measurements. For DNA, the concentration was calculated based on the absorbance at 260 nm, while the 260/280 ratio was used to check for sample purity of the purified proteins. For proteins, the concentration was measured based on the absorbance at 280 nm and extinction coefficients obtained from the corresponding amino acid sequence using the ExPASy ProtParam tool (see Section 7.3). The calculation of the concentration is based on the Beer-Lambert law, defined as:

$$c = A/(\varepsilon \times d)$$

where c is the protein concentration, A is the absorption at 280 nm, ε is the molar extinction coefficient (M^{-1} cm^{-1}), and d is the path length (cm) of the light through the sample.

2.2.3.2 SDS-Polyacrylamide Gel Electrophoresis (PAGE)

Protein samples obtained after purification or from gel-based assays were analyzed *via* SDS-PAGE. The sample is denatured by heating it in the presence of a reducing agent and sodium-dodecyl-sulphate (SDS), an anionic detergent. The proteins unfold into linear chains with a negative charge proportional to the polypeptide chain length. The sample is then subjected to an electric field through a polyacrylamide gel that acts as a sieve and separates the denatured proteins based on their size as they move towards the positive electrode.

Separating gel:	15% acrylamide-bisacrylamide mix (37.5:1), 167 mM Tris-HCl (pH 8.8), 0.1% SDS; freshly added: 0.1% APS, 0.4% TEMED
Stacking gel:	5% acrylamide-bisacrylamide mix (37.5:1), 125 mM Tris-HCl (pH 6.8), 0.1% SDS; freshly added: 0.1% APS, 1% TEMED
SDS-PAGE sample buffer (4x):	200 mM Tris-HCl (pH 6.8), 8% SDS, 40% glycerol, 4% β-mercaptoethanol, 50 mM EDTA, 0.08% bromophenol blue
SDS-PAGE running buffer (10x):	14.4% glycine, 1% SDS, 3% Tris
G-250 staining solution:	80 mg Coomassie brilliant blue (G-250), 3 ml of 37% (w/w) HCl (filled up to 1 L with ultrapure water)

Gels were prepared using the Mini Protean II system by sequentially casting the separating and stacking gels. Samples were mixed with 1x sample buffer and incubated at 95 °C for 5 min. 3-5 µl of the protein samples and 2 µl of the standard protein marker were loaded onto the gels and placed in an electrophoresis chamber filled with 1x SDS-PAGE running buffer. Electrophoresis was performed at 100-200 V at room temperature until the dye front nearly crossed the gel. Prior to staining, the gels were rinsed three times with hot water for about a minute, then stained with Coomassie G-250 for 5 minutes and destained with ultrapure water. For gel-based ubiquitin cleavage assays, 3 µl of the non-denatured samples were loaded onto 4-20% Mini-PROTEAN® TGX™ pre-cast protein gels. Electrophoresis was performed as

described above, and the gels were stained using the Pierce™ Silver stain kit, as per the manufacturer's instructions.

2.2.3.3 ThermoFluor assay

ThermoFluor or Thermal shift assay (TSA) was performed to analyze the thermal stability and overall fold of the USP28 and USP25 point mutants. TSA measures the melting temperature of a protein (Tm). Protein denaturation, achieved through an increase in temperature, is monitored *via* a rise in fluorescence of the SYPRO Orange dye, which binds to hydrophobic residues that are exposed as the target protein unfolds in this process. Purified WT and mutant proteins at a final concentration of 2 μM were mixed with 2.5x SYPRO Orange dye utilizing identical buffer conditions in a 96-well PCR plate (in triplicates) and sealed with an optical quality sealing foil. The plate was transferred into a real-time PCR cycler, and fluorescence was measured from 25 °C to 95 °C with an increment of 1 °C/min at an excitation maximum wavelength of 490 nm and emission maximum wavelength of 575 nm. Data evaluation and determination of the melting temperature was performed using the MxPro qPCR software (Agilent Technologies).

2.2.3.4 Multi-angle light scattering (MALS)

MALS analysis combined with SEC was used to test the effect of the inhibitors on the oligomeric state of USP25. In SEC-MALS, the SEC column separates molecules by their hydrodynamic volume. After exiting the column of the HPLC or FPLC system, the molecules pass through a MALS detector coupled to a refractive index monitor and are probed by a laser beam. The MALS signals and UV absorbance and/or differential refractive index (dRI) signals are analyzed to quantify the analyte's physical properties.

20 μM of USP25cat WT protein was incubated with 3x concentration of the inhibitors and incubated at room temperature for 1 hour. The mixture was centrifuged at 25,000 x g shortly, and ~100 μl of this was injected into a Superdex® 200 Increase 10/300 GL column, pre-equilibrated with freshly prepared GF buffer. Light scattering data were processed and analyzed using the ASTRA® VI software.

2.2.3.5 Microscale Thermophoresis

Microscale thermophoresis (MST) was employed to determine the affinity and stoichiometry of protein-inhibitor binding. MST monitors changes in the fluorescence of a target molecule as a function of the temperature and concentration of the cognate ligand molecule. The thermophoretic mobility of the molecules along microscopic temperature gradients, which is defined by changes in their hydration shell, charge or size, causes the shift in fluorescence.

In this approach, a moderately focused IR-laser (1480 nm) is applied to generate a local, precise, and steep temperature gradient in the focal volume of glass capillaries that contain the protein-ligand sample. The molecules migrate thermophoretically as the temperature rises, which is detected using the intrinsic tryptophan fluorescence (ex: 280 nm, em: 360 nm) of the protein molecule in the sample. The thermophoretic movement and the temperature-related intensity change (TRIC) are analyzed for MST quantification.

MST buffer:	20 mM HEPES (pH 8.0), 150 mM NaCl, 1mM TCEP, 0.3% Tween-80

All MST experiments were performed in a Monolith NT.LabelFree instrument. The inhibitors AZ1, Vismodegib and FT206 were diluted from a 10 mM stock (in 100% DMSO) with the MST buffer in a two-fold, 16-point dilution series with final assay concentrations ranging from 100 μM to 0.003 μM. The USP28cat (Δtip) WT and variant proteins were diluted to a final assay concentration of 50 nM with the MST buffer. 25 μl each of the protein and the inhibitor dilutions were mixed and incubated at RT for 15 minutes before aspiration into the NTLabelFree glass capillaries. MST measurements were recorded at 25 °C using the following parameters: LED power= 10%, MST power= 40%, laser on (heating)= 25 s, laser off (cooling)= 5 s.

All observed data were normalized against the baseline obtained from a control sample without the inhibitor compound and the maximal response at the highest inhibitor concentration. Data analysis was performed with the NT Analysis Software (NanoTemper Technologies), and resulting MST curves were plotted using OriginPro 2020 Software (version 9.7.0; OriginLab Corporation).

2.2.3.6 Isothermal Titration Calorimetry

Isothermal titration calorimetry (ITC) was used to evaluate the thermodynamics of protein-inhibitor binding. An ITC instrument consists of a sample cell that generally holds the protein of interest and a reference cell with buffer/water. The ligand sample, stored in a syringe, is titrated into the cell containing the protein while constant stirring takes place.

The heat generated or absorbed upon the protein-ligand interaction is recorded by measuring the changes in the power needed to maintain isothermal conditions between the reference and the sample cell. Injections are performed repeatedly and result in gradually smaller peaks as the biomolecule becomes saturated. Eventually, the peak sizes remain constant and represent only the heats of dilution. The resulting binding curve can be analyzed to determine the dissociation constant (K_d), molar free energy change (ΔG), molar enthalpy change (ΔH), molar entropy change (ΔS) and stoichiometry of the interaction.

ITC Buffer:	20 mM HEPES (pH 8.0), 150 mM NaCl, 1mM TECP

All experiments were performed in a MicroCal™ iTC200 instrument at 25 °C. Protein samples used for the analyses were dialyzed in a D-Tube™ Dialyzer (Midi, MWCO: 3.5 kDa) against the ITC buffer overnight at 4 °C. On the following day, the samples were centrifuged at 25,000 x g at 4 °C for ~30 minutes, and the dialysate buffer was filtered and degassed to serve as a reference. The concentration of the protein samples was determined as described above. The inhibitors were diluted from their stock solutions (in 100% DMSO) with the dialysate buffer. To minimize heat effects due to buffer mismatch, the protein samples were diluted in dialysate buffer supplemented with DMSO at a final concentration of 2%. Both protein and inhibitor samples were degassed at 25 °C for ~10 minutes prior to the experiment. 2 µl aliquots of 0.2 mM inhibitor contained in the syringe were titrated against 200 µl of 0.02 mM protein sample stored in the cell of the instrument. A total of 20 injections were carried out with a 180 s delay between each injection, allowing the signal to return to the baseline. The syringe spin speed was set to 600 rpm and the reference power at 11 µcal/s.

An inhibitor to buffer titration was performed as control and subtracted from the protein-inhibitor data prior to curve fitting. Data analysis was performed with the MicroCal Origin software.

2.2.3.7 Ubiquitin chain synthesis

Ub chain buffer:	40 mM Tris-HCl, 10 mM ATP, 10 mM $MgCl_2$, 0.6 mM DTT
Reaction mix A (for K48-linked chains)	2.8 mM Ub, 1 µM UBA, 25 µM Cdc34 (in Ub chain buffer)
Reaction mix B (for K63-linked chains)	1.4 mM Ub, 1 µM UBA, 81 µM UBA Ubc13, 8 µM Mms2 (in Ub chain buffer)

The ubiquitin chains were generated as per the protocol described in (Komander et al., 2008). 3-5 ml of Reaction mix A and Reaction mix B were incubated at 37 °C for approx. 4 h and diluted to 20-fold with Ub buffer A (Section 2.2.2.4) to stop the reaction. The samples were applied to a RESOURCE™ S cation exchange column and eluted with a 60 CV gradient using Ub buffer A and Ub buffer B (Section 2.2.2.4). Fractions comprising the different ubiquitin chains (monoubiquitin, diubiquitin, tri-ubiquitin and tetra-ubiquitin) were pooled separately, and the buffer was exchanged to the Ub storage buffer (Section 2.2.2.4) during concentration using an ultrafiltration device. The samples were subsequently aliquoted into 50 µl volumes, flash-frozen in liquid nitrogen and stored at -80 °C until further use.

2.2.3.8 DUB activity assays

To assess the DUB enzymatic activity, a fluorogenic, synthetic monoubiquitin substrate was utilized. Here, the Ub-molecule is covalently bound at its C-terminus to a quenched fluorophore (Rhodamine110/AMC), which is released by DUB activity. This leads to a robust increase in the fluorescent signal in the presence of an active enzyme.

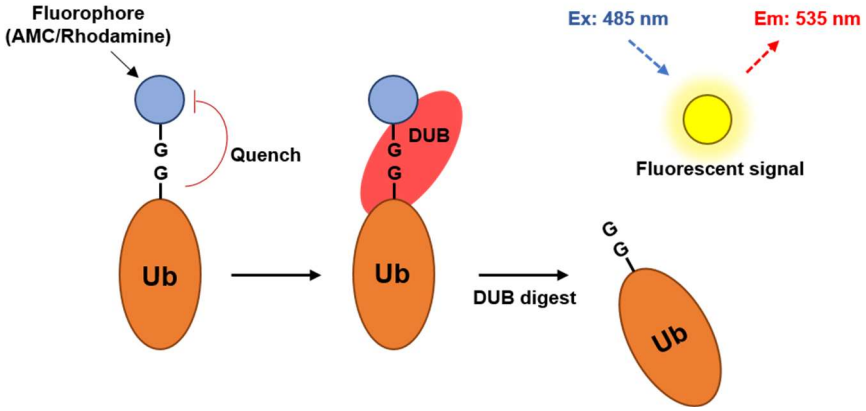

Figure 2.1: Principle of Ub-Rhodamine assay. Cleavage of the amide bond between the C-terminal glycine of ubiquitin and rhodamine by the DUB results in an increase in rhodamine fluorescence at 535 nm (Ex. 485 nm).

Dose-response assays

Assay buffer:	20 mM HEPES (pH 7.5), 150 mM NaCl, 1 mM TCEP, 50 μg/ml BSA

To validate the binding site of the inhibitors, mutational analyses of the residues constituting the binding pocket of the proteins were pursued. Activity measurements and determination of compound inhibition (IC_{50}) for USP28/25 WT protein and its variants were performed using the fluorogenic substrate, Ub-Rhodamine110Gly (Ub-Rho110) (UbiQ Bio). 2 mM stock solutions of Ub-Rho110 were prepared in 50% DMSO, as per the manufacturer's instructions and stored at -80 °C.

For IC_{50} (half maximal inhibitory concentration) determinations, each compound of interest was diluted from a 10 mM stock (in 100% DMSO) with the assay buffer in a threefold, ten-point dilution series, starting from 100 μM. The assay was performed in black, 384-well, non-binding plates (Greiner Bio-One). The WT proteins and their variants (final concentration: 20 nM) were incubated with the respective compound for 15 minutes at room temperature. To initiate the reaction, Ub-Rho110 (final concentration: 250 nM) was added to each well. The fluorescence was measured using the CLARIOstar microplate reader (BMG Labtech) at 25 °C (excitation λ: 485 nm; emission λ: 585 nm). The initial slope of the curves was measured, and the % inhibition was determined using the following equation:

$$\%\ \text{inhibition} = \left(1 - \frac{\text{Rate}_{\text{inhibited}} - R_0}{\text{Rate}_{\text{uninhibited}} - R_0}\right) \times 100$$

where $\text{Rate}_{\text{inhibited}}$ is the initial slope of the progress curves of the proteins in the presence of the inhibitor; $\text{Rate}_{\text{uninhibited}}$ is the initial slope of the progress curve in the absence of the inhibitor. R_0 is the slope of the background fluorescence in the absence of the enzyme. The resulting % inhibition was plotted as a function of inhibitor concentration. The IC_{50} values were derived using the function log(inhibitor) *vs* response-variable slope (four parameters) using the GraphPad Prism (9.1.2) software.

Gel-based ubiquitin hydrolysis assay

K48-linked diubiquitin and K63-linked tetra-ubiquitin were used as substrates to analyze the ubiquitin chain cleavage activity of the WT and the variant proteins in the presence and absence of the inhibitors. The enzymes and the inhibitors (or 2% DMSO as control) were diluted in assay buffer, mixed at a final concentration of 0.5 μM and 30 μM, respectively, and incubated at room temperature for 15 minutes. This mixture was later transferred to a block thermostat set to 37 °C and further incubated for 5 minutes. To initiate the reaction, 10 μM (final concentration) of the substrate was added to the mixture in an equimolar ratio. A 20 μl aliquot was removed from the sample at time points 0', 1', 5', 10', 20' and 60' and added to 10 μl of 1x SDS loading buffer to stop the reaction. The samples were analyzed with silver staining as described in Section 2.2.3.2.

2.2.4 X-ray Crystallography

2.2.4.1 Protein crystallization

Different constructs of USP28 and USP25 were initially screened using various crystallization solutions at different concentrations with the sitting-drop vapor diffusion method. Prior to the crystallization setup, the proteins were centrifuged at 25,000 x g at 4 °C for ~30 minutes. Primary screening was performed using the HoneyBee 963 and the NT8® liquid handling systems and CrystalQuick™ 96-well, sitting-drop vapor diffusion plates. For USP28cat (Δtip) and USP25cat (Δtip) crystals, the drops comprised 0.3 μl of the protein solution at a desired concentration, 0.3 μl of the mother liquor (1:1 ratio) and a reservoir solution with 40 μl of the mother liquor. For USP28cat (ΔUCID) crystals, 0.3 μl of the protein solution at the desired concentration was added to 0.1 μl of the mother liquor. The plates were then sealed with Polyolefin adhesive seal using RoboSeal. Plates containing identical crystallization conditions were simultaneously screened at 4 °C and 20 °C and monitored using the ROCK IMAGER® (RI 1000) documentation system.

Subsequent optimization screens were prepared using the automated liquid handling platform LISSY®. Fine screens from previously identified optimized conditions were set up manually using the 24-well, hanging-drop vapor diffusion setup. The protein-reservoir solutions were mixed in a ratio of 1:1 (1-2 μl each) on a siliconized coverslip, sealed with silicon grease and equilibrated over 500-1000 μl of the reservoir solution.

2.2.4.2 Inhibitor soaking

Since all the inhibitor compounds used in this study are highly hydrophobic, DMSO was chosen as the solvent. Therefore, it was also crucial to test the maximum DMSO concentration that the protein crystals could withstand without affecting their growth and diffraction quality. This was done by either incubating the purified protein with different concentrations of DMSO (ranging from 1%-10%) for 1 hour and setting up crystallization plates with the hanging drop vapor diffusion setup or soaking pre-grown crystals in a 1 µl drop of the reservoir solution, supplemented with varying DMSO concentrations.

For inhibitor soaking, the pre-formed USP28cat (Δtip) crystals were taken out of the original solution where they were grown and placed into a 1 µl drop of the respective inhibitor diluted from a 10 mM stock (in 100% DMSO) in the reservoir solution with a final inhibitor concentration of 100 µM, 150 µM or 200 µM. The final DMSO concentration in the inhibitor drop was 1%, 1.5% and 2%, respectively. The incubation time was varied from 10 minutes, 1 hour, 3 hours to overnight. Afterwards, a cryoprotectant solution containing the respective inhibitor concentration, supplemented with 25% glycerol, was added in a 1:1 ratio. The soaked crystals were allowed to remain in this drop for about 3-5 s before briefly submerging in a separate drop containing only the cryo solution and then being immediately flash-frozen in liquid nitrogen.

For the USP28cat (ΔUCID) crystals, the same method was adopted with a few changes; the soaking time was varied between 3-6 hours and 25% ethylene glycol was used as cryo-protectant.

2.2.4.3 Data collection and processing

X-ray diffraction datasets used in this thesis were collected at the European Sychrotron Radiation Facility (ESRF-Grenoble, France), Berliner Elektronenspeicherring-Gesellschaft für Synchrotronstrahlung (BESSY-Berlin, Germany) and at the Deutsches Elektronen-Synchrotron (DESY-EMBL, Hamburg, Germany) using the following parameters:

Table 2.17 – Data collection parameters

	USP28-AZ compounds	**USP28-Vismodegib**		**USP28-FT206**	
	Δtip	**Δtip**	**ΔUCID**	**Δtip**	**ΔUCID**
Beamline	BESSY BL 14.1	ESRF ID 30A	ESRF ID 23-2	ESRF ID 23-2	EMBL Beamline P14
Detector	PILATUS3 S 6M	EIGER X 4M	PILATUS3 X 2M	PILATUS3 X 2M	EIGER2 CdTe 16M
Wavelength (Å)	0.918	0.967	0.873	0.873	0.976
No. of images	3600	3600	3600	3600	3600
Exposure time (s)	0.01	0.05	0.02	0.02	0.01

Data integration and scaling were performed with the programs XDS (Kabsch, 2010) and Aimless (Evans & Murshudov, 2013), respectively, from the CCP4 program suite. Since the datasets for USP28cat (Δtip) crystals showed a high degree of anisotropy, the same was corrected using the STARANISO webserver (Tickle I. J et al., 2019).

2.2.4.4 Structure solution and refinement

The USP28-inhibitor bound complex structures were solved by Dr. Florian Sauer (AG Kisker, RVZ). Molecular replacement was performed with Phaser (McCoy et al., 2007) using one chain of the USP28cat *apo* structure (PDB ID:6H4I, Sauer et al., 2019) as the search model. Initially, the model was divided into the core USP domain and the isolated UCID region. Subsequent model building was performed using Coot (Emsley et al., 2010) and the coordinates, TLS parameters and B-factors were refined with either autoBUSTER (Blanc et al., 2004) or PHENIX-refine (Adams et al., 2010). Data collection, phasing and refinement statistics for all structures are described in further detail in Section 3.1.

3. RESULTS

3.1 Structural characterization of USP28-Inhibitor complex

3.1.1 Purification and Crystallization of USP28cat constructs

Crystal structures of the USP28 catalytic domain (USP28cat) in its *apo* and Ub-bound forms have previously been reported by our group and others (Sauer et al., 2019; Gersch et al., 2019). Crystals of the full-length catalytic domain typically diffracted to a resolution of approx. 3 - 3.5 Å. It was, therefore, essential to obtain protein crystals with higher diffraction quality to study inhibitor-bound structures. Various constructs of USP28cat (Figure 3.1a) were cloned, purified and subjected to extensive crystallization trials to identify the optimal form for the subsequent inhibitor-soaking experiments.

A two-step purification approach was adopted for all USP28 constructs studied thus far: immobilized metal affinity chromatography (IMAC; Section 2.2.2.1) followed by SEC (Section 2.2.2.3). A representative SDS-PAGE following IMAC and the SEC purification profile for the USP28cat (Δtip) construct is shown in Figure 3.1 b & c.

During the early phases of this experimental thesis work, crystallization trials were performed with the full-length catalytic domain (aa 149-703 and 149-707). As seen from our previous studies, these crystals diffracted very poorly (~3 to 4 Å resolution) (Figure 7.1), and they exhibited a high degree of anisotropy, characterized by variation in diffraction quality with reciprocal lattice direction. Anisotropic data often result in ambiguous electron density maps, stalled model improvement and inferior refinement statistics, which is not ideal for characterizing small-molecule binding with high accuracy. To overcome this hurdle and obtain superior diffracting crystal forms, other constructs of the USP28cat domain lacking either the UCID (ΔUCID) or the UCID-tip (ΔUCID-tip/Δtip) region were analyzed (Figure 3.1a).

The UCID-tip of USP28 comprises a mainly disordered region of the catalytic domain. However, its removal does not hamper the oligomerization of the protein (Sauer et al., 2019). Removal of the UCID leads to a monomeric protein. Gersch et al. showed that crystals grown from the ΔUCID protein diffract to a significantly higher resolution of 2.3 Å, compared to the full-length catalytic domain protein (Gersch et al., 2019). Based on the results published by Gersch et al., crystallization screens were set up for the USP28 (149-ΔUCID-707) and USP28 (149-ΔUCID-703) proteins using the hanging drop vapor diffusion method and a

grid screen of the condition reported by Gersch et al., with varying pH, salt and PEG concentrations. However, this approach did not lead to crystal growth. Additionally, USP28 (149-ΔUCID-703) was also subjected to microseeding with USP28 (149-707) (full-length catalytic domain) protein crystals (Sauer et al., 2019), but this was also unsuccessful.

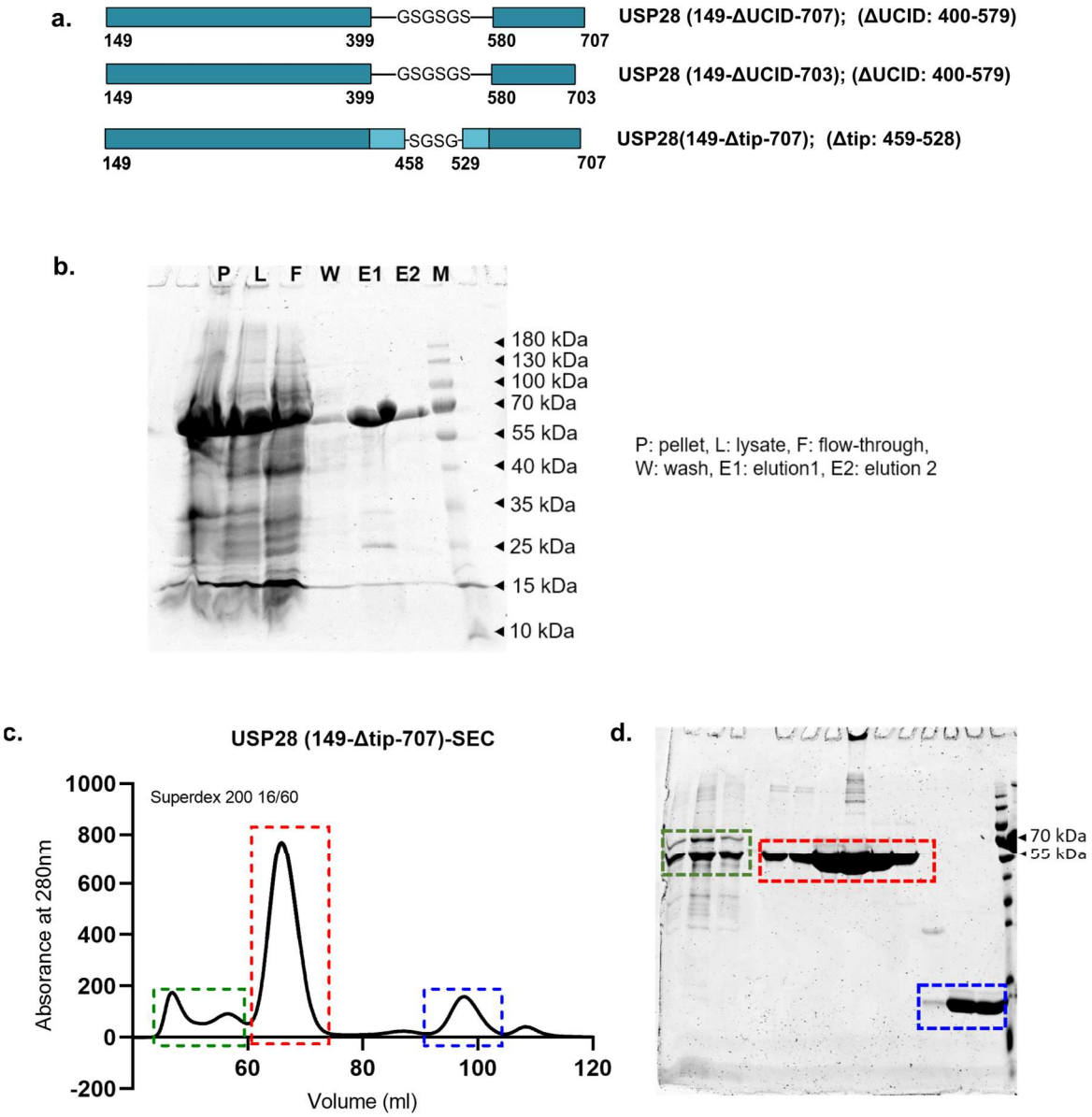

Figure 3.1: Purification of USP28cat domain constructs (a) Schematic of the USP28 catalytic domain constructs utilized for crystal screening. The residue range is depicted for each construct, along with the truncated regions and the linker residues **(b)** SDS-PAGE analysis following Ni-IDA purification of the USP28cat (Δtip) construct. Elution fractions E1 & E2 were pooled, dialyzed and concentrated for SEC. Molecular weight markers are indicated on the right. **(c)** Elution profile from SEC and SDS-PAGE analysis **(d)** of the peak fractions, indicated by the colored boxes. The blue box shows the peak corresponding to the thioredoxin tag, while the green box corresponds to aggregated protein. Fractions within the red box were pooled and concentrated for subsequent experiments. Molecular weight marker highlighted at 70 kDa and 55 kDa are also shown.

3.1.1.1 USP28cat (Δtip)

Single crystals of the USP28 (149-Δtip-707) protein were obtained with a reservoir solution containing 0.5 M sodium malonate (pH 6.0) and 0.1 M sodium salts (citrate or acetate; pH: 5.0 and 5.5) using the sitting drop vapor diffusion setup (0.25 µl of 5 mg/ml protein was mixed with 0.25 µl of the reservoir solution and equilibrated over 50 µl of the reservoir solution at 20 °C). Crystals could also be reproduced in the hanging drop vapor diffusion setup (1 µl of 5 mg/ml protein mixed with 1 µl of the reservoir solution, equilibrated over 500 µl of the reservoir solution at 20 °C). Crystals appeared within 2-5 days, reached their maximum size (~200 µm in length) in a week and diffracted to about 2.6 Å (Figure 3.2). They belong to the orthorhombic space group $P2_122_1$ and contain two protein molecules in the asymmetric unit. The crystal lattice displays an arrangement of the densely ordered USP-core domains separated by a layer of solvent and dimerization domains. The high solvent content of the crystal (~70%) provides for easy diffusion of the ligand to a prospective binding channel making it a suitable candidate for inhibitor-soaking experiments.

The initial inhibitor-bound structures were obtained with the USP28cat (Δtip) crystals and the AZ compounds, Vismodegib and FT206. The crystals diffracted to higher resolutions compared to the USP28cat WT protein crystals. However, as seen with the previously reported crystal forms of the dimeric USP28cat variants, these structures also exhibit a high degree of anisotropy which was corrected using the STARANISO webserver (data cutoff for anisotropy correction: $I/\sigma I > 1.0$, $CC_{1/2} = 30\%$), allowing the use of data extending to maximum resolutions ranging from 2.6 Å to 3.2 Å.

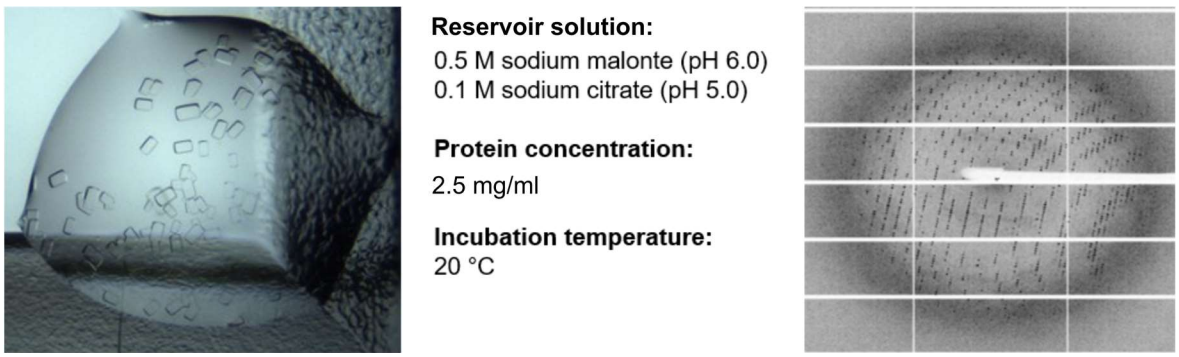

Figure 3.2: Optimized crystals and representative diffraction image of the native USP28 (149-Δtip-707) protein. The composition of the final, refined crystallization condition, protein concentration and temperature are as indicated (center). The crystals (left) diffracted up to 2.6 Å at BESSY (right).

3.1.1.2 USP28cat (ΔUCID)

In an effort to improve the quality of the data sets, protein crystals grown from another construct of USP28cat lacking the UCID region (149-ΔUCID-698) were tested (design and initial screening were performed by Dr. Florian Sauer). This new construct is similar to the one previously reported by Gersch et al. (149-ΔUCID-703). They also showed that the crystals grown from their construct diffracted to 2.2 Å and belonged to space group $I4_132$.

USP28cat (149-ΔUCID-698) formed large, single, cuboidal crystals (Figure 3.3c) at a concentration of 15 mg/ml and 20 °C. The reservoir solution comprised 0.05 M NaCl, 0.1 M Li2SO4, 0.1 M MES (pH 6.4), and 14% PEG 10,000, similar to the above-reported crystal form.

However, unlike the USP28cat (Δtip) crystals, the USP28cat (149-ΔUCID-698) crystals only grew in the sitting drop vapor-diffusion setup and could not be reproduced by the hanging drop method. This observation was later supported by the propensity for the crystals to adhere to the bottom of the crystallization plate, making it difficult to dislodge them from the base without breaking them. This observation suggests that the crystals require a polycarbonate base for efficient nucleation. The crystals appeared within 1-2 days and reached a maximum size in about 5 days. They diffracted to a higher resolution than the previously obtained crystals ranging from 2.1 Å to 2.57 Å while maintaining the high solvent content of 70%. This crystal form belonged to space group $H3_2$ and contained one protein molecule per asymmetric unit.

At the time of writing this thesis, datasets for the USP28cat (149-ΔUCID-698) *apo* protein (Section 7.4.7) and bound to Vismodegib (Figure 3.10, Table 3.2) and FT206 (Figure 3.12, Table 3.3) were obtained.

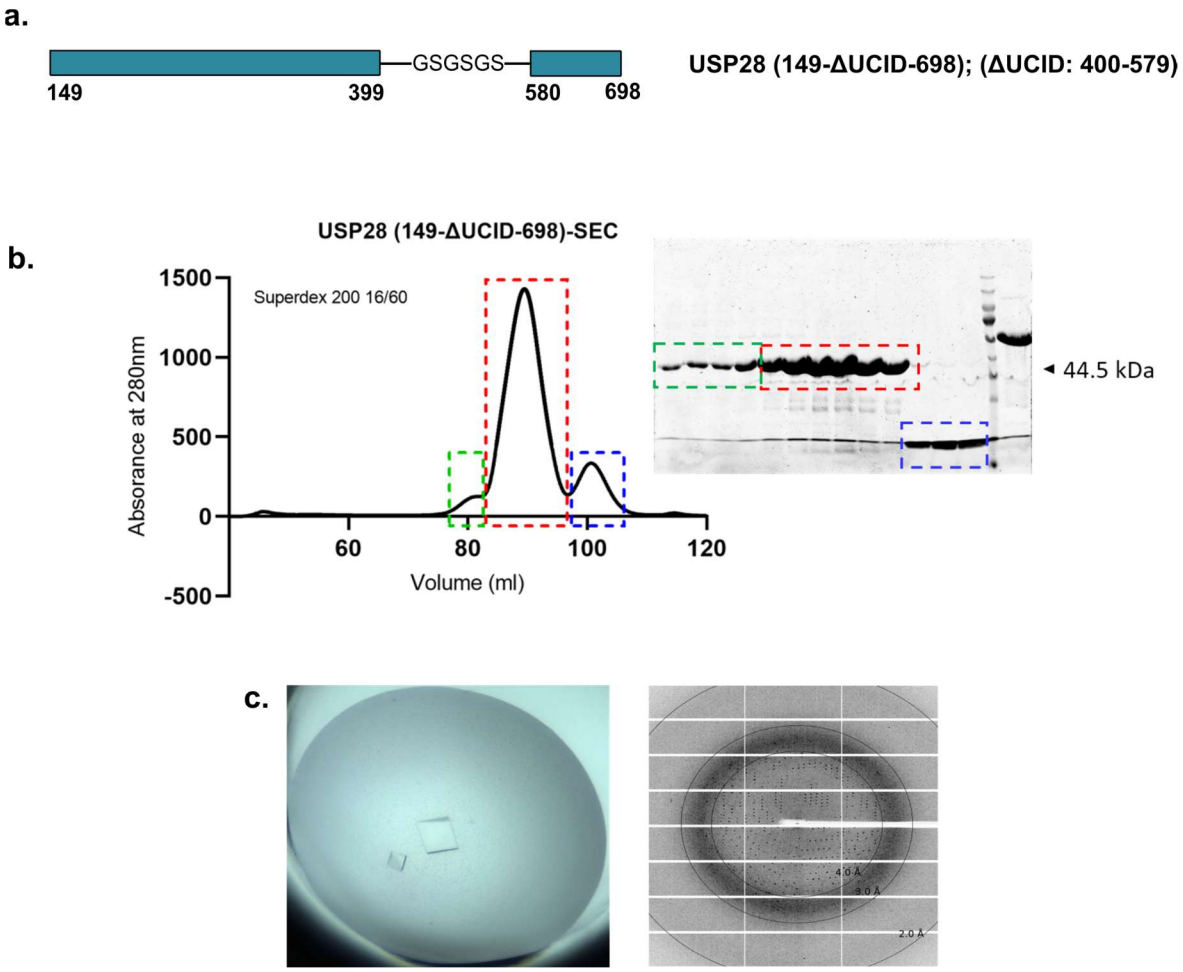

Figure 3.3: Purification and crystallization of the USP28cat (ΔUCID) protein. (a) Schematic of the USP28cat (ΔUCID) construct used in this study. It has a shorter C-terminal end than the previously tested ΔUCID constructs **(b)** Elution profile obtained from the Superdex 200 16/60 column, and SDS-PAGE analysis of the peak fractions are indicated by the colored boxes. The green box shows protein aggregates, while the blue box corresponds to the thioredoxin tag. Fractions within the red box were pooled and concentrated for subsequent experiments. **(c)** The protein formed large, cuboid-shaped crystals that diffract to up to 2.57 Å (represented here for the *apo* protein).

3.1.1.3 Inhibitor soaking

Prior to inhibitor soaking, the USP28cat (149-Δtip-707) and (149-ΔUCID-698) protein crystals were subjected to a DMSO test by incubating them in the mother liquor containing 1-10% (v/v) DMSO for 1 hour (as described in Section 2.2.4.2). Crystals were found to tolerate up to 5% DMSO without observable cracking. Accordingly, all inhibitors were dissolved to have maximum molarity of 200 μM at 2% DMSO. Inhibitor soaking was performed as described in Section 2.2.4.3. The best diffraction data were obtained from crystals soaked with 100 μM and 150 μM of the inhibitor for 3 hours for the (Δtip) protein and 150 μM for ~6 hours for the (ΔUCID) protein.

3.1.2 USP28-inhibitor complexes – an overview

The initial complex structures obtained for the AZ compounds, Vismodegib and FT206, were obtained with the USP28cat (Δtip) variant. For all three compound classes, the corresponding electron density was observed in the same region of the protein.

The inhibitors bind into a pocket located at the intersection of the thumb and palm subdomains of the core USP domain. It is lined with residues present on the helices α5, α6 and the β-strands 3, 5 & 7. This region is predominantly hydrophobic (Figure 3.4a) and comprises the tail-distal part of the S1-binding site, which is involved in binding the globular Ub-domain (Figure 3.4b).

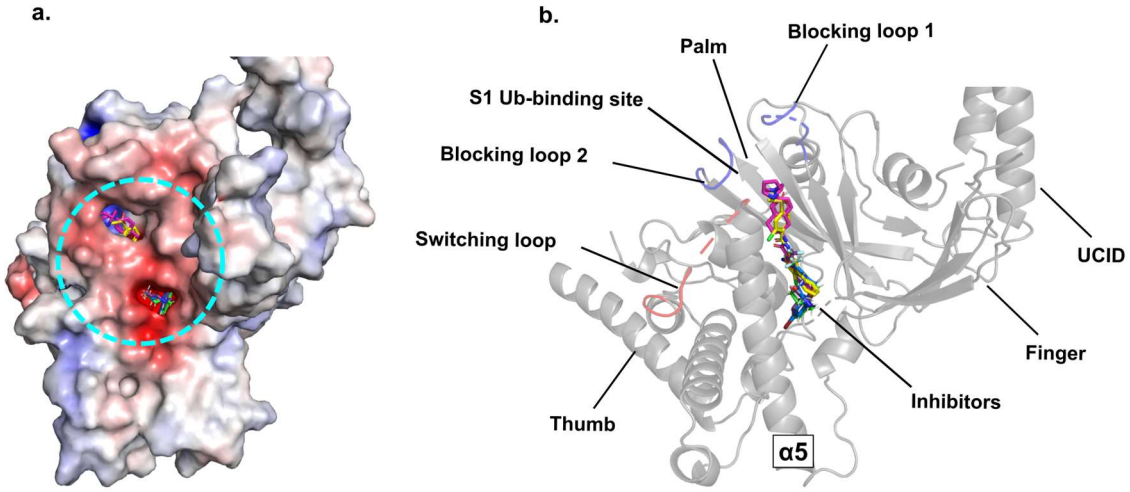

Figure 3.4: Overview of inhibitor binding in USP28. (a) Electrostatic surface representation of the inhibitor binding pocket (positively charged patches in blue, negatively charged patches in red). Bound-inhibitors highlighted within the dotted circle (in cyan) **(b)** A superposition of the inhibitor-bound structures of the USP28cat (Δtip) protein, shown in cartoon representation. The inhibitors AZ1 (green), AZ2 (purple), AZ4 (blue), Vismodegib (yellow) and FT206 (magenta) are shown in stick representation. The blocking loops 1 and 2 (blue) and the switching loop (red) are also indicated.

3.1.2.1 Structure of USP28-AZ inhibitor complex

The AZ compounds (AZ1, AZ2 and AZ4) were acquired from AstraZeneca and used for soaking experiments. These compounds are benzylic aminoethanol derivatives, where the second ring comprises fluorine group substitutions at positions 2, 4, 5 in AZ4; a trifluoromethyl group (-CF3) at position 3 and a single fluorine group substitution at the *para*-position in AZ1 or a trifluoromethoxy group(-OCF3) at the *meta*-position in AZ2 (Figure 1.14).

The USP28cat (Δtip) complex structures with all three AZ compounds (Figure 3.5) were solved by molecular replacement using one chain of the USP28cat *apo* structure (PDB ID: 6H4I; Sauer et al., 2019) as the search model. This model was initially divided into the core USP domain and the isolated UCID region. In all the crystal structures, the compounds occupied identical pockets in both molecules of the asymmetric unit. However, the second molecule in the asymmetric unit was badly ordered with poorly defined electron density for the chains and showed a slightly higher B-factor when compared to the first molecule.

The highest resolution dataset among the three compounds was obtained for AZ2 at a resolution of 2.66 Å, while AZ1 and AZ4 diffracted to 2.75 Å and 3.15 Å, respectively (for Data collection and refinement statistics, please see Table 3.1). For the USP28-AZ4 complex, refinement of the structure was not completed due to poor data quality. Nonetheless, molecular replacement clearly showed that the inhibitor was bound to the same pocket as observed for AZ1 and AZ2 (see Figure 7.6).

The aromatic rings of the compounds are oriented approximately perpendicular to each other and appear entirely buried in the pocket between the palm and thumb subdomains of USP28 (Figure 3.5). The aminoethanol chain extends towards the protein surface and forms an H-bond with Asp265 (Figure 3.6a). The bromobenzene moiety of the AZ compounds appears to be the major contributor to protein binding, involving hydrophobic residues of the USP28 pocket, namely: Leu180, Phe186, Leu264, Met288 & Phe292. The latter interacts with the bromobenzene moiety *via* a parallel displaced π-stacking interaction.

Although the trifluoromethyl/methoxy group in AZ1 and AZ2 is directed towards residues Glu366 and His261 (Figure 3.5a, b), it is not involved in any direct interactions. Interestingly, His261, which was considered to be protonated (pK_a=7.45), forms a salt bridge with Glu366 (Figure 3.6a). This interaction might presumably lock/close the binding pocket and prevent the inhibitors from dissociating, thus contributing to longer residence time. In the USP28-AZ2 structure, the electron density of the -OCF3 group of AZ2 is fused with the side-chain density of Glu366 (Figure 7.6b). AZ1 and AZ2 showed relatively stronger binding affinities of 0.2 μM and 0.9 μM, respectively (reported K_d values, based on ITC experiments), compared to the single fluorine substituted AZ4 (2.7 μM). The non-substituted compound in the series, AZ3, showed very weak binding (>100 μM, based on MST experiments) (Wrigley et al., 2017). Therefore, the fluorine-group substitutions might act as H-bond acceptors, leading to stable interactions with USP28 compared to the non-substituted AZ3.

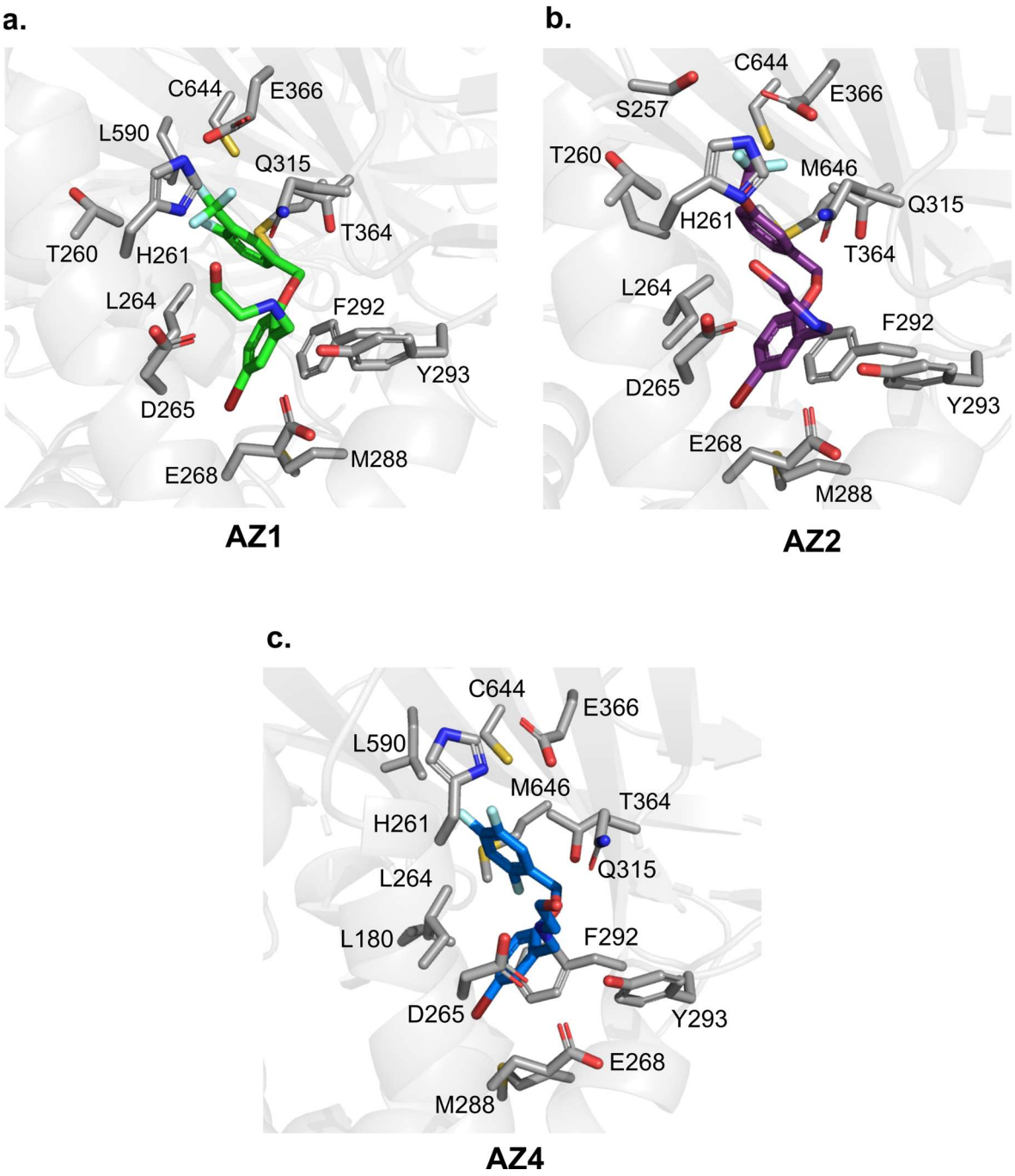

Figure 3.5: The USP28-AZ inhibitor complex. Crystal structures USP28cat (Δtip) in complex with AZ1 (in green, **a**), AZ2 (in purple, **b**) and AZ4 (in blue, **c**). The inhibitors are shown as stick models. The USP28 protein is shown in cartoon representation (background). The side-chains of the residues within 4 Å distance of the inhibitors are represented as sticks (gray). The fluorine group substitutions present on the second ring (in AZ1 and AZ2) extend towards the surface and lie in close proximity to residues H261 and Glu366. The bromobenzene moiety of the compounds forms a π-stacking interaction with the aromatic side-chain of Phe292.

The formation of the inhibitor-binding pocket requires a shift in helix α5 (Figure 3.6b) to provide sufficient space for the intercalation of the bromobenzene moiety of the AZ compounds between amino acids Leu264 and Phe292, resulting in an increased distance between these residues. This displaced orientation of helix α5 is reminiscent of the accommodation of the auto-inhibitory tip (UCID-tip) in USP25, where the C-terminal part of the tip from one molecule of a dimer extends into the USP domain of another dimer molecule and binds into a cleft formed between helix α5 and the palm region (Figure 3.7a).

In the USP25 structure (PDB ID: 6H4J, Sauer et al., 2019), the UCID-tip is stabilized by H-bond interactions between Phe522 and the residues of the palm, thumb and finger subdomains. Residues Pro521, Phe522 and Thr523 bind into a hydrophobic pocket (Figure 3.7b), similar to the one occupied by the second ring group of AZ1 containing the trifluoromethyl substitution, as seen from the USP28-complex structure (Figure 3.7c). The interaction of Pro521 and Phe522 of the USP25-UCID tip with the USP core domain can be described as a wedge that pushes helix α5 away from the catalytic domain (see Figure 1.9b). Lys520 of the USP25-UCID tip forms H-bond interaction with residues Asp272 and Tyr300 and a salt bridge with Glu275. The corresponding residues in USP28 (Asp265, Tyr293, and Glu268, respectively) are not only involved in inhibitor binding but also stabilize Ub binding by coordinating with the ε-amino group Ub-K48.

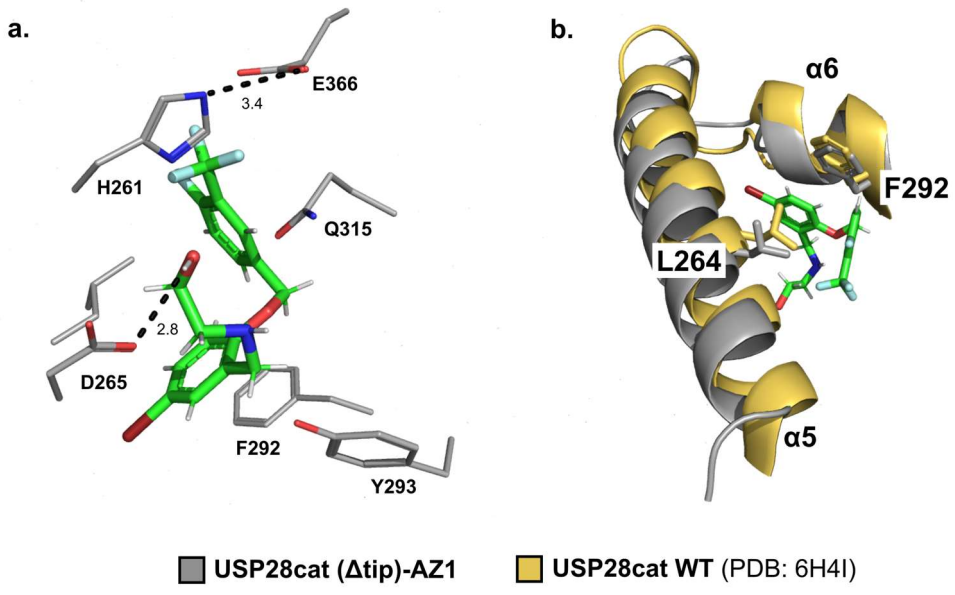

Figure 3.6: AZ1 binding (a) Close-up view of AZ1 (sticks, green) interacting residues in USP28cat (Δtip) (lines, gray). H-bonds are depicted as dotted lines. Distances are given in Å **(b)** Superposition of the AZ1-bound structure (gray) with the catalytic WT USP28 *apo* structure (yellow), showing a shift in helix α5 leading to an increased distance between residues L264 and F292.

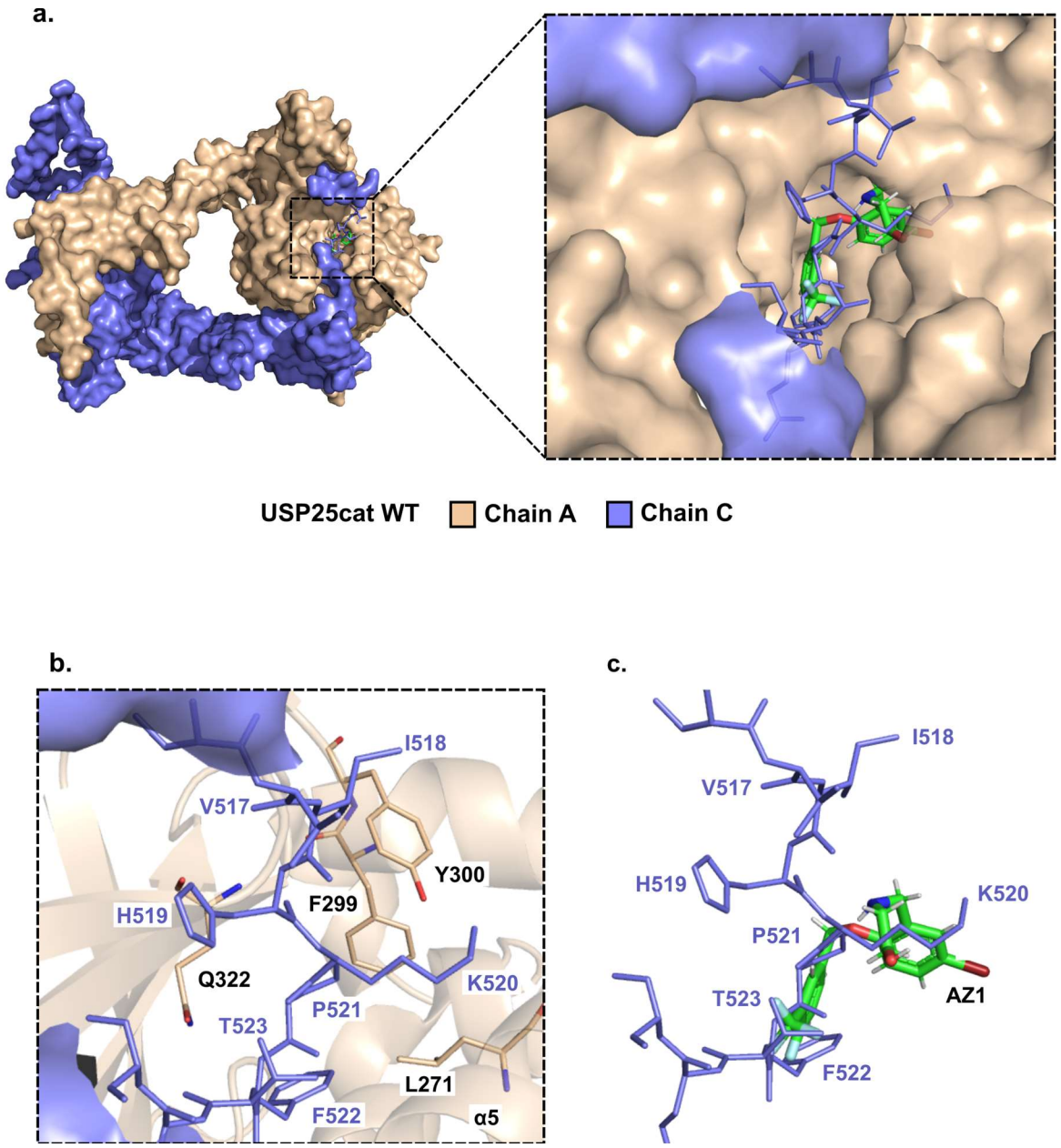

Figure 3.7: AZ1 binding site overlaps the UCID-tip binding in USP25 (a) Superposition of the USP28-AZ1 complex and the auto-inhibited, tetrameric USP25cat structure (PDB ID: 6H4J; Sauer et al., 2019). The inhibitor binds into a pocket similar to where the UCID-tip of chain A binds (lines, purple) into the USP-core domain of chain C (wheat) in USP25. Only two chains of the USP25 tetramer are shown here for clarity (in surface representation). A close-up view of the UCID-tip binding site shows the overlapping AZ1-binding region from the USP28 complex structure (sticks, green). **(b)** Residues of the UCID-tip of chain C interacting with the USP-core domain residues of chain A in USP25. The side-chains of the interacting residues are represented as sticks and labelled in purple and black for chain C and chain A, respectively. **(c)** The residues of UCID-tip of chain C (lines, purple) overlapping with AZ1 (sticks, green) binding.

Previously, USP28 was assayed across a range of tetra-Ub substrates in the presence of increasing AZ1 concentrations. Lineweaver-Burk analysis was performed to characterize the mode of inhibition in the presence of AZ1. The apparent K_m for tetra-Ub and K_i for AZ1 were in agreement with the observed IC_{50} values, suggesting AZ1 to be a non-competitive inhibitor of USP28 (Wrigley et al., 2017). This result is substantiated by the modeling of ubiquitin from the Ub-PA bound USP28cat (ΔUCID) structure (PDB ID: 6HEI; Gersch et al., 2019) to the USP28cat (Δtip)-AZ1 bound structure which shows that the compound does not directly compete with Ub at the S1 site. This analysis suggests that the mode of inhibition is possibly purely allosteric, induced by the shift in helix α5 and the resulting conformational changes in the switching loop (SL) and blocking loop 2 (BL2) distort the Ub-binding site in the protein. AZ1 lies ~15 Å away from the catalytic cysteine, C171. Although the SL and BL2 are not fully resolved in the USP28cat (Δtip)-AZ1 structure, a comparison with the Ub-bound structure shows an apparent shift in the position of the loop accompanied by the movement of helix α5.

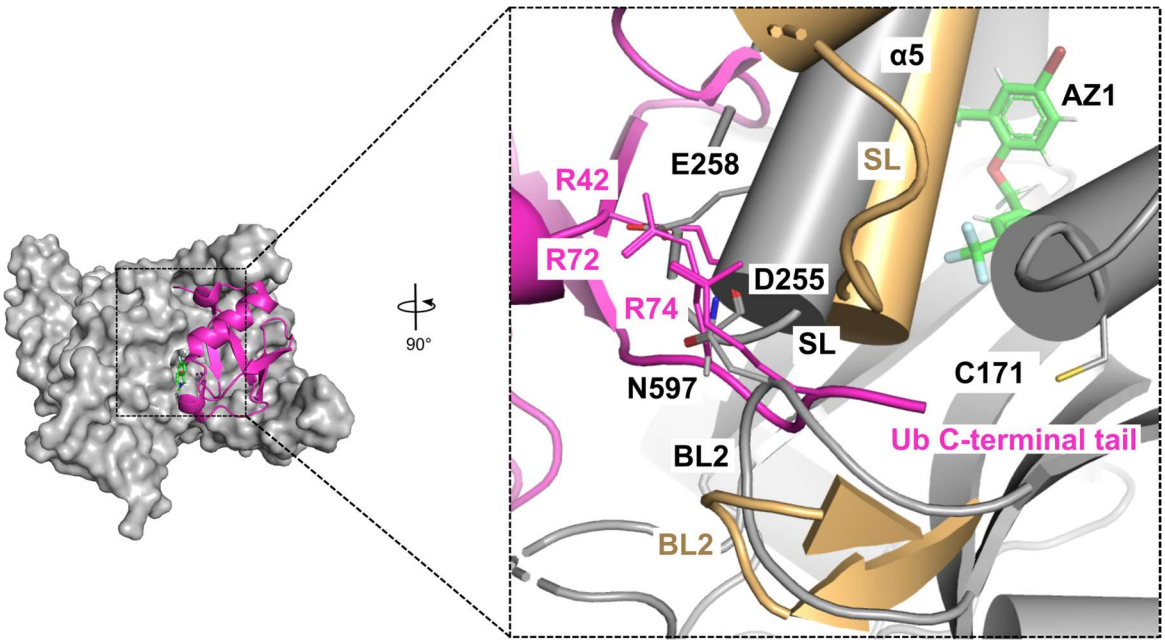

Figure 3.8: Modelling of Ub to the S1 site of USP28cat (Δtip)-AZ1 bound structure. Superposition of the USP28cat (ΔUCID)-Ub-PA bound structure (Ub in cartoon representation, colored in magenta) reported by Gersch et al., with the USP28cat (Δtip)-AZ1 bound structure (surface representation, gray). The close-up view shows the positioning of the Ub C-terminal tail and the binding region of AZ1. Although not fully refined in the AZ1 structure (gray, cylinder), there is an apparent shift in the positioning of the SL and BL2 compared to the Ub-bound structure of USP28 (light orange, cylinder). The Ub C-terminal tail residues and the interfering residues in USP28 are shown as lines. AZ1 (green) is shown as a stick model. The switching loop (SL), blocking loop 2 (BL2), and the catalytic cysteine residue are also indicated.

A mutation of the USP28cat (Δtip) protein, Pro280His, was identified during structure refinement. The USP28cat (Δtip)-AZ inhibitor bound structures contain this mutation. This residue is located at the C-terminal end of helix α5 and is not involved in any interactions with the inhibitor binding pocket. Nevertheless, to clarify if this change influenced the activity or overall fold of the protein, the mutation was reversed to obtain the wild type protein. An activity assay with the synthetic mono Ub-substrate (Ub-Rho110) showed that the variant and the wild-type protein exhibited the same activity (Figure 3.9). The subsequent USP28-inhibitor bound structures with Vismodegib and FT206 were obtained with the WT protein (for both Δtip and ΔUCID forms).

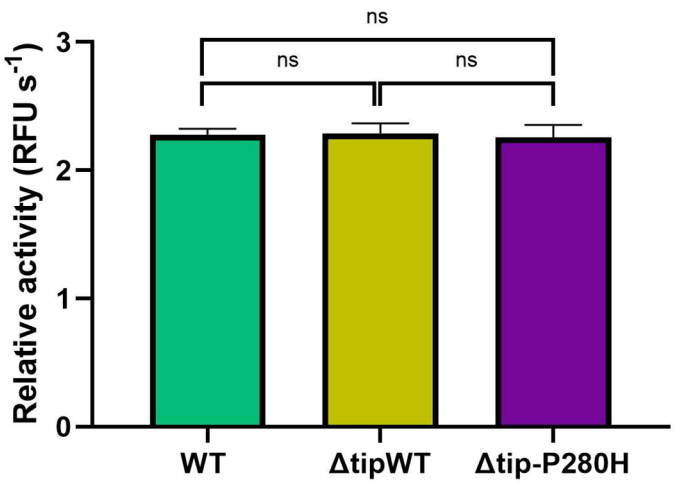

Figure 3.9: Relative activities of USP28cat WT and Δtip variants. The catalytic activities of USP28cat WT (full-length), Δtip-WT and the Δtip-P280H variant as determined by the Ub-rhodamine assay show that the mutation detected during structural refinement does not impact the protein's ability to cleave Ub. The initial slope of the fluorescence curves representing the initial activity is depicted in bar graphs. Error bars represent the standard deviation of triplicate measurements from two independent experiments.

Table 3.1: Data collection and refinement statistics for USP28-AZ inhibitor structures. Statistics for the highest resolution shell are shown in parentheses.

	USP28cat (Δtip) P280H-AZ1	USP28cat (Δtip) P280H-AZ2	USP28cat (Δtip) P280H-AZ4
Data collection			
Beamline	BESSY BL 14.1	BESSY BL 14.1	BESSY BL 14.1
Wavelength (Å)			
Resolution range (Å)	48.35-2.75 (2.92-2.75)	48.35-2.66 (2.84-2.66)	46.34-3.19 (3.48-3.19)
Space group	$P2_122_1$	$P2_122_1$	$P2_122_1$
Unit cell dimensions:			
a, b, c (Å)	100.44 105.54 178.70	100.45 104.98 178.68	98.67 104.97 179.02
α, β, γ (°)	90 90 90	90 90 90	90 90 90
Observed reflections	459,151 (23,917)	448,117 (21,155)	163,104 (12,757)
Unique reflections	34,461 (1723)	33,723 (1688)	7497 (638)
R_{merge}	0.24 (2.86)	0.23 (2.69)	0.44 (1.64)
R_{meas}	0.26 (3.0)	0.24 (2.81)	0.46 (1.71)
CC1/2	0.998 (0.393)	0.998 (0.413)	0.992 (0.641)
Mean $I/\sigma I$	10.9 (1.0)	11.4 (1.1)	6.1 (1.8)
Completeness (%):			
Spherical	69.1 (15.2)	61.6 (12.6)	52.7 (8.6)
Ellipsoidal	94.3 (69.9)	94.2 (71.7)	89.9 (57.0)
Wilson B-factor (Å^2)	74.28	78.97	78.32
Refinement			
Protein molecules/ASU	2	2	2
Reflections	34423	33723	16614
R_{work}/R_{free} (%)	22.9/24.5	23.0/25.0	20.0/26.1
No. of atoms:			
Protein	7228	7230	7079
Water	41	28	0
Ligand/ion	72	82	76
Average B-factors (Å^2):			
Protein	88.97	86.26	106.49
Ligand/ion	78.18	72.22	117.54
Water	49.42	45.11	-
RMSD:			
Bond lengths (Å)	0.008	0.008	0.009
Bond angles (°)	0.94	0.90	0.99
Ramachandran statistics:			
Favored/allowed/outliers (%)	93.8/5.9/0.3	94.8/4.7/0.5	88.2/10.7/1.1

3.1.2.2 Structure of USP28-Vismodegib complex

The initial crystal structure of the USP28-Vismodegib complex was solved with the (Δtip) variant of the protein at a resolution of 3 Å, using the USP28cat (Δtip)-AZ1 structure (without the inhibitor) as the search model for molecular replacement. Although this data set provided initial insights into the Vismodegib site, the corresponding electron density was insufficient to determine the correct orientation of the compound within the binding pocket. Subsequent crystallization trials with the monomeric ΔUCID variant led to better diffracting crystals and higher resolution data sets (for Data collection and refinement statistics, please see Table 3.2).

Simultaneously, a high-resolution structure (2.45 Å) of the *apo*-form of USP28cat (149-ΔUCID-698) was also obtained (Section 7.4.7). A superposition of this monomeric ΔUCID structure with the previously solved dimeric, full-length catalytic domain structure (PDB ID: 6H4I; Sauer et al., 2019) showed a root-mean-square deviation (RMSD) of 0.6 Å, indicating that the two structures are highly similar to each other.

In the structure with USP28cat (149-ΔUCID-698), Vismodegib appears to be present with 75% occupancy and binds into the same pocket as the AZ compounds. However, the binding site is shifted compared to the one found for the AZ compounds. Vismodegib sits comparatively lower than the AZ compounds in the pocket which is lined by the residues Ser257, Thr260, His261, Phe292, Tyr293, Gln315 and Glu366 (Figure 3.10a). Although there is remarkable overlap between the previously published experimentally determined and modeled binding regions for Vismodegib (Figure 1.15), the binding site in the crystal structure is directed more towards the Ub-tail interacting region at the S1-site. The chlorobenzyl ring of Vismodegib is deeply buried into the pocket while the methyl-sulfone group is directed towards the switching loop at the N-terminal end of helix α5. The amide linker that connects the chlorophenyl-methylsulfone moiety forms an H-bond interaction with the side chain of Glu366, present on β6.

A superposition of the Vismodegib-USP28 (149-ΔUCID-698) complex with the *apo* USP28 (149-ΔUCID-698) structure (Figure 3.10b) reveals significant changes that occur upon inhibitor binding. As seen with the AZ compounds, helix α5 is shifted outwards by about 6° resulting in side chains of residues Ser 257, His 261 and Leu 264 moving accordingly, thereby 'opening' the cleft. The side chain of Gln315 flips outward by a distance of 5.6 Å to accommodate the compound. This movement was also suggested by the docking analysis and the accompanying experimental studies performed by Wang et al. A significantly lower IC_{50}

value of the Gln315Ala variant compared to the WT was obtained and attributed to the movement of the Glu315 side chain by a distance of 3.2 Å (Section 1.4.1.2).

Figure 3.11 depicts the superposition of the Vismodegib-bound structure with the Ub-bound structure of USP28cat (ΔUCID) (PDB ID: 6HEI; Gersch et al., 2019). The methyl-sulfone group of Vismodegib is positioned towards the blocking loops and the switching loop in the protein that undergo conformational changes upon Ub-binding. As observed with AZ1, the compound is located at a distance of ~13 Å from the catalytic cysteine residue (Cys 171). Therefore, one could assume that Vismodegib may also inhibit Ub-binding allosterically by altering the binding site upon changes in helix α5 and restricting the movement of the switching and blocking loops.

The binding of Vismodegib leads to conformational changes in USP28 that would block the Ub-substrate from interacting with the S1 site of the protein. In the Vismodegib-bound structure, the side chains of the aromatic residues Phe370, present on BL1 and Tyr643 are flipped out (also seen in AZ1), to presumably accommodate the methyl-sulfone group of the compound. In the Ub-bound structure, the Ub-tail, which is anchored by Leu73 in Ub is bound into a pocket formed by the 90° flip of these residues. Although the SL is not well resolved in the Vismodegib-bound structure, it could be assumed that, as seen with the USP28cat (Δtip)-AZ1 structure, Asp255 present on helix α5 would occlude the side chain of Arg72 of Ub and subsequently prevent the salt-bridge formation with Glu258.

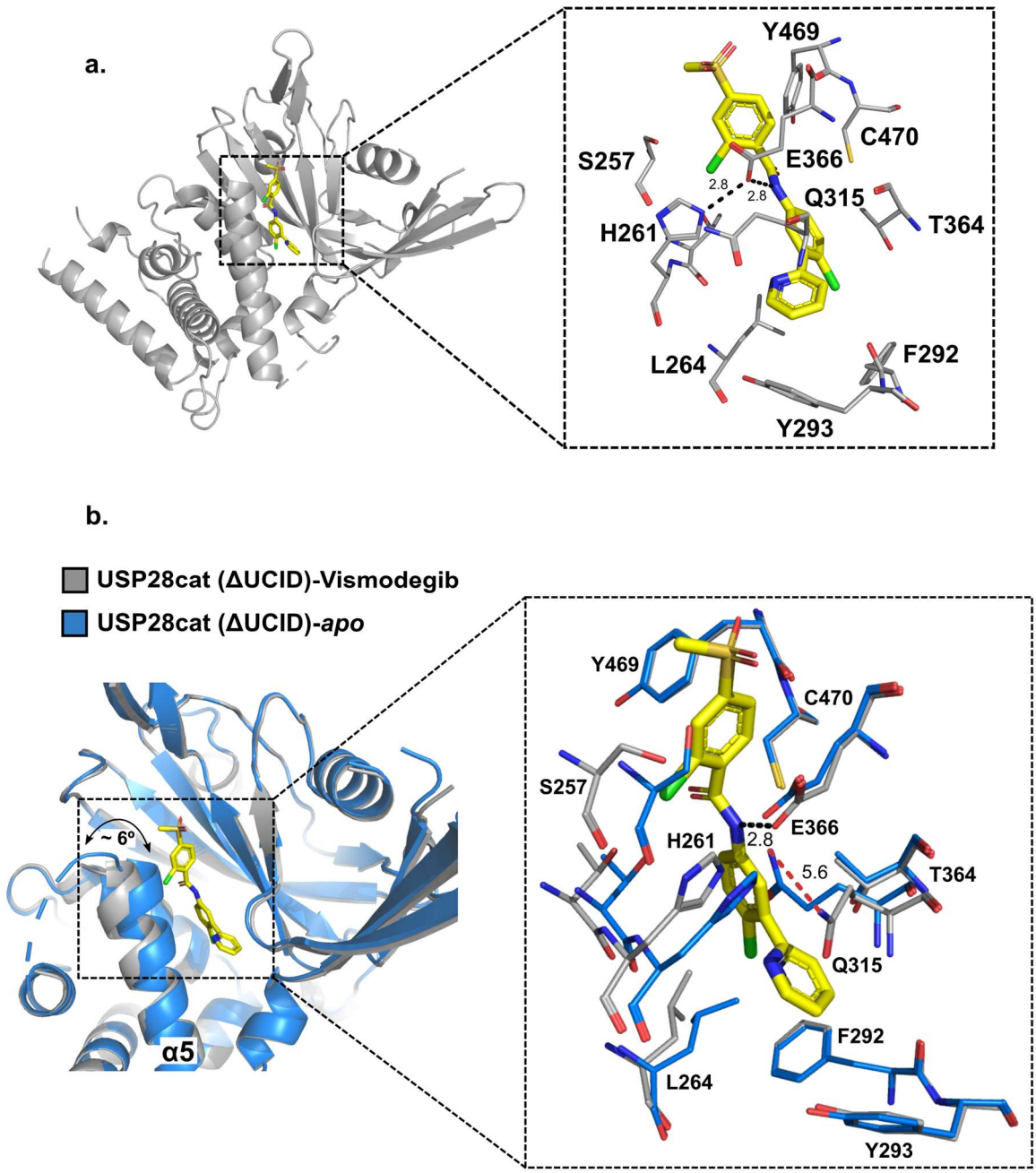

Figure 3.10: The USP28-Vismodegib complex. (a) Crystal structure of USP28cat (149-ΔUCID-698) (gray, cartoon) bound to Vismodegib (yellow, sticks). The close-up view shows the key interacting residues of USP28, represented as thin lines **(b)** Superposition of the USP28cat (149-ΔUCID-698) *apo* (cartoon, blue) and Vismodegib bound (cartoon, gray) structures. Upon Vismodegib binding, helix α5 shifts outward by ~6° to accommodate the molecule. A close-up view compares changes in the position of the residues surrounding the molecule in the *apo* (blue, lines) and Vismodegib-bound (gray, lines) structures. The side-chain of the Gln315 residue flips out to increase the area for Vismodegib binding (depicted as maroon dotted lines). H-bonds are depicted as black dotted lines. Distances are given in Å.

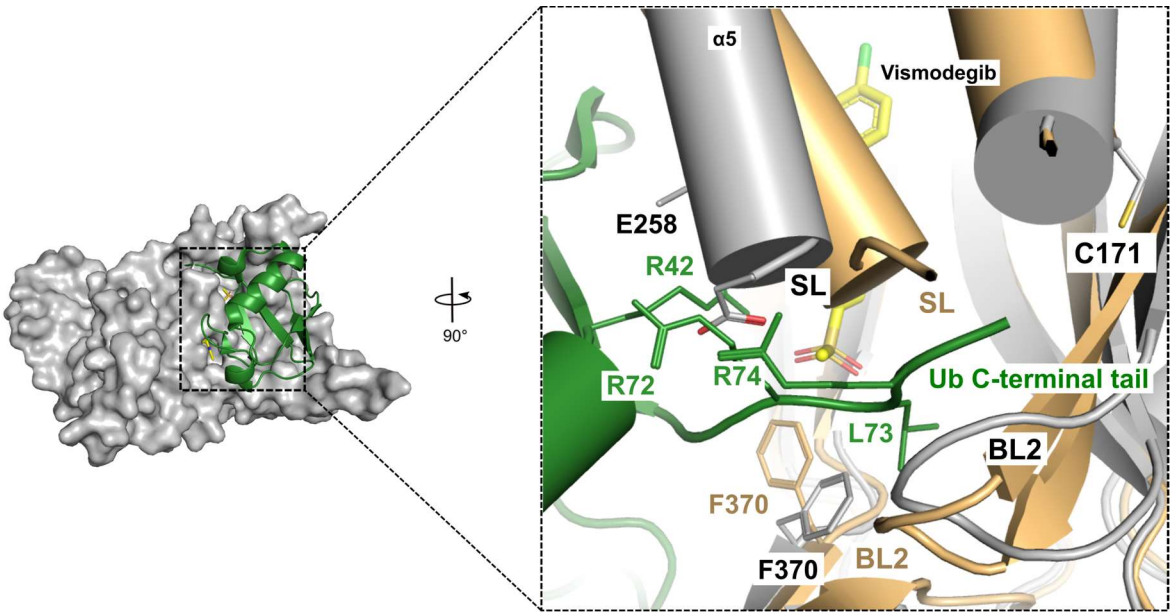

Figure 3.11: Modelling of Ub to the S1 site of USP28cat (ΔUCID)-Vismodegib bound structure. Superposition of the USP28cat (149-ΔUCID-703)-Ub-PA bound structure (Ub in cartoon representation, colored in green) reported by Gersch et al., with the USP28cat (149-ΔUCID-698)-Vismodegib bound structure (surface representation, gray). The close-up view shows the positioning of the Ub C-terminal tail and the binding region of Vismodegib. Although not fully refined in the Vismodeib structure (gray, cylinder), there is an apparent shift in the positioning of the SL and BL2 compared to the Ub-bound structure of USP28 (light orange, cylinder). The Ub C-terminal tail residues and the interfering residues in USP28 are shown as lines. Vismodegib (yellow) is shown as a stick model. The switching loop (SL), blocking loop 2 (BL2), and the catalytic cysteine residue are also indicated.

Table 3.2: Data collection and refinement statistics for USP28-Vismodegib structures. Statistics for the highest resolution shell are shown in parentheses.

	USP28cat (Δtip)-Vismodegib	USP28cat (ΔUCID)-Vismodegib
Data collection		
Beamline	ESRF ID30A-3	ESRF ID 23-2
Wavelength (Å)	0.967	0.873
Resolution range (Å)	46.63-2.86 (3.06-2.86)	47.97 2.57 (2.68-2.57)
Space group	$P2_122_1$	$H3_2$
Unit cell dimensions:		
a, b, c (Å)	100.53 105.33 180.43	106.63 106.63 329.85
α, β, γ (°)	90 90 90	90 90 120
Observed reflections	291,390 (13.532)	448,422 (56,011)
Unique reflections	24,459 (1125)	23,472 (2825)
R_{merge}	0.20 (1.98)	0.17 (4.12)
R_{meas}	0.21 (2.08)	0.17 (4.23)
CC1/2	0.998 (0.430)	0.999 (0.402)
Mean $I/\sigma I$	11.0 (1.0)	13.5 (0.9)
Completeness (%):		
Spherical	69.1 (15.2)	100.0 (100.0)
Ellipsoidal	94.3 (69.9)	100.0 (100.0)
Wilson B-factor (Å^2)	96.27	85.06
Refinement		
Protein molecules/ASU	2	1
Reflections	31,332	23,471
R_{work}/R_{free} (%)	21.9/24.6	20.0/23.1
No. of atoms:		
Protein	7017	2685
Water	3	89
Ligand/ion	69	27/4
Average B-factors (Å^2):		
Protein	126.04	91.32
Ligand/ion	133.24	71.32/105.01
Water	93.07	73.36
RMSD:		
Bond lengths (Å)	0.009	0.008
Bond angles (°)	0.93	0.92
Ramachandran statistics:		
Favored/allowed/outliers (%)	94.2/5.0/0.8	95.6/4.1/0.3

3.1.2.3 Structure of USP28-FT206 complex

The compound FT206 was synthesized by Dr. Victor Hernandez Olmos (Frauenhofer ITMP) as a racemic mixture of the (R) and (S) enantiomers. However, the name FT206 refers explicitly to the S-form in the reported study by Ruiz et al. (Section 1.4.1.3). The initial complex structures were solved with the Δtip form using the USP28cat (Δtip)-AZ1 structure as the search model for molecular replacement. The compound occupies the same binding pocket as observed for AZ1 and Vismodegib and partially coincides with the proposed binding site for Compound-19, based on the reported docking studies (Z. Liu et al., 2020; Section 1.4.1.4). Based on the electron density observed for the compound from the crystallographic dataset, the geometric restraints for the S-enantiomer were assigned for subsequent refinements. However, the electron density for the terminal bicyclic ring was not well-defined and could not be improved upon multiple rounds of refinement.

FT206-soaked USP28cat (149-ΔUCID-698) crystals diffracted to a higher resolution among all the data sets obtained thus far. (2.12 Å) (Figure 3.12a; for Data collection and refinement statistics, see Table 3.3). In this structure (Figure 3.12a), the thienopyridine ring of FT206 is buried into the hydrophobic binding pocket, coinciding with the chlorobenzene-ring portion of Vismodegib and the bromobenzene moiety of the AZ compounds. The terminal bicyclic ring extends towards the Ub-tail binding site of the protein. As observed with Vismodegib, the amide linker connecting the theinopyridine ring and the terminal bicyclic ring of FT206 also forms an H-bond interaction with the side chain of Glu366. Although the electron densities were well-defined for the thienopyridine ring and the central double-ring system, the bicyclic ring displayed poor/weak electron density (Figure 7.6). The compound showed only a partial occupancy of ~60-70%, but this was a considerable improvement compared to the Δtip-bound structures.

A comparison of the FT206-bound structure with the *apo* structure of the ΔUCID protein (Figure 3.12b) led to the following observations – the residues present on helix α5, Asp255, Val256, Ser257, His261 and Leu264 move outward to accommodate the compound. Similar to the Vismodegib-bound complex, the side chain of Gln315 flips out by ~5 Å because it would otherwise clash with the thienopyridine ring of the compound. The side chain of Glu366 is positioned towards the N-atom of the amide linker to form a direct interaction with the compound. It also forms an H-bond interaction with the side chain of His261.

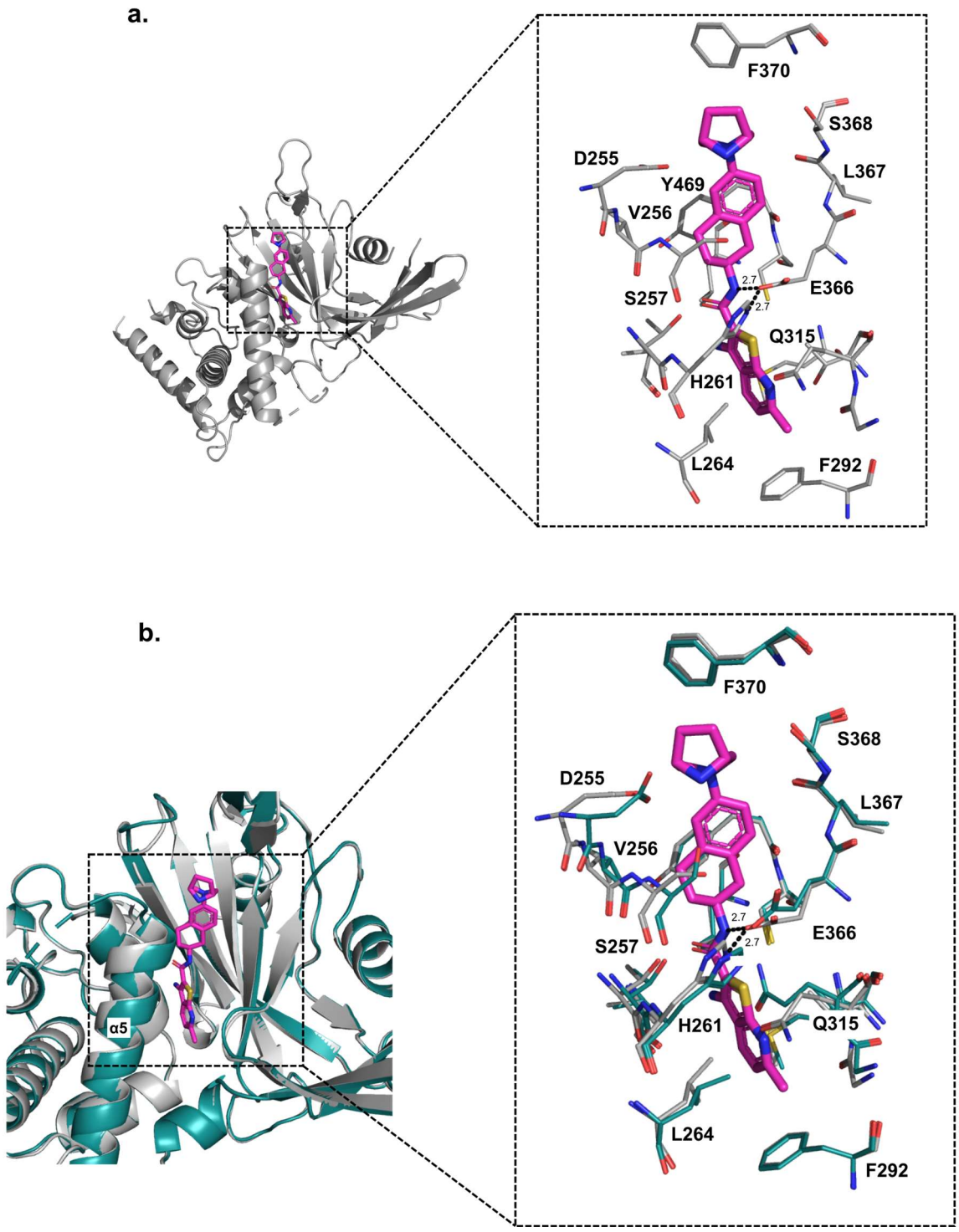

Figure 3.12: The USP28-FT206 complex. (a) Crystal structure of USP28cat (ΔUCID) bound to FT206 (magenta, sticks). The key interacting residues of USP28 are shown as thin lines (inset). **(b)** Superposition of the USP28cat (ΔUCID) *apo* (cartoon, deep teal) and FT206 (cartoon, gray) bound structures. Upon FT206 biding, helix α5 shifts outward, with residues Asp25, Val 256, Ser257, H261 and Leu264 opening the pocket to accommodate the compound. The side chain of Gln315 flips out by about 5 Å to accommodate the thienopyridine ring, while Glu366 moves towards the central ring to form a direct interaction with the NH atom of the amide linker. Glu366 also interacts with His261. A close-up view comparing changes in the position of residues surrounding the molecule in the *apo* (deep teal, lines) and FT206-bound (gray lines) structures (inset) is shown. H-bonds are depicted as dotted lines. Distances are given in Å.

As seen with AZ1 and Vismodegib, the salt bridge formed between His261 and Glu366 can create a lid, potentially locking the inhibitor binding pocket and preventing the compound from dissociation.

The superposition of the FT206-bound structure with the Ub-bound structure of USP28cat (ΔUCID) (PDB ID: 6HEI; Gersch et al., 2019) (Figure 3.13) shows that in contrast to AZ1 and Vismodegib, the terminal bicyclic ring of FT206 extends more towards the Ub-tail binding channel. The inhibitor is located ~14 Å away from the catalytic cysteine, C171. FT206 is in close proximity to residues Asp255, Phe 370 and Tyr643 involved in stabilizing the Ub C-terminal tail region. Interestingly, BL2 comes into close proximity to the bicyclic ring of FT206, virtually blocking the passage of the Ub C-terminal tail. The SL in the USP28-FT206 structure is positioned close to Arg72 of Ub, which is obstructed by Ser257 and Glu258, and is also seen with AZ1 and Vismodegib structures. Although the SL is not well resolved in this complex structure, the position of Asp255 (helix α5) indicates that it moves to open the binding pocket for FT206.

These observations suggest that while FT206 is not directly involved with residues from the Ub, the conformational changes upon its binding seem to potentially block the required positioning of the C-terminal tail region of Ub (lies closer than AZ1 and Vismodegib) and hence it is unable to reach the catalytic center. This has also been proven with the lower IC_{50} values of the compound with USP28 (Figure 3.18).

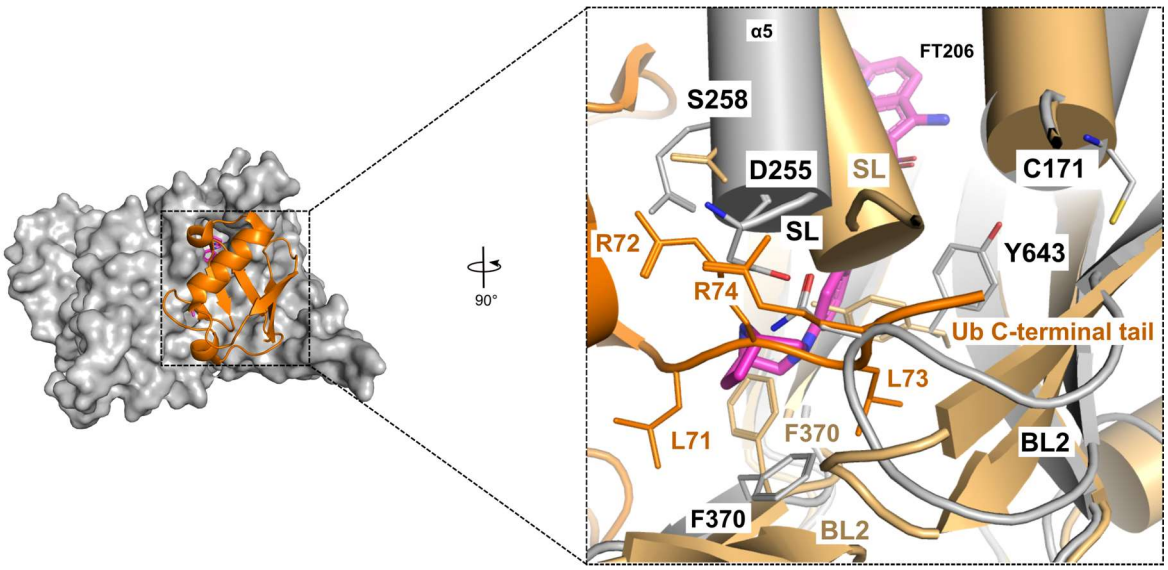

Figure 3.13: Modelling of Ub to the S1 site of USP28cat (ΔUCID)-FT206 bound structure. Superposition of the USP28cat (149-ΔUCID-703)-Ub-PA bound structure (Ub in cartoon representation, colored in orange) reported by Gersch et al., with the USP28cat (149-ΔUCID-698)-FT206 bound structure (surface representation, gray). The close-up view shows the positioning of the Ub C-terminal tail and the binding region of FT206. Although not fully refined in the FT206 structure (gray, cylinder), there is an apparent shift in the positioning of the SL and BL2 compared to the Ub-bound structure of USP28 (light orange, cylinder). The Ub C-terminal tail residues and the interfering residues in USP28 are shown as lines. FT206 (magenta) is shown as a stick model. The switching loop (SL), blocking loop 2 (BL2), and the catalytic cysteine residue are also indicated.

Table 3.3: Data collection and refinement statistics for USP28-FT206 structures. Statistics for the highest resolution shell are shown in parentheses.

	USP28cat (Δtip)-FT206	USP28cat (ΔUCID)-FT206
Data collection		
Beamline	ESRF ID 23-2	DESY PETRA III (P14)
Wavelength (Å)	0.873	0.976
Resolution range (Å)	46.07-2.79 (2.93-2.79)	47.76-2.12 (2.18-2.12)
Space group	$P2_122_1$	$H3_2$
Unit cell dimensions:		
a, b, c (Å)	100.08 104.43 179.37	106.37 106.37 325.69
α, β, γ (°)	90 90 90	90 90 120
Observed reflections	437,676 (22,565)	809,334 (40,729)
Unique reflections	34,236 (1713)	51,898 (3297)
R_{merge}	0.14 (0.24)	0.06 (4.82)
R_{meas}	0.15 (0.25)	0.06 (4.98)
CC1/2	0.93 (0.43)	1.0 (0.37)
Mean $I/\sigma I$	10.9 (1.0)	21.9 (0.7)
Completeness (%):		
Spherical	70.0 (10.39)	100.0 (99.9)
Ellipsoidal	94.3 (70.1)	100.0 (100.0)
Wilson B-factor ($Å^2$)	86.88	
Refinement		
Protein molecules/ASU	2	1
Reflections	33426	40638
R_{work}/R_{free} (%)	22.1/23.5	21.2/21.6
No. of atoms:		
Protein	6774	2700
Water	14	68
Ligand/ion	126	60/3
Average B-factors ($Å^2$):		
Protein	109.26	90.26
Ligand/ion	101.17	72.61/60.84
Water	64.85	75.96
RMSD:		
Bond lengths (Å)	0.008	0.019
Bond angles (°)	0.94	1.84
Ramachandran statistics:		
Favored/allowed/outliers (%)	95.8/4.0/0.2	95.3/4.4/0.3

3.2 Biochemical characterization of inhibitor binding

To validate the binding mode of the inhibitor complex and analyze the importance of interacting residues, mutational analysis of these residues accompanied by several biochemical assays was pursued.

A sequence alignment of USP28 with USP25 was performed, and the residues in USP25 corresponding to the inhibitor-binding pocket in USP28 were chosen for subsequent mutational analysis.

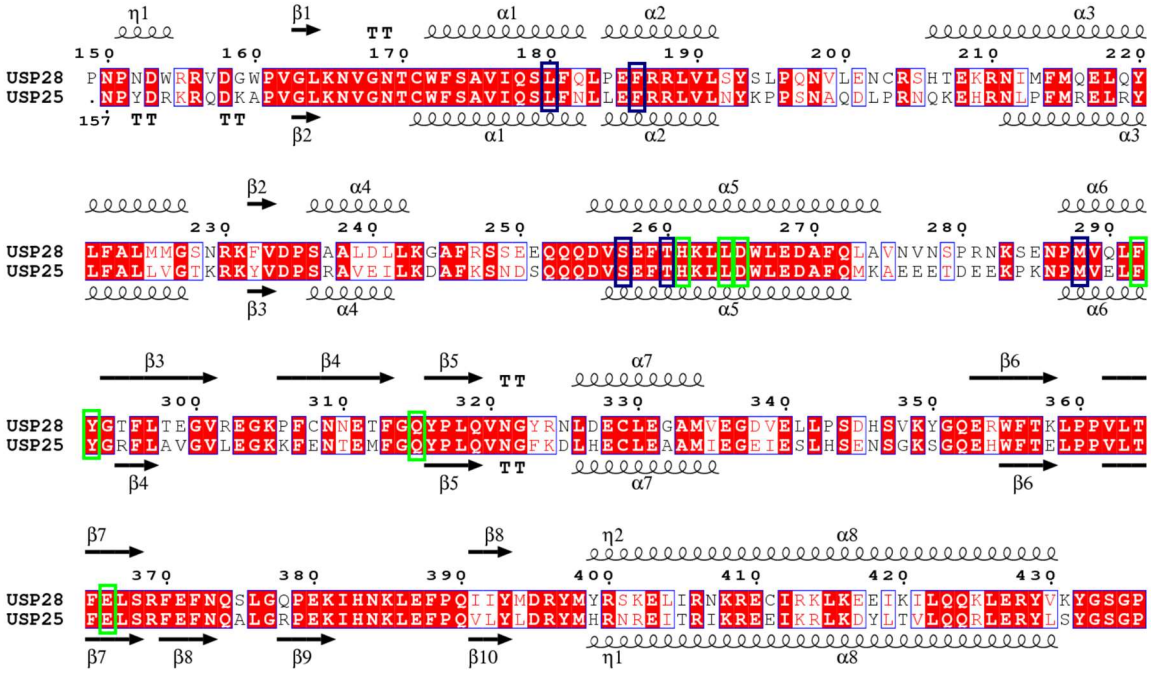

Figure 3.14: Sequence alignment of the catalytic domains of USP28 and USP25. Residues 149-436 (USP28) and 156-443 (USP25) are shown for clarity. Identical residues are highlighted in red, and secondary structural elements are shown above the sequence as squiggles for α-helices and arrows for β-strands. The green boxes represent the residues chosen for mutational studies. The dark blue boxes represent other residues lining the inhibitor binding pocket. Simple protein alignment and illustration were performed with the T-Coffee and ESPritpt 3.0 alignment program, respectively.

Since the initial structures were obtained with the USP28cat (Δtip) protein, all mutational studies were performed with this variant. Moreover, the dimeric USP28cat (Δtip) protein was previously shown to have similar activity to the WT, while the monomeric ΔUCID protein showed lower catalytic activity (~3-fold reduction in K_m). The USP25cat (Δtip) led to a dimeric protein that was 6-fold more active than the tetrameric wild-type protein (Gersch et

al., 2019; Sauer et al., 2019). As seen with USP28, the monomeric ΔUCID variant of USP25 also displayed diminished catalytic activity compared to the tetrameric WT protein (> 5-fold reduction in K_m) (Gersch et al., 2019). Hence, the Δtip form was utilized for the subsequent mutational analyses to test the effects on inhibitor binding to USP25.

3.2.1 Mutational analysis of binding pocket residues

All residues mentioned in Table 3.4 were cloned using SDM (as described in Section 2.2.1.1. The variants were expressed in BL21(DE3)-star-pRARE2 cells and purified to homogeneity using IMAC followed by SEC. An exemplary purification profile for the USP28cat (Δtip) Q315A variant is shown in Figure 3.15 and for all other variants in the Appendix (Supplementary figures 7.4.2 and 7.4.5).

USP28cat (Δtip) variants	**USP25cat (Δtip) variants**
H261A	-
D265S	-
L264F	L271F
F292A	F299A
Y293A/Y293R/Y293H	Y300A/Y300R/Y300H
Q315A/Q315R	Q322A/Q322R
E366A	E373A

Table 3.4: Binding site variants in USP28cat (Δtip) and USP25cat (Δtip)

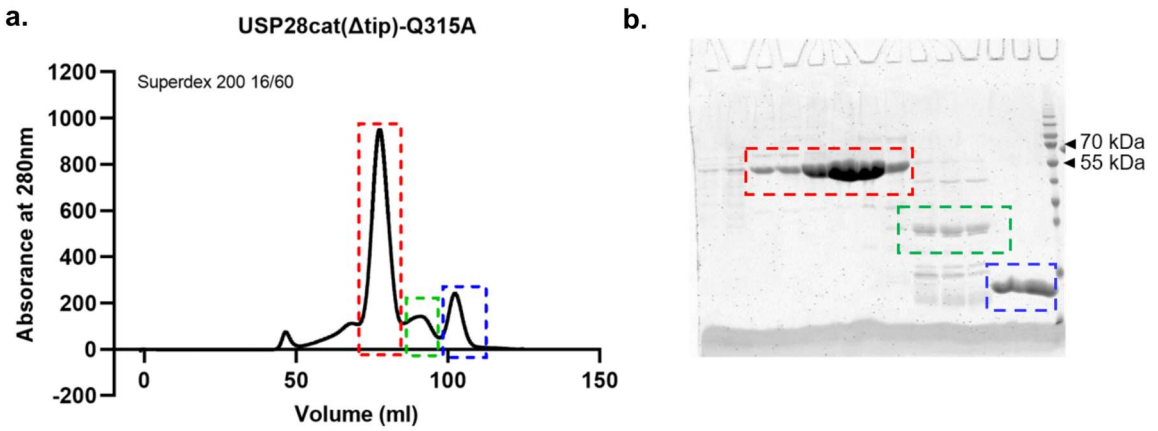

Figure 3.15: Purification of a USP28cat (Δtip) variant. (a) An exemplary elution profile from SEC with the **(b)** SDS-PAGE analysis of the peak fractions (inset) for the USP28cat (Δtip) Q315A variant. Fractions within the red box were pooled and concentrated for subsequent experiments. The blue box shows the peak corresponding to the thioredoxin tag.

The thermal stability of the variant proteins was compared to the wild type protein to ensure that the mutations did not affect the overall fold and stability of the catalytic domain. The thermal stability was assessed in a ThermoFluor experiment as described in Section 2.2.3.3. All variants showed a clear transition in fluorescence, as expected upon protein unfolding, indicating that they were well folded (Figure 3.16). Overall, the melting temperatures varied by 5 °C. A significant decrease in melting temperature, which indicates a marked destabilization of the fold compared to the WT protein, was observed for the F292A variant of USP28 (and the corresponding variant in USP25, F299A). All other variants differed only by a maximum of 2 °C compared to the WT protein. The results of this assay thus showed that the variant proteins, maybe with the exception of the F292A (USP28) and F299A (USP25), were well-folded, and any artefacts due to unstable folding in subsequent analyses were not likely.

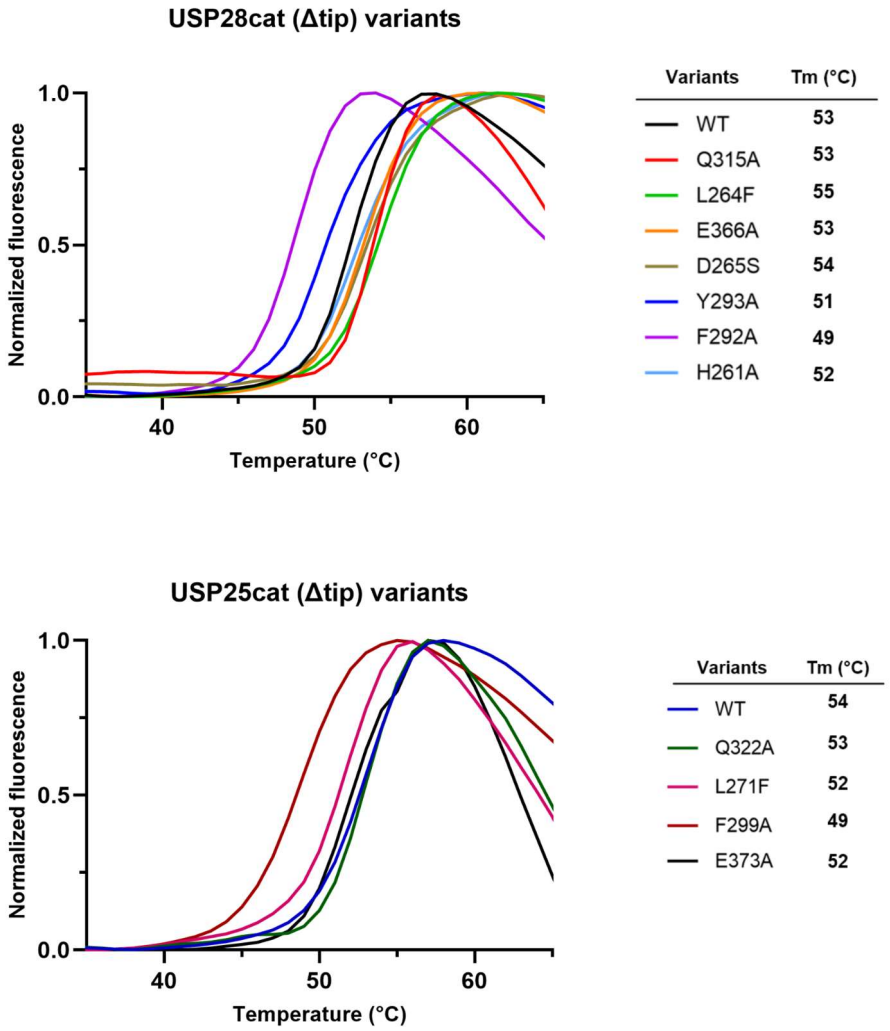

Figure 3.16: Thermal stability of USP28cat (Δtip) and USP25cat (Δtip) variants. Protein unfolding was monitored on a ThermoFluor instrument using the SYPRO Orange dye (2.5x final concentration) at a protein concentration of 2 μM. Normalization was achieved using the Boltzmann Equation, and the melting curves were plotted in GraphPad Prism v 9.0.2. The melting temperatures were calculated using the MxPro software. The Tm observed from the curves are indicated in the respective tables. Data are shown from one of the two independent experiments with n=3 technical replicates.

Next, the catalytic activity of the variant proteins was tested using the Ub-Rhodamine assay (Section 2.2.3.8), wherein the rise in fluorescence due to cleavage of the Ub-Rho110 substrate was measured over time. In this experiment, proteins at a fixed concentration (20 nM) were incubated with a saturating concentration of the substrate (250 nM) and then introduced to a plate reader. The fluorescence increase was monitored for 90 minutes, and the initial activity of the variants was determined by the slope of the initial linear phase of the fluorescence curves.

Figure 3.17 depicts the initial activities of all the variants that were tested compared to the wild type USP28cat (Δtip) and USP25cat (Δtip). The bar graphs for the USP28 variants- H261A, L264F, D265S and F292A indicate a significant decrease in the cleavage of the Ub-Rho110 substrate when compared to the WT protein. The correct positioning of helix α5 is necessary for the efficient catalysis of USP28. In the WT protein, a putative conformational relay mechanism links the positioning of helix α5 through the side-chain conformation of the hydrophobic core residue F259 to the catalytic C171 (Section 1.2.1.2). This mechanism has been noted for other USP enzymes, such as USP7 (Rougé et al., 2016). Mutation of residues H261, L264 and D265 which are present on helix α5, might interfere with its movement, leading to reduced activities. Similarly, the USP25 variants L217F, F299A and Q322A also showed very low catalytic activity compared to the WT protein. Interestingly, the E366A variant of USP28 showed similar activity as the WT, while in USP25, the E373A showed a ~2.3-fold increase in substrate cleavage activity compared to the WT protein.

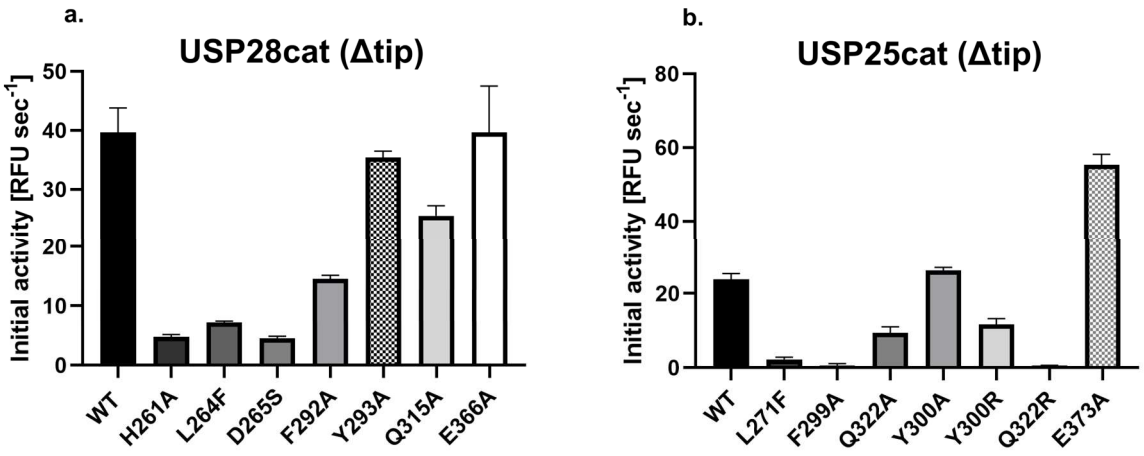

Figure 3.17: Initial activities of inhibitor-binding site variants. The catalytic activities of **(a)** USP28cat (Δtip) and **(b)** USP25cat (Δtip) WT and variants, as determined by the Ub-rhodamine assay. The initial slope of the fluorescence curves which represents the initial activity, is depicted in bar graphs. Error bars represent the standard deviation of triplicate measurements from three independent experiments.

3.2.2 Compound inhibition of the variants

3.2.2.1 Dose-response assays

To further confirm the binding mode of the inhibitors to USP28, enzymatic inhibition activities and binding affinities of the variants were determined. Dose-response assays to determine compound inhibition (IC_{50}) were performed with Ub-Rho110 as the substrate (as described in Section 2.2.3.8).

In the presence of AZ1: AZ1 inhibited USP28cat (Δtip) WT (Figure 3.18a) and USP25cat (Δtip) WT (Figure 3.19a) with IC_{50} values of 1.87 μM and 1.02 μM, respectively, which is in line with the previously published data (Wrigley et al., 2017). In agreement with the binding pose of AZ1, the USP28 variants H261A, Y293A and Q315A showed a slight decrease in the inhibitory potency of AZ1 to the protein. Variants L264F, F292A and E366A, showed significantly higher IC_{50} values, indicating that they abrogated inhibitor binding. A possible explanation is that the L264F exchange results in a π-stacking interaction with F292 that competes with the bromobenzene moiety of AZ1. L264 and F292 are also important for the formation of the binding pocket upon the shift of helix α5, and the mutations may affect the flexibility of its movement, thereby affecting efficient inhibitor binding. It must also be noted that while folded, these mutants showed reduced catalytic activity compared to the WT protein as the movement of helix α5 is essential for catalysis of the Ub-substrate as described previously (Figure 3.17a).

Despite not being involved in direct interaction with AZ1, the mutation of E366 to alanine causes a significant decrease in the inhibitory potency of the compound in USP28. The mutation might also affect the correct positioning of H261, which is presumed to form H-bond interactions with the $-CF_3$/$-OCF_3$ groups of AZ1 and AZ2, respectively, under physiological conditions. As seen from the USP28-AZ1 structure, the H261-E366 interaction locks the inhibitor binding pocket. One could thus also speculate that the WT protein displays a lower ligand dissociation rate (K_{off}) compared to the alanine variant.

In USP25 (Figure 3.19a), variants Y300A and Q322A displayed only a slight decrease in binding potency. However, similar to USP28 L264F, the L271F variant abrogates inhibition with an IC_{50} value of > 100 μM. This suggests that the binding mode of AZ1 might be identical or highly similar to that seen in USP28 with the bromobenzene moiety of AZ1 buried in the pocket. The F299A variant, although assumed to be folded, showed almost no catalytic activity and hence did not permit obtaining conclusive results within the dose-response assays. Interestingly, the E373A variant, unlike its counterpart in USP28 (E366A), did not entirely abrogate inhibitor binding but exhibited a lower IC_{50} value compared to the WT protein while still being significantly more active.

In the presence of Vismodegib: With Vismodegib (Figures 3.18b & 3.19b), the IC_{50} values for USP28cat (Δtip) WT and USP25cat (Δtip) WT were 4.30 μM and 2.83 μM, respectively, which are also close to the values determined by Wang et al. (Section 1.4.1.2).

In agreement with our structure and the biochemical studies by Wang et al., the USP28 Q315A variant exhibited a strong inhibitory activity with an IC_{50} value greater than the WT protein. The same result was also obtained for USP25 with the Q322A variant. From the USP28cat (149-ΔUCID-698)-Vismodegib complex structure, we know that the side chain of Gln315 flips outwards to favor compound binding. Mutating it to alanine might accommodate Vismodegib preferentially by reducing any steric hindrance due to the smaller side chain. However, this effect was disrupted when Gln315 (USP28)/Gln322 (USP25) was mutated to arginine, although the IC_{50} values were still lower than for the WT protein (Q315R (USP28): 1.68 μM; Q322R(USP25): 1.46 μM).

As observed with AZ1, Vismodegib also showed a significantly decreased binding in the presence of the USP28 E366A variant (IC_{50} >100 μM). Unlike AZ1, Vismodegib forms a direct H-bond interaction *via* the N-atom on the amide linker region with the side chain of Glu366. Mutation of this residue presumably disrupts the interaction, thereby abrogating compound binding and inhibition. Although the E373A variant in USP25 does not exhibit high resistance, it does show a decrease in compound binding and inhibitory potency.

In the presence of FT206: For FT206 (Figures 3.18c & 3.19c), the IC_{50} values for USP28cat (Δtip) WT and USP25cat (Δtip) WT were 0.2 μM and 1.12 μM, respectively, which is in agreement with the previously reported data (Section 1.4.1.3). The inhibitory potency of FT206 against the USP28 variants H261A, L264F, F292A and Q315A were similar to the WT protein, except for the Y693A variant, which showed a significant increase in the IC_{50} value (11.97 μM). The E366A variant again showed very high resistance to compound binding with an IC_{50} value > 100 μM.

Inhibition of the USP25 variants with FT206 showed that L271F, Y300A, and Q322A displayed IC_{50} values close to the WT protein, whereas the E373A variant abrogated compound binding, suggesting a high probability of a near-identical binding pocket for FT206 in both USP28 and USP25.

These results thus support the notion that although the inhibitor binding sites in both USP28 and USP25 appear to be roughly similar, they harbor certain differences, especially in the case of the Glu366 (USP28) and Glu373 (USP25).

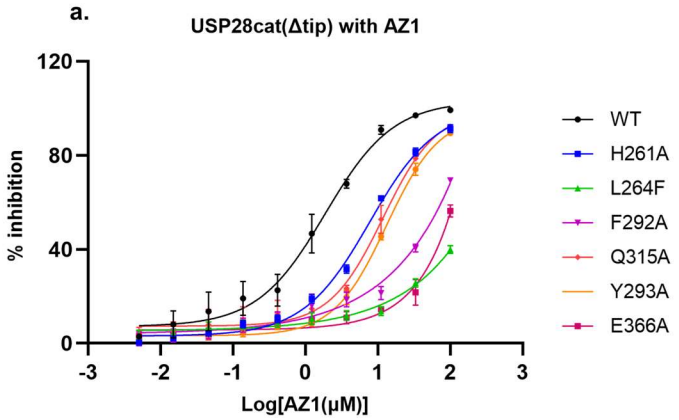

USP28cat (Δtip) variant	IC50 (μM)
WT	1.87
H261A	7.74
L264F	>100
F292A	60.92
Y293A	13.25
Q315A	11.82
E366A	>100

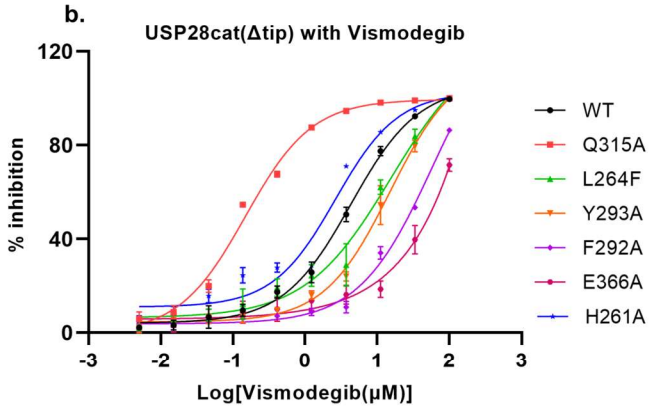

USP28cat (Δtip) variant	IC50 (μM)
WT	4.30
H261A	2.62
L264F	15.37
F292A	58.08
Y293A	15.06
Q315A	0.15
E366A	>100

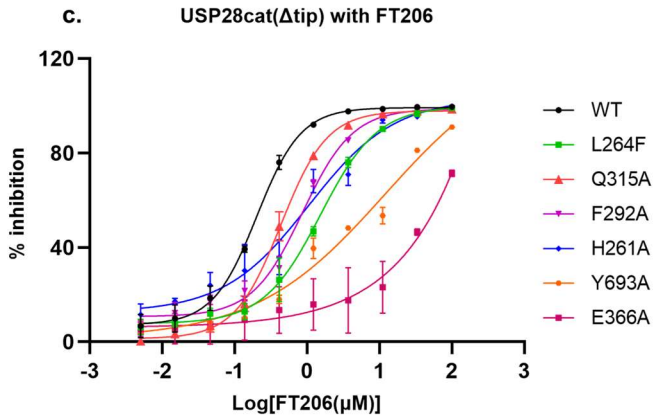

USP28cat (Δtip) variant	IC50 (μM)
WT	0.20
H261A	1.05
L264F	1.53
F292A	0.86
Q315A	0.43
E366A	>100
Y693A	11.97

Figure 3.18: Dose-response curves of USP28cat (Δtip) with AZ1 (a), Vismodegib (b) and FT206 (c). IC_{50} values for the inhibitors were determined from dose-dependent percent inhibition of USP28cat (Δtip) WT and variants against cleavage of Ub-Rho110 substrate. Error bars represent the standard deviation of triplicate measurements from three independent experiments. Calculated values are shown in the respective tables.

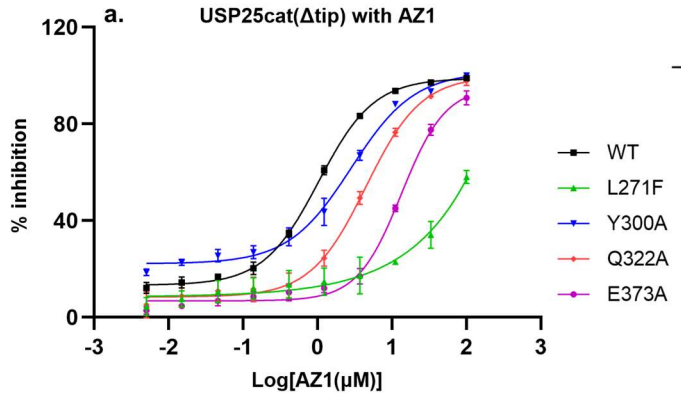

USP25cat (Δtip) variant	IC50 (μM)
WT	1.03
L271F	>100
Y300A	2.43
Q322A	4.47
E373A	13.38

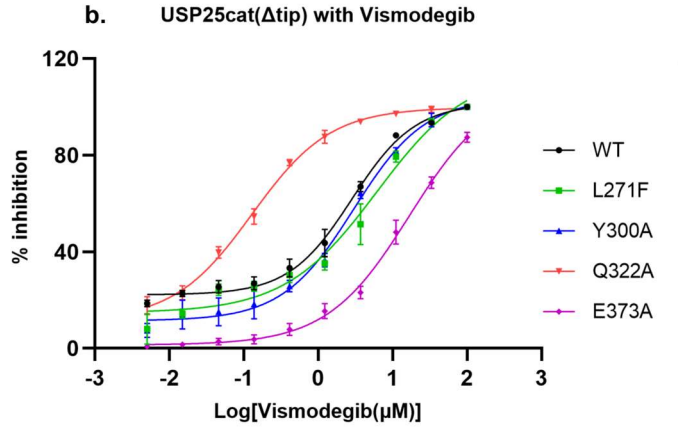

USP25cat (Δtip) variant	IC50 (μM)
WT	2.83
L271F	6.14
Y300A	3.00
Q322A	0.12
E373A	16.92

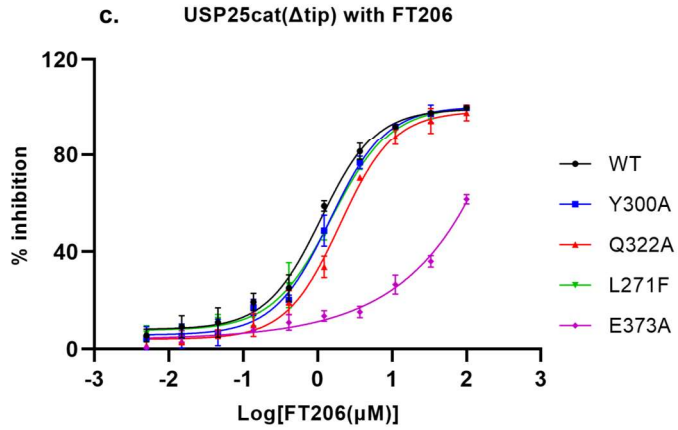

USP25cat (Δtip) variant	IC50 (μM)
WT	1.12
L271F	1.68
Y300A	1.47
Q322A	2.00
E373A	>100

Figure 3.19: Dose-response curves of USP25cat (Δtip) with AZ1 (a), Vismodegib (b) and FT206 (c). IC_{50} values for the inhibitors were determined from dose-dependent percent inhibition of USP25cat (Δtip) WT and variants against cleavage of Ub-Rho110 substrate. Error bars represent the standard deviation of triplicate measurements from three independent experiments. Calculated values are shown in the respective tables.

3.2.2.2 Gel-based ubiquitin hydrolysis assays

To assess the significance of the USP28 binding-site residues with a physiological substrate, hydrolysis of *in vitro* generated polyubiquitin substrates (K48-linked di-ubiquitin and K63-linked tetra-ubiquitin) was performed using a gel-based assay, as described in Section 2.2.3.8. Previous studies report that USP28 shows no preference for either K48- or K63-linked tetra-ubiquitin chains but a marginally stronger interaction with K48-linked over K63-linked diubiquitin substrates (Zhen et al., 2014; Klemm, 2020).

The catalytic activity of the USP28cat (Δtip) WT and variant proteins was tested against a DMSO control and in the presence of an excess of the inhibitor compounds. As observed previously with the hydrolysis of the monoubiquitinated, synthetic substate Ub-Rho110 (Figure 3.17), the catalytic activities of the USP28 variants L264F and Q315A showed a slower rate of substrate cleavage compared to the WT protein, and the E366A variant exhibited similar activity to the WT protein.

The WT protein with all three inhibitor classes showed a reduced rate of polyubiquitin substrate cleavage compared to the DMSO control (Figure 3.20 for K63-linked tetra-ubiquitin cleavage). Considering the IC_{50} values of AZ1 and FT206 are lower compared to Vismodegib (Figure 3.18) for the WT protein, this was also seen with the latter showing a comparatively slower rate of cleavage. Also, in agreement with the dose-response assay data, the Q315A variant clearly presented a very slow hydrolysis rate of up to 40 minutes in the presence of Vismodegib, indicating a strong binding of the inhibitor to the protein. For AZ1 and FT206, this variant showed similar cleavage activity to the control lanes. The L264F variant in the presence of AZ1 showed a marked decrease in substrate hydrolysis compared to the WT protein, while in the presence of Vismodegib hydrolysis seemed to be getting slower up until the 60-minute mark. However, with FT206, L264F showed no significant hydrolysis until 60 minutes. In the presence of the E366A variant, all three inhibitors showed a very high cleavage rate, faster than the one observed for the WT protein, indicating complete inhibition resistance, further confirming the mono-Ub based dose-response assay results.

Interestingly, an additional band above the diubiquitin band, at approximately 16 kDa, was observed consistently in all lanes in the presence of the inhibitors Vismodegib and FT206, but only with the K63-linked tetra-ubiquitin substrate and not with the K48-linked diubiquitin substrate (Figure 7.8).

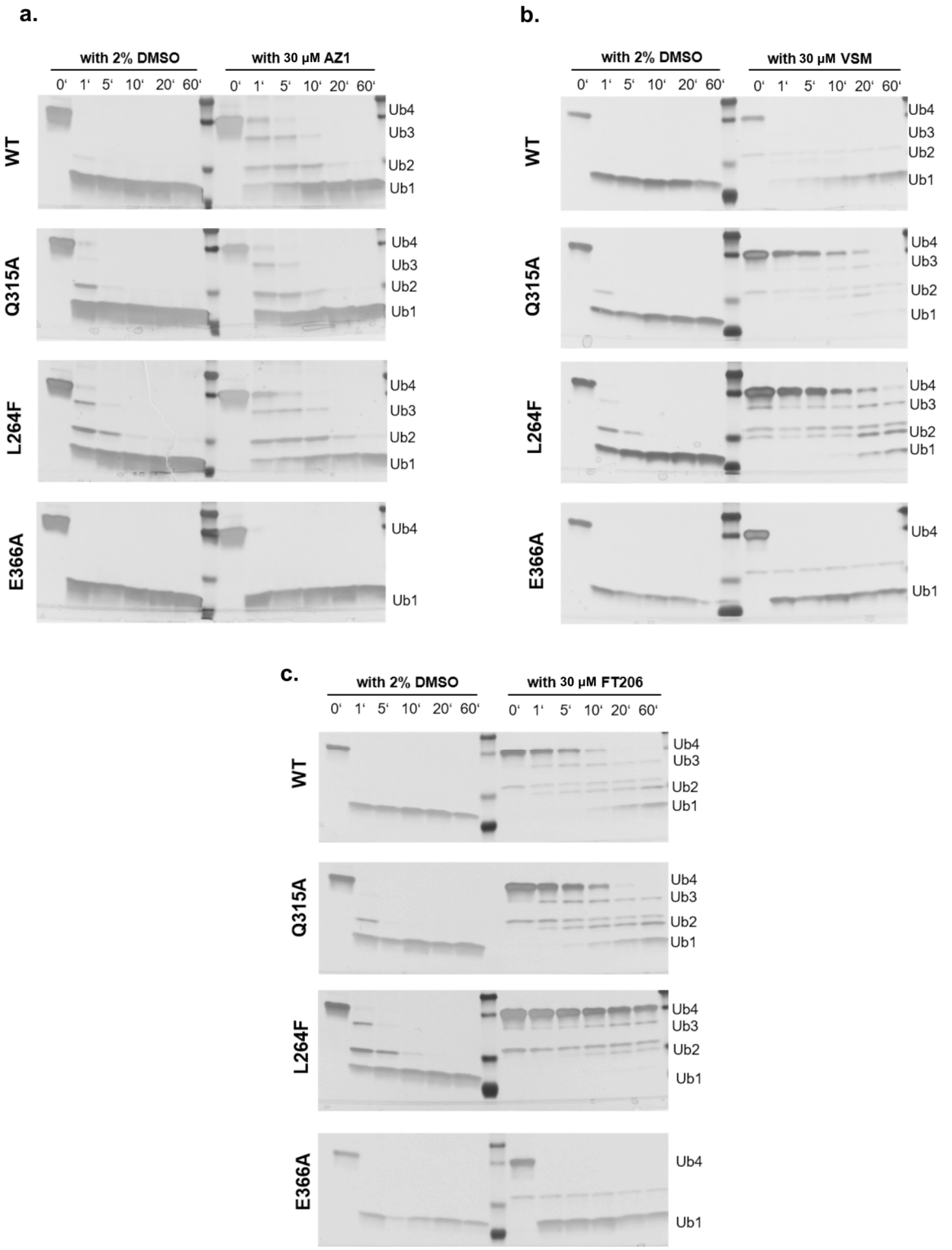

Figure 3.20: Gel-based K63-linked tetra-ubiquitin hydrolysis assay. Silver-stained SDS-PAGE gels depicting cleavage by the USP28cat (Δtip) WT protein and the Q315A, L264F and E3663A variants, in the presence and absence of the inhibitor compounds (AZ1, a; Vismodegib/VSM, b; FT206, c). The left panel in the gels indicate the control lanes where the proteins were incubated with 2% DMSO and the right panel in the presence of 30 µM inhibitor. The time points are depicted above the bands. The tetra-, tri-, di- and monoubiquitin are shown as Ub4, Ub3, Ub2 and Ub1, respectively.

3.2.2.3 Determination of inhibitor binding affinities

To further characterize the inhibitor-binding pocket and determine the binding affinity of the compounds to the WT and variant proteins, microscale thermophoresis (MST) and isothermal titration calorimetry (ITC) were pursued.

As an initial approach, the label-free form of MST, which utilizes the intrinsic fluorescence of tryptophan residues ($\lambda_{excitation}$: 281 nm, $\lambda_{emission}$: 320 nm) in the protein, was chosen for analysis. Another advantage of this method is that it requires very low amounts of samples. The experiment was performed as described in Section 2.2.3.5. A UV fluorescence capillary scan was performed and compared with distilled water to eliminate any absorbance or background fluorescence from the MST buffer or the inhibitor compounds. Neither the buffer nor the compounds show any intrinsic fluorescence at tryptophan wavelengths.

First, the USP28cat (Δtip) WT and Q315A variant proteins were tested with all the three compounds: AZ1, Vismodegib and FT206. The proteins displayed a trend indicating positive thermophoresis in the presence of FT206 (Figure 3.21), and the K_d values for the interaction were 0.3 μM for the WT and 0.9 μM for the Q315A variant. However, the quality of fit for these two proteins with the other two inhibitors AZ1 and Vismodegib was unsatisfactory. Moreover, issues with reproducibility, protein aggregation and unspecific adsorption of the sample to the capillary tubes were also observed with the other variants that were tested. This method was therefore not pursued any further.

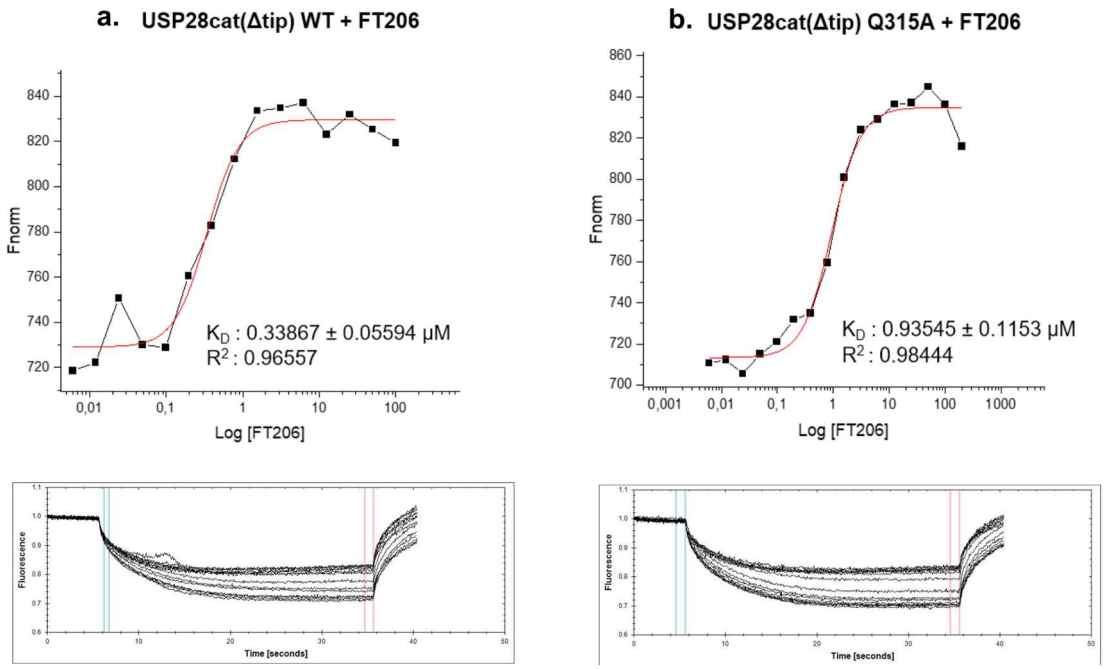

Figure 3.21: MST analysis for the determination of inhibitor binding affinities. Dose-response curves (top) and MST curves (bottom) titrated against FT206 using the NT.LabelFree MST instrument. All graphs display data from duplicate readings from one experiment, and the reading was recorded at 20 % LED power and 40% MST power. The observed K_d value for the WT protein was 0.3 µM and 0.9 µM for the Q315 variant. Fnorm=normalized fluorescence.

Next, ITC measurements were performed to determine the dissociation constants (K_d), molar entropy and enthalpy changes and stoichiometry of the USP28-inhibitor interactions. All experiments were performed as mentioned in Section 2.2.3.6. 200 µM of the inhibitor compound was injected into the vial containing 20 µM of the USP28cat (Δtip) WT or the variant protein. The background heat was measured by injecting the inhibitor into the ITC buffer containing 2% DMSO and subtracted from the inhibitor-protein injections. The binding affinities for the WT and Q315A variant were in the lower micromolar range (Table 3.5), as expected from the dose-response assays. However, for the other variants, H261A, L264F, E366A and F292A, the signal/noise ratio was very low, and the curves did not reach saturation. Optimization of the protein or ligand concentration did not seem to decrease the heat of dilution, and neither did a change in temperature from 25 °C to 20 °C.

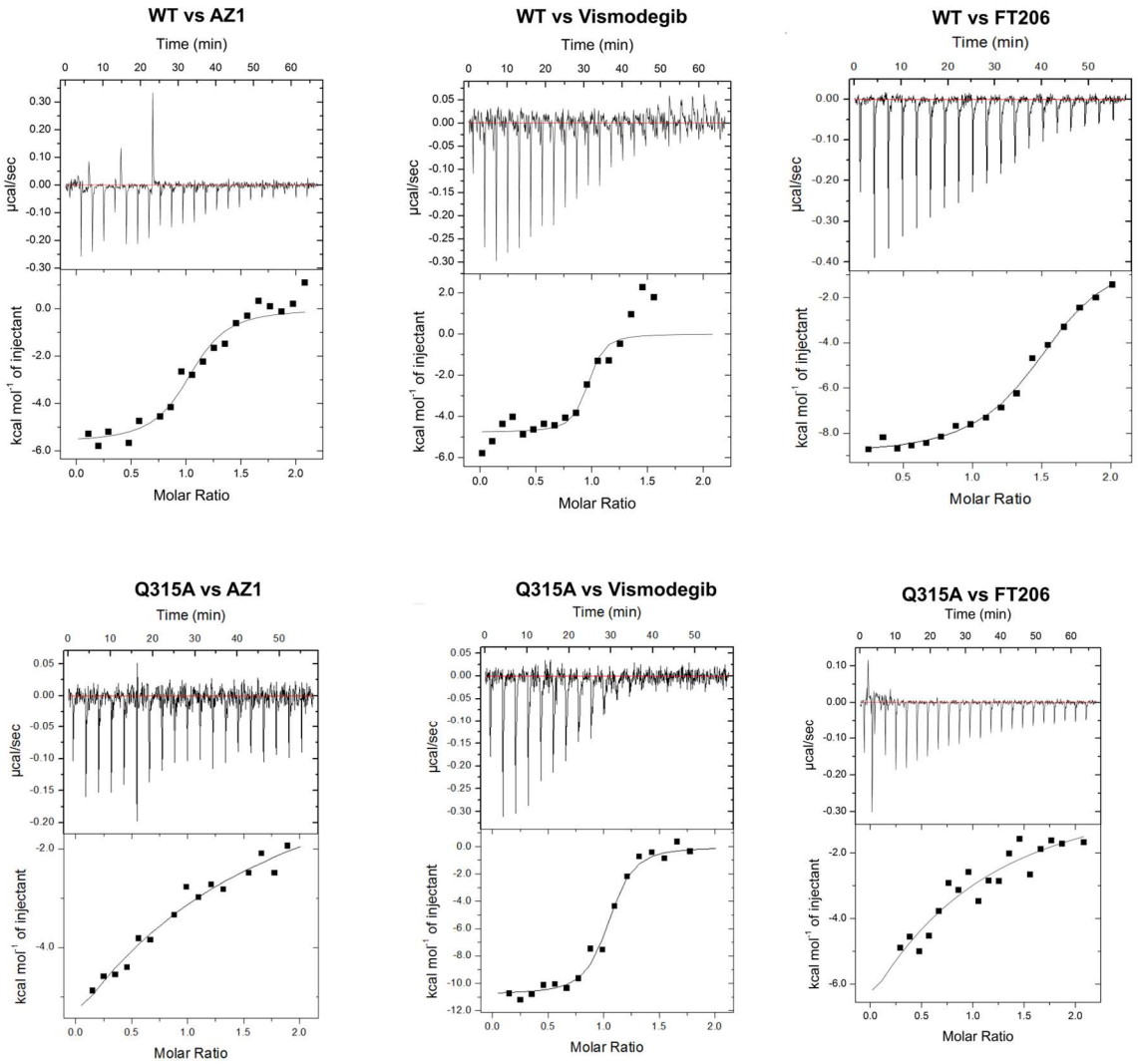

Figure 3.22: ITC analysis for the determination of inhibitor binding affinities. Binding isotherms derived from ITC experiments demonstrating AZ1, Vismodegib and FT206 compound interaction with the USP28cat (Δtip) WT protein and the Q315A variant. The heat released upon each injection was measured as a function of time (upper panels). Curves for the integrated heats of binding obtained from the raw data were plotted with one binding site model (performed with the MicroCal Origin software). K_d values derived from these analyses are summarized in Table 3.5.

USP28cat (Δtip) sample	Observed K_d (µM)	Reported K_d (µM)
WT vs AZ1	1.72	0.2
WT vs Vismodegib	4.61	1.42
WT vs FT206	1.22	-
Q315A vs AZ1	2.13	-
Q315A vs Vismodegib	1.53	0.34
Q315A vs FT206	3.06	-

Table 3.5: The observed binding affinities for the AZ1 and Vismodegib compounds to the USP28cat (Δtip) protein and the Q315A variant, as determined by ITC analysis.

3.2.2.4 Effect of inhibitors on USP25 tetramerization

A comparison of the structures of the USP28-inhibitor bound complexes to the USP25cat domain tetramer and the analysis of the USP25cat (Δtip) variant proteins indicated that the compounds bind into the cleft in USP25, which is responsible for UCID-tip binding, leading to tetramerization and thus resulting in an auto-inhibited protein.

To assess the effect of the inhibitors on USP25 tetramerization, thereby acting as both USP25 inhibitors/activators, the full-length, tetrameric protein (20 µM) was mixed with a three-fold excess of the inhibitor compounds (60 µM) as well as 1% DMSO as a control. The mixture was incubated at room temperature for 1 hour and then injected into a Superdex 200 10/300 GL column linked to a MALS and RI detector (for concentration measurements). Although a slight decrease in the molecular weight of the protein incubated with the inhibitors compared to the *apo* protein was observed, this difference is not significant, indicating that the interaction with the inhibitors does not induce a quantitative dissociation of the USP25 tetramer from its auto-inhibited state to a dimeric, active state. Thus, the exposure to the inhibitors does not appear to be sufficient to displace the USP25 tip from the tip-binding cleft.

The measured molecular weight for the *apo*-protein and in complex with the three inhibitor classes is summarized in Table 3.6.

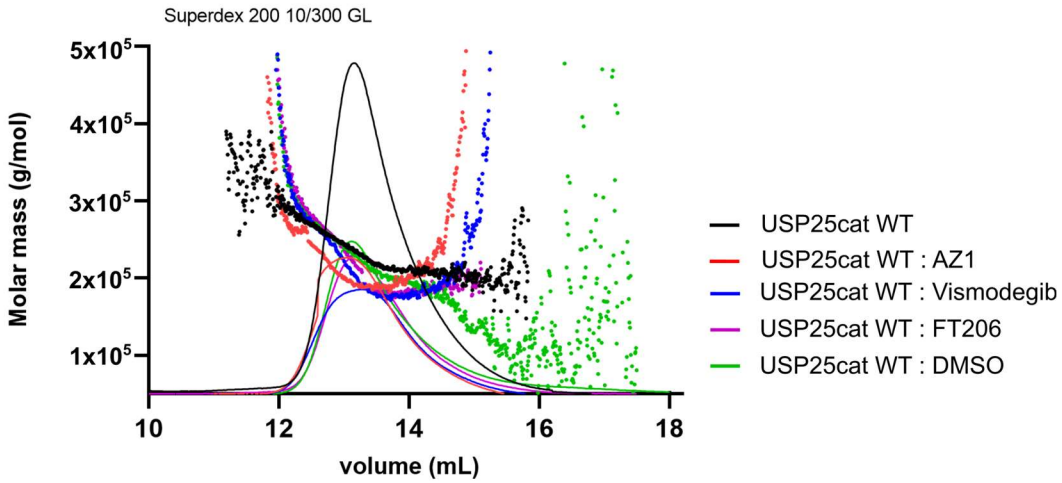

Figure 3.23: SEC-MALS analysis of the USP25cat WT-complexes. The molar mass and refractive index of the auto-inhibited, tetrameric USP25cat WT protein in the presence and absence of AZ1, Vismodegib and FT206 are plotted against the elution volume from a Superdex 200 10/300 SEC column. A control run of the WT protein in the presence of DMSO was also performed. Incubation of the WT protein with the inhibitors does not induce disruption of the tetramer or activation of the protein. The peaks in the chromatogram represent the dRI signal (colors indicated in the legend), and the corresponding molar mass is represented as dotted lines.

Sample	Molecular weight (kDa)	
	Measured	Theoretical
USP25cat WT *apo*	240.7 ± 3.9	256.4
USP25cat WT : AZ1	226.0 ± 4.1	-
USP25cat WT : Vismodegib	221.6 ± 3.2	-
USP25cat WT: FT206	237.7 ± 3.7	-
USP25cat WT :DMSO	238.3 ± 3.6	-

Table 3.6: The molecular mass of the USP25cat WT protein in the presence of the inhibitors as determined from the SEC-MALS analysis. The theoretical mass of the tetrameric WT protein is also indicated.

3.3 Crystallization of the dimeric USP25cat (Δtip) protein

As of today, structural information on the catalytic domain of USP25 is limited to the tetrameric, auto-inhibited form in which the UCID-tip blocks the Ub-substrate-binding S1 site. The comparison of this structure with the USP28-inhibitor bound complexes indicates that the compounds bind into the same cleft which is occupied by the UCID-tip in USP25 (Figure 3.7). To facilitate the characterization of inhibitor binding to USP25, detailed structural information on USP25 in its activated form is essential.

USP25cat (Δtip), which is catalytically active and dimeric, was subjected to extensive crystallization screening trials. Initial hits were observed in a condition containing 0.4 M or 0.6 M $MgSO_4$, 0.1 M Bis-Tris Propane (pH 7.0) and 16% PEG 6000 at protein concentrations ranging from 1.5-3.5 mg/ml, using the sitting-drop vapor diffusion method at 20 °C. However, these crystals were too thin, needle-like, and delicate to handle (Figure 3.24). To improve the observed crystal form, an additive screen was utilized in the presence of the above-described crystallization condition while also altering the cations. Interestingly, the protein formed bigger crystals in a condition comprising 0.4 M $MgCl_2$, 0.1 M Bis-Tris Propane (pH 7.0), 16% PEG 6000 with the additives 0.02 M NDSB-201, 0.02 M NDSB-211, 0.3% (w/v) D-(+)-Glucose monohydrate or 0.3% (w/v) D-(+)-Galactose. Although the crystals showed a diffraction pattern indicative of a protein, the resolution was too low (>5 Å) to collect diffraction data of sufficient quality for structure determination.

To obtain a complex structure of USP25cat (Δtip) bound to a ubiquitin substrate, the purified Δtip protein was incubated with a 3-fold excess of the suicide probe Ub-PA and incubated on ice for ~ 2 hours. Following incubation, the mixture was subjected to size-exclusion

chromatography to remove the excess of unbound PA molecules (Section 7.4.4), and the purified complex was subjected to crystallization screening. However, no crystal hits could be obtained so far.

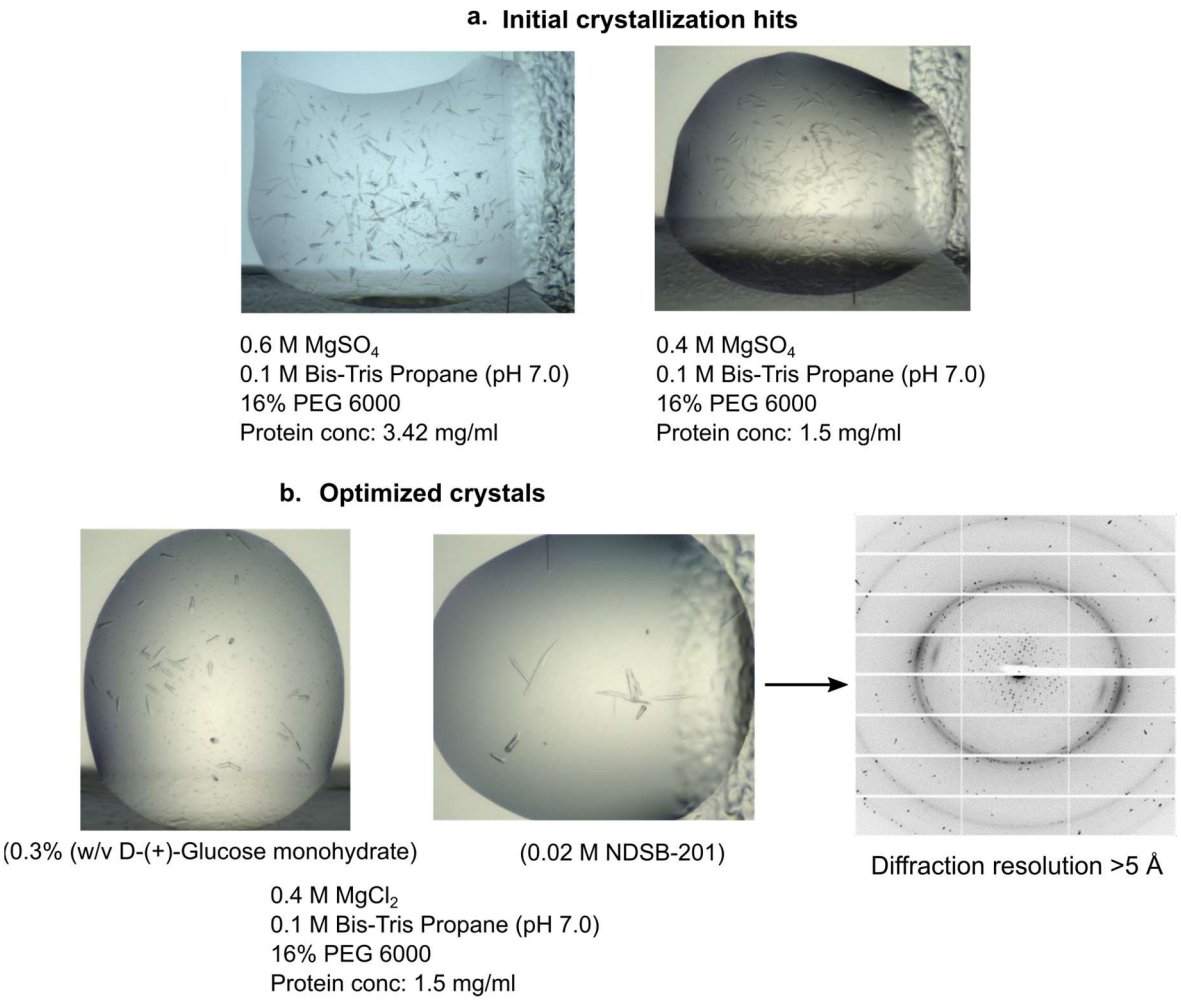

Figure 3.24: USP25cat (Δtip) crystallization. (a) Images of the initial crystal hits which led to the formation of very thin, needle-like clusters and **(b)** their optimization to much bigger, single crystals, which also grew longer in size. Crystallization conditions and the additive screen components are also mentioned. Diffraction pattern of one of the optimized crystals collected at the ESRF beamline ID 23-2.

4. DISCUSSION

Ubiquitination is a post-translational modification (PTM) process that plays an important role in a myriad of cellular processes in eukaryotic cells and thus dictates protein-protein interactions, localization, enzymatic function and stability of the modified substrate. Like most PTMs, ubiquitination is reversible, and the removal of ubiquitin from the substrates is catalyzed by deubiquitinases (DUBs). Dysregulation of DUBs can lead to imbalances in protein levels and contributes to various sporadic and genetic disorders. Research over the last 20 years to understand the mechanisms that govern the activity, substrate specificity, and regulation of DUBs has resulted in their emergence as novel therapeutic targets for the treatment of cancer, neurodegenerative diseases and various immune disorders.

A major hurdle in the development of DUB inhibitors is attributed to poor specificity. Developing covalent inhibitors that specifically target a given DUB among related DUBs is challenging yet not impossible. This was proven with the recent advances in small-molecule inhibitor development leading to the discovery of potent and specific inhibitors, especially for USP7. However, selective compounds have only been obtained for a minimal number of DUBs as a majority of the reported inhibitors display weak inhibitory activity, undesirable off-target effects and/or possess poor selectivity across the DUB enzyme family. Several DUBs, especially USPs, are closely related and share similar catalytic pockets (Ye et al., 2009), which adds an additional layer of complexity towards inhibitor development. Nevertheless, distinct mechanisms, substrate specificity determinants, and regulatory activities suggest that they can be selectively targeted.

USP28 and USP25 are two such related DUBs that have emerged as interesting targets for therapeutic development because of their involvement in various cellular processes (see Section 1.2.1). Recently reported small-molecule inhibitors targeting USP28 also displayed activity against USP25 (see Section 1.4.1). However, some specificity may have been achieved. In ABPP assays performed in cell lysates, specificity was observed for USP25 in the case of AZ1 and the newly discovered compounds reported by Varca et al. (Varca et al., 2021; Section 1.4.1.5). USP25 was also suggested to be the primary target of AZ1 in colonic tumorigenesis models (X.-M. Wang et al., 2020; Section 1.4.1.1). Another recent report indicated a targeted inhibition of USP25 by FT206 in PDAC organoids (Nelson et al., 2022; Section 1.4.1.3). Previous studies by our group and others have shown that despite sharing a high sequence and structural similarity, USP28 and USP25 exhibit major differences in their

oligomeric composition and regulation of their enzymatic activities (see Section 1.2.2). To understand the mode of inhibition of these compounds, it was thus important to obtain structural information on the protein-inhibitor complexes. This thesis reports the first complex structures of USP28 bound to three of the eight reported inhibitor classes: the AZ compounds, Vismodegib and FT206. The following sections discuss the key findings of this thesis and provide a molecular basis for the small-molecule inhibition of USP28 and USP25.

USP28 and USP25 adopt the canonical USP fold composed of the thumb, palm and finger subdomains (B. Liu et al., 2018; Sauer et al., 2019; Gersch et al., 2019). While USP28 is a constitutively active dimeric protein, USP25 assumes an auto-inhibited, tetrameric composition. Oligomerization is facilitated by an extended insertion site, UCID, consisting of the UCID-rod and the UCID-tip; the latter represents the most dissimilar region between the two enzymes (only 6 of 24 positions within the C-terminal region of the UCID-tip are identical).

In USP28, the introduction of a charged amino acid into the hydrophobic dimer interface or the partial removal of the UCID led to a monomeric variant (Sauer et al., 2019; Klemm, 2020) which retained the same catalytic activity and efficiency as the dimeric WT protein. However, the complete removal of the UCID resulted in a strong reduction of both activity and stability of USP28 (Gersch et al., 2019). The UCID-tip in USP28 is mainly disordered, and removal of this region does not affect the dimerization or the catalytic activity of the protein. These observations indicate that the UCID is only partially responsible for USP28 activity by mediating the stabilization of the core USP domain. It was also shown that the dimeric WT and the monomeric variant of USP28 showed a similar activity on LSD1 *in vivo,* suggesting that the oligomeric nature is not relevant for the interaction with this substrate (Gersch et al., 2019). Hence, it remains unclear why the enzyme must adopt a dimeric form *via* the UCID. Various substrates of USP28 themselves exist as oligomers (predominantly dimeric), suggesting the requirement of USP28 to adopt the same stoichiometry, which could facilitate the interaction with its substrates.

In USP25, however, the UCID-tip is at least partially ordered and binds into an open cleft in the USP core domain of the adjacent dimer. The removal of the UCID-tip leads to the formation of a dimeric protein that is ~6-fold more active than the tetrameric WT protein (but is still ~6-fold less active than the dimeric USP28cat). It is currently unclear if the 'open cleft' conformation is also present in the active dimeric protein. Previous *in vitro* studies have shown that a dissociated tetramer does not reassemble from dimers, suggesting that the cleft

closes upon tetramer disruption (Klemm, 2020). The formation of the 'open cleft' is facilitated by a shift in the helix α5 and stabilized by π-stacking interactions between Phe253 and Phe266 on helices α4 and α5, respectively (Figure 1.9c). The importance of helix α5 in regulating the catalytic activity has been demonstrated previously for USP7. The catalytic triad residues of USP7 in its *apo*-form are misaligned, resulting in a non-functional, catalytically inactive protein. For its activation, upon Ub binding, the conformational rearrangement of the switching loop results in the formation of a cleft into which the C-terminal peptide of USP7 binds, pushing helix α5 outward into an active conformation and thereby stabilizing it (Hu et al., 2002; Rougé et al., 2016). This helix α5 rearrangement is also essential for inhibitor binding, as seen from the USP28-inhibitor structures in this study. However, the hitherto known *apo* and Ub-bound structures of USP28 do not exhibit the 'open cleft' conformation, but the current inhibitor-bound structures provide evidence that such a cleft also exists in USP28 and is seemingly stabilized upon inhibitor-binding.

4.1 The inhibitor binding pocket is highly conserved in USP28 and USP25

Previously reported crystal forms of the USP28cat WT protein led to low diffraction quality crystals, which was not ideal for obtaining inhibitor-complex structures at a resolution which would permit a clear interpretation of the protein-inhibitor interactions. An extensive screening campaign was performed to identify optimal crystal forms for the subsequent inhibitor soaking experiments. The initial inhibitor-bound structures were obtained utilizing the dimeric USP28cat Δtip variant. Further optimization of the protein construct led to better diffracting crystals with the protein devoid of the entire UCID region (monomeric USP28 149-ΔUCID-698). Interestingly, despite having only a small truncation at its C-terminus, which is not involved in any crystal contacts, these crystals belonged to a different space group than the monomeric USP28 (149- ΔUCID-703) crystals reported by Gersch et al. (Gersch et al., 2019) (Section 3.1.1.2).

The inhibitor-bound structures revealed unambiguous electron density for all the three compound classes in USP28 at identical regions – at a cleft located between the thumb and the palm subdomains; an allosteric site distant from the catalytic cysteine 171. Binding of the inhibitors is achieved through interactions stemming from USP28 residues lining the pocket with atoms of the inhibitors. The interacting residues are present primarily on helices α5, α6 and β-strands 3, 5 & 7. Importantly, this region comprises the tail-distal part of the S1-binding

site, which interacts with the globular Ub-domain. Comparing the inhibitor-bound and the *apo* structures of USP28 revealed two significant conformational changes, both presumed to be induced upon inhibitor binding. The first is a shift of helix α5. In the AZ inhibitor-bound structures, this shift could be attributed to an increase in the distance between Leu264 (present on helix α5) and Phe292 (present on helix α6), triggered by the intercalation of the bromobenzene moiety between the two residues. This rearrangement of helix α5 is comparable to the USP25 UCID-tip binding, occupying a pocket below helix α5, similar to the inhibitor-binding region in USP28 (Figure 3.7c). This shift is also observed in the Vismodegib and FT206-bound structures. The catalytic triad residues of USP28 (Cys171, His600 and Asn617) undergo limited movement between the inhibitor-bound and *apo* conformations. The shift in helix α5 further triggers conformational changes in the orientations of the switching loop (SL) and blocking loop 2 (BL2), which would prevent the efficient binding of Ub, thus impeding catalysis. However, it should be mentioned that there is no direct interaction of the compounds with BL2 and that this loop is not directly linked to helix α5. It is thus currently unclear if the movement of helix α5 causes the conformational change of BL2. Furthermore, it is not known if inhibitor-binding leads to the shift in helix α5 and thus the formation of the binding pocket or if the compounds occupy and stabilize a pre-formed region occurring in USP28.

The inhibitor binding site represents the region of highest identity between the USP28 and USP25 catalytic domains (Figure 4.1). A superposition of the USP28-inhibitor bound structures and the tetrameric USP25cat structure (PDB ID: 6H4J, Sauer et al., 2019) shows that the USP25 UCID-tip residues ranging from aa 516-537 occupy the same region as the inhibitors in the USP28 binding pocket. Structural information on the USP25cat is currently limited to the auto-inhibited tetrameric state where the UCID-tip predominantly blocks the S1 site, as described before. It was previously reported that tetramerization in USP25 is a unidirectional process. The dissociated tetramer does not reassemble from dimers, suggesting that the cleft accommodating the UCID-tip is closed upon tetramer disruption (Klemm, 2020). Biochemical characterization of the dimeric USP25cat Δtip variants (described in Section 4.2) suggests that the inhibitor-binding to USP25 is highly comparable to that observed in USP28. However, structural elucidation of the active dimeric form of USP25cat and in complex with the inhibitors would shed light on whether inhibitor-binding leads to any difference in the conformational changes as observed in USP28, and this information could be used to address the issues pertaining to USP28/25 specific drug design.

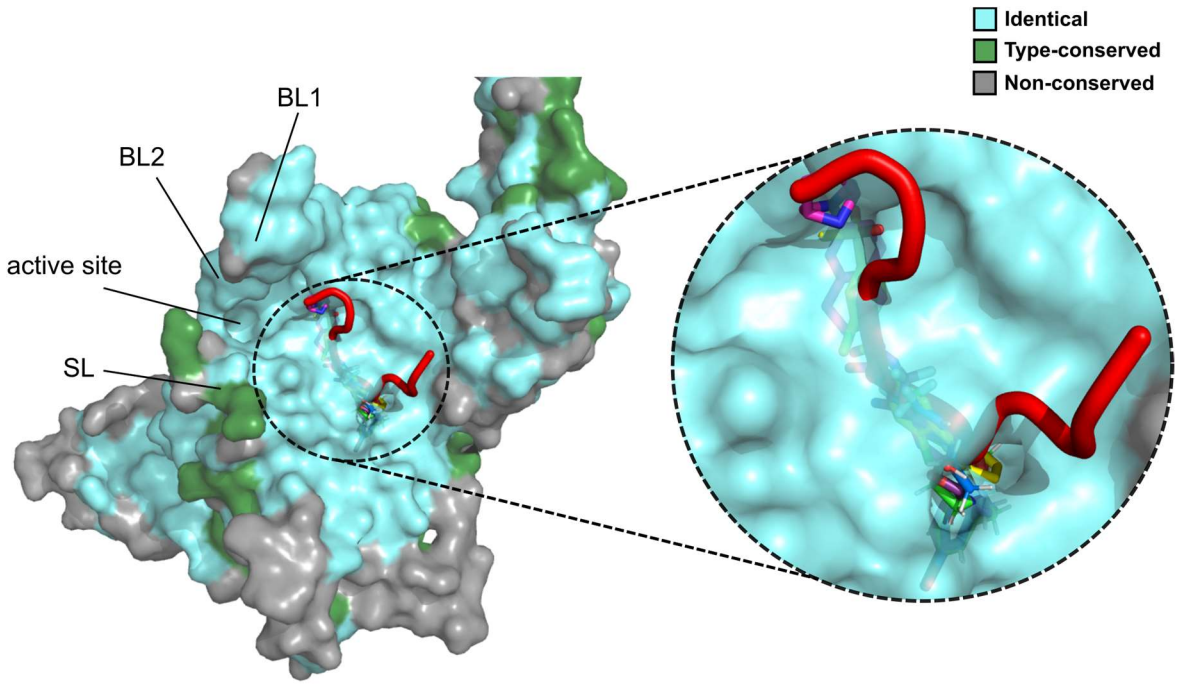

Figure 4.1: Sequence conservation between USP25 and the USP28-inhibitor binding site. Identical residues are shown in cyan, type-conserved residues in green and non-conserved residues in gray. The regions comprising the blocking loops (BL) 1 & 2, the switching loop (SL) and the catalytic active site are also indicated. The inhibitor binding pocket of USP28 is highlighted in the dotted circle. The AZ compounds, Vismodegib and FT206, are shown as sticks. This region also encompasses the UCID-tip (residues 516-537, colored in red, shown here in ribbon representation) binding pocket in USP25.

4.2 The compounds inhibit USP28 allosterically

The USP28-inhibitor complex structures suggest that the compounds function *via* allosteric regulation and not competitive inhibition as they bind in a region away from the catalytic active site residues. Based on the classification of DUB inhibitors by Lange et al. (please refer to Section 1.4), these compounds belong to the Type III-D class of inhibitors, characterized as compounds that exhibit allosteric binding at the distal Ub (S1). This class also represents the highest number of potent DUB inhibitors currently known.

Allosteric inhibition has been previously reported for USPs. For example, two inhibitors of USP7, GNE6640 and GNE6776, were shown to bind to the thumb-finger cleft, approximately 12 Å away from the catalytic triad and sterically inhibit Ub-binding by preventing the transition of the USP7 helix α5 to the active conformation (Kategaya et al., 2017). Another example involving misalignment of the catalytic triad is seen with compounds ALM2 and ALM5 reported as non-competitive USP7 inhibitors (Gavory et al., 2018). The

co-crystal structure with USP7 revealed that the compounds bind outside of the active site situated ~ 5 Å away from the catalytic cysteine in a previously undisclosed allosteric pocket. However, unlike the GNE compounds, these inhibitors bind between the thumb-palm sub-domains. The co-crystal structures indicated that the overall fold of USP7 was similar to the USP7 *apo*-structure. Thus, the compounds were presumed to prevent the alignment of the catalytic triad within the USP7 active site and induce local distortion of the Ub C-terminal tail binding channel by partially protruding into it. A similar mode of inhibition was also reported for USP14 with the IU inhibitors, which bind underneath BL2 in the substrate-binding cleft, 8.3 Å away from the catalytic cysteine (Y. Wang et al., 2018).

While the USP28 inhibitors studied in this thesis do not completely block the distal S1 site, the shift in helix α5 and the accompanying conformational rearrangement of the SL and BL2 suggests a similar mechanism of action as observed with USP7 inhibition. Since the helix α5 itself contributes to the concave Ub-binding site, any change in its native position would affect the Ub-binding surface. One may speculate that the structural changes induced upon inhibitor binding trigger a local distortion at the Ub C-terminal tail binding channel, thus impeding catalysis. Unfortunately, the switching loop and blocking loop 2 are not fully resolved in the inhibitor complex structures. Hence, the mechanism of inhibition could only be postulated by comparison with previously reported allosteric inhibitors of other USPs. Additional kinetic experiments to characterize the mode-of-inhibition of Vismodegib and FT206 is necessary.

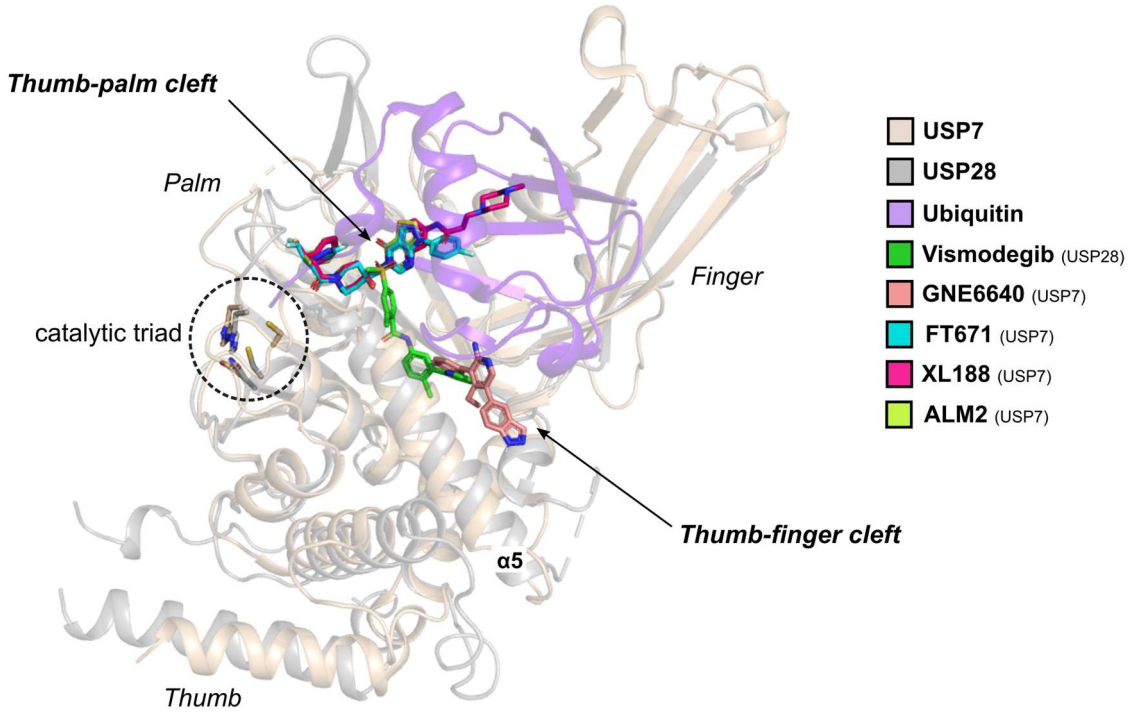

Figure 4.2: Allosteric inhibitors of USP7 in comparison with USP28-Vismodegib. A superposition of USP7-inhibitors (allosteric, non-active site) was performed with the USP28cat (ΔUCID)-Vismodegib complex structure obtained from this study. The catalytic domains of USP7 (wheat) and USP28 (gray) are shown in cartoon representations. The inhibitor compounds are shown in stick representation. GNE6670 (salmon pink) binds into the thumb-finger cleft, while compounds FT671 (cyan), XL188 (magenta) and ALM2 (lime green) bind in the thumb-palm cleft of USP7. Vismodegib (green) binds into the thumb-palm cleft of USP28. The thumb-palm cleft also represents the Ubiquitin (violet) S1-site of the proteins. The catalytic triad/active site residues of both proteins are highlighted within the dotted circle.

4.3 Characterization of compound binding in USP28 and USP25

The binding mode of the AZ inhibitors to USP28 reveals the importance of the fluorine group substitutions in dictating the potency of the inhibitors. AZ1 and AZ2, which possess trifluoromethyl (-CF_3) and trifluoromethoxy (-OCF_3) group substitutions, respectively, exhibit higher inhibition towards USP28 and USP25 than the single fluorine group substituted AZ4. The non-substituted compound of the series AZ3 does not inhibit the proteins sufficiently (IC_{50} > 50 µM). Fluorine displays favorable properties like effective electron withdrawal, high lipophilicity and small size. It exhibits an amphipathic characteristic, i.e., a dual property to act as an H-bond acceptor or a hydrophobic moiety. One plausible explanation for the increased potency of AZ1/AZ2 compounds over AZ4 could be because the C-F bond forms favorable interactions with strong H-bond donors (in this case, the side chain of His261) (Meanwell, 2018).

The binding pocket for Vismodegib, based on HDX-MS and docking simulations, was previously identified to be mainly composed of two helical structures spanning Asp255-Asn278 (helix α5) and Asn286-Tyr293 (helix α6). Mutational analysis of residues presumed to play key roles in the USP28-Vismodegib interaction confirmed the generated docking models (H. Wang et al., 2020). The USP28-Vismodegib complex structure obtained in this study is in close agreement with the previously published docking model. However, it appears that in the crystal structure, the chlorobenzene-moiety and the sulfonyl-phenyl ring are oriented in the opposite direction compared to the docking model and extend more towards the S1 site (Figure 4.3). Vismodegib interacts directly with Glu366, which forms a salt bridge with His261 and presumably locks the binding pocket and thereby preventing the dissociation of the compound. The flip of Gln315, as reported by Wang et al., was also observed in the crystal structure.

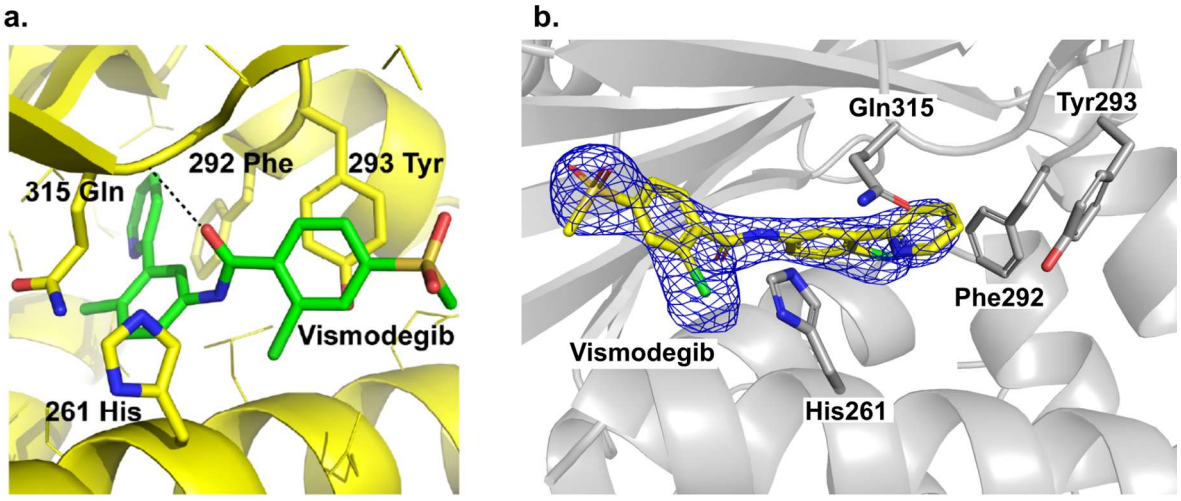

Figure 4.3: Docking model *vs* crystal structure of the USP28-Vismodegib complex. In the docking model of Vismodegib bound to USP28 reported by Wang et al. **(a)**, the chlorobenzene moiety and the sulfonyl-phenyl ring of the compound are positioned in the opposite direction compared to that observed in the crystal structure obtained in this study **(b).** Also, in the crystal structure, the compound lies further towards the Ub S1-site. The 2Fo-Fc electron density omit map (blue) of Vismodegib contoured at 1.0σ is also shown (at 2.57 Å).

The USP28-FT206 structure revealed that the terminal bicyclic moiety is approaching the Ub-tail binding site, thus blocking its path from reaching the active site. Interestingly, comparing the three inhibitor classes shows that the AZ inhibitors are located the furthest away from the Ub-tail binding site, while Vismodegib assumes an intermediate position and FT206 is in closest proximity to the Ub-tail binding site.

The USP28-inhibitor complex structures suggest that while inhibitor binding presumably induces conformational changes in BL2 (G594-G599) and SL (K243-D255), the compounds have no direct interaction with the residues present on either loop. Mutational analysis of residues lining the inhibitor binding pocket (H261, L264, D265, F292, Y293, Q315 and E366) confirmed the compound-binding mode as observed in the crystal structures. Four of the seven variants (H261A, L264F, D265S and F292A) exhibited a marked reduction in the cleavage activity towards the synthetic monoubiquitin substrate, Ub-Rho110. In contrast, the Q315A variant displayed only a slightly reduced activity compared to the WT protein (Figure 3.17a). Notably, the E366A variant retained substrate cleavage activity at WT levels but was highly resistant to inhibition by all three compound classes (IC_{50}>100 μM) (Figure 3.18).

The corresponding binding site variants in the dimeric USP25cat (Δtip) (L271F, F299A, Q322A) also showed a marked reduction in substrate cleavage activity except for Y300A, which was similar to the WT protein. More importantly, E373A (the corresponding residue to USP28 E366A) showed a ~2.3-fold increase in activity (Figure 3.17b) compared to WT. In the study reported by Liu et al. (B. Liu et al., 2018), the USP25 NCD construct (N-terminal domain + catalytic domain) expresses two stable oligomeric states: a dimer and a tetramer, where the dimeric species is substantially more active than the tetramer. E373A mutation of this construct exhibited similar catalytic activity as the dimeric species. They deduce that this mutation disrupts H-bond formation with the IL-loop (UCID-tip in this study) and compromises the tetramer assembly. However, the E373A mutation of the USP25cat (Δtip) construct used in this study was more active than the USP25cat (Δtip) WT. It is important to note that while USP25cat (Δtip) E373A, like its USP28 counterpart E366A, also showed resistance to FT206 binding, the IC_{50} values for Vismodegib and AZ1 were not greater than 20 μM (IC_{50}=16.92 μM and 13.38 μM, respectively; Figure 3.19). A possible reason for the difference in inhibitory potencies in the presence of this variant could be attributed to its structural orientation.

The E373 side-chain in the tetrameric, auto-inhibited USP25cat structure is positioned away from helix α5 (Figure 4.4). It could be envisioned that in the active, dimeric state, the side chain of E373 rotates, accompanied by a simultaneous conformational change in H268 (corresponds to H261 in USP28) and assumes a position similar to that seen in all USP28 structures from the *apo* form to the Ub and inhibitor-bound forms. Upon inhibitor-binding, the salt-bridge formed between these two residues locks the potential inhibitor-binding pocket. Mutation of the E366/E373 residue to a smaller aa like alanine might create a

significant gap for the inhibitors, thus facilitating dissociation from the binding pocket leading to a reduced residence time and diminished potency. However, the marked differences in the IC_{50} values for this USP25 E373A in the presence of AZ1/Vismodegib and FT206 indicate that there might be other conformational rearrangements occurring when the different inhibitors bind. These changes may be noticeably different to the binding mode in USP28 since it displays resistance against all three inhibitor classes in the presence of the E366A variant. This difference in inhibitory potencies may also provide a clue to identifying areas or regions within USP25 that pose an advantage in designing compounds that could achieve specific inhibition.

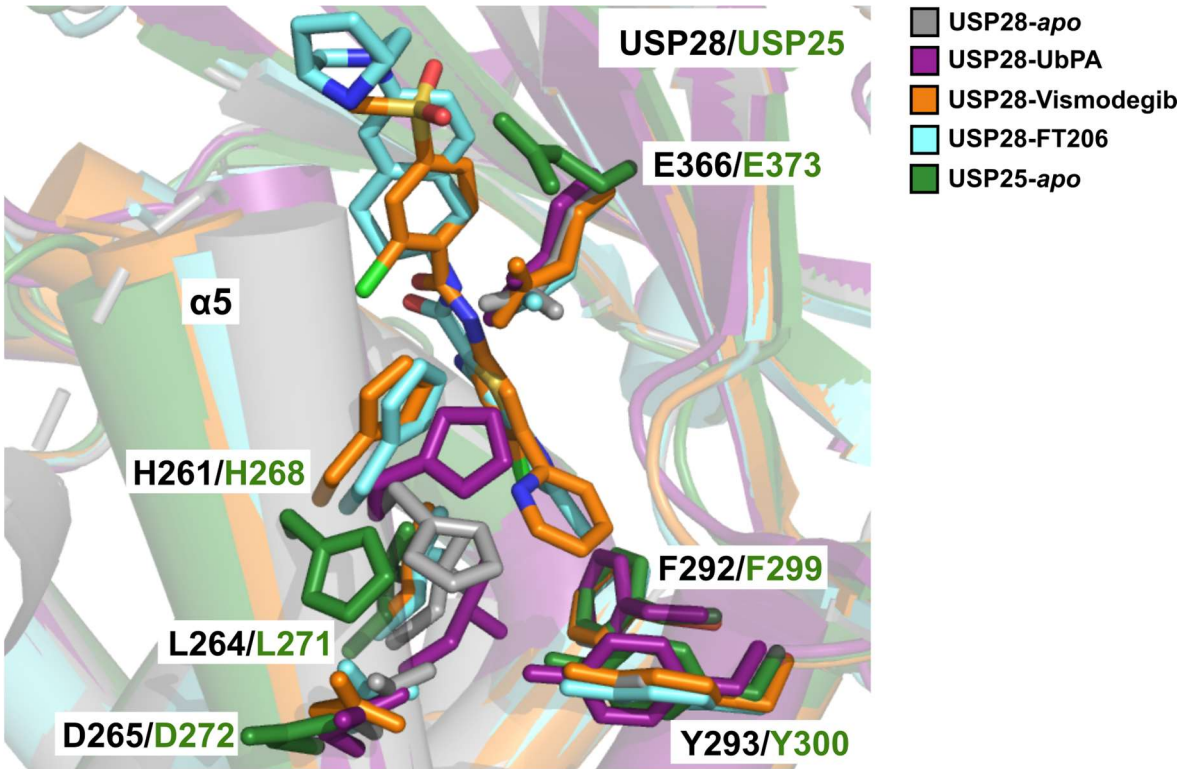

Figure 4.4: The orientation of E373 in USP25. A superposition of the inactive, tetrameric USP25cat structure (green) with the USP28cat *apo* (gray), Ub-bound (purple) and inhibitor-bound (Vismodegib-orange and FT206-cyan) show that the USP25 E373 residue is oriented away from helix α5 and the inhibitor-binding pocket, relative to USP28 E366. The other USP28 inhibitor-binding pocket residues (L264, D265, F292 and Y293) and the corresponding residues in USP25 (L271, D272, F299, Y300) are positioned relatively similar to one another, except for H261/H268. H268 in USP25 assumes a similar orientation as H261 in the USP28 *apo* structure, but H261 is directed towards the E366 residues in the Ub-bound and inhibitor-bound USP28 structures. The proteins are shown in cartoon representation. The side chain and inhibitors are shown as sticks and colored according to the legend in the figure.

Gel-based ubiquitin hydrolysis assays with *in vitro* generated polyubiquitin substrates (K48-linked di-ubiquitin and K63-linked tetra-ubiquitin) further confirmed the compound binding mode (please see Section 3.2.2.2). However, determination of the equilibrium dissociation constant (K_d) and stoichiometry using MST and ITC were inconclusive as they require further optimization of experimental conditions. Estimating the association (K_{on}) and dissociation constants (K_{off}) for the downstream pharmacokinetics and pharmacodynamic investigations would also be crucial. Surface plasmon resonance (SPR) could be utilized to obtain the binding and kinetic data in addition to biolayer interferometry (BLI). Although both are label-free techniques, SPR provides the advantage by enabling the measurement of real-time inhibitor-binding affinities and kinetics using relatively small amounts of the protein in a native or native-like environment (Olaru et al., 2015).

4.4 The inhibitors do not disrupt USP25 tetramerization

The UCID-tip in USP25 is responsible for the tetrameric and inactive nature of the protein. Removal of the UCID-tip leads to a dimeric entity that is ~6-fold more active than the tetramer (Sauer et al., 2019). The residual activity of tetrameric USP25cat, despite the blocked Ub S1-site by the UCID-tip, was presumed to be due to the partially degraded tetramer obtained after protein purification leading to residual dimer concentrations. (Sauer et al., 2019; Klemm, 2020). As mentioned earlier, a difference between the oligomeric states was also observed in proteins purified from various constructs of the USP25cat domain (B. Liu et al., 2018; Gersch et al., 2019). Furthermore, Gersch et al. also showed that endogenous levels of the active, dimeric USP25cat (obtained upon mutation of the UCID-tip) were higher than the inactive tetrameric protein, indicating a constant cycle of activation within the cells (Gersch et al., 2019). However, it was also shown that Ubiquitin does not affect the oligomeric status and the activation of the protein (Sauer et al., 2019).

As described in Section 4.1, the inhibitors interact with USP28/25 in a region where the UCID-tip of USP25 binds. SEC-MALS analysis of the inactive, tetrameric USP25cat protein with the inhibitors did not significantly alter the oligomeric state of the protein (Section 3.2.2.4). These results indicate that the inhibitors do not influence the disruption of the tetramer and thereby activate the protein. Their inability to destabilize the USP25 tetramer presents an additional advantage towards improving/modifying the current inhibitor molecules to obtain USP28 specificity, while a large majority of the cellular USP25 pool remains in an inactive state.

5. OUTLOOK

The structural and biochemical studies of USP28/25 with their inhibitors reported in this thesis open unique opportunities for developing novel compounds with improved selectivity and potency. The structural insights into inhibitor binding and the mechanism of inhibition provide a framework for design strategies to obtain modified inhibitor compound(s) that would, for example, specifically abrogate USP28 activity while leaving the pool of inactive USP25 unaffected. Differences in the binding mode derived from docking calculations (Y. Wang et al., 2018) and the crystal structure of the USP28-Vismodegib complex underscore the need for high-resolution structural data for the precise characterization of the inhibitor binding sites to assist drug design efforts further.

Based on the structural information available now, two strategies could be adopted for the computational design of new inhibitors. The first approach would utilize the known inhibitor scaffolds and optimize them for improved potency. The Vismodegib scaffold, for example, offers a wide range of possibilities to introduce different substitutions at its aromatic rings. The scaffold also has the added advantage of comprising an arylamide structure that could be synthesized readily and the commercial availability of numerous compounds sharing a common sub-structure.

Most of the reported inhibitors of the DUBs take advantage of the structural plasticity of the blocking and/or switching loops and induce a conformational change not seen in the *apo* or Ub-bound structures (Schauer et al., 2020). A case in point is the 'open cleft' conformation in USP28 upon inhibitor binding, which was not observed in the previously reported structures. Many USPs vary in the length of the blocking and switching loops, and substrate specificity could be achieved by the differences found therein. For example, the switching loop (SL) in USP28 (K243-D255) is longer and more flexible compared to the SL in USP25 (K251-D262). This difference in length is due to a shortening of helix α4 in USP28 by half a turn compared to USP25 (Figure 5.1). In the USP28-*apo* structure, the SL appears to be disordered, which is reversed upon Ub-binding (see Figure 1.9c). As described earlier, the mode-of-inhibition of the USP28/25 inhibitors is to impede Ub-binding by inducing movement of the helix α5 and the associated conformational changes in BL2 and SL. Thus, extending the length of the inhibitor such that it is directed closer to the Ub-binding channel or the active site could be explored. Ideally, an extension of the inhibitor towards an area

where differences between USP28 and USP25 exist, like the switching loop, should be designed to achieve selectivity/specificity.

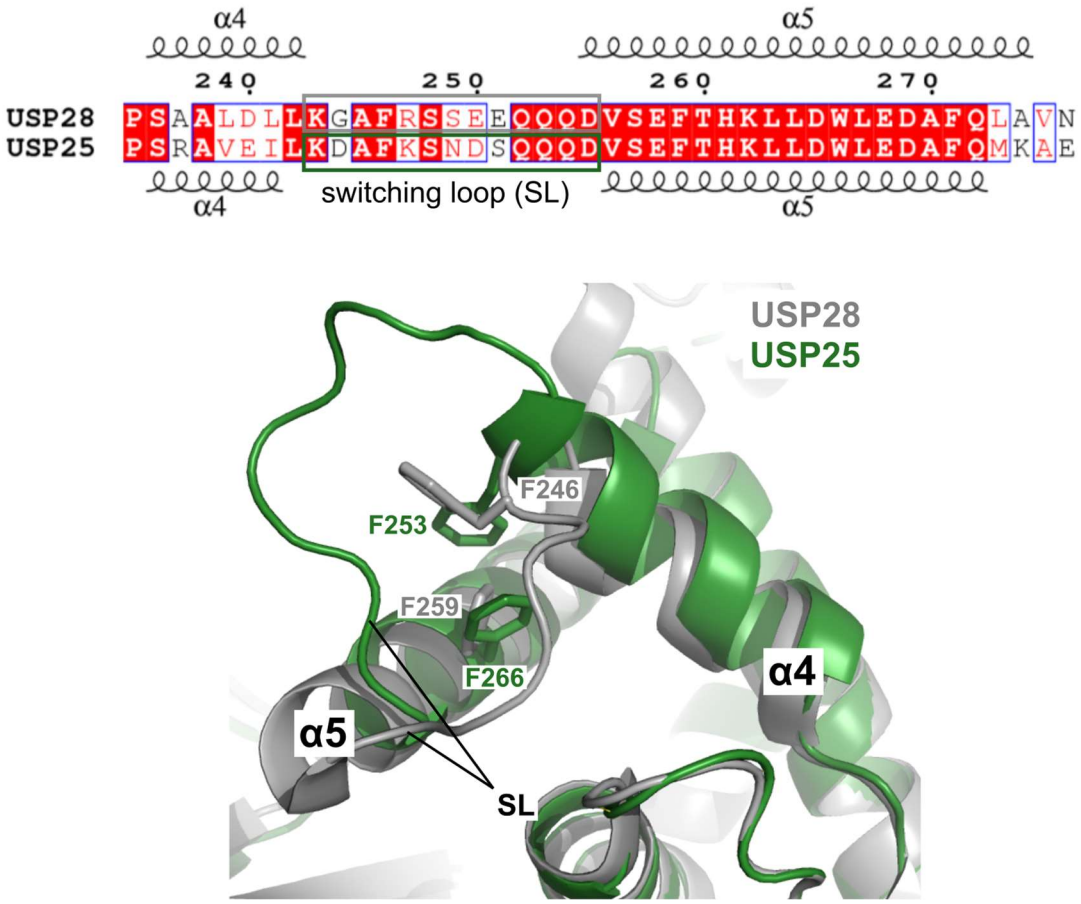

Figure 5.1: USP28 and USP25 switching loop. Sequence alignment of USP28 and USP25 switching loop (SL) sequences show differences in their amino acid composition. A close-up view illustrates that helix α4 in USP28 (gray) is shorter than the corresponding helix in USP25 (green). As a result, the SL is longer and more flexible in USP28, while in USP25, the shorter SL stabilizes the open conformation due to the π-stacking interactions between F253 and F259. This interaction is missing in USP28. These differences between the two proteins could be harnessed by designing a suitable compound that would be directed closer to the SL..

Another approach would be to merge the known scaffolds such that the entire stretch of the inhibitor binding cavity is covered. The USP28-inhibitor bound complex structures reveal that the position of the fluorinated ring of AZ1 overlaps with the chlorobenzene ring of Vismodegib (Figure 5.2a). A novel compound could be envisaged by merging the bromobenzene moiety of AZ1 and the sulfonyl-phenyl ring of Vismodegib, linked by a suitable aromatic linker (Figure 5.2b) such as a naphthalene moiety or benzimidazole thereby increasing the affinity substantially. The discovery of new compounds that exhibit higher inhibitory potency than AZ1 (Varca et al., 2021; Section 1.4.1.5) also offers multiple scaffolds

that could be potentially considered as building blocks for tuning selectivity. Another important aspect in achieving target selectivity is the ligand residence time. A compound with a longer residence time on one target can select kinetically over another, even if the affinity for both targets is comparable (Copeland et al., 2006). A nuanced route to modulating residence times could include introducing small, rational changes to the inhibitor compound, e.g., by the addition and/or removal of a group to (de)stabilize a specific interaction. This could be particularly crucial to attaining selectivity as energetic barriers determining binding kinetics often arise in non-conserved regions which are distal from the binding site (Pan et al., 2013).

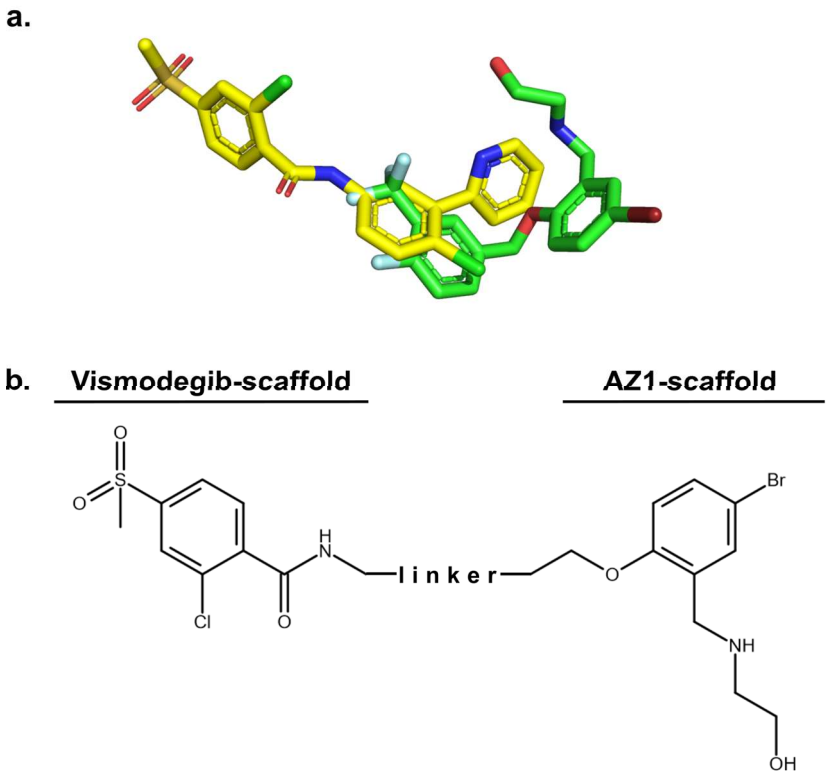

Figure 5.2. Design strategy for improving inhibitor potencies. (a) The chlorobenzene ring of Vismodegib (yellow) overlaps with the trifluoromethyl ring in AZ1 (green). The compounds as seen from the USP28-complex structures are shown here as sticks. **(b)** A possible strategy for attaining higher affinity and increased potency could be to design a merged compound comprising the bromophenyl ring scaffold of AZ1 and the sulfonyl-phenyl ring scaffold of Vismodegib using an aromatic linker.

Other promising strategies include proteolysis-targeting chimera (PROTAC) based approaches and the design of bivalent molecules. The PROTAC approach involves designing inhibitor scaffolds that would act as molecular glues that bind to the DUB interface and an E3 ligase to selectively degrade the DUB, e.g., USP28 or USP25, according to their

subcellular location. Bivalent molecules that simultaneously bind two regions of a DUB were described as a yet-to-be-discovered class of DUB inhibitors (Lange et al., 2021; Section 1.4). These inhibitors would essentially tether the catalytic domain to an adjacent inhibitory domain and lock the protein in an inhibited conformation. An advantage of such a bivalent molecule would be that it invariably increases target specificity with compounds directed against non-catalytic regions. Such a development could be envisioned with respect to USP25, in which small compounds would stabilize two dimers to maintain the inhibited tetrameric complex. Recently, a DUB targeting-chimera (DUBTAC) based approach was used to develop a covalent inhibitor of the DUB OTUB1 for the treatment of cystic fibrosis (Henning et al., 2022; Willson, 2022). The authors demonstrate the use of a DUBTAC to stabilize and restore the function of an unstable mutant form of the chloride channel CFTR, the aberrant degradation of which is linked to cystic fibrosis pathogenicity. The authors developed a covalent, small-molecule recruiter for OTUB1 that interacts with a CFTR-targeting warhead, bringing them in close proximity and inducing deubiquitination and subsequent stabilization of CFTR.

Covalent modifiers targeting non-catalytic cysteine(s) offer a promising premise for attaining prolonged residence time and even irreversible binding. For example, the inhibitor-complex structures present the accessibility of a cysteine residue (Cys644) in USP28 (or Cys 651 in USP25) that could be harnessed for such an approach.

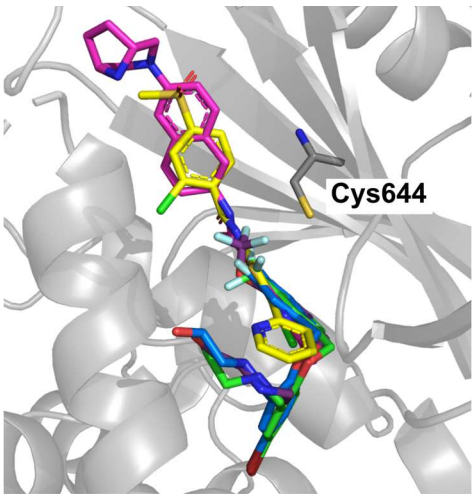

Figure 5.3: Targeting non-catalytic cysteines. The residue Cysteine 644 in USP28 which is present in the vicinity of the inhibitor molecules, could be targeted to develop a covalent inhibitor.

Molecular dynamics (MD) simulations could be used with a set of suitable candidates to investigate the stability of the interactions and also to substantiate the computational-binding site analysis. With the identification of new, high-resolution diffraction quality crystals of USP28cat, fragment-based library screening could also be used to facilitate *de novo* inhibitor development. Elucidation of the active USP25cat structures in its *apo*, Ub-bound and inhibitor-bound states would be essential to characterize inhibitor binding. Since initial crystallization trials of the active, dimeric USP25cat led to positive hits, further optimization efforts could result in high-resolution diffraction quality crystals. Moreover, MD simulations of the compounds bound to USP28 and USP25 may also reveal subtle differences in their dynamical aspects, which are not apparent from mere sequence or structural comparisons but may be more evident from ligands designed to achieve specificity. Currently reported *in vivo* USP25-inhibitor studies have supposedly utilized the less active mixtures of dimeric and tetrameric protein. Extending these studies with the active, dimeric USP25 catalytic domain proteins would offer insights into the full extent of the inhibitory potency and a comparable data platform for USP28 and USP25, which is critical in achieving specificity.

Concluding remarks

The first small-molecule inhibitors of DUBs emerged over 15 years ago. Since then, advances in the understanding of DUB biology and the development of high throughput screening technologies have led to key breakthroughs in discovering more potent and selective DUB inhibitory probes. Despite their many similarities, USP28 and USP25 perform very diverse biological roles. The current knowledge of small molecule binding opens more avenues to explore the nuances of their inhibition and the associated off-target effects. Developing more diverse inhibitor scaffolds with higher potencies and specificity would ultimately help in targeted, disease-specific therapeutics.

6. BIBLIOGRAPHY

Abdul Rehman, S. A., Kristariyanto, Y. A., Choi, S.-Y., Nkosi, P. J., Weidlich, S., Labib, K., Hofmann, K., & Kulathu, Y. (2016). MINDY-1 Is a Member of an Evolutionarily Conserved and Structurally Distinct New Family of Deubiquitinating Enzymes. *Molecular Cell*, *63*(1), 146–155. https://doi.org/10.1016/j.molcel.2016.05.009

Adams, P. D., Afonine, P. V., Bunkóczi, G., Chen, V. B., Davis, I. W., Echols, N., Headd, J. J., Hung, L.-W., Kapral, G. J., Grosse-Kunstleve, R. W., McCoy, A. J., Moriarty, N. W., Oeffner, R., Read, R. J., Richardson, D. C., Richardson, J. S., Terwilliger, T. C., & Zwart, P. H. (2010). PHENIX: a comprehensive Python-based system for macromolecular structure solution. *Acta Crystallographica. Section D, Biological Crystallography*, *66*(Pt 2), 213–221. https://doi.org/10.1107/S0907444909052925

Amerik, A. Y., & Hochstrasser, M. (2004). Mechanism and function of deubiquitinating enzymes. *Biochimica et Biophysica Acta*, *1695*(1–3), 189–207. https://doi.org/10.1016/j.bbamcr.2004.10.003

Avvakumov, G. V., Walker, J. R., Xue, S., Finerty, P. J. J., Mackenzie, F., Newman, E. M., & Dhe-Paganon, S. (2006). Amino-terminal dimerization, NRDP1-rhodanese interaction, and inhibited catalytic domain conformation of the ubiquitin-specific protease 8 (USP8). *The Journal of Biological Chemistry*, *281*(49), 38061–38070. https://doi.org/10.1074/jbc.M606704200

Bachovchin, D. A., Brown, S. J., Rosen, H., & Cravatt, B. F. (2009). Identification of selective inhibitors of uncharacterized enzymes by high-throughput screening with fluorescent activity-based probes. *Nature Biotechnology*, *27*(4), 387–394. https://doi.org/10.1038/nbt.1531

Basters, A., Geurink, P. P., Röcker, A., Witting, K. F., Tadayon, R., Hess, S., Semrau, M. S., Storici, P., Ovaa, H., Knobeloch, K.-P., & Fritz, G. (2017). Structural basis of the specificity of USP18 toward ISG15. *Nature Structural & Molecular Biology*, *24*(3), 270–278. https://doi.org/10.1038/nsmb.3371

Blanc, E., Roversi, P., Vonrhein, C., Flensburg, C., Lea, S. M., & Bricogne, G. (2004). Refinement of severely incomplete structures with maximum likelihood in BUSTER-TNT. *Acta Crystallographica. Section D, Biological Crystallography*, *60*(Pt 12 Pt 1), 2210–2221. https://doi.org/10.1107/S0907444904016427

Blount, J. R., Burr, A. A., Denuc, A., Marfany, G., & Todi, S. V. (2012). Ubiquitin-specific protease 25 functions in Endoplasmic Reticulum-associated degradation. *PloS One*, *7*(5), e36542. https://doi.org/10.1371/journal.pone.0036542

Bohgaki, M., Hakem, A., Halaby, M. J., Bohgaki, T., Li, Q., Bissey, P. A., Shloush, J., Kislinger, T., Sanchez, O., Sheng, Y., & Hakem, R. (2013). The E3 ligase PIRH2 polyubiquitylates CHK2 and regulates its turnover. *Cell Death & Differentiation*, *20*(6), 812–822. https://doi.org/10.1038/cdd.2013.7

Bosch-Comas, A., Lindsten, K., Gonzàlez-Duarte, R., Masucci, M. G., & Marfany, G. (2006). The ubiquitin-specific protease USP25 interacts with three sarcomeric proteins. *Cellular and Molecular Life Sciences*, *63*(6), 723–734. https://doi.org/10.1007/s00018-005-5533-1

Burkhart, R. A., Peng, Y., Norris, Z. A., Tholey, R. M., Talbott, V. A., Liang, Q., Ai, Y., Miller, K., Lal, S., Cozzitorto, J. A., Witkiewicz, A. K., Yeo, C. J., Gehrmann, M., Napper, A., Winter, J. M., Sawicki, J. A., Zhuang, Z., & Brody, J. R. (2013). Mitoxantrone targets human ubiquitin-specific peptidase 11 (USP11) and is a potent inhibitor of pancreatic cancer cell survival. *Molecular Cancer Research : MCR*, *11*(8), 901–911. https://doi.org/10.1158/1541-7786.MCR-12-0699

Callis, J. (2014). The ubiquitination machinery of the ubiquitin system. *The Arabidopsis Book*, *12*, e0174. https://doi.org/10.1199/tab.0174

Cao, C., Vasilatos, S. N., Bhargava, R., Fine, J. L., Oesterreich, S., Davidson, N. E., & Huang, Y. (2017). Functional interaction of histone deacetylase 5 (HDAC5) and lysine-specific demethylase 1 (LSD1) promotes breast cancer progression. *Oncogene*, *36*(1), 133–145. https://doi.org/10.1038/onc.2016.186

Chen, Z. J. (2005). Ubiquitin signalling in the NF-kappaB pathway. *Nature Cell Biology*, *7*(8), 758–765. https://doi.org/10.1038/ncb0805-758

Cheng, H., Li, X., Wang, C., Chen, Y., Li, S., Tan, J., Tan, B., & He, Y. (2019). Inhibition of tankyrase by a novel small molecule significantly attenuates prostate cancer cell proliferation. *Cancer Letters*, *443*, 80–90. https://doi.org/10.1016/j.canlet.2018.11.013

Cholay, M., Reverdy, C., Benarous, R., Colland, F., & Daviet, L. (2010). Functional interaction between the ubiquitin-specific protease 25 and the SYK tyrosine kinase. *Experimental Cell Research*, *316*(4), 667–675. https://doi.org/10.1016/j.yexcr.2009.10.023

Ciechanover, A. (2003). The ubiquitin proteolytic system and pathogenesis of human diseases: A novel platform for mechanism-based drug targeting. *Biochemical Society Transactions*, *31*(2), 474–481. https://doi.org/10.1042/bst0310474

Ciechanover, A. (2015). The unravelling of the ubiquitin system. *Nature Reviews Molecular Cell Biology*, *16*(5), 322–324. https://doi.org/10.1038/nrm3982

Ciechanover, A., & Schwartz, A. L. (2004). The ubiquitin system: Pathogenesis of human diseases and drug targeting. *Biochimica et Biophysica Acta*, *1695*(1–3), 3–17. https://doi.org/10.1016/j.bbamcr.2004.09.018

Clague, M. J., Urbé, S., & Komander, D. (2019). Breaking the chains: Deubiquitylating enzyme specificity begets function. *Nature Reviews Molecular Cell Biology*, *20*(6), 338–352. https://doi.org/10.1038/s41580-019-0099-1

Copeland, R. A., Pompliano, D. L., & Meek, T. D. (2006). Drug-target residence time and its implications for lead optimization. *Nature Reviews. Drug Discovery*, *5*(9), 730–739. https://doi.org/10.1038/nrd2082

Cravatt, B. F., Wright, A. T., & Kozarich, J. W. (2008). Activity-based protein profiling: From enzyme chemistry to proteomic chemistry. *Annual Review of Biochemistry*, *77*, 383–414. https://doi.org/10.1146/annurev.biochem.75.101304.124125

Cremona, C. A., Sancho, R., Diefenbacher, M. E., & Behrens, A. (2016). Fbw7 and its counteracting forces in stem cells and cancer: Oncoproteins in the balance. *Seminars in Cancer Biology*, *36*, 52–61. https://doi.org/10.1016/j.semcancer.2015.09.006

Das, T., Shin, S. C., Song, E. J., & Kim, E. E. (2020). Regulation of Deubiquitinating Enzymes by Post-Translational Modifications. *International Journal of Molecular Sciences*, *21*(11), 4028. https://doi.org/10.3390/ijms21114028

Deng, S., Zhou, H., Xiong, R., Lu, Y., Yan, D., Xing, T., Dong, L., Tang, E., & Yang, H. (2007). Over-expression of genes and proteins of ubiquitin specific peptidases (USPs) and proteasome subunits (PSs) in breast cancer tissue observed by the methods of RFDD-PCR and proteomics. *Breast Cancer Res Treat*, 10.

Denuc, A., & Bosch-Comas, A. (2009). The UBA-UIM Domains of the USP25 Regulate the Enzyme Ubiquitination State and Modulate Substrate Recognition. *PLoS ONE*, *4*(5), 13.

Diefenbacher, M. E., Chakraborty, A., Blake, S. M., Mitter, R., Popov, N., Eilers, M., & Behrens, A. (2015). Usp28 Counteracts Fbw7 in Intestinal Homeostasis and Cancer. *Cancer Research*, *75*(7), 1181–1186. https://doi.org/10.1158/0008-5472.CAN-14-1726

Diefenbacher, M. E., Popov, N., Blake, S. M., Schülein-Völk, C., Nye, E., Spencer-Dene, B., Jaenicke, L. A., Eilers, M., & Behrens, A. (2014). The deubiquitinase USP28 controls intestinal homeostasis and promotes colorectal cancer. *Journal of Clinical Investigation*, *124*(8), 3407–3418. https://doi.org/10.1172/JCI73733

Dlugosz, A., Agrawal, S., & Kirkpatrick, P. (2012). Vismodegib. *Nature Reviews Drug Discovery*, *11*(6), 437–438. https://doi.org/10.1038/nrd3753

Doran, E., Keator, D., Head, E., Phelan, M. J., Kim, R., Totoiu, M., Barrio, J. R., Small, G. W., Potkin, S. G., & Lott, I. T. (2017). Down Syndrome, Partial Trisomy 21, and Absence of Alzheimer's Disease: The Role of APP. *Journal of Alzheimer's Disease : JAD*, *56*(2), 459–470. https://doi.org/10.3233/JAD-160836

Dove, K. K., & Klevit, R. E. (2017). RING-Between-RING E3 Ligases: Emerging Themes amid the Variations. *Journal of Molecular Biology*, *429*(22), 3363–3375. PubMed. https://doi.org/10.1016/j.jmb.2017.08.008

Emsley, P., Lohkamp, B., Scott, W. G., & Cowtan, K. (2010). Features and development of Coot. *Acta Crystallographica. Section D, Biological Crystallography*, *66*(Pt 4), 486–501. https://doi.org/10.1107/S0907444910007493

Ernst, A., Avvakumov, G., Tong, J., Fan, Y., Zhao, Y., Alberts, P., Persaud, A., Walker, J. R., Neculai, A.-M., Neculai, D., Vorobyov, A., Garg, P., Beatty, L., Chan, P.-K., Juang, Y.-C., Landry, M.-C., Yeh, C., Zeqiraj, E., Karamboulas, K., … Sidhu, S. S. (2013). A strategy for modulation of enzymes in the ubiquitin system. *Science (New York, N.Y.)*, *339*(6119), 590–595. https://doi.org/10.1126/science.1230161

Evans, P. R., & Murshudov, G. N. (2013). How good are my data and what is the resolution? *Acta Crystallographica. Section D, Biological Crystallography*, *69*(Pt 7), 1204–1214. PubMed. https://doi.org/10.1107/S0907444913000061

Faesen, A. C., Luna-Vargas, M. P. A., Geurink, P. P., Clerici, M., Merkx, R., van Dijk, W. J., Hameed, D. S., El Oualid, F., Ovaa, H., & Sixma, T. K. (2011). The Differential Modulation of USP Activity by Internal Regulatory Domains, Interactors and Eight Ubiquitin Chain Types. *Chemistry & Biology*, *18*(12), 1550–1561. https://doi.org/10.1016/j.chembiol.2011.10.017

Fang, D., & Lu, G. (2020). Expression and role of nuclear receptor-interacting protein 1 (NRIP1) in stomach adenocarcinoma. *Annals of Translational Medicine*, *8*(20), 1293. https://doi.org/10.21037/atm-20-6197

Fang, S., & Weissman, A. M. (2004). A field guide to ubiquitylation. *Cellular and Molecular Life Sciences : CMLS*, *61*(13), 1546–1561. https://doi.org/10.1007/s00018-004-4129-5

Flügel, D., Görlach, A., & Kietzmann, T. (2012). GSK-3β regulates cell growth, migration, and angiogenesis via Fbw7 and USP28-dependent degradation of HIF-1α. *Blood*, *119*(5), 1292–1301. https://doi.org/10.1182/blood-2011-08-375014

Fujimoto, A., Totoki, Y., Abe, T., Boroevich, K. A., Hosoda, F., Nguyen, H. H., Aoki, M., Hosono, N., Kubo, M., Miya, F., Arai, Y., Takahashi, H., Shirakihara, T., Nagasaki, M., Shibuya, T., Nakano, K., Watanabe-Makino, K., Tanaka, H., Nakamura, H., … Nakagawa, H. (2012). Whole-genome sequencing of liver cancers identifies etiological influences on mutation patterns and recurrent mutations in chromatin regulators. *Nature Genetics*, *44*(7), 760–764. https://doi.org/10.1038/ng.2291

Galmozzi, A., Dominguez, E., Cravatt, B. F., & Saez, E. (2014). Application of Activity-Based Protein Profiling to Study Enzyme Function in Adipocytes. In *Methods in Enzymology* (Vol. 538, pp. 151–169). Elsevier. https://doi.org/10.1016/B978-0-12-800280-3.00009-8

Gasteiger, E., Hoogland, C., Gattiker, A., Duvaud, S., Wilkins, M. R., Appel, R. D., & Bairoch, A. (2005). Protein Identification and Analysis Tools on the ExPASy Server. In J. M. Walker (Ed.), *The Proteomics Protocols Handbook* (pp. 571–607). Humana Press. https://doi.org/10.1385/1-59259-890-0:571

Gavory, G., O'Dowd, C. R., Helm, M. D., Flasz, J., Arkoudis, E., Dossang, A., Hughes, C., Cassidy, E., McClelland, K., Odrzywol, E., Page, N., Barker, O., Miel, H., & Harrison, T. (2018). Discovery and characterization of highly potent and selective allosteric USP7 inhibitors. *Nature Chemical Biology*, *14*(2), 118–125. https://doi.org/10.1038/nchembio.2528

Gersch, M., Wagstaff, J. L., Toms, A. V., Graves, B., Freund, S. M. V., & Komander, D. (2019). Distinct USP25 and USP28 Oligomerization States Regulate Deubiquitinating Activity. *Molecular Cell*, *74*(3), 436-451.e7. https://doi.org/10.1016/j.molcel.2019.02.030

Goldberg, A. L. (2007). Functions of the proteasome: From protein degradation and immune surveillance to cancer therapy. *Biochemical Society Transactions*, *35*(Pt 1), 12–17. https://doi.org/10.1042/BST0350012

Haq, S., & Ramakrishna, S. (2017). Deubiquitylation of deubiquitylases. *Open Biology*, *7*(6), 170016. https://doi.org/10.1098/rsob.170016

Harrigan, J. A., Jacq, X., Martin, N. M., & Jackson, S. P. (2018). Deubiquitylating enzymes and drug discovery: Emerging opportunities. *Nature Reviews Drug Discovery*, *17*(1), 57–78. https://doi.org/10.1038/nrd.2017.152

Heal, W. P., Dang, T. H. T., & Tate, E. W. (2011). Activity-based probes: Discovering new biology and new drug targets. *Chemical Society Reviews*, *40*(1), 246–257. https://doi.org/10.1039/c0cs00004c

Henning, N. J., Boike, L., Spradlin, J. N., Ward, C. C., Liu, G., Zhang, E., Belcher, B. P., Brittain, S. M., Hesse, M. J., Dovala, D., McGregor, L. M., Valdez Misiolek, R., Plasschaert, L. W., Rowlands, D. J., Wang, F., Frank, A. O., Fuller, D., Estes, A. R., Randal, K. L., … Nomura, D. K. (2022). Deubiquitinase-targeting chimeras for targeted protein stabilization. *Nature Chemical Biology*, *18*(4), 412–421. https://doi.org/10.1038/s41589-022-00971-2

Hershko, A., & Ciechanover, A. (1998). The ubiquitin system. *Annual Review of Biochemistry*, *67*, 425–479. https://doi.org/10.1146/annurev.biochem.67.1.425

Hicke, L. (2001). Protein regulation by monoubiquitin. *Nature Reviews. Molecular Cell Biology*, *2*(3), 195–201. https://doi.org/10.1038/35056583

Hochstrasser, M. (1996). Ubiquitin-dependent protein degradation. *Annual Review of Genetics*, *30*, 405–439. https://doi.org/10.1146/annurev.genet.30.1.405

Hu, M., Li, P., Li, M., Li, W., Yao, T., Wu, J.-W., Gu, W., Cohen, R. E., & Shi, Y. (2002). Crystal structure of a UBP-family deubiquitinating enzyme in isolation and in complex with ubiquitin aldehyde. *Cell*, *111*(7), 1041–1054. https://doi.org/10.1016/s0092-8674(02)01199-6

Hu, M., Li, P., Song, L., Jeffrey, P. D., Chenova, T. A., Wilkinson, K. D., Cohen, R. E., & Shi, Y. (2005). Structure and mechanisms of the proteasome-associated deubiquitinating enzyme USP14. *The EMBO Journal*, *24*(21), 3747–3756. https://doi.org/10.1038/sj.emboj.7600832

Ito, F., Yoshimoto, C., Yamada, Y., Sudo, T., & Kobayashi, H. (2018). The HNF-1β-USP28-Claspin pathway upregulates DNA damage-induced Chk1 activation in ovarian clear cell carcinoma. *Oncotarget*, *9*(25), 17512–17522. https://doi.org/10.18632/oncotarget.24776

Iwai, K., & Tokunaga, F. (2009). Linear polyubiquitination: A new regulator of NF-kappaB activation. *EMBO Reports*, *10*(7), 706–713. https://doi.org/10.1038/embor.2009.144

Jung, E. S., Hong, H., Kim, C., & Mook-Jung, I. (2015). Acute ER stress regulates amyloid precursor protein processing through ubiquitin-dependent degradation. *Scientific Reports*, *5*, 8805. https://doi.org/10.1038/srep08805

Kabsch, W. (2010). XDS. *Acta Crystallographica. Section D, Biological Crystallography*, *66*(Pt 2), 125–132. https://doi.org/10.1107/S0907444909047337

Kargbo, R. B. (2017). Ubiquitin-Specific Inhibitors for the Treatment of Cancers, Autoimmune, and Infectious Diseases. *ACS Medicinal Chemistry Letters*, *8*(12), 1211–1212. PubMed. https://doi.org/10.1021/acsmedchemlett.7b00449

Kategaya, L., Di Lello, P., Rougé, L., Pastor, R., Clark, K. R., Drummond, J., Kleinheinz, T., Lin, E., Upton, J.-P., Prakash, S., Heideker, J., McCleland, M., Ritorto, M. S., Alessi, D. R., Trost, M., Bainbridge, T. W., Kwok, M. C. M., Ma, T. P., Stiffler, Z., … Wertz, I. E. (2017). USP7 small-molecule inhibitors interfere with ubiquitin binding. *Nature*, *550*(7677), 534–538. https://doi.org/10.1038/nature24006

Kawaguchi, K., Uo, K., Tanaka, T., & Komada, M. (2017). Tandem UIMs confer Lys48 ubiquitin chain substrate preference to deubiquitinase USP25. *Scientific Reports*, *7*, 45037. https://doi.org/10.1038/srep45037

Kim, H. T., & Goldberg, A. L. (2017). The deubiquitinating enzyme Usp14 allosterically inhibits multiple proteasomal activities and ubiquitin-independent proteolysis. *The Journal of Biological Chemistry*, *292*(23), 9830–9839. https://doi.org/10.1074/jbc.M116.763128

Kim, H. T., & Goldberg, A. L. (2018). UBL domain of Usp14 and other proteins stimulates proteasome activities and protein degradation in cells. *Proceedings of the National Academy of Sciences of the United States of America*, *115*(50), E11642–E11650. https://doi.org/10.1073/pnas.1808731115

Kim, R. (2019). *Structural and Mechanistic Studies on Deubiquitinating Enzymes USP7 and USP40* [Erasmus University Rotterdam]. http://hdl.handle.net/1765/115598

Kim, S., Lee, D., Lee, J., Song, H., Kim, H.-J., & Kim, K.-T. (2015). Vaccinia-Related Kinase 2 Controls the Stability of the Eukaryotic Chaperonin TRiC/CCT by Inhibiting the Deubiquitinating Enzyme USP25. *Molecular and Cellular Biology*, *35*(10), 1754–1762. https://doi.org/10.1128/MCB.01325-14

Klemm, T. A. (2020). *Minor differences cause major effects: How differential oligomerization regulates the activities of USP25 and USP28* [Doctoralthesis, Universität Würzburg]. https://doi.org/10.25972/OPUS-19108

Knobel, P. A., Belotserkovskaya, R., Galanty, Y., Schmidt, C. K., Jackson, S. P., & Stracker, T. H. (2014). USP28 Is Recruited to Sites of DNA Damage by the Tandem BRCT Domains of 53BP1 but Plays a Minor Role in Double-Strand Break Metabolism. *Molecular and Cellular Biology*, *34*(11), 2062–2074. https://doi.org/10.1128/MCB.00197-14

Komander, D., Clague, M. J., & Urbé, S. (2009). Breaking the chains: Structure and function of the deubiquitinases. *Nature Reviews Molecular Cell Biology*, *10*(8), 550–563. https://doi.org/10.1038/nrm2731

Komander, D., Lord, C. J., Scheel, H., Swift, S., Hofmann, K., Ashworth, A., & Barford, D. (2008). The structure of the CYLD USP domain explains its specificity for Lys63-linked polyubiquitin and reveals a B box module. *Molecular Cell*, *29*(4), 451–464. https://doi.org/10.1016/j.molcel.2007.12.018

Komander, D., & Rape, M. (2012). The Ubiquitin Code. *Annual Review of Biochemistry*, *81*(1), 203–229. https://doi.org/10.1146/annurev-biochem-060310-170328

Kwasna, D., Abdul Rehman, S. A., Natarajan, J., Matthews, S., Madden, R., De Cesare, V., Weidlich, S., Virdee, S., Ahel, I., Gibbs-Seymour, I., & Kulathu, Y. (2018). Discovery and Characterization of ZUFSP/ZUP1, a Distinct Deubiquitinase Class Important for Genome Stability. *Molecular Cell*, *70*(1), 150-164.e6. https://doi.org/10.1016/j.molcel.2018.02.023

Lamoliatte, F., McManus, F. P., Maarifi, G., Chelbi-Alix, M. K., & Thibault, P. (2017). Uncovering the SUMOylation and ubiquitylation crosstalk in human cells using sequential peptide immunopurification. *Nature Communications*, *8*, 14109. https://doi.org/10.1038/ncomms14109

Lange, S. M., Armstrong, L. A., & Kulathu, Y. (2021). Deubiquitinases: From mechanisms to their inhibition by small molecules. *Molecular Cell*, S1097276521009473. https://doi.org/10.1016/j.molcel.2021.10.027

Li, J., Yakushi, T., Parlati, F., Mackinnon, A. L., Perez, C., Ma, Y., Carter, K. P., Colayco, S., Magnuson, G., Brown, B., Nguyen, K., Vasile, S., Suyama, E., Smith, L. H., Sergienko, E., Pinkerton, A. B., Chung, T. D. Y., Palmer, A. E., Pass, I., … Deshaies, R. J. (2017). Capzimin is a potent and specific inhibitor of proteasome isopeptidase Rpn11. *Nature Chemical Biology*, *13*(5), 486–493. https://doi.org/10.1038/nchembio.2326

Lin, D., Zhang, M., Zhang, M.-X., Ren, Y., Jin, J., Zhao, Q., Pan, Z., Wu, M., Shu, H.-B., Dong, C., & Zhong, B. (2015). Induction of USP25 by viral infection promotes innate antiviral responses by mediating the stabilization of TRAF3 and TRAF6. *Proceedings of the National Academy of Sciences of the United States of America*, *112*(36), 11324–11329. https://doi.org/10.1073/pnas.1509968112

Liu, B., Sureda-Gómez, M., Zhen, Y., Amador, V., & Reverter, D. (2018). A quaternary tetramer assembly inhibits the deubiquitinating activity of USP25. *Nature Communications*, *9*(1), 4973. https://doi.org/10.1038/s41467-018-07510-5

Liu, Z., Chen, M., Xu, X., Zhang, L., Pan, Y., & Chen, D. (2021). USP28 promotes aerobic glycolysis of colorectal cancer by increasing stability of FOXC1. *Acta Biochimica Polonica*, *68*(4), 633–639. https://doi.org/10.18388/abp.2020_5504

Liu, Z., Zhao, T., Li, Z., Sun, K., Fu, Y., Cheng, T., Guo, J., Yu, B., Shi, X., & Liu, H. (2020). Discovery of [1,2,3]triazolo[4,5-d]pyrimidine derivatives as highly potent, selective, and cellularly active USP28 inhibitors. *Acta Pharmaceutica Sinica B*, *10*(8), 1476–1491. https://doi.org/10.1016/j.apsb.2019.12.008

Mann, M. K., Franzoni, I., de Freitas, R. F., Tempel, W., Houliston, S., Smith, L., Vedadi, M., Arrowsmith, C. H., Harding, R. J., & Schapira, M. (2019). Discovery of Small Molecule Antagonists of the USP5 Zinc Finger Ubiquitin-Binding Domain. *Journal of Medicinal Chemistry*, *62*(22), 10144–10155. https://doi.org/10.1021/acs.jmedchem.9b00988

McCoy, A. J., Grosse-Kunstleve, R. W., Adams, P. D., Winn, M. D., Storoni, L. C., & Read, R. J. (2007). Phaser crystallographic software. *Journal of Applied Crystallography*, *40*(Pt 4), 658–674. https://doi.org/10.1107/S0021889807021206

Meanwell, N. A. (2018). Fluorine and Fluorinated Motifs in the Design and Application of Bioisosteres for Drug Design. *Journal of Medicinal Chemistry*, *61*(14), 5822–5880. https://doi.org/10.1021/acs.jmedchem.7b01788

Meulmeester, E., Kunze, M., Hsiao, H. H., Urlaub, H., & Melchior, F. (2008). Mechanism and Consequences for Paralog-Specific Sumoylation of Ubiquitin-Specific Protease 25. *Molecular Cell*, *30*(5), 610–619. https://doi.org/10.1016/j.molcel.2008.03.021

Mevissen, T. E. T., & Komander, D. (2017). Mechanisms of Deubiquitinase Specificity and Regulation. *Annual Review of Biochemistry*, *86*(1), 159–192. https://doi.org/10.1146/annurev-biochem-061516-044916

Mistry, H., Hsieh, G., Buhrlage, S. J., Huang, M., Park, E., Cuny, G. D., Galinsky, I., Stone, R. M., Gray, N. S., D'Andrea, A. D., & Parmar, K. (2013). Small-molecule inhibitors of USP1 target ID1 degradation in leukemic cells. *Molecular Cancer Therapeutics*, *12*(12), 2651–2662. https://doi.org/10.1158/1535-7163.MCT-13-0103-T

Mohapatra, A. (2020). Chapter 72—Software tools for toxicology and risk assessment. In P. Wexler (Ed.), *Information Resources in Toxicology (Fifth Edition)* (pp. 791–812). Academic Press. https://doi.org/10.1016/B978-0-12-813724-6.00072-4

Mohideen, F., & Lima, C. D. (2008). SUMO takes control of a ubiquitin-specific protease. *Molecular Cell*, *30*(5), 539–540. https://doi.org/10.1016/j.molcel.2008.05.010

Moon, S., Muniyappan, S., Lee, S.-B., & Lee, B.-H. (2021). Small-Molecule Inhibitors Targeting Proteasome-Associated Deubiquitinases. *International Journal of Molecular Sciences*, *22*(12), 6213. https://doi.org/10.3390/ijms22126213

Murshudov, G. N., Skubák, P., Lebedev, A. A., Pannu, N. S., Steiner, R. A., Nicholls, R. A., Winn, M. D., Long, F., & Vagin, A. A. (2011). REFMAC5 for the refinement of macromolecular crystal structures. *Acta Crystallographica. Section D, Biological Crystallography*, *67*(Pt 4), 355–367. https://doi.org/10.1107/S0907444911001314

Nelson, J.K., Thin, M.Z., Evan, T. *et al.* USP25 promotes pathological HIF-1-driven metabolic reprogramming and is a potential therapeutic target in pancreatic cancer. *Nat Commun* 13, 2070 (2022). https://doi.org/10.1038/s41467-022-29684-9.

Niño, C. A., Wollscheid, N., Giangreco, G., Maspero, E., & Polo, S. (2020). USP25 Regulates EGFR Fate by Modulating EGF-Induced Ubiquitylation Dynamics. *Biomolecules*, *10*(11). https://doi.org/10.3390/biom10111548

Notredame, C., Higgins, D. G., & Heringa, J. (2000). T-Coffee: A novel method for fast and accurate multiple sequence alignment. *Journal of Molecular Biology*, *302*(1), 205–217. https://doi.org/10.1006/jmbi.2000.4042

Olaru, A., Bala, C., Jaffrezic-Renault, N., & Aboul-Enein, H. Y. (2015). Surface plasmon resonance (SPR) biosensors in pharmaceutical analysis. *Critical Reviews in Analytical Chemistry*, *45*(2), 97–105. https://doi.org/10.1080/10408347.2014.881250

Pan, A. C., Borhani, D. W., Dror, R. O., & Shaw, D. E. (2013). Molecular determinants of drug–receptor binding kinetics. *Drug Discovery Today*, *18*(13–14), 667–673. https://doi.org/10.1016/j.drudis.2013.02.007

Park, C.-W., & Ryu, K.-Y. (2014). Cellular ubiquitin pool dynamics and homeostasis. *BMB Reports*, *47*(9), 475–482. https://doi.org/10.5483/bmbrep.2014.47.9.128

Pettersen, E. F., Goddard, T. D., Huang, C. C., Couch, G. S., Greenblatt, D. M., Meng, E. C., & Ferrin, T. E. (2004). UCSF Chimera?A visualization system for exploratory research and analysis. *Journal of Computational Chemistry*, *25*(13), 1605–1612. https://doi.org/10.1002/jcc.20084

Popov, N., Wanzel, M., Madiredjo, M., Zhang, D., Beijersbergen, R., Bernards, R., Moll, R., Elledge, S. J., & Eilers, M. (2007). The ubiquitin-specific protease USP28 is required for MYC stability. *Nature Cell Biology*, *9*(7), 765–774. https://doi.org/10.1038/ncb1601

Prieto-Garcia, C., Hartmann, O., Reissland, M., Braun, F., Fischer, T., Walz, S., Schülein-Völk, C., Eilers, U., Ade, C. P., Calzado, M. A., Orian, A., Maric, H. M., Münch, C., Rosenfeldt, M., Eilers, M., & Diefenbacher, M. E. (2020). Maintaining protein stability of ΔNp63 via USP 28 is required by squamous cancer cells. *EMBO Molecular Medicine*, *12*(4). https://doi.org/10.15252/emmm.201911101

Prieto-Garcia, C., Tomašković, I., Shah, V. J., Dikic, I., & Diefenbacher, M. (2021). USP28: Oncogene or Tumor Suppressor? A Unifying Paradigm for Squamous Cell Carcinoma. *Cells*, *10*(10), 2652. https://doi.org/10.3390/cells10102652

Qian, G., Hu, X., Li, G., Ding, Y., Zhu, L., Zheng, H., Li, M., Li, Z., Pan, J., Li, Y., Li, G., Yang, C., Liu, Y., Xie, Y., & Lv, H. (2018). Smurf1 restricts the antiviral function mediated by USP25 through promoting its ubiquitination and degradation. *Biochemical and Biophysical Research Communications*, *498*(3), 537–543. https://doi.org/10.1016/j.bbrc.2018.03.015

Quesada, V., Díaz-Perales, A., Gutiérrez-Fernández, A., Garabaya, C., Cal, S., & López-Otín, C. (2004). Cloning and enzymatic analysis of 22 novel human ubiquitin-specific proteases. *Biochemical and Biophysical Research Communications*, *314*(1), 54–62. https://doi.org/10.1016/j.bbrc.2003.12.050

Ritorto, M. S., Ewan, R., Perez-Oliva, A. B., Knebel, A., Buhrlage, S. J., Wightman, M., Kelly, S. M., Wood, N. T., Virdee, S., Gray, N. S., Morrice, N. A., Alessi, D. R., & Trost, M. (2014). Screening of DUB activity and specificity by MALDI-TOF mass spectrometry. *Nature Communications*, *5*, 4763. https://doi.org/10.1038/ncomms5763

Robert, X., & Gouet, P. (2014). Deciphering key features in protein structures with the new ENDscript server. *Nucleic Acids Research*, *42*(W1), W320–W324. https://doi.org/10.1093/nar/gku316

Rougé, L., Bainbridge, T. W., Kwok, M., Tong, R., Di Lello, P., Wertz, I. E., Maurer, T., Ernst, J. A., & Murray, J. (2016). Molecular Understanding of USP7 Substrate Recognition and C-Terminal Activation. *Structure*, *24*(8), 1335–1345. https://doi.org/10.1016/j.str.2016.05.020

Ruiz, E. J., Pinto-Fernandez, A., Turnbull, A. P., Lan, L., Charlton, T. M., Scott, H. C., Damianou, A., Vere, G., Riising, E. M., Da Costa, C., Krajewski, W. W., Guerin, D., Kearns, J. D., Ioannidis, S., Katz, M., McKinnon, C., O'Connell, J., Moncaut, N., Rosewell, I., … Behrens, A. (2021). USP28 deletion and small-molecule inhibition destabilizes c-MYC and elicits regression of squamous cell lung carcinoma. *ELife*, *10*, e71596. https://doi.org/10.7554/eLife.71596

Sarikas, A., Hartmann, T., & Pan, Z.-Q. (2011). The cullin protein family. *Genome Biology*, *12*(4), 220. https://doi.org/10.1186/gb-2011-12-4-220

Sauer, F., Klemm, T., Kollampally, R. B., Tessmer, I., Nair, R. K., Popov, N., & Kisker, C. (2019). Differential Oligomerization of the Deubiquitinases USP25 and USP28 Regulates Their Activities. *Molecular Cell*, *74*(3), 421-435.e10. https://doi.org/10.1016/j.molcel.2019.02.029

Schauer, N. J., Magin, R. S., Liu, X., Doherty, L. M., & Buhrlage, S. J. (2020). Advances in Discovering Deubiquitinating Enzyme (DUB) Inhibitors. *Journal of Medicinal Chemistry*, *63*(6), 2731–2750. https://doi.org/10.1021/acs.jmedchem.9b01138

Schrödinger, LLC. (2015). *The PyMOL Molecular Graphics System, Version 1.8*.

Schülein-Völk, C., Wolf, E., Zhu, J., Xu, W., Taranets, L., Hellmann, A., Jänicke, L. A., Diefenbacher, M. E., Behrens, A., Eilers, M., & Popov, N. (2014). Dual Regulation of Fbw7 Function and Oncogenic Transformation by Usp28. *Cell Reports*, *9*(3), 1099–1109. https://doi.org/10.1016/j.celrep.2014.09.057

Shibata, N., Ohoka, N., Tsuji, G., Demizu, Y., Miyawaza, K., Ui-Tei, K., Akiyama, T., & Naito, M. (2020). Deubiquitylase USP25 prevents degradation of BCR-ABL protein and ensures proliferation of Ph-positive leukemia cells. *Oncogene*, *39*(19), 3867–3878. https://doi.org/10.1038/s41388-020-1253-0

Terzic, J., Marinovic-Terzic, I., Ikeda, F., & Dikic, I. (2007). Ubiquitin signals in the NF-kappaB pathway. *Biochemical Society Transactions*, *35*(Pt 5), 942–945. https://doi.org/10.1042/BST0350942

Turnbull, A. P., Ioannidis, S., Krajewski, W. W., Pinto-Fernandez, A., Heride, C., Martin, A. C. L., Tonkin, L. M., Townsend, E. C., Buker, S. M., Lancia, D. R., Caravella, J. A., Toms, A. V., Charlton, T. M., Lahdenranta, J., Wilker, E., Follows, B. C., Evans, N. J., Stead, L., Alli, C., … Komander, D. (2017). Molecular basis of USP7 inhibition by selective small-molecule inhibitors. *Nature*, *550*(7677), 481–486. https://doi.org/10.1038/nature24451

Valero, R., Bayés, M., Francisca Sánchez-Font, M., González-Angulo, O., Gonzàlez-Duarte, R., & Marfany, G. (2001). Characterization of alternatively spliced products and tissue-specific isoforms of USP28 and USP25. *Genome Biology*, *2*(10), RESEARCH0043. https://doi.org/10.1186/gb-2001-2-10-research0043

Varca, A. C., Casalena, D., Chan, W. C., Hu, B., Magin, R. S., Roberts, R. M., Liu, X., Zhu, H., Seo, H.-S., Dhe-Paganon, S., Marto, J. A., Auld, D., & Buhrlage, S. J. (2021). Identification and validation of selective deubiquitinase inhibitors. *Cell Chemical Biology*, S2451945621002579. https://doi.org/10.1016/j.chembiol.2021.05.012

Wang, F., Wang, L., Wu, J., Sokirniy, I., Nguyen, P., Bregnard, T., Weinstock, J., Mattern, M., Bezsonova, I., Hancock, W. W., & Kumar, S. (2017). Active site-targeted covalent irreversible inhibitors of USP7 impair the functions of Foxp3+ T-regulatory cells by promoting ubiquitination of Tip60. *PloS One*, *12*(12), e0189744. https://doi.org/10.1371/journal.pone.0189744

Wang, H., Meng, Q., Ding, Y., Xiong, M., Zhu, M., Yang, Y., Su, H., Gu, L., Xu, Y., Shi, L., Zhou, H., & Zhang, N. (2020). USP28 and USP25 are downregulated by Vismodegib in vitro and in colorectal cancer cell lines. *The FEBS Journal*, febs.15461. https://doi.org/10.1111/febs.15461

Wang, J., Dong, Y., Ma, H., Wu, L., Zhen, X., Tang, L., Jin, J., Han, S., Zhang, P., & Peng, J. (2021). The Deubiquitinase USP28 Stabilizes Expression of RecQ Family Helicases and Maintains

the Viability of Triple Negative Breast Cancer Cells. *Journal of Biological Chemistry*, 101443. https://doi.org/10.1016/j.jbc.2021.101443

Wang, X., Liu, Z., Zhang, L., Yang, Z., Chen, X., Luo, J., Zhou, Z., Mei, X., Yu, X., Shao, Z., Feng, Y., Fu, S., Zhang, Z., Wei, D., Jia, L., Ma, J., & Guo, X. (2018). Targeting deubiquitinase USP28 for cancer therapy. *Cell Death & Disease*, *9*(2), 186. https://doi.org/10.1038/s41419-017-0208-z

Wang, X.-M., Yang, C., Zhao, Y., Xu, Z.-G., Yang, W., Wang, P., Lin, D., Xiong, B., Fang, J.-Y., Dong, C., & Zhong, B. (2020). The deubiquitinase USP25 supports colonic inflammation and bacterial infection and promotes colorectal cancer. *Nature Cancer*, *1*(8), 811–825. https://doi.org/10.1038/s43018-020-0089-4

Wang, Y., Jiang, Y., Ding, S., Li, J., Song, N., Ren, Y., Hong, D., Wu, C., Li, B., Wang, F., He, W., Wang, J., & Mei, Z. (2018). Small molecule inhibitors reveal allosteric regulation of USP14 via steric blockade. *Cell Research*, *28*(12), 1186–1194. https://doi.org/10.1038/s41422-018-0091-x

Ward, S. J., Gratton, H. E., Indrayudha, P., Michavila, C., Mukhopadhyay, R., Maurer, S. K., Caulton, S. G., Emsley, J., & Dreveny, I. (2018). The structure of the deubiquitinase USP15 reveals a misaligned catalytic triad and an open ubiquitin-binding channel. *Journal of Biological Chemistry*, *293*(45), 17362–17374. https://doi.org/10.1074/jbc.RA118.003857

Wen, J., Bai, H., Chen, N., Zhang, W., Zhu, X., Li, P., & Gong, J. (2019). USP25 promotes endotoxin tolerance via suppressing K48-linked ubiquitination and degradation of TRAF3 in Kupffer cells. *Molecular Immunology*, *106*, 53–62. https://doi.org/10.1016/j.molimm.2018.12.017

Willson, J. (2022). DUBTACs for targeted protein stabilization. *Nature Reviews Drug Discovery*, *21*(4), 258–258. https://doi.org/10.1038/d41573-022-00039-9

Winn, M. D., Ballard, C. C., Cowtan, K. D., Dodson, E. J., Emsley, P., Evans, P. R., Keegan, R. M., Krissinel, E. B., Leslie, A. G. W., McCoy, A., McNicholas, S. J., Murshudov, G. N., Pannu, N. S., Potterton, E. A., Powell, H. R., Read, R. J., Vagin, A., & Wilson, K. S. (2011). Overview of the CCP4 suite and current developments. *Acta Crystallographica. Section D, Biological Crystallography*, *67*(Pt 4), 235–242. https://doi.org/10.1107/S0907444910045749

Wrigley, J. D., Gavory, G., Simpson, I., Preston, M., Plant, H., Bradley, J., Goeppert, A. U., Rozycka, E., Davies, G., Walsh, J., Valentine, A., McClelland, K., Odrzywol, K. E., Renshaw, J., Boros, J., Tart, J., Leach, L., Nowak, T., Ward, R. A., … Andrews, D. M. (2017). Identification and Characterization of Dual Inhibitors of the USP25/28 Deubiquitinating Enzyme Subfamily. *ACS Chemical Biology*, *12*(12), 3113–3125. https://doi.org/10.1021/acschembio.7b00334

Wu, Y., Wang, Y., Yang, X. H., Kang, T., Zhao, Y., Wang, C., Evers, B. M., & Zhou, B. P. (2013). The Deubiquitinase USP28 Stabilizes LSD1 and Confers Stem-Cell-like Traits to Breast Cancer Cells. *Cell Reports*, *5*(1), 224–236. https://doi.org/10.1016/j.celrep.2013.08.030

Xu, D., Liu, J., Fu, T., Shan, B., Qian, L., Pan, L., & Yuan, J. (2017). USP25 regulates Wnt signaling by controlling the stability of tankyrases. *Genes & Development*, *31*(10), 1024–1035. https://doi.org/10.1101/gad.300889.117

Xu, W., Taranets, L., & Popov, N. (2016). Regulating Fbw7 on the road to cancer. *Seminars in Cancer Biology*, *36*, 62–70. https://doi.org/10.1016/j.semcancer.2015.09.005

Yamada, H., Yanagisawa, K., Tokumaru, S., Taguchi, A., Nimura, Y., Osada, H., Nagino, M., & Takahashi, T. (2008). Detailed characterization of a homozygously deleted region corresponding to a candidate tumor suppressor locus at 21q11-21 in human lung cancer. *Genes, Chromosomes & Cancer*, *47*(9), 810–818. https://doi.org/10.1002/gcc.20582

Yang, Y., Shi, L., Ding, Y., Shi, Y., Hu, H.-Y., Wen, Y., & Zhang, N. (2017). Structural and Functional Investigations of the N-Terminal Ubiquitin Binding Region of Usp25. *Biophysical Journal*, *112*(10), 2099–2108. https://doi.org/10.1016/j.bpj.2017.04.022

Ye, Y., Scheel, H., Hofmann, K., & Komander, D. (2009). Dissection of USP catalytic domains reveals five common insertion points. *Molecular BioSystems*, *5*(12), 1797–1808. https://doi.org/10.1039/b907669g

Zhang, D., Zaugg, K., Mak, T. W., & Elledge, S. J. (2006). A Role for the Deubiquitinating Enzyme USP28 in Control of the DNA-Damage Response. *Cell*, *126*(3), 529–542. https://doi.org/10.1016/j.cell.2006.06.039

Zhen, Y., Knobel, P. A., Stracker, T. H., & Reverter, D. (2014). Regulation of USP28 deubiquitinating activity by SUMO conjugation. *The Journal of Biological Chemistry*, *289*(50), 34838–34850. https://doi.org/10.1074/jbc.M114.601849

Zheng, Q., Li, G., Wang, S., Zhou, Y., Liu, K., Gao, Y., Zhou, Y., Zheng, L., Zhu, L., Deng, Q., Wu, M., Di, A., Zhang, L., Zhao, Y., Zhang, H., Sun, H., Dong, C., Xu, H., & Wang, X. (2021). Trisomy 21–induced dysregulation of microglial homeostasis in Alzheimer's brains is mediated by USP25. *Science Advances*, *7*(1), eabe1340. https://doi.org/10.1126/sciadv.abe1340

Zhong, B., Liu, X., Wang, X., Chang, S. H., Liu, X., Wang, A., Reynolds, J. M., & Dong, C. (2012). Negative regulation of IL-17-mediated signaling and inflammation by the ubiquitin-specific protease USP25. *Nature Immunology*, *13*(11), 10.

Zhong, B., Liu, X., Wang, X., Liu, X., Li, H., Darnay, B. G., Lin, X., Sun, S.-C., & Dong, C. (2013). Ubiquitin-Specific Protease 25 Regulates TLR4-Dependent Innate Immune Responses Through Deubiquitination of the Adaptor Protein TRAF3. *Science Signaling*, *6*(275), ra35–ra35. https://doi.org/10.1126/scisignal.2003708

Zhu, W., Zheng, D., Wang, D., Yang, L., Zhao, C., & Huang, X. (2021). Emerging Roles of Ubiquitin-Specific Protease 25 in Diseases. *Frontiers in Cell and Developmental Biology*, *9*, 698751. https://doi.org/10.3389/fcell.2021.698751

Zhu, X., Ménard, R., & Sulea, T. (2007). High incidence of ubiquitin-like domains in human ubiquitin-specific proteases. *Proteins*, *69*(1), 1–7. https://doi.org/10.1002/prot.21546

7. APPENDIX

7.1 Abbreviations

Abbreviation	Name
53BP1	P53 binding protein 1
aa	Amino acid
ABPP	Activity-based probe profiling
AD	Alzheimer's disease
Amp	Ampicillin
APC/C	Anaphase-promoting complex/ cyclosome
APP	β-Amyloid precursor protein
APS	Ammonium persulfate
ATM	Ataxia-telangiectasia mutated
ATP	Adenosine-5'-triphosphate disodium salt
AUC	Analytical ultracentrifuge
BCR	Breakpoint cluster region
BESSY	Berliner Elektronenspeicherring-Gesellschaft für Synchrotronstrahlung
BL	Blocking loop
BLAST	Basic local alignment search tool
BSA	Bovine serum albumin
Cam	Chloramphenicol
Catalytic domain	cat
CCNE	Cyclin E1
CDC34/44	Ubiquitin-conjugating enzyme E2-34 kDa/44
Chk	Checkpoint kinase
CML	Chronic myeloid leukemia
CRL	cullin-RING E3 ligases
CSN5	COP9 signalosome complex subunit 5
Cul1	Cullin 1
CYLD	Cylindromatosis
dATP	2'-Deoxyadenosine 5'-triphosphate
dCTP	2'-Deoxycytidine 5'-triphosphate
DDR	DNA damage response
DESY	Deutsches Elektronen-Synchrotron
dGTP	2'-Deoxyguanosine 5'-triphosphate
DMSO	Dimethyl sulfoxide
DNA	Deoxyribonucleic acid
dRI	Differential refractive index

DSF	Differential scanning fluorimetry
DTT	Dithiothreitol
dTTP	2'-Deoxythymidine 5'-triphosphate
DUB	Deubiquitinase
DUBTAC	Deubiquitinase targeting chimera
E. coli	*Escherichia coli*
EDTA	Ethylenediaminetetraacetic acid
EGFR	Epidermal growth factor receptor
EMBL	European molecular biology laboratory
EMT	Epithelial-mesenchymal-transition
ER	Endoplasmic reticulum
ERAD	ER-associated degradation
ESRF	European synchrotron radiation facility
FAD	Familial Alzheimer's disease
FBXW7	F-box/WD repeat-containing protein 7
FDA	Food and Drug Administration (US)
FOXC1	Forkhead Box C1
FT	Forma Therapeutics
GSK-3β	Glycogen synthase kinase 3 beta
H5N1	Influenza A virus subtype H5N1
HA-tag	Haemagglutinin tag
H-bond	Hydrogen bond
HCC	Hepatocellular carcinoma
HCl	Hydrochloric acid
HDAC5	Histone deacetylase 5
HDX-MS	Hydrogen-deuterium exchange mass spectroscopy
HECT	Homologous to the E6-AP Carboxyl Terminus
HEPES	4-(2-hydroxyethyl)-1-piperazineethanesulfonic acid
HIF-1α	Hypoxia-inducible factor 1-alpha
IFN	Type I interferons
IL-17	Interleukin 17
IPTG	Isopropyl-β-D-thiogalactopyranoside
IRF3	Interferon regulatory factor 3
ITC	Isothermal titration calorimetry
JAMM/ MPN+	JAB1/ MPN/ MOV34
JNK1	c-Jun kinase 1
Kan	Kanamycin sulfate
LB	Lysogeny broth
LC-MS	Liquid chromatography–mass spectrometry

LPS	Lipopolysaccharide
LSCC	Laryngeal squamous cell carcinoma
LSD1	Lysine-specific demethylase 1
MALDI	Matrix-assisted laser desorption ionization time-of-flight
MDC1	Mediator of DNA damage checkpoint protein 1
$MgCl_2$	Magnesium chloride
$MgSO_4$	Magnesium sulfate
MINDY	MIU containing novel DUB family
MIU	Motif interacting with ubiquitin
MIX	Mitoxantrone
MJD	Machado Joseph Disease
MMS2	Ubiquitin-conjugating enzyme variant
MR	Molecular replacement
MTOR	Mammalian target of rapamycin
MyBPC1	Myosin binding protein C1
MYC	Avian myeloblastosis virus oncogene cellular homolog
Na_2HPO_4	Disodium hydrogen phosphate
NaCl	Sodium chloride
NaH_2PO_4	Sodium dihydrogen phosphate
NaOH	Sodium hydroxide
NF-κ B	Nuclear factor κ B
NH_4Cl	Ammonium chloride
NSCLC	Non-small cell lung cancer
OD	Optical density
OTU	Ovarian tumor protease
OTULIN	OTU deubiquitinase with Linear Linkage Specificity
PA	Propargylamine
PCR	Polymerase chain reaction
PDAC	Pancreatic ductal adenocarcinoma
PDB	Protein Data Bank
PEG	Polyethylene glycol
POI	Protein of interest
PROTAC	Proteolysis targeting chimera
PTCH1	Patched homologue 1
PTM	Posttranslational modifications
qRT-PCR	Quantitative real-time PCR
RBR	RING-between-RING
RING	Really Interesting New Gene
RMSD	Rout mean square deviation
RNA	Ribonucleic acid

RVZ	Rudolf Virchow Zentrum
S1	Subsite 1
SAR	Structure-activity relationships
SARS	Severe acute respiratory syndrome
SAXS	Small-angle X-ray scattering
SCC	Squamous cell carcinoma
SCF	Skp1/Cul1/F-box protein
SD	Superdex
SDM	Site-directed mutagenesis
SDS	Sodium dodecyl sulfate
SDS-PAGE	SDS polyacrylamide gel electrophoresis
SEC	Size exclusion chromatography
SEC-MALS	Size exclusion chromatography coupled to multi-angle light scattering
shRNA	Short hairpin RNA
SIM	SUMO interacting motif
SKP1	S-phase kinase-associated protein 1
SL	Switching loop
SLIC	Sequence and ligation independent cloning
SMO	Smoothened homolog
SMURF1	SMAD specific E3 ubiquitin-protein ligase 1
SPR	Surface plasmon resonance
STAT3	Signal transducer and activator of transcription 3
STD-NMR	Saturation transfer difference-Nuclear magnetic resonance
Strep	Streptomycin sulfate
SUMO	Small-ubiquitin-like modifier
SV-AUC	Sedimentation velocity analytical ultracentrifugation
SYK	Spleen Tyrosine Kinase
TB	Terrific Broth
TCEP	Tris-(2-carboxyethyl)-phosphine
TEMED	Tetramethylethylenediamine
TLR4	Toll-like receptor 4
TNBC	Triple-negative breast cancer
TNKS	Tankyrases
TRAF	Tumor necrosis factor receptor-associated factor
TRiC	Chaperon TCP-1 ring complex
Tris	Tris-(hydroxymethyl)-aminomethane
trx	Thioredoxin
Ub	Ubiquitin
UBA	Ubiquitin associated domain
Ub-AMC	Ubiquitin with 7-amino-4-methylcoumarin

UBB	Ubiquitin-B
UBC	Ubiquitin-conjugating enzyme
UBL	Ubiquitin-like
Ub-PA	Ubiquitin propargylamide
UBR	Ubiquitin binding region
Ub-Rho110	Ubiquitin-rhodamine110Gly
Ub-TAMRA	Ubiquitin tetramethylrhodamine
Ub-VME	Ubiquitin vinylmethylester
Ub-VS	Ubiquitin vinylmethyl sulfone
UCH	Ubiquitin C-terminal hydrolase
UCID	USP25/28 catalytic domain inserted domain
UCK1	Uridine-Cytidine Kinase 1
UFM1	Ubiquitin Fold Modifier 1
UIM	Ubiquitin interacting motif
USP	Ubiquitin specific protease
USP25m	USP25 muscle-specific isoform
VRK2	Vaccinia-related kinase 2
WT	Wild type
ZnF	Zinc finger
ZUFSP	Zinc finger with UFM1-specific peptidase domain protein

7.2 Expression constructs

List of all expression constructs used in this study-

Construct	**Range/Mutation**	**Vector**	**Tag**
USP28cat WT	149-703 and 149-707	pCDF-22	trx-6xHis-3C
USP28cat (Δtip)	149-458-SGSG-529-707 (Δtip: 459-528)	pCDF-22	trx-6xHis-3C
	149-458-SGSG-529-707 (Δtip: 459-528) H261A	pCDF-22	trx-6xHis-3C
	149-458-SGSG-529-707 (Δtip: 459-528) L264F	pCDF-22	trx-6xHis-3C
	149-458-SGSG-529-707 (Δtip: 459-528) D265S	pCDF-22	trx-6xHis-3C
	149-458-SGSG-529-707 (Δtip: 459-528) F292A	pCDF-22	trx-6xHis-3C
	149-458-SGSG-529-707 (Δtip: 459-528) Y293A	pCDF-22	trx-6xHis-3C
	149-458-SGSG-529-707 (Δtip: 459-528) Y293H	pCDF-22	trx-6xHis-3C
	149-458-SGSG-529-707 (Δtip: 459-528) Y293R	pCDF-22	trx-6xHis-3C
	149-458-SGSG-529-707 (Δtip: 459-528) Q315A	pCDF-22	trx-6xHis-3C
	149-458-SGSG-529-707 (Δtip: 459-528) Q315R	pCDF-22	trx-6xHis-3C
	149-458-SGSG-529-707 (Δtip: 459-528) E366A	pCDF-22	trx-6xHis-3C
	149-458-SGSG-529-707 (Δtip: 459-528) Y643A	pCDF-22	trx-6xHis-3C

USP28cat (ΔUCID)	149-399-GSGSGS-580-703 (ΔUCID: 400-579)	pCDF-22	trx-6xHis-3C
	149-399-GSGSGS-580-707 (ΔUCID: 400-579)	pCDF-22	trx-6xHis-3C
	149-399-GSGSGS-580-698 (ΔUCID: 400-579)	pCDF-22	trx-6xHis-3C
USP25cat WT	157-706	pCDF-14	6xHis-3C
USP25cat (Δtip)	157-464-GSGS-538-706 (Δtip: 465-537)	pCDF-14	6xHis-3C
	157-464-GSGS-538-706 (Δtip: 465-537) L271F	pCDF-14	6xHis-3C
	157-464-GSGS-538-706 (Δtip: 465-537) F299A	pCDF-14	6xHis-3C
	157-464-GSGS-538-706 (Δtip: 465-537) Y300A	pCDF-14	6xHis-3C
	157-464-GSGS-538-706 (Δtip: 465-537) Y300H	pCDF-14	6xHis-3C
	157-464-GSGS-538-706 (Δtip: 465-537) Y300R	pCDF-14	6xHis-3C
	157-464-GSGS-538-706 (Δtip: 465-537) Q322A	pCDF-14	6xHis-3C
	157-464-GSGS-538-706 (Δtip: 465-537) Q322R	pCDF-14	6xHis-3C
	157-464-GSGS-538-706 (Δtip: 465-537) E373A	pCDF-14	6xHis-3C
Ubiquitin	1-76	pET30a	-

7.3 Extinction coefficients

Protein	**Molecular weight (Da)**	**Extinction coefficient (M^{-1} cm^{-1})***	**Absorption at 280 nm (1 g/l)***
USP28cat WT (149-703)	64,450	94,770	1.470
USP28cat WT (149-707)	64,936	94,770	1.459
USP28cat (149-Δtip-703)	57,277	94,770	1.655
USP28cat (149-Δtip-707)	57,763	94,770	1.641
USP28cat (149-ΔUCID-703)	44,486	83,310	1.873
USP28cat (149-ΔUCID-707)	44,972	83,310	1.852
USP28cat (149-ΔUCID-698)	43,927	83,310	1.897
USP25cat WT (157-706)	63,833	73,800	1.156
USP25cat (157-Δtip-706)	56,757	73,800	1.300

* assuming all cysteine residues are reduced

7.4 Supplementary figures

7.4.1 Purification of full-length USP28 catalytic domain constructs

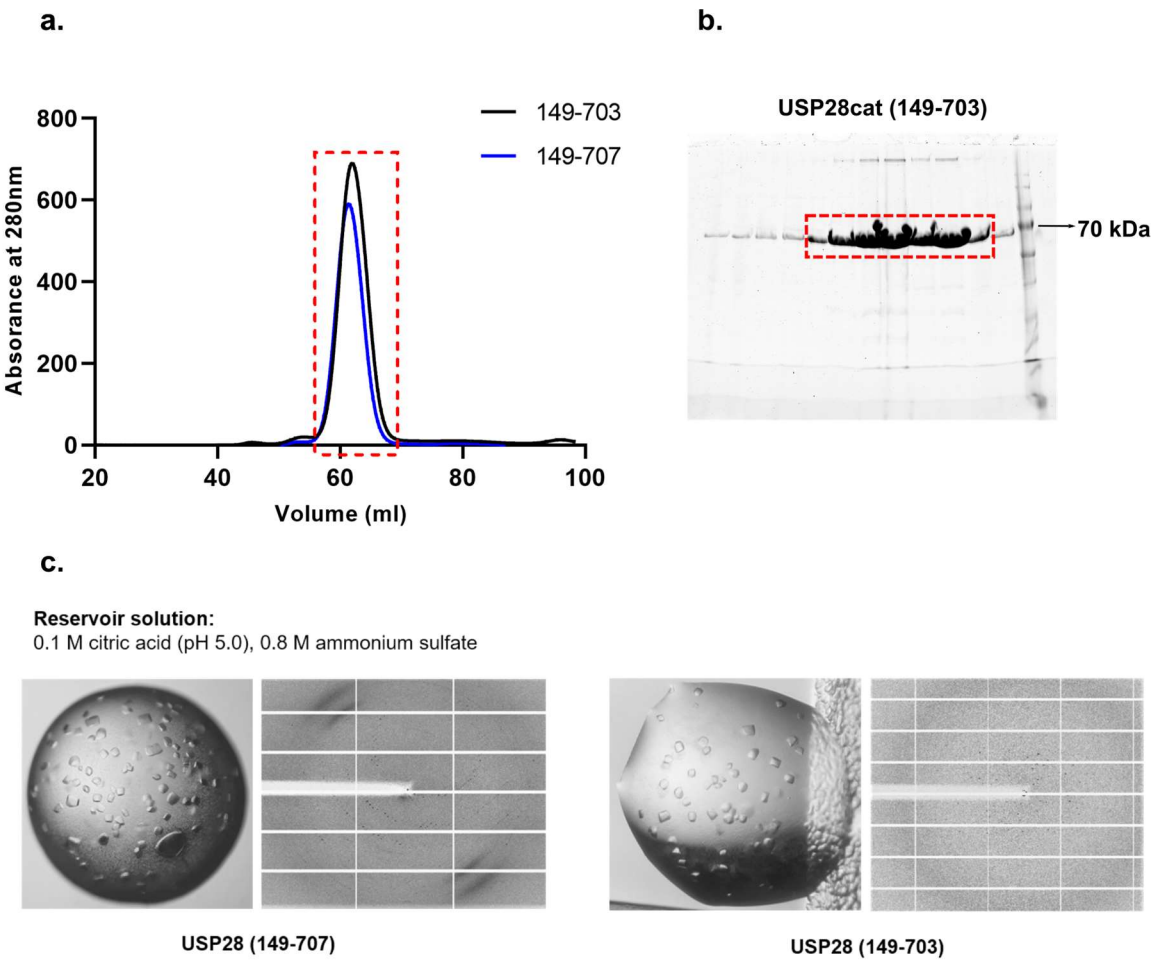

Figure 7.1: Purification of USP28cat full-length proteins. Elution fractions of USP28cat (149-703) and (149-707) constructs obtained from ion-exchange purifications were injected to a Superdex 200 16/60 column. **(a)** SEC profile for independent purifications depicted together. The peak fractions (indicated by the dotted red box) were analyzed by SDS-PAGE (**b**; representative gel for 149-703 construct), pooled and concentrated for subsequent experiments. Molecular weight marker at 70 kDa is indicated on the gel. **(c)** The proteins were crystallized in the reservoir solution as mentioned, but they did not diffract sufficiently. However, these crystals were later utilized for microseeding experiments as described in Section 3.1.1.

7.4.2 Purification of USP28cat (Δtip) variants

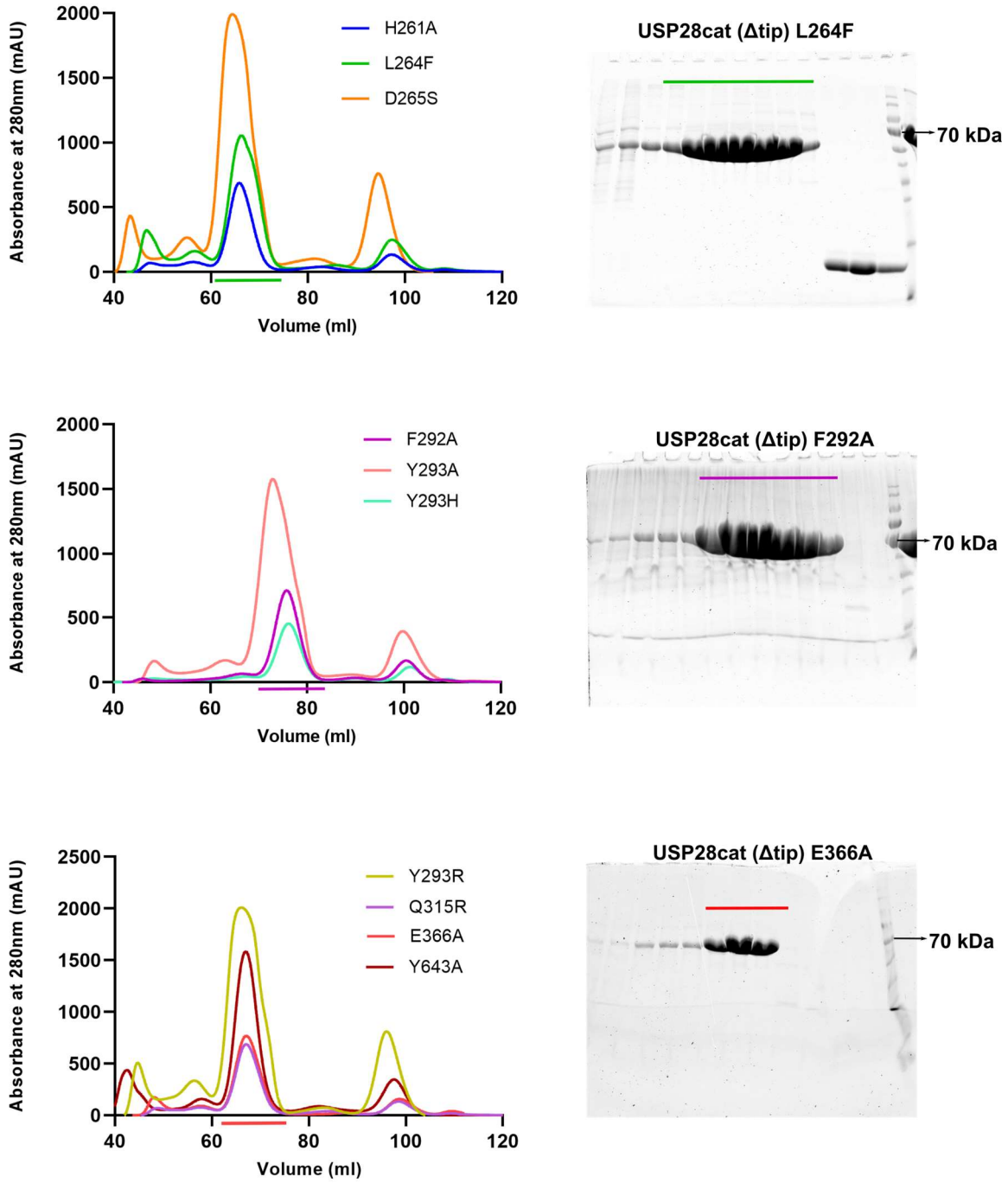

Figure 7.2: Purification of USP28cat (Δtip) variants. Elution fractions from affinity purifications were injected into a Superdex 200 16/60 column. SEC profiles (left) of all the USP28cat (Δtip) variants used in this study are shown in three groups. The elution fractions were analyzed by SDS-PAGE (right; shown here for one representative variant from each group). The colored lines represent the peak fractions that were pooled and concentrated for subsequent experiments. Molecular weight marker at 70 kDa is indicated on the gel.

7.4.3 Purification of USP25cat (Δtip) WT

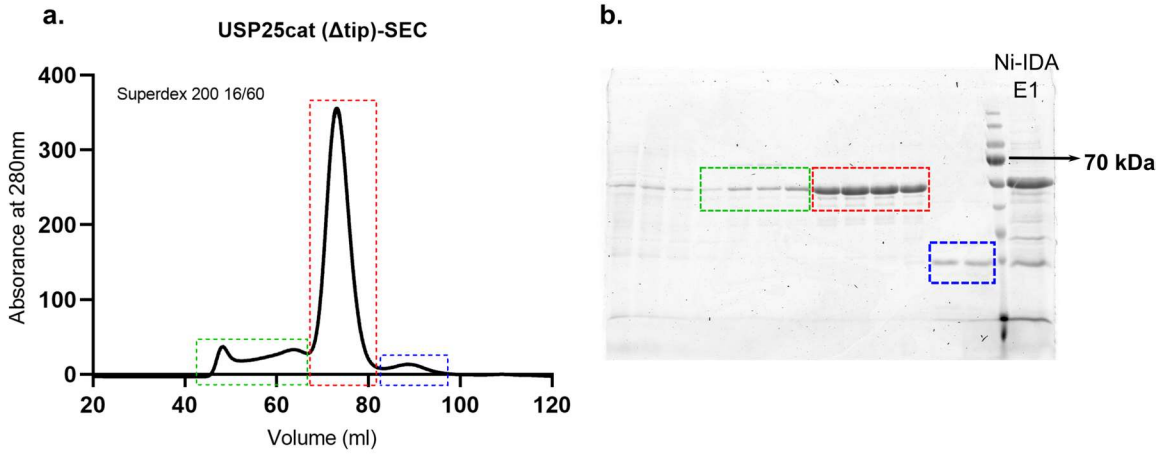

Figure 7.3: Purification of USP25cat (Δtip) WT. Elution fractions from affinity purifications were injected into a Superdex 200 16/60 column. Elution profile from SEC **(a)** and SDS-PAGE analysis **(b)** of the peak fractions are indicated by the colored boxes. The blue box shows the peak corresponding to the HRV3C-His tag, while the green box corresponds to aggregated protein. Fractions within the red box were pooled and concentrated for subsequent experiments. Molecular weight marker highlighted at 70 kDa is also shown. Elution fraction following affinity purification is also shown for reference (Ni-IDA E1).

7.4.4 Purification of USP25cat (Δtip) – Ub-PA complex

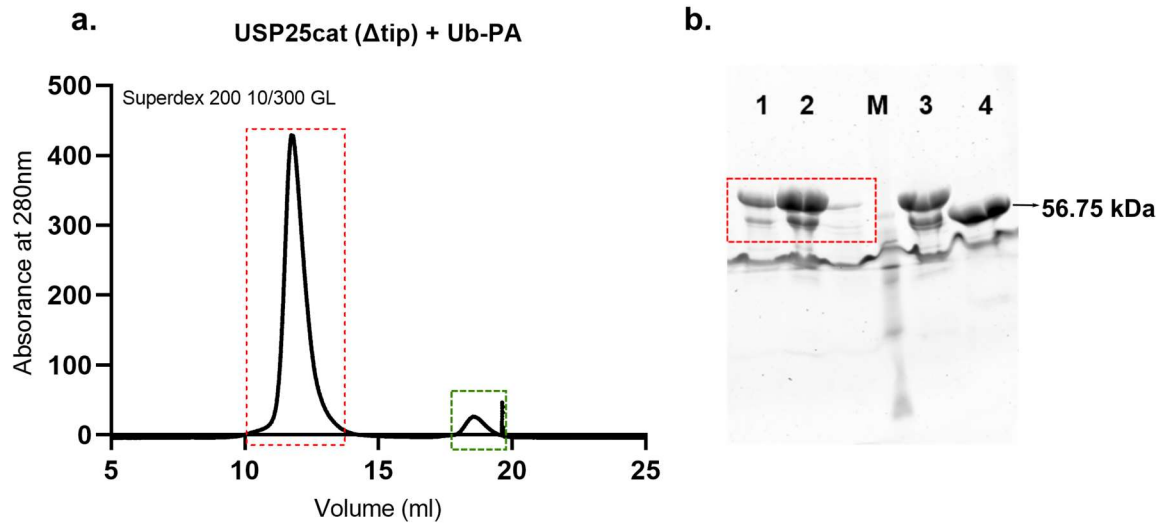

Figure 7.4: Purification of USP25cat (Δtip) – Ub-PA complex. USP25cat (Δtip) WT protein was incubated with a three-fold excess of Ub-PA. Following incubation, the mixture was injected into a Superdex 200 10/300 GL column to remove the excess, unbound Ub-PA **(a)**. The elution fractions were analyzed by SDS-PAGE **(b)**. Lanes 1 and 2 represent the peak fraction under the red box, as seen from the SEC profile. Lane 3 represents the incubated mixture before injection into the column, and lane 4 represents the USP25cat (Δtip)-only control (MW: 56.7 kDa). A shift in the molecular weight upon Ub-PA binding is seen in lane 3.

7.4.5 Purification of USP25cat (Δtip) variants

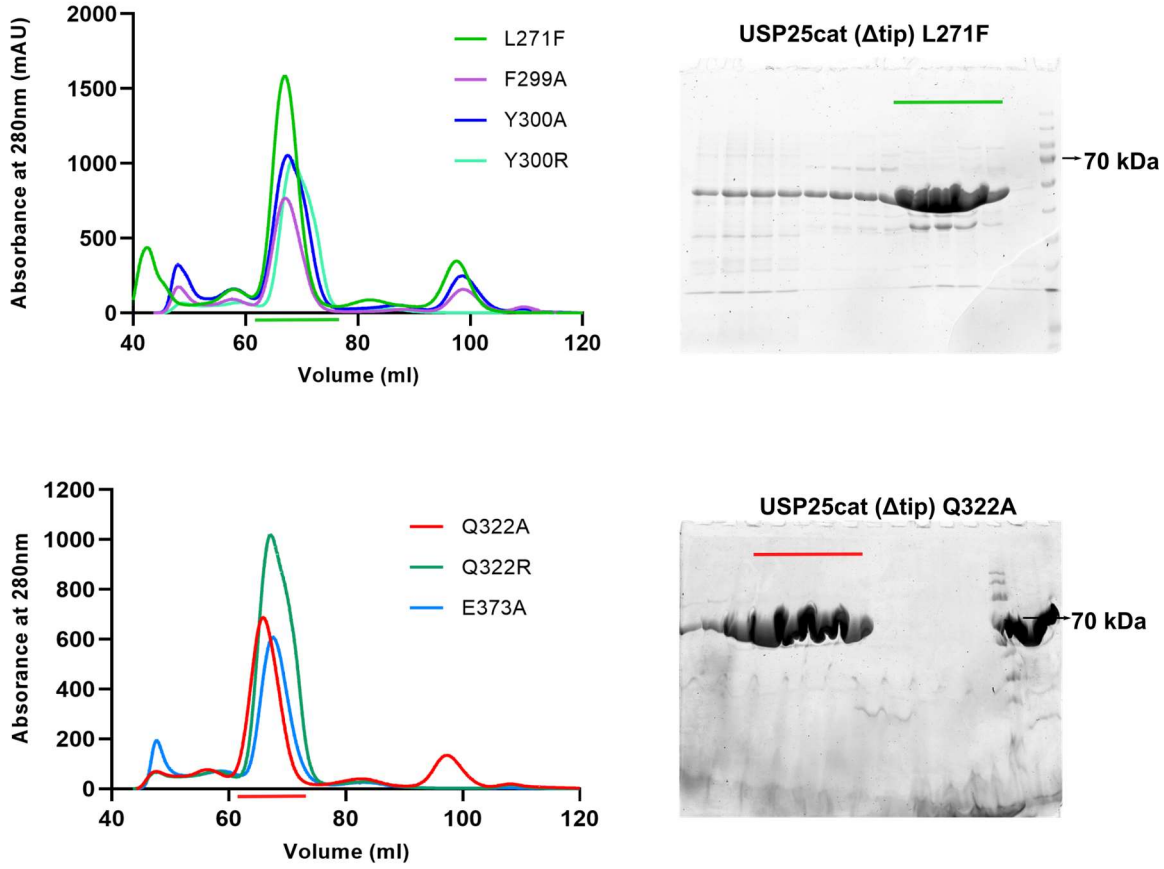

Figure 7.5: Purification of USP25cat (Δtip) variants. Elution fractions from affinity purifications were injected into a Superdex 200 16/60 column. SEC profiles of all the USP25cat (Δtip) variants used in this study are shown in two groups (left). The elution fractions were analyzed by SDS-PAGE (right; shown here for one representative variant from each group). The colored lines represent the peak fractions that were pooled and concentrated for subsequent experiments. Molecular weight marker at 70 kDa is indicated on the gel.

7.4.6 Electron density maps

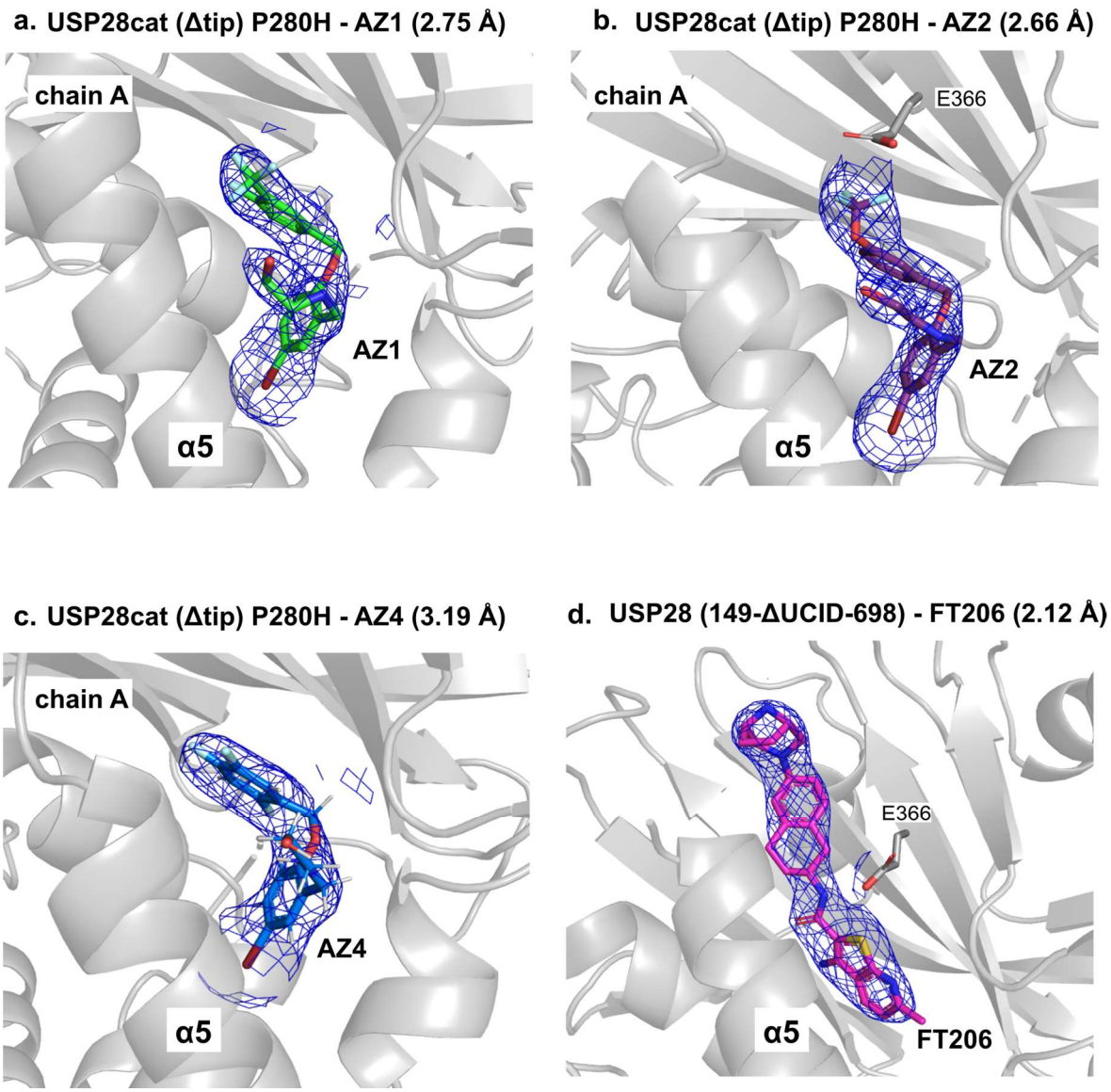

Figure 7.6: Electron density maps of the inhibitor compounds. The 2Fo-Fc electron density omit maps (blue) of the compounds **(a)** AZ1, **(b)** AZ2, **(c)** AZ4 in chain A of the USP28cat (Δtip) P280H-complex crystal structures and **(d)** FT206 in the USP28cat (ΔUCID)-complex crystal structure, contoured at 1.0σ level. The USP28 protein is shown in cartoon representation (gray).

7.4.7 USP28cat (ΔUCID) *apo*

Data collection and refinement statistics for USP28cat (149-ΔUCID-698) *apo* structure. Statistics for the highest resolution shell are shown in parentheses.

Data collection	
Beamline	ESRF ID 23-2
Wavelength (Å)	0.873
Resolution range (Å)	47.91 2.45 (2.55-2.45)
Space group	$H3_2$
Unit cell dimensions:	
a, b, c (Å)	106.63 106.63 327.67
α, β, γ (°)	90 90 120
Observed reflections	519,735 (60,001)
Unique reflections	26,861 (3008)
R_{merge}	0.17 (4.11)
R_{meas}	0.18 (4.22)
CC1/2	0.999 (0.369)
Mean $I/\sigma I$	13.7 (0.9)
Completeness (%):	
Spherical	100.0 (100.0)
Ellipsoidal	100.0 (100.0)
Wilson B-factor (Å^2)	76.60
Refinement	
Protein molecules/ASU	1
Reflections	26,861
R_{work}/R_{free} (%)	20.0/23.8
No. of atoms:	
Protein	2699
Water	110
Ligand/ion	9
Average B-factors (Å^2):	
Protein	82.82
Ligand/ion	84.43/85.76
Water	69.32
RMSD:	
Bond lengths (Å)	0.008
Bond angles (°)	0.93
Ramachandran statistics:	
Favored/allowed/outliers (%)	95.05/4.95/0.0

7.4.8 Ubiquitin purification and chain synthesis

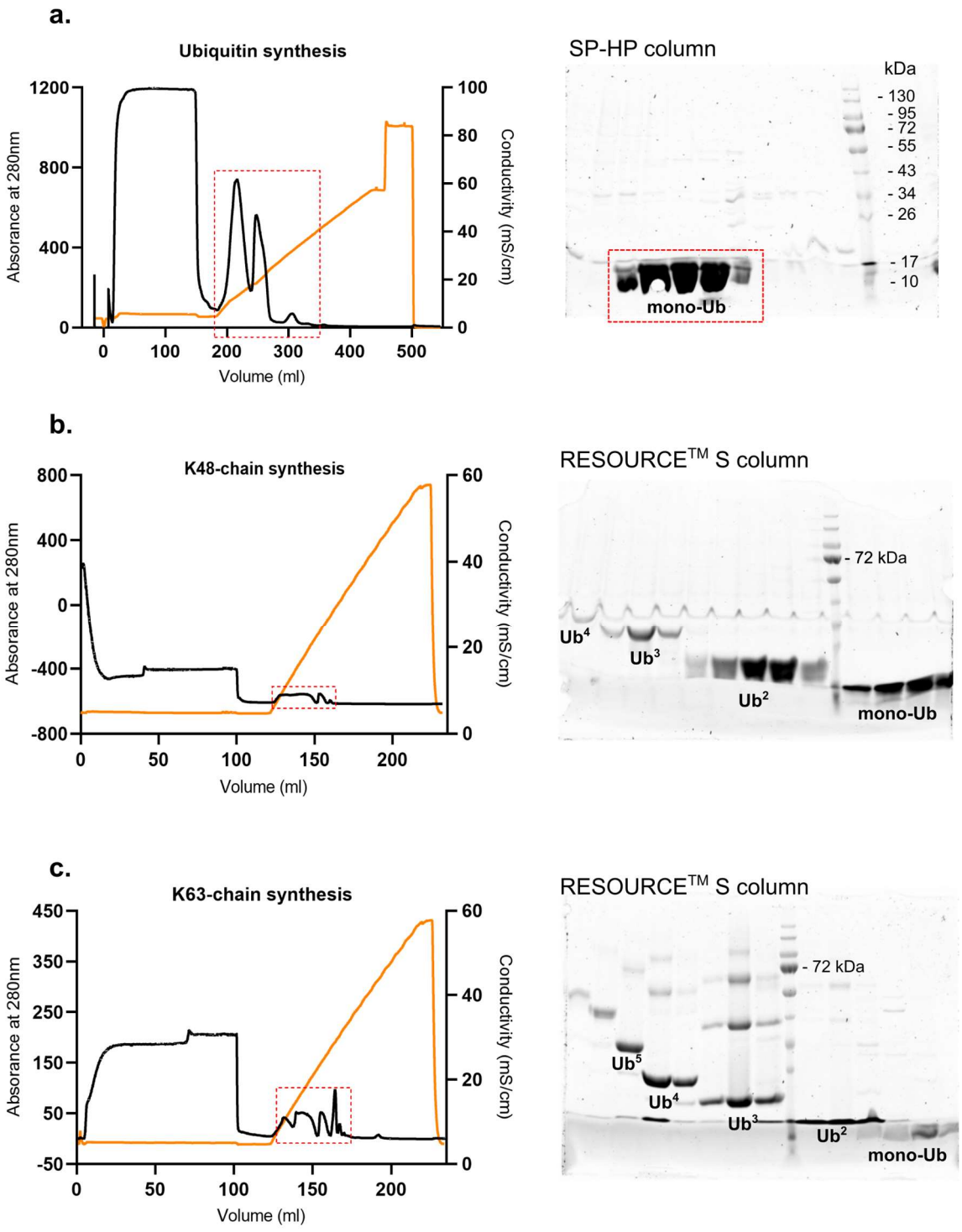

Figure 7.7: Ubiquitin purification and chain synthesis (Section 2.2.2.4 & 2.2.2.7). (a) After the ammonium acetate precipitation step, the lysate was applied to a SP-HP cation exchange column equilibrated with Ub buffer A. Ubiquitin was eluted with a linear gradient using Ub buffer B. The fractions containing ubiquitin (dotted red box) were analyzed by SDS-PAGE (right). Following incubation with the respective E1 and E2 enzymes, the K48-linked **(b)** and the K63-linked chains **(c)** were applied to a RESOURCE™ S cation exchange column and eluted using Ub buffer A and B. Fractions comprising the different ubiquitin chains (mono-ub, di-ub/Ub2, tri-ub/Ub3 and tetra-ub/Ub4) were analyzed by SDS-PAGE and pooled separately. Orange line represents buffer conductivity; black line denotes UV280 absorbance.

7.4.9 Gel-based K48-linked diubiquitin hydrolysis assay

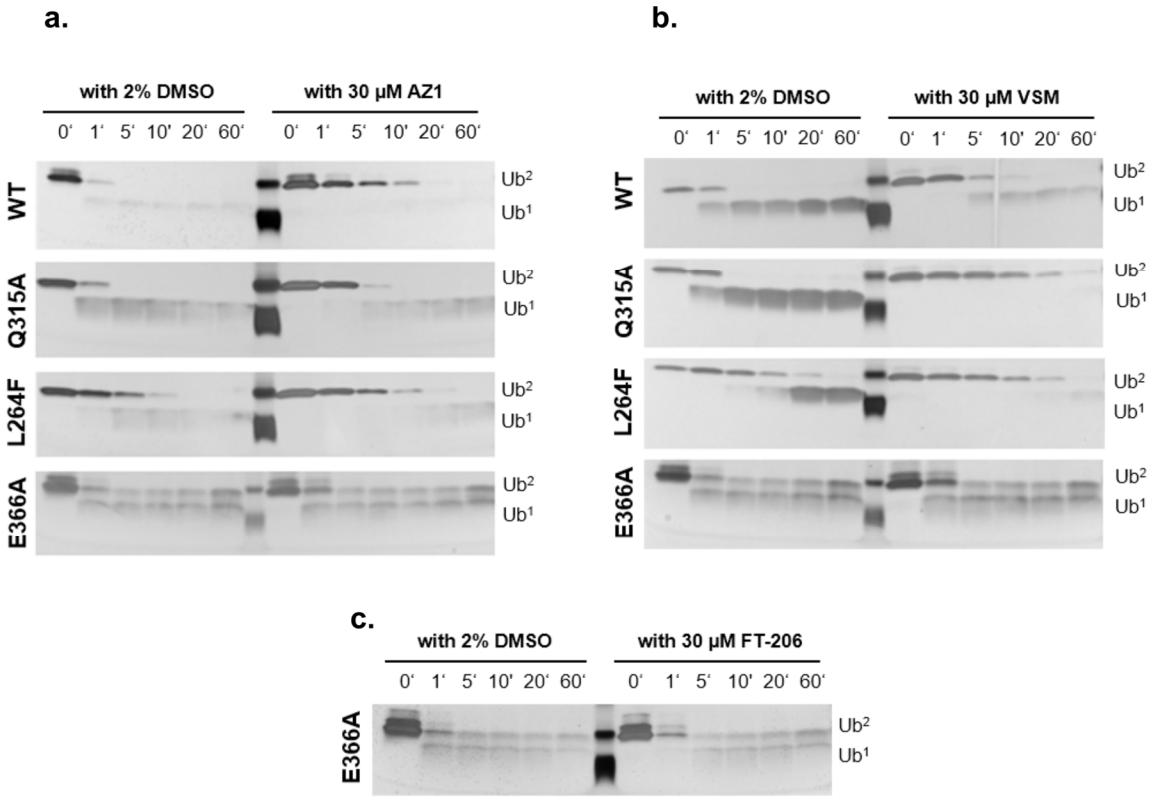

Figure 7.8: Gel-based K48-linked di-ubiquitin hydrolysis assay. Silver-stained SDS-PAGE gels depicting cleavage by the USP28cat (Δtip) WT protein and the Q315A, L264F and E3663A variants in the presence and absence of the inhibitor compounds (AZ1, a; Vismodegib/VSM, b; FT206, c). The left panel in the gels indicate the control lanes where the proteins were incubated with 2% DMSO and the right panel in the presence of 30 µM inhibitor. The time points are depicted above the bands. The di- and monoubiquitin are shown as Ub2 and Ub1, respectively.

LIST OF FIGURES

LIST OF TABLES

LIST OF PUBLICATIONS

Peer-reviewed publications:

Sauer F, Klemm T, Kollampally RB, Tessmer I, Nair RK, Popov N, Kisker C. Differential Oligomerization of the Deubiquitinases USP25 and USP28 Regulates Their Activities. Mol Cell. 2019 May 2;74(3):421-435.e10. doi: 10.1016/j.molcel.2019.02.029. Epub 2019 Mar 26. PMID: 30926243.

Joshi AC, Kaur P, Nair RK, Lele DS, Nandicoori VK, Gopal B. Selectivity among Anti-σ Factors by *Mycobacterium tuberculosis* ClpX Influences Intracellular Levels of Extracytoplasmic Function σ Factors. J Bacteriol. 2019 Feb 25;201(6):e00748-18. doi: 10.1128/JB.00748-18. PMID: 30617240; PMCID: PMC6398269.

Congress contributions:

Poster presentation –

14th International GSLS Student Symposium "EUREKA!" (October 9th-10th 2019). Poster title: *Structural and functional characterization of USP28 interaction partners.*

13th International GSLS Student Symposium "EUREKA!" (October 10th-11th 2018). Poster title: *Structural and functional analysis of USP28 interaction partners.*

ACKNOWLEDGEMENTS

I want to express my deepest and most sincere gratitude to my primary supervisor, **Prof. Caroline Kisker,** for welcoming me to join her team and work on this project. Thank you for understanding and supporting me when times got tough, both professionally and personally and for staying true to being a 'guide'. Her optimism is contagious, and it encourages you to work harder than before.

I would also like to thank my thesis advisory committee – **Prof. Nikita Popov,** for mentoring me during the initial years and sharing ideas to design this project; **Prof. Alexander Buchberger** for the thorough discussions during the meetings and for providing logical suggestions and constructive criticism. I am also grateful to **Prof. Christoph Sotriffer** for kindly agreeing to join the committee at a later stage and for brainstorming new ideas for the future of this project.

I am highly indebted to **Dr. Florian Sauer**, who was a constant source of support and helped me shape the project the way it is today and finally steer it to fruition. Thank you for the numerous discussions, suggestions and guidance. I have learnt a great deal from him – be it related to structural biology or science in general. I would also like to thank **Dr. Theresa Klemm**, my (former) USP28-partner and a dear friend, for helping me first understand the challenging yet fascinating world of DUBs. Thank you for checking in on me, even though we are miles apart!

I would like to acknowledge **Dr. Jochen Kuper** and **Prof. Hermann Schindelin** for their helpful suggestions and feedback during the group meetings.

This project could not have been completed without the support and funding from the DFG grants - **GRK2243** and **FOR2314**. The workshops and training modules organized by GRK2243 were a great addition to my learning process.

I am forever grateful to our secretaries – **Teresa Frank, Gabriele Ries, Andrea Schott-Heinzmann** and **Julia Seubert (GRK2243)**, for their help and support in the administrative part of my PhD tenure. Thanks to our technicians – **Monika Kuhn** and **Nicole Bader,** for the smooth functioning of our labs, making it easier for us PhD students; **Dr. Niklas Terhoeven**, **Roland Merkert** and **Dr. Bernhard Fröhlich** for providing IT support.

Thanks to all my friends and colleagues of the structural biology group **(Strubis)** at RVZ for creating a comfortable and wholesome work atmosphere. Special mention to the current and former members of **AG Kisker**, **AG Schindelin, AG Lorenz** (now at Max Planck Institute) and **AG Popov** (now at Universität Tübingen), whom I have had the pleasure of working with.

Most importantly, this work could not have been accomplished without the unwavering love, encouragement, and support of my family: my parents, **Preetha** and **Rajan**, for their unconditional love and blind faith in me; my sister – **Shree**, for her quirky ways of cheering me up and telling me that it is all going to be okay and my friends, for just being there whenever I needed them.

My husband, **Gaurav**, for his relentless belief in me, even at times when I lost mine; for his patience and motivation, for defying all odds and staying through it until the end – my personal cheerleader. Words fall short of describing what you mean to me. But in essence, *thank you for everything!*